

UC Berkeley

UC Berkeley Electronic Theses and Dissertations

Title

Unraveling Neptune's Atmospheric Structure from Multi-Wavelength Observations

Permalink

<https://escholarship.org/uc/item/2q61p881>

Author

Tollefson, Joshua Wayne

Publication Date

2019

Peer reviewed|Thesis/dissertation

Unraveling Neptune's Atmospheric Structure from Multi-Wavelength Observations

by

Joshua W Tollefson

A dissertation submitted in partial satisfaction of the

requirements for the degree of

Doctor of Philosophy

in

Earth and Planetary Science

in the

Graduate Division

of the

University of California, Berkeley

Committee in charge:

Professor Imke de Pater, Chair

Professor Burkhard Militzer

Professor Philip Marcus

Summer 2019

Unraveling Neptune's Atmospheric Structure from Multi-Wavelength Observations

Copyright 2019
by
Joshua W Tollefson

Abstract

Unraveling Neptune’s Atmospheric Structure from Multi-Wavelength Observations

by

Joshua W Tollefson

Doctor of Philosophy in Earth and Planetary Science

University of California, Berkeley

Professor Imke de Pater, Chair

Uranus and Neptune are representatives of the ‘ice giants’, one of the most common classes of exoplanets (Fressin et al., 2013). Thousands of exoplanets have been discovered thanks to the *Kepler* mission, and soon the James Webb Space Telescope will characterize their atmospheres in unprecedented detail. Such work will rely on the observations, techniques, and analysis used to study the Solar System’s gas giants. However, in many ways our own ice giants remain poorly understood. In this dissertation, I use multi-wavelength observations of Neptune to better constrain the bulk properties and dynamic patterns within the planet’s upper atmosphere.

At visible and near-infrared wavelengths, sunlight is reflected off the cloud tops and hazes populating the upper atmospheres of the giant planets. Bright cloud features can be tracked to extract velocities. By doing this over many latitudes, a global velocity field called the ‘zonal wind profile’ can be made. Here, I present zonal wind profiles for Jupiter and Neptune. These are constructed from *Hubble Space Telescope* WFC3 global maps of Jupiter taken between 2009 – 2016 and Keck NIRC2 images of Neptune taken in the H-band ($1.4 - 1.8\mu\text{m}$) and Kp-band ($2.0 - 2.4\mu\text{m}$) in 2013 and 2014.

I show that Jupiter’s zonal wind profile is stable throughout the observed period, apart from variations on the order of 10 m/s at the 24°N Northern Temperature Belt (NTB). These variations arise during periodic plume outbreaks at the NTB and are coupled to a decrease in the albedo. These findings suggest that material, normally unseen, is dredged upward due to these plumes. If plumes are a signature of deeper activity, the decrease in velocity we see at the NTB during outbreaks may be evidence of vertical wind shear.

I also find evidence of vertical wind shear at Neptune’s equator, with the H-band zonal wind profile offset eastward by 100 m/s at the equator relative to the Kp-band profile. I apply a new thermal wind equation applicable at the equator to reconcile this observed vertical wind shear with Neptune’s horizontal thermal and composition profiles. In order to match *Voyager*/IRIS derived temperatures (Fletcher et al., 2014), the equator must be enriched in methane compared to the mid-latitudes at pressures greater than 1 bar. I discuss

the implications of this finding with regards to global dynamics and compare and contrast to the other giant planets.

Radio wavelengths probe below the visible cloud deck. I analyze maps of Neptune taken with the Atacama Large Millimeter/Submillimeter Array (ALMA) and extended Very Large Array (VLA) to constrain Neptune’s deep opacity sources. The opacity source at radio wavelengths is dominated by H_2S and NH_3 as well as the collision-induced absorption of H_2 with H_2 , He, and CH_4 . Clear brightness temperature variations are present across Neptune’s disk caused by variations in these trace gases. These observations are the first to achieve the sensitivity, resolution, and wavelength coverage required to simultaneously extract the abundance profiles of H_2S , CH_4 , and NH_3 . I retrieve disk-average properties assuming both wet and dry adiabats. The disk-averaged data are consistent with profiles where trace gases are enriched by $30\times$ their protosolar value, apart from NH_3 which is $1\times$ its protosolar value.

In both the ALMA and VLA maps, I identify seven distinct latitudinal bands with discrete transitions in the brightness temperature. I use the radiative transfer code Radio-BEAR to generate model spectra of Neptune’s brightness temperature as a function of temperature and composition. I find best-fitting parameters to the H_2S , NH_3 , and CH_4 abundance profiles in each of the seven identified latitude bands using χ^2 -statistics and MCMC retrievals. Of note, the equator is more complicated than expected. Trace gases are enriched in the $2 - 12^\circ\text{N}$ band compared to neighboring latitudes. Here, the best-fit deep CH_4 abundance is $45\times$ the protosolar value (or 2.2% mixing ratio). H_2S is $30\times$ solar (or 7×10^{-4} mixing ratio) and supersaturated at the H_2S -ice cloud formation. I relate these findings to my near-infrared work and present a new schematic of Neptune’s global circulation structure.

To my friends, family, and teachers.

Contents

Contents	ii
List of Figures	iv
List of Tables	vi
1 Introduction	1
1.1 Planetary Spectroscopy	3
1.2 Neptune before <i>Voyager 2</i>	4
1.3 Neptune viewed by <i>Voyager 2</i>	6
1.4 Neptune 30 years after <i>Voyager 2</i>	10
1.5 Outline	12
2 Changes in Jupiter’s Zonal Wind Profile during and preceding the <i>Juno</i> Mission	13
2.1 Introduction	13
2.2 Description of Observations	15
2.3 Methods	16
2.4 Results	22
2.5 Discussion	29
2.6 Conclusion	36
2.7 Acknowledgements	37
3 Vertical Wind Shear in Neptune’s Upper Atmosphere Explained with a Modified Thermal Wind Equation	42
3.1 Introduction	43
3.2 Data	44
3.3 Atmospheric Feature Tracking	48
3.4 Results	50
3.5 Interpreting Differences in The H and K’ Zonal Wind Profiles	60
3.6 Conclusion	79
3.7 Acknowledgements	80

3.8	Appendix	81
4	Neptune’s Latitudinal Variations Viewed with ALMA	83
4.1	Introduction	83
4.2	Observations	85
4.3	Models	87
4.4	Results	90
4.5	Discussion	104
4.6	Conclusion	113
4.7	Acknowledgements	114
5	Neptune’s Latitudinal Variations Viewed with VLA	115
5.1	Introduction	115
5.2	Observations	116
5.3	Modeling	117
5.4	Results	119
5.5	Discussion and Conclusion	129
6	Conclusion and Future Work	131
6.1	Jupiter and Neptune in the Visible and Near-Infrared	131
6.2	Neptune in the Radio	133
A	A Derivation of the Equatorial Thermal Wind Equation	136
	Bibliography	142

List of Figures

1.1	Timeline of Neptune imaging	5
1.2	Jupiter and Neptune’s zonal wind profiles	7
1.3	Neptune’s upper atmosphere and depths probed at different wavelengths	8
2.1	Global map of Jupiter (2009)	17
2.2	Global map of Jupiter (2012)	18
2.3	Global map of Jupiter (2015)	18
2.4	Global map of Jupiter (2016, OPAL)	19
2.5	Global map of Jupiter (2016, <i>Juno</i> PJ3)	20
2.6	Residual maps (2016, OPAL)	23
2.7	Jupiter’s zonal wind profiles and residuals (2008 – 2016)	25
2.8	Jupiter’s zonal wind profiles and residuals (2009 hemispheres)	26
2.9	Jupiter’s zonal wind profiles and residuals (2012 interleaved)	27
2.10	Periodogram analysis	30
2.11	Timeline of 24N jet peak velocities and contrast (2000 – 2016)	33
2.12	NTB velocity profiles (2008 – 2016)	34
2.13	Jupiter NTB plume outbreak (2016, IRTF)	35
2.14	STB velocity profiles (2008 – 2016)	35
3.1	Keck H- and Kp-band images of Neptune (2013 – 2014)	46
3.2	Image combination method	47
3.3	Neptune moon orbits (2013)	49
3.4	Projected images and potential trackable clouds	50
3.5	Example of cloud-tracking over image slices	51
3.6	Example of cloud-tracking with cross-correlation	52
3.7	Example H-band tracked feature velocities (2013)	53
3.8	Example Kp-band tracked feature velocities (2013)	54
3.9	Neptune’s zonal wind profile in H- and Kp-bands (2013)	55
3.10	Neptune’s zonal wind profile in H- and Kp-bands (2014)	56
3.11	Neptune’s zonal wind profile in H- and Kp-bands from low-error data (2013)	57
3.12	Neptune’s zonal wind profile in H- and Kp-bands from low-error data (2014)	58
3.13	Neptune’s meridional velocities in H- and Kp-bands (2013)	59

3.14	Neptune’s meridional velocities in H- and Kp-bands (2014)	60
3.15	Kp-to-H I/F ratios and zonal wind velocities versus latitude	61
3.16	H- and Kp-band contribution functions	62
3.17	<i>Voyager</i> /IRIS derived temperature profile	65
3.18	<i>Voyager</i> /IRIS derived temperature uncertainties	66
3.19	Temperature profile needed to match observed vertical wind shear (no CH ₄)	71
3.20	Latitudinal-varying CH ₄ models	73
3.21	Virtual temperature needed to match observed vertical wind shear (with CH ₄)	74
3.22	Temperature profile needed to match observed vertical wind shear (with CH ₄)	76
3.23	Schematic of Neptune’s global circulation	78
4.1	Radio contribution functions and cloud formation altitudes	91
4.2	30× solar temperature and compositional profiles	92
4.3	Radio disk-averaged brightness temperatures and models	94
4.4	ALMA residual maps (2016 – 2017)	95
4.5	Residual temperatures (nominal model)	95
4.6	Residual temperatures (south pole models)	97
4.7	South pole H ₂ S and CH ₄ profiles	98
4.8	Spectral and opacity source impact on brightness temperature	100
4.9	H ₂ S profiles	102
4.10	Residual temperatures (H ₂ S models)	102
4.11	Residual temperatures (CH ₄ models)	103
4.12	Residual temperatures (<i>Ortho/Para</i> H ₂)	103
4.13	Best fit H ₂ S and CH ₄ abundances versus altitude and latitude	105
4.14	Residual temperatures (best fit model)	105
4.15	Residual temperatures (KT 2011)	105
4.16	Histogram of clouds tracked versus latitude	111
4.17	Schematic of Neptune’s global circulation	112
5.1	Expanded VLA maps of Neptune (2015)	118
5.2	Radio contribution functions and cloud formation altitudes	121
5.3	Temperature profiles for wet and dry adiabats	122
5.4	Corner plot of MCMC retrieved parameters (disk-average models)	123
5.5	MCMC retrieved abundance profiles (disk-average)	124
5.6	Disk-average temperatures and MCMC retrieved spectra	124
5.7	Corner plot of MCMC retrieved parameters (12°S – 32°S, wet adiabat)	126
5.8	Corner plot of MCMC retrieved parameters (12°S – 32°S, wet adiabat)	127
5.9	MCMC retrieved abundance profiles (12°S – 32°S)	128
5.10	Disk-average temperatures and MCMC retrieved spectra	129

List of Tables

1.1	Basic planetary properties	2
2.1	Compilation of Jupiter’s zonal wind profiles in the literature (1979 – 2016)	38
2.2	Summary of observations (2009 – 2016)	39
2.3	Year-to-year uncertainties and differences (2008 – 2016)	40
2.4	Year-to-year uncertainties and differences (2009 and 2012 hemispheres)	41
2.5	Year-to-year uncertainties and differences (2012 interleaved)	41
3.1	Zonal wind velocity fit parameters	52
3.2	List of planetary variables and values used in the thermal wind equation	64
3.3	Errors in temperature fits to Nth-degree polynomials	67
4.1	Summary of ALMA Observations (2016 – 2017)	85
4.2	Summary of ALMA observation configurations (2016 – 2017)	86
4.3	Summary of observed and modeled millimeter disk-averaged brightness temperatures.	88
4.4	Model descriptions	106
4.5	Model χ^2 -statistics	107
5.1	Summary of VLA Observations (2015)	116
5.2	Summary of observed and modeled millimeter disk-averaged brightness temperatures.	120
5.3	MCMC fit results (disk-average models)	122
5.4	MCMC fit results (12°S – 32°S)	128

Acknowledgments

During particularly stressful times at Berkeley, I sometimes lamented that I should have taken a gap year between undergrad and grad school. I had little experience with jobs outside of summer research stints and teaching, and wondered if I was only interested in graduate school because it was an ‘easy’ choice - a comfortable path, one where I could put off big life decisions. Easing into grad school was hard for me, because I doubted whether being an academic and researcher was actually right for me. Was I actually passionate about my work, or was I just phoning in the hours? Six years after first entering Berkeley, I can confidently say that I thoroughly love the work I’ve done and feel more accomplished than I thought possible. This is due in no small part to the wonderful advisers I’ve had: Professors Imke de Pater, Burkhard Militzer, and Phil Marcus, whose enthusiastic support, patience, and flexible attitudes allowed me pursue my own research interests and made me feel confident in my own abilities.

The planetary science community at Berkeley is one-of-a-kind. Thanks especially to Mike Wong and Statia Luszcz-Cook, who patiently brought me up to speed with planetary atmospheres, image processing, and radiative transfer. Fellow students Ned Molter and Chris Moeckel were also amazing collaborators, openly sharing their knowledge and insight when I had questions.

I would also like to mention the number of delightfully diverse LGBTQ+ scientists I have met over these years. Their visibility at conferences and online was so important in helping me navigate my own career and personal growth. I thank them for sharing their unique stories regarding work, family, and overcoming adversity.

My amazing friends were always there to remind me that there is life outside of school and research. Chris Hallacy, Michael Meador, Adam Hart, and Craig Day, I probably owe you each hundreds of dollars in rent after all the weekends I’ve crashed at your places. Thank you for not collecting on it. Helen and Kyle Merson-Wi, I’m so happy that I got to know you both better - your wedding was beautiful and I’m so glad to have been a part of it. The Pacheco family: Mal, Michelle, Nicole, and Jake - you are truly home-away-from-home. Christine Chang and Christine Wu, you are my oldest, closest college friends, and I deeply value our companionship, even if our careers have kept us apart.

My parents, Michele and Mark Tollefson, cultivated my interest in math and science from an early age. Looking back, I am amazed at all the time and resources you sacrificed to ensure I received a quality education. Even though I am now many states away, I still feel your unconditional love and support everyday. Thank you so so much.

Most of all, I need to extend my sincerest thanks to my partner Avin Andrade, who was witness to it all. You’ve always had confidence in me, even during times when I had none in myself.

Chapter 1

Introduction

After the Sun, our Solar System is dominated in mass by the four giant planets: Jupiter, Saturn, Uranus, and Neptune. This fact pervades formation and evolution theories of the solar system. At the start of their formation, the giant planets began as small clumps of rocky material, slowly accreting other planetesimals into cores. After a few million years, these cores became large enough to experience ‘runaway growth’, quickly gobbling up leftover rocky material and gas in and around their orbits. Simultaneously, the cumulative mass of these bodies gravitationally perturbed one-another, driving the radial movement of everything from dust-sized grains up to the giant planets. Today, planetary scientists work to piece together how the initial formation and evolution of the giant planets explain the current observed distribution of material within our Solar System. The thousands of newly discovered exosolar systems and planets put these theories to the test (de Pater and Lissauer, 2010).

Much of our understanding of the solar system relies on telescope observations taken millions of miles away from the target. Unfortunately, *in-situ* probes to directly measure planetary sizes, masses, composition, and structure are rare due to their expense. Thankfully, these fundamental quantities can still be calculated even at vast distances.

The diameter d of these bodies is calculated by their apparent size δ and distance D from the observer. If the apparent size is small, these quantities are related:

$$\delta \sim \frac{d}{D} \quad (1.1)$$

An object’s distance from the Sun, and therefore its diameter, can be derived by calculating its orbital parameters from repeated observations. The mass M of the planet can be estimated via Kepler’s second law if a moon with measured period T and semi-major axis a orbits the planet:

$$\frac{a^3}{T^2} \approx \frac{GM}{4\pi^2} \quad (1.2)$$

From both the diameter and mass, the planet’s mean density ρ can be calculated, assuming a spherical body:

	Earth	Jupiter	Saturn	Uranus	Neptune
Semi-Major Axis (A.U.)	1.0	5.2	9.5	19.1	30.1
Equatorial Radius (km)	6371	71492	60268	25559	24766
Mass (10^{27} g)	5.9736	1898.6	568.46	86.832	102.43
Density (g cm^{-3})	5.515	1.327	0.6873	1.318	1.638

Table 1.1: Planetary properties. The equatorial radius for the gas giants is defined at 1 bar.

$$\rho = \frac{3M}{4\pi(d/2)^3} \quad (1.3)$$

Table 1 lists current measurements of each planet’s diameter, mass, and mean density (de Pater and Lissauer, 2010). The planet’s mean density is the most interesting of these quantities, as it hints at the interior structure and composition of the body. Planets with $\rho \sim 1$ g/cc (e.g. Saturn) must contain considerable quantities of hydrogen and helium. The terrestrial planets have much higher densities, $\rho \sim 5$ g/cc, implying mostly rocky constituents. Uranus and Neptune lie in between these regimes, meaning their compositions are a mixture of light gas and rocky material, or contain substantial icy material, which is lighter than rock.

The interior structure of planets can be retrieved by solving equations of state, i.e. relationships between density, temperature, and pressure at thermal equilibrium for a given material. In these models, the interiors of planets are assumed to resemble spherical shells of some unknown thickness, mass, and composition. At low pressures and temperatures, the theory is relatively straightforward (e.g., the equation of state follows the ideal gas law). But at the extreme temperatures and pressures within the interiors of these bodies, the equations of state are complex. Modern laboratory and computational work seek to fill the voids in phase space for a variety of materials and apply these results to Solar System bodies and exoplanets alike (Stevenson, 1982; Seager et al., 2007; Militzer and Hubbard, 2013).

Broadly speaking, these models find that the interiors of giant planets resemble spherical shells, consisting of a large rocky core underlying a molecular envelope of hydrogen and helium gas. This is in contrast to the terrestrial planets, whose interiors were too small to amass and retain a substantial hydrogen and helium atmosphere in the early history of the Solar System. Uranus and Neptune are also rich in trace ice gases like methane, water, hydrogen sulfide, and ammonia, and are therefore referred to as the ‘ice giants’.

The compositions of planets are tied to their formation history and the planetary nebula from which they formed. For instance, in cold environments past the ‘snow line’, the condensation of water and other ices will lead to planetary enrichment or depletion in carbon and oxygen that varies in space and time. Thus, determining the elemental abundance ratios within the planets is needed to fully understand their formation histories. Telescope observations are a powerful means of informing theories about planetary formation and evo-

lution, even though only the outer sliver of a planet’s atmosphere is seen. Knowledge of the size, temperature structure, molecular abundances, and dynamic patterns of the outer atmosphere constrains these same properties deeper down.

In the remainder of this chapter, I briefly discuss planetary spectroscopy and a timeline of observations and analysis of Neptune. Neptune is the least studied planet in our Solar System, being the farthest planet from the Sun and only imaged up-close once with *Voyager 2*. Neptune lies in the middle between two extremes in our solar system: the small, rocky terrestrial bodies and larger, hydrogen-dominated gas giants. The *Kepler* mission revolutionized planetary science with the discovery of thousands of exoplanets. Using different techniques than described above, the radii, masses, and mean densities of hundreds of exoplanets have been calculated and soon new spacecraft will obtain high-resolution spectroscopy of their atmospheres. After accounting for observational biases, sub-Neptune to Neptune sized planets (radii 2–4 times that of Earth’s) are the most common types of planets in existence (Fressin et al., 2013). For these reasons, Neptune and its largest moon Triton have been targets for proposed spacecraft missions to be launched in the 2030’s. Observing Neptune today has never been more relevant.

1.1 Planetary Spectroscopy

In the upper atmospheres of planets, the primary means of energy transport is the absorption and re-emission of photons. The process of how the intensity of radiation changes through the atmosphere is known as radiative transfer.

A planetary spectrum, i.e. how intensity varies with wavelength, can be constructed from many observations of the target object. The aim of radiative transfer modeling is to compare the measured spectrum to that modeled through the equation of radiative transfer (de Pater and Lissauer, 2010). The optical depth τ is a particularly important quantity in this analysis. The optical depth is a dimensionless measure of the amount of radiation that is lost or modified through an atmospheric layer and is strongly dependent on wavelength. The type and quantity of atoms and molecules and the temperature and pressure of their environment all impact τ . As a rule of thumb, an observation at a certain wavelength probes altitudes for which $\tau \approx 1$. This is because the transmittance of radiation falls off by $e^{-\tau}$ following Beer’s Law. As we’ll see in the following sections, modelers of planetary atmospheres take advantage of this fact to construct temperature and composition profiles by inverting measured intensities over many wavelengths.

To first order, planetary spectra resemble two blackbody curves. At visible wavelengths, a planet’s atmosphere reflects light from the Sun. This includes both scattering from cloud particles, aerosols, and other gases, as well as absorption and emission from these molecules. At infrared and radio wavelengths, the spectrum is made of the planet’s own thermal emission. In particular, the expression for blackbody radiation can be approximated at long, radio wavelengths via the Rayleigh-Jeans law, which relates the spectral radiance $B_\nu(T)$ to the brightness temperature T and frequency ν :

$$B_\nu(T) = \frac{2\nu^2 k_b T}{c^2}, \quad (1.4)$$

where c is the speed of light and k_b is the boltzmann constant. This result is especially useful in Chapters 4 and 5.

Planetary spectra also consist of absorption and emission lines resulting from transitions in energy levels as atoms or molecules absorb or emit photons. These lines are the main means of quantifying the composition of a planet's atmosphere. The deeper the line, the more abundant the absorbing/emitting atom or molecule. Through these features, it was eventually seen that planets are diverse in their compositions (Slipher, 1909, 1933; Adel and Slipher, 1934a,b).

1.2 Neptune before *Voyager 2*

Their far distance from the Sun makes the ice giants difficult to observe and study. For over a century since its discovery in 1846, Neptune looked like a blurry blue disk. The angular resolution in radians, θ , of a telescope is approximated as:

$$\theta \sim \frac{\lambda}{D}, \quad (1.5)$$

where λ is the wavelength of the observation and D is the diameter of the telescope. The angular diameter (the apparent size of the planetary disk on the sky) of Neptune is $\sim 2.4''$. For a 1.0 m optical telescope, $\theta \sim 0.1 - 0.2''$, meaning roughly one-tenth of Neptune's disk can be resolved (though in practice, this is limited further by Earth's atmosphere). With the best ground-based telescopes available in optimal seeing conditions, Neptune's apparent fuzziness could be mitigated and both temporal and spatial brightness variations could be discerned (Cruikshank, 1985). Studies of Neptune's diurnal variations showed brightness changes in the near-infrared ($1 - 3 \mu\text{m}$), thought to be caused by bright methane clouds. The first detection of discrete cloud features on Neptune was presented by Smith et al. (1979) in the 890 nm strong methane-band. Hammel (1989) summarized a decades worth of observations of Neptune and reported on new images with excellent seeing, finding that the brightest clouds were between latitudes of $30 - 60^\circ\text{S}$, with some fainter features seen as far poleward as 70°S . Prior to 1986, bright northern hemisphere clouds were also seen, but in Hammel's 1987 observations, none appeared. Neptune's equatorial region remained quiescent throughout the entire observing program. Interestingly, short-term variability in the observed brightness was seen in both the discrete features and the featureless atmosphere. Not only is there distinct latitudinal structure in the clouds of Neptune, but Neptune's clouds and atmosphere can change morphology and disappear on the order of years or less.

Given Neptune's distance from the Sun, it is perhaps surprising that such dynamic atmospheric activity could be driven from solar insolation alone. A planet's energy balance is analyzed by comparing the power received from the sunlit hemisphere to that reradiated.

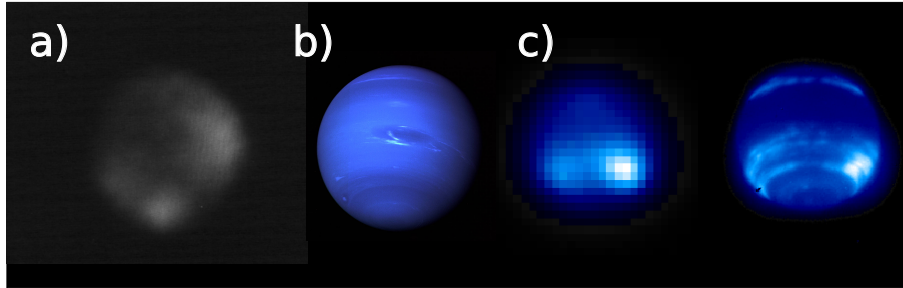


Figure 1.1: Sample images of Neptune, showing how spacecraft and improved instrumentation changed our view of the planet forever. a) Methane-band image taken from a 2-m telescope on June 1987 (Hammel, 1989). b) *Voyager 2* visible image of Neptune taken August 20, 1989 (image credit: NASA). c) Keck images of Neptune without and with (left and right respectively) adaptive optics taken on June 1999 (image credit: Center for Adaptive Optics).

Murphy and Trafton (1974) made the first determination of Neptune’s energy balance by utilizing measured thermal fluxes, spectral albedo data, and effective temperatures from the literature. They found that Neptune emitted 2 – 3 times as much energy as it received, implying evidence of vigorous convection as a means of transporting energy upwards. Cloud formation is one means of powering convection and the observed latitudinal brightness/cloud distribution could be explained with convection, as mass motions of rising (sinking) air correspond to wet (dry) air.

For a radio telescope array with a maximum baseline of 1.0 km observing at 1 cm, $\theta \sim 2.0''$, roughly the diameter of Neptune. Thus, only disk-averaged properties could be determined from early radio observations. Unlike the visible and NIR wavelengths, mid-infrared and radio wavelengths probe Neptune’s stratospheric and tropospheric thermal emission. The first radio observations of Neptune were taken at 1.9 cm with a 140-ft. telescope at the National Radio Astronomy Observatory by Kellermann and Pauliny-Toth (1966). Their observations found disk-averaged brightness temperatures of 180 ± 40 K, considerably larger than the expected equilibrium temperature due to solar heating of 40 K at this wavelength. The main opacity source in the radio is ammonia gas, meaning this species was expected to be depleted to account for the observed high temperatures. Future radio work constrained H_2S , another major opacity source, requiring 30 – 60 \times the protosolar S/H abundances (de Pater and Richmond, 1989; de Pater et al., 1991). Moreover, good fits to the data were obtained only if the deep NH_3 abundance did not exceed the protosolar N value.

To summarize, before 1989 we knew Neptune was dynamic, containing enough energy to generate bright cloud activity. It was known that Neptune was comprised primarily of hydrogen, helium, and trace icy material: CH_4 , H_2S , and NH_3 . The *Voyager 2* flyby of Neptune would expand our understanding of Neptune forever, producing the first high-resolution images of the planet. The launch of the *Hubble Space Telescope*, rise of ground

based telescopes and the implementation of adaptive optics, and the expansion of radio arrays ensured that regular, high-resolution studies of Neptune across the wavelength spectrum would continue long after *Voyager* came and went.

1.3 Neptune viewed by *Voyager 2*

Voyager 2 was the only human-made object to visit Neptune. The spacecraft reached its closest approach on August 25, 1989, flying 5000 km above Neptune's cloud tops. In its flyby, *Voyager 2* snapped thousands of high-resolution photos of Neptune with the Imaging Science System. These images revealed that Neptune was more exotic and dynamic than even the best ground-based observations had predicted.

Magnetic Field

The rotation period (day length) of gas giants is hard to determine as they lack definable surfaces and atmospheric clouds may not rotate at the same rate as the interior. Instead, the rotation period is estimated by the magnetic field, which is a direct proxy for the motions of the convective interior. Warwick et al. (1989) were the first to calculate Neptune's length of day, 16.11 ± 0.05 hr, from periodic radio bursts and smooth radio emissions within the planet's magnetosphere as *Voyager 2* approached the planet.

Perhaps more interestingly, *Voyager 2* found that the magnetic fields of Uranus and Neptune were significantly tilted and off-center (Ness et al., 1986, 1989; Connerney et al., 1987, 1991). These findings violated the idea that global magnetic fields are dominated by axially-symmetric dipoles, as seen on Earth, Jupiter, and Saturn. Their strange magnetic fields are another example of the unique characteristics of the ice giants. In fact, dynamo models demonstrated that their unusual magnetic fields is the result of convective regions different than that of the other planets (Stanley and Bloxham, 2004, 2006).

Zonal Wind Profiles

One of the most surprising findings from the *Voyager 2* flyby was the immense display of atmospheric activity on Neptune. Uranus, by contrast, appeared quite bland, lacking any notable bright cloud features. Other than sharing a blue hue, Uranus and Neptune could not appear more different.

These bright cloud features that populate the upper atmosphere of Neptune are assumed to be passive tracers of the background atmospheric motions. The now-known rotation period (16.11 hr) of Neptune is subtracted from the extracted cloud velocity to obtain the east-west or zonal wind speed. Using many high-resolution images, Limaye and Sromovsky (1991) tracked dozens of bright cloud features and extracted a zonal wind profile, i.e. the east-west wind speed as a function of latitude. Their results showed that Neptune's winds speeds are the fastest in the solar system, reaching wind speeds of 400 m/s or 900 mph.

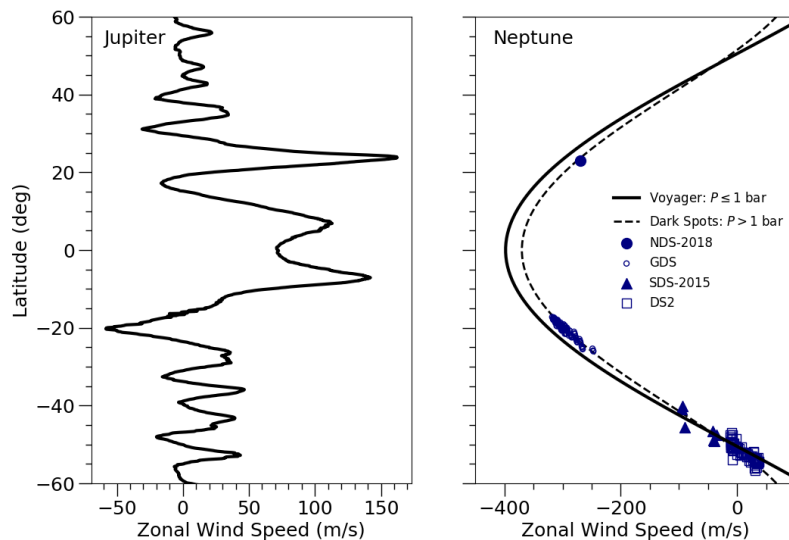


Figure 1.2: The zonal wind profiles of Jupiter and Neptune (solid black lines). Neptune’s winds reach peak speeds much larger than Jupiter’s. The zonal wind speed of Neptunian dark spots for which there are data are also plotted as blue points (Sromovsky et al., 1993; Wong et al., 2018; Simon et al., 2019). The dark spots fit a profile which is offset eastward (less negative values) from *Voyager* by 30 m/s, shown as a dashed black line.

By contrast, Jupiter’s wind speeds peak at 150 m/s. A comparison of these planets’ zonal wind profiles are shown in Figure 1.2. However, high-dispersion in the cloud tracking results and Neptune’s tilt away from the Earth and spacecraft limited both the precision and global scope of the results.

The zonal wind profile is an important dynamical quantity as it relates to the density distribution (in both temperature and composition) within the atmosphere and interior. How the zonal wind field is powered in the giant planets and how deep the winds are driven remains an open question.

Atmospheric Structure

The first profiles of Neptune’s upper atmosphere were possible thanks to the high quality of *Voyager 2* measurements across the electromagnetic spectrum. This is because different types of observations probe different parts of the atmosphere. For example, emission in the infrared is primarily thermal and originates in the stratosphere, whereas the radio probes deep into the troposphere. The pressures seen for some of the observations done by *Voyager 2* are shown to the right of Figure 1.3.

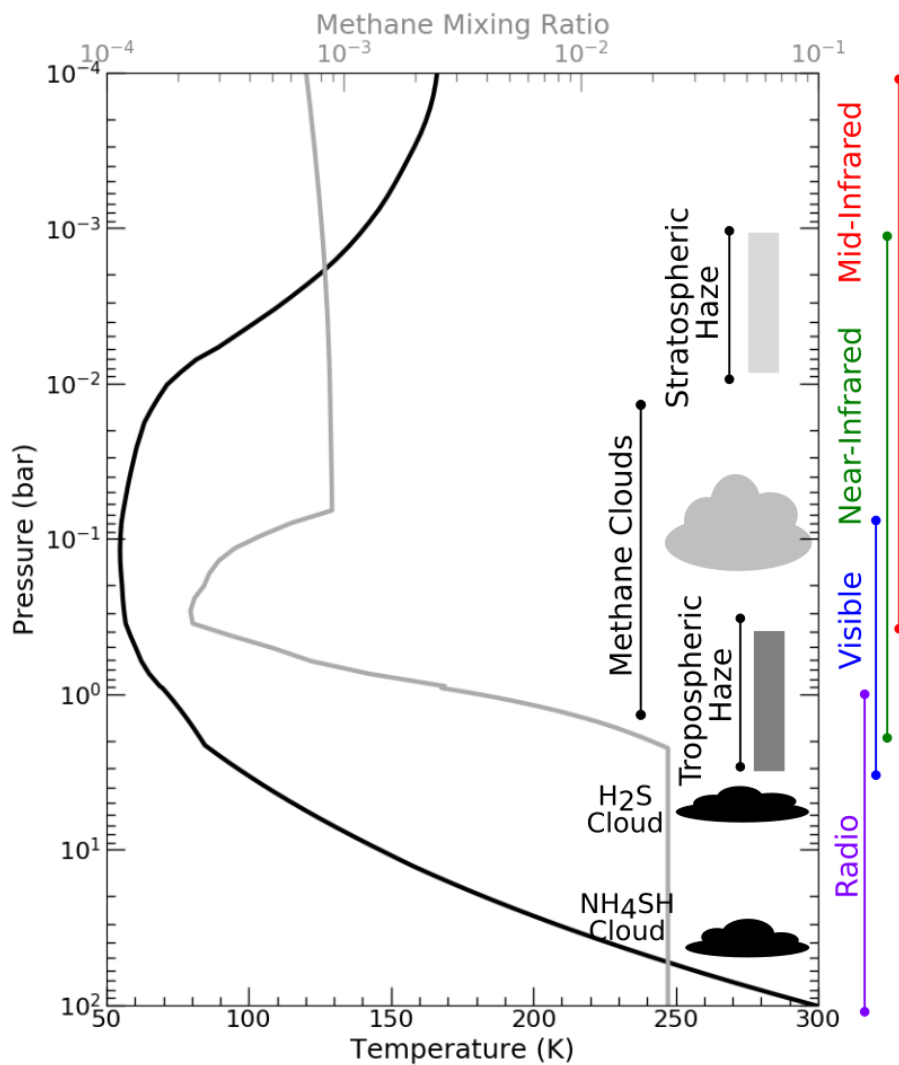


Figure 1.3: Vertical profile of Neptune’s upper atmosphere. The solid black line is Neptune’s temperature profile set by radio occultation measurements at 1 bar by Lindal (1992) and a wet adiabat below 1 bar. The solid gray line is Neptune’s methane profile. The deep abundance was determined by Baines et al. (1995).

Conrath et al. (1991) determined Neptune’s stratospheric temperature profile using *Voyager 2*’s infrared spectrometer (IRIS). They also found latitudinal variations in temperature, with the equator a few degrees warmer than the mid-latitudes and the south pole even warmer than both. These variations are related to Neptune’s zonal winds via the thermal wind equation. This relation and the wind and thermal results from Limaye and Sromovsky (1991) and Conrath et al. (1991) predict that Neptune’s zonal winds should decrease in strength with increasing altitude, providing an interesting dynamic constraint for future work.

Pearl and Conrath (1991) used these IRIS measurements to determine Neptune’s energy balance and narrow the error bars present in earlier work. Their results showed Neptune emits about 2.6 times as much flux as it receives from the Sun, in line with pre-*Voyager* estimates. This confirmed that Neptune’s troposphere is convective and follows either a dry or wet adiabat:

$$\frac{dT}{dz} = -\frac{g}{c_p}, \quad (1.6)$$

$$\frac{dT}{dz} = -\frac{g}{c_p + L_s dw_s/dT}. \quad (1.7)$$

Here, T is the temperature as a function of altitude z , g is the gravitational constant, c_p is the specific heat at constant pressure, L_s is the latent heat of condensation, and w_s is the mass fraction of the condensate. Radio occultation measurements as *Voyager 2* flew by Neptune constrained the temperature at 1 bar to 72 K Lindal (1992). This measurement is an anchor point from which the above equations can be solved once the main constituents are known. Lindal (1992) also derived a CH_4 tropospheric abundance of 2.3%, enabling the tropospheric temperature profile to be computed. This high abundance of CH_4 also explains Neptune’s blue appearance, as CH_4 readily absorbs red light. Both the temperature and methane profiles are shown in Figure 1.3.

By synthesizing ground-based observations, *Voyager* IRIS and radio occultation results, and theoretical work, Baines et al. (1995) constructed a model structure of Neptune’s upper atmosphere, also shown in Figure 1.3. The upper stratosphere is dominated by hydrocarbon haze layers, formed by photolysis of CH_4 . The absorption of sunlight by these hazes results in a warming of the atmosphere and a temperature inversion. In Neptune’s troposphere, the temperature decreases with increasing altitude. As a result of this cooling, trace gases: CH_4 , H_2S , and NH_3 , all condense to form clouds. Around 1 bar, a methane haze extends from the tropopause down to the methane condensation pressure. Between 0.01 – 1 bar, bright methane clouds populate the planet, reflecting visible and near-infrared light. Clouds formed by H_2S and NH_3 condensation exist at deeper pressures. In particular, an optically-thick H_2S cloud layer is believed to form around 4.5 bar, blocking all but the longest wavelength radiation. These long wavelengths are in turn blocked by the NH_4SH cloud layer, which forms at 43 bar.

Dark Spots

Perhaps most mysterious of all was the discovery of ‘The Great Dark Spot’, an Earth-sized feature characterized by its low contrast compared to the background atmosphere. A sister feature to the Great Dark Spot, creatively named ‘Dark Spot 2’, was also discovered at high southern latitudes. Based on their behavior, Neptune’s dark spots are believed to be anticyclones, analogous to the Great Red Spot on Jupiter (Smith et al., 1989). Dark spots have the highest contrast at blue visible wavelengths and disappear at longer and shorter wavelengths (Wong et al., 2018). As a result, Neptunes dark spots are believed to originate deep in the atmosphere, providing a rare window into the atmosphere below the cloud deck at visible wavelengths.

Planetary vortices are extremely sensitive to background horizontal wind shear. Sromovsky et al. (1993) measured the east-west drift rate of the Great Dark Spot and Dark Spot 2 as they travelled latitudinally over several months, finding they moved at a predictable eastward offset from the *Voyager* wind profile (see: Figure 1.2). Due to the high-dispersion in bright cloud tracking, Neptune’s dark spots may be a more reliable tracer of the background atmospheric winds. Moreover, since bright clouds are located at higher altitudes ($P < 1$ bar) than the dark spots ($P > 1$ bar), the observed wind speed differences imply vertical wind shear in Neptunes atmosphere. This wind shear is opposite of that predicted by the IRIS measurements in Conrath et al. (1991), complicating our understanding of the dynamics within Neptune’s upper atmosphere.

1.4 Neptune 30 years after *Voyager 2*

In a timely coincidence, this thesis will be submitted almost exactly 30 years after the *Voyager* close encounter flyby with Neptune. Since that encounter, advances in ground-based observing and the launch of the *Hubble Space Telescope* enabled regular, high-resolution observations of Neptune. Observations from ground-based telescopes (Keck, VLA, and ALMA), and the *Hubble Space Telescope* are all heavily featured in this dissertation.

Ground-Based Observing

The largest problem facing ground-based observations is Earth’s own atmosphere. Incoming light interacts with the atmosphere in ways that can significantly degrade the quality of an image. Water, carbon dioxide, and oxygen molecules are the worst culprits, as they absorb radiation over a broad range of wavelengths. Therefore, ground-based facilities are limited to ‘windows’ in the radiation spectrum in which there are no absorption features from Earth’s own atmosphere. Even within these windows, ground-based observers must contend with atmospheric turbulence, which distorts incoming light from a planet or star, reducing the angular resolution of the image.

At facilities like the Keck Observatory, a technique called Adaptive Optics (AO) was implemented in the late 90’s to mitigate these effects. AO uses a deformable mirror to

correct for the distortions in the wavefront from atmospheric turbulence in real time. The improvement in image quality is shown in Figure 1.1; numerous, small distinct cloud features and latitudinal-bands are seen in the AO image.

Another technique, called interferometry, is also used to improve the angular resolution. At radio wavelengths, the angular resolution of an image of Neptune would be poor if a single antenna was used. Instead, several antennas are arranged to form an array, with the resolved scales determined by the distances between antennas. Since each antenna is spaced at slightly different distances from the observed body, the incoming wavefront hits each antenna at a different time. These signals are correlated between antenna pairs to produce visibility measurements. Visibilities are measured in the u - v plane, where u - v are the distances between antenna pairs projected onto the sky in the direction of the source. An image of the body is produced by taking the Fourier Transform of the visibilities over the u - v plane. However, the quality of the image is limited to the spacing and number of antennas in the array, as gaps in the u - v plane mean some aspect of the image is lost. Over the past decade, the addition of more radio telescopes, improvements in instrument sensitivity, and expanded wavelength coverage have all improved image quality and the number of ways we can look at Neptune.

The *Hubble Space Telescope*

The launch of the *Hubble Space Telescope* (HST) in 1990 revolutionized astronomy forever. While the improvements in ground-based facilities are novel, they are always at the mercy of the local weather. HST was the first optical observatory to be placed in space, far above Earth's turbulent atmosphere, clouds, and light pollution. Its impact on our understanding of Neptune can not be overstated.

In 1994, HST discovered that both the Great Dark Spot and Dark Spot 2 disappeared without a trace. In their stead, HST found new dark spots pop up and dissipate as suddenly as they appeared. Not only are dark spots rare, but they are dynamic, moving at velocities different than the zonal wind profile would predict. To date, HST has discovered four dark spots on Neptune. But due to their transient nature, it is hard to time observations to study dark spots in much detail. It is believed that dark spots are a window into the deep atmosphere of Neptune, which is normally obscured by a bright haze.

HST has also been invaluable in monitoring the physical properties and variations on Neptune, following up on the findings pre-*Voyager*. HST/STIS spectroscopy has revealed latitudinal variations in Neptune's haze and methane content (Karkoschka and Tomasko, 2011). Neptune has also become significantly cloudier since *Voyager* and is much brighter from the time its albedo was first regularly tracked in the 1950s (Lockwood and Jerzykiewicz, 2006). In the last few years, Keck and HST have monitored massive bright clouds that erupted at the equator of Neptune, a normally cloud-free region (Molter et al., 2019). These changes are remarkable, given Neptune's long, 40-year seasons. What causes this global, local, and temporal dynamism is not well understood, but is almost certainly related to the

mass circulation within Neptune’s upper atmosphere, its composition, and how material is brought upward from the interior.

1.5 Outline

This thesis presents multi-wavelength observations Neptune. Since each type of observation probes a different part of a planetary atmosphere, a crude 3D construction of Neptune’s upper atmosphere can be made by synthesizing these data.

In Chapter 2, I divert my focus off of Neptune to first analyze changes in Jupiter’s zonal wind field over the past decade. I show that Jupiter’s zonal winds are relatively stable globally apart from a strong northern jet. This global stability and local variation is compared and contrasted to Neptune’s own zonal wind field in Chapter 3. Here, I present Keck near-infrared images of Neptune and use cloud-tracking software to derive new zonal wind profiles of Neptune in two filters. Differences in the zonal wind field between these filters are evidence of vertical wind shear. I use a new thermal wind equation that is applicable at the equator to determine what the observed wind shear implies about Neptune’s latitudinal methane and temperature field. A derivation of this new equatorial thermal wind equation is presented in Appendix A. In Chapter 4, I report on millimeter continuum observations of Neptune taken with the Atacama Large Millimeter/Submillimeter Array (ALMA). I use a radiative transfer code to analyze latitudinal variations in the brightness temperature across Neptune’s disk. These variations are related to the local abundance of trace gases. Additional radio maps of Neptune are shown in Chapter 5. These observations were taken with the extended Very Large Array (VLA). Like the ALMA maps, these are spatially-resolved. I retrieve composition profiles of Neptune’s trace gases using an MCMC implementation of our radiative transfer code. Combining the results within this thesis and from other instruments, I present a schematic of Neptune’s upper atmospheric structure and dynamics.

Chapter 2

Changes in Jupiter’s Zonal Wind Profile during and preceding the *Juno* Mission

We present five epochs of WFC3 HST Jupiter observations taken between 2009–2016 and extract global zonal wind profiles for each epoch. Jupiter’s zonal wind field is globally stable throughout these years, but significant variations in certain latitude regions persist. We find that the largest uncertainties in the wind field are due to vortices or hot-spots, and show residual maps which identify the strongest vortex flows. The strongest year-to-year variation in the zonal wind profiles is the 24°N jet peak. Numerous plume outbreaks have been observed in the Northern Temperate Belt and are associated with decreases in the zonal velocity and brightness. We show that the 24°N jet peak velocity and brightness decreased in 2012 and again in late 2016, following outbreaks during these years. Our February 2016 zonal wind profile was the last highly spatially resolved measurement prior to *Juno*’s first science observations. The final 2016 data were taken in conjunction with *Juno*’s perijove 3 pass on 11 December, 2016, and show the zonal wind profile following the plume outbreak at 24°N in October 2016.¹

2.1 Introduction

The most striking feature of Jupiter is its banded structure, home to swaths of bright, colorful clouds and immense vortices. The observed zonal flow, defined as the longitudinal average of the east-west winds in the visible cloud deck, is one of the most fundamental constraints on the circulation of Jupiter’s atmosphere (Ingersoll et al. (2004)). Jupiter’s zonal wind profile (ZWP) has been a subject of intense study since the Voyager missions. Despite regular derivations of Jupiter’s ZWP over the past 30 years, listed in Table 1, the winds have

¹This work has been previously published in *Icarus* (Tollefson et al., 2017) and has been reproduced with permission from all co-authors.

remained remarkably stable, with speeds up to 150 m s^{-1} and with variability on the order of 10 m s^{-1} . In contrast, the clouds of Neptune have displayed evidence of peculiar dynamics ever since Neptune’s ZWP was first derived from Voyager 2 data (Limaye and Sromovsky (1991)). In particular, individual bright cloud features on Neptune can move with velocities more than 100 m s^{-1} off the Voyager-derived ZWP (Sromovsky et al. (1993); Martin et al. (2012); Fitzpatrick et al. (2014); Tollefson et al. (2018)). What drives Jupiter’s stable zonal flow, characterizing the magnitude and timescale of variability (if any) in Jupiter’s jet peaks, and predicting how the zonal flow changes with depth remain outstanding questions today.

Three primary methods are used to directly calculate Jupiter’s ZWP: 1D correlation, 2D correlation, and discrete feature tracking. In addition, the zonal winds may be indirectly determined by using the thermal wind relationship (Gierasch et al. (1986); Flasar et al. (2004); Simon et al. (2015)). 1D correlation methods compute the zonal velocity by calculating longitudinal correlations of the clouds between sets of image pairs in a mosaic, typically in narrow latitude windows, but along a large range of longitudes. This method is insensitive to the north-south component of the velocity field, but meridional velocities are generally small when intense vortices are absent. The 1D correlation method is favored for its computational efficiency, and it reduces uncertainties due to bad pixels and random errors (Asay-Davis et al. (2011)).

The 2D correlation method involves computing full horizontal flow fields, and averaging the east-west components over longitude to obtain the zonal velocity. This method has the advantage that longitudinal variations in the zonal winds are preserved and north-south velocities can be measured in high spatial resolution data. This is particularly important for obtaining accurate zonal wind measurements of the dark projections (associated with the $5 \mu\text{m}$ hotspots) at 8°N , whose velocities do not move with the true zonal flow at the visible cloud deck (Ortiz et al. (1998); Arregi et al. (2006); García-Melendo et al. (2011); Asay-Davis et al. (2011)).

Discrete tracking methods determine zonal velocities by tracking large-scale features over long periods of time to generate one-dimensional or two-dimensional velocity fields. These fields are then averaged over their east-west components to give the mean zonal wind speed in a particular latitude bin.

‘Global’ correlation methods are an umbrella term to describe both 1D and 2D correlation methods - each utilize correlations at all longitudes of Jupiter. In contrast, feature tracking is often localized to longitude regions containing high-contrast trackable features. In data at low spatial resolution, including even amateur data, global methods can be used by combining results from multiple image pairs (Barrado-Izagirre, N. et al. (2013); Hueso et al. (2017)).

Among the past three decades of Jupiter ZWP derivations at the visible cloud deck, minimal wavelength dependence has been found (García-Melendo and Sánchez-Lavega (2001)), in contrast to the case for Saturn (Sánchez-Lavega et al. (2016), Pérez-Hoyos and Sánchez-Lavega (2006)). Images of Jupiter in the ultraviolet have been made to determine zonal wind profiles above the visible cloud deck (Li et al. (2006)). Thus, all observations listed in Table 1, with the exception of Li et al. 2006, probe the same cloud vertical levels and any changes in the ZWP reflect temporal changes in Jupiter’s atmosphere. Under this assump-

tion, we derive ZWPs to examine changes in the 2009–2016 period, using data acquired with the Wide Field Camera 3 (WFC3) on the Hubble Space Telescope (HST). We use the 1D method to derive ZWPs, but also measure 2D velocity residuals from these mean profiles, preserving information on small vortex circulation, turbulence, and waves. The February 2016 ZWP is the last one measured from high spatial resolution data prior to *Juno*’s first science observations at perijove 1 (PJ1), which took place 27 August, 2016 (Bolton et al., 2017). We also present a ZWP taken coincident to perijove 3 (PJ3), which occurred on December 11, 2016.

2.2 Description of Observations

We derive zonal velocities from multiple HST image sets taken with the WFC3 from 2009 to 2016. The sub-observer pixel resolution of these images ranged from ~ 130 km/pixel at opposition to 170 km/pix at the PJ3 perijove distance of 5.85 AU. Table 2 gives details of each dataset, including filters, number of images used, and times of each image. We perform analysis on filters at red optical wavelengths to optimize feature contrast. Contrast can be reduced at shorter or longer wavelengths, due to Rayleigh scattering and/or haze reflectivity.

We collected data from four different WFC3 programs. The 2009 dataset was the first global mapping effort with WFC3 after it was installed in Hubble’s final servicing mission. At opposition, Jupiter easily fits within a WFC3 2K subarray. Subarrays greatly increase duty cycle efficiency for WFC3 observations, because the instrument buffer can only hold two full frame (4K x 4K) exposures. But instrument modes were limited in WFC3’s first observing cycle, so the only way to read out subarrays was to use quad filters (Wong et al. (2010)). To increase HST scheduling flexibility, the 2009 observations imaged two hemispheres separately, one on 18-19 September, and the other on 22-23 September (Table 2). Figure 1 shows a combined map of the two hemispheres, with the derived zonal wind profile overlaid (discussed in the following section).

The 2012 dataset (Fig. 2) was proposed as an attempt to measure a photometric dimming from the shadow of Venus, during a solar transit event as seen from Jupiter. The transit signal itself was never observed, due to the much greater contribution from horizontal inhomogeneity in Jupiter’s lightcurve (Karalidi et al. (2015)). The choice of a medium bandwidth filter (F763M) to image Jupiter’s bright disk necessitated the shortest WFC3/UVIS integration time (0.48 sec).²

Datasets from 2015 and early 2016 are part of the Outer Planet Atmospheres Legacy (OPAL) program (Simon et al. (2015)). This program observes each of the giant planets

²In short exposures, the WFC3/UVIS shutter introduces an expected variability of about 2% in exposure time (Hilbert (2009)), which should have dwarfed the predicted 0.01% signal (Pasachoff et al. (2013)) from the Venus transit. However, the observed lightcurve seemed to be stable against shutter non-repeatability to within 1 part per thousand. This result raises the possibility that the Hilbert (2009) shutter repeatability analysis may have been limited by lower signal-to-noise ratio, compared to the very high signal-to-noise ratio of the Karalidi et al. (2015) Jupiter lightcurve, which integrated the flux over the full planetary disk.

at an annual cadence, for long-duration time-domain studies of storm activity, wind field variability, and changes in aerosol distributions and spectral properties. The program, which began in 2014, has led to discoveries of a new dark vortex on Neptune (Wong et al. (2016)), rare wave phenomena on Jupiter (Simon et al. (2015)), and new insights into variable cloud features on Uranus (Wong et al. (2015b); Irwin et al. (2016)). The 2015 and 2016 global maps and zonal wind profiles are shown in Figures 3 and 4 respectively.

The December 2016 dataset is part of the Wide Field Coverage for Juno (WFCJ) program. This program is synchronized with perijove passes of the NASA Juno mission. Juno made its third perijove (PJ3) pass on 11 December 2016. For subsequent perijove passes, the WFCJ program will either acquire global map pairs to derive the wind field at the time of perijove, or it will obtain only a ~ 50 -min observation covering the longitudes of the Juno sub-spacecraft track. Our global map from the WFCJ program is shown in Figure 2.5

All images in a given data set were navigated and deprojected using the same methods outlined in (Lii et al. (2010)). The formal navigational uncertainty for each frame is ≤ 0.10 degrees at the sub-observer point. Images were deprojected onto a regular grid in planetographic latitude and System-III longitude with 0.05° spacing. Reflectivity data were corrected for limb-darkening by dividing by a factor of μ^k , where μ is the cosine of the emission angle and k ranged from 0.80–0.90 depending on the filter used. For a Lambertian surface, $k = 1.0$. The accuracy of the limb-darkening correction is generally unimportant for our results since we are only interested in correlations in brightness and not exact photometric values - see Supplementary Material in Tollefson et al. (2017) for more discussion on the limb-darkening technique.

We also reference results from Cassini maps obtained on December 11 to 13, 2000 during the Jupiter flyby (Porco et al. (2003); Li et al. (2004); Asay-Davis et al. (2011)), and from HST/WFPC2 maps from 2008 (Asay-Davis et al. (2011)). The HST/WFPC2 maps generally have larger uncertainties in the navigation and zonal wind profiles than the WFC3 maps for several reasons: 1) The WFPC2 pixel scale is slightly larger than the WFC3 pixel scale; 2) Jupiter’s full disk did not fit entirely on the PC1 detector resulting in larger navigation uncertainty; 3) the distortion solution may be better for WFC3.

2.3 Methods

1D correlation method for zonal velocity extraction

Our 1D correlation method for zonal velocity extraction is identical to the global method described in Asay-Davis et al. (2011). In summary, maps are sliced into latitude strips, and correlations are derived between pairs of strips as a function of horizontal shift. A given horizontal shift, divided by the time separation of the map strips, is the velocity. Correlations are determined for every point where there is a pair of time-separated maps covering a given longitude. The velocity that maximizes the total correlation is the derived zonal velocity for that latitude bin. This method has advantages over local techniques, where velocities

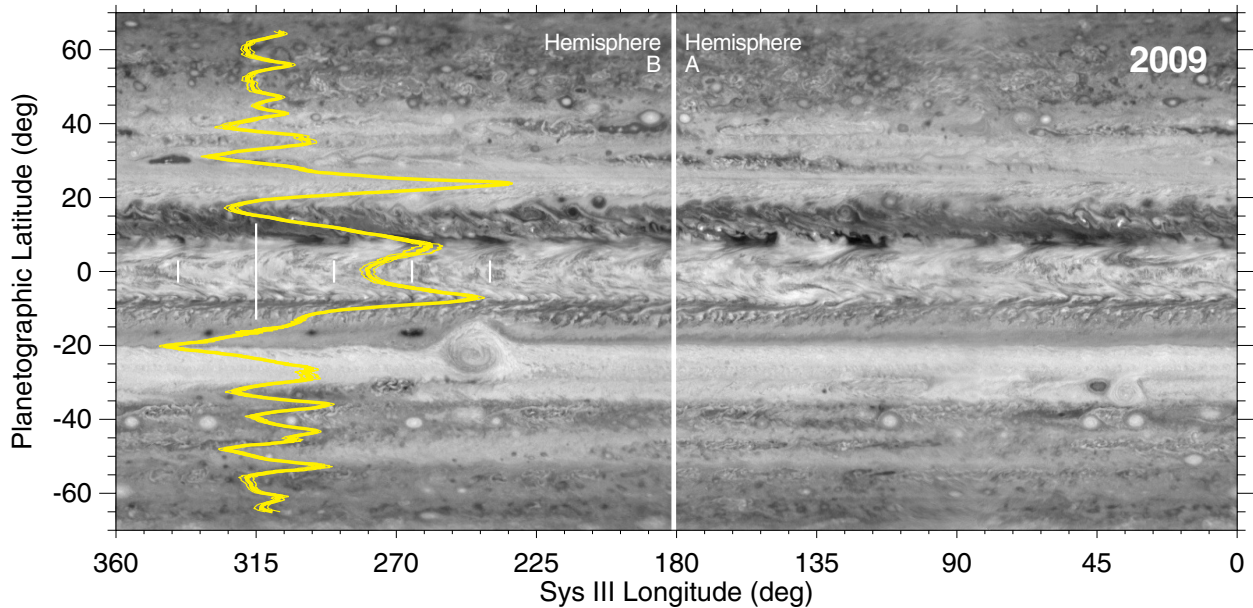


Figure 2.1: A global map of Jupiter created by combining frames in the 2009 dataset. Overplotted is the derived ZWP (yellow); thin, white vertical lines are 50 m s^{-1} increments in the zonal wind velocity, with the longest line representing 0 m s^{-1} . Hemispheres A and B (labeled at top) were observed about 4 days apart, with the intention of increasing HST scheduling flexibility (see Section 4.2 and Tables 3 and 4). Subsequent datasets (Figs. 2-5) continuously imaged over full Jupiter rotations, rather than imaging hemispheres separately.

are extracted by tracking features frame-to-frame. Mainly, correlations are computed for all overlapping longitudes in all image pairs. While longitudinal velocity variations are smeared away with the 1D method, the overall error due to random navigation errors and bad pixels is reduced. It is also important to note that there is not necessarily a direct correspondence between the observed cloud motions and the true zonal flow. Features may be driven by a number of mechanisms, including wave phenomena, shear, or local turbulence. Moreover, photometric centers may vary over time due to changes in cloud morphologies. Such processes will affect the uncertainty of our extracted zonal wind profiles. Regardless, we make the assumption that there is a strong correlation between the observed cloud motions and extracted zonal velocities, and show that our mean, global uncertainties are around 5–6 m s^{-1} .

Specifically, we are interested in computing the correlation between a reference image $I_k(\theta, v)$ and an image advected by velocity v to a time in common with the reference, called $I'_k(\theta, v)$, where θ is the planetographic latitude. The velocity that maximizes the correlation function over a sum of all such image pairs in a latitude bin is the derived zonal velocity at the latitude centered in the bin. The correlation function to be maximized used here and by Asay-Davis et al. (2011) is:

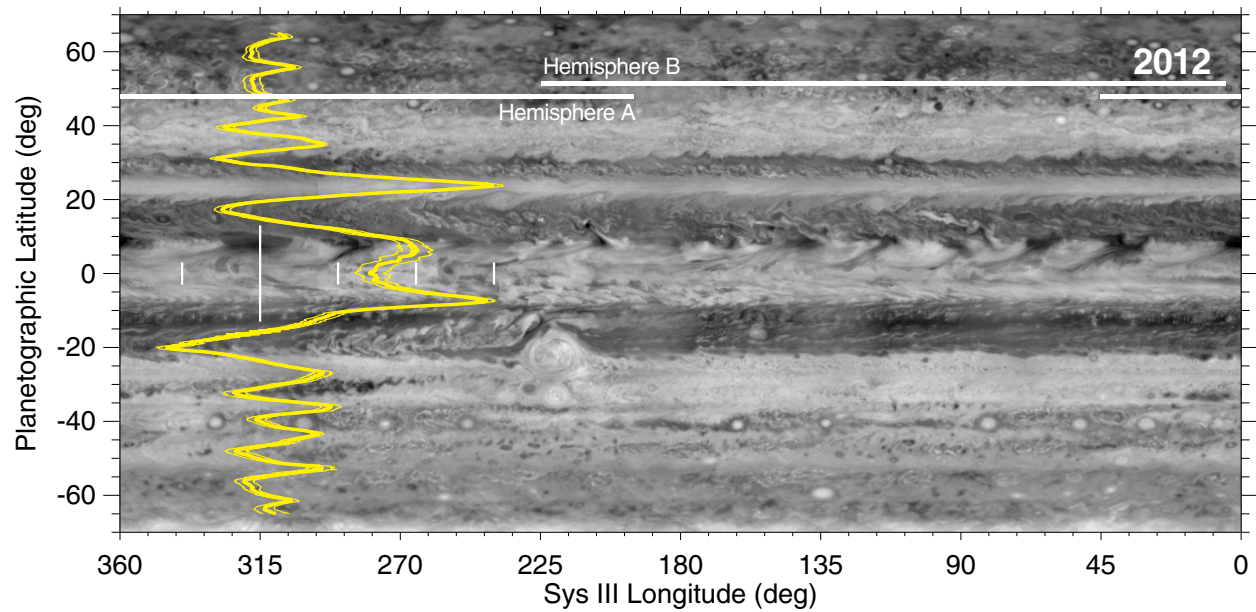


Figure 2.2: As Figure 1. For one analysis (Sec. 2.4), the data were divided into two hemispheres (marked with horizontal white lines) to determine whether using hemispherical or global imaging influenced the retrieved zonal wind profile.

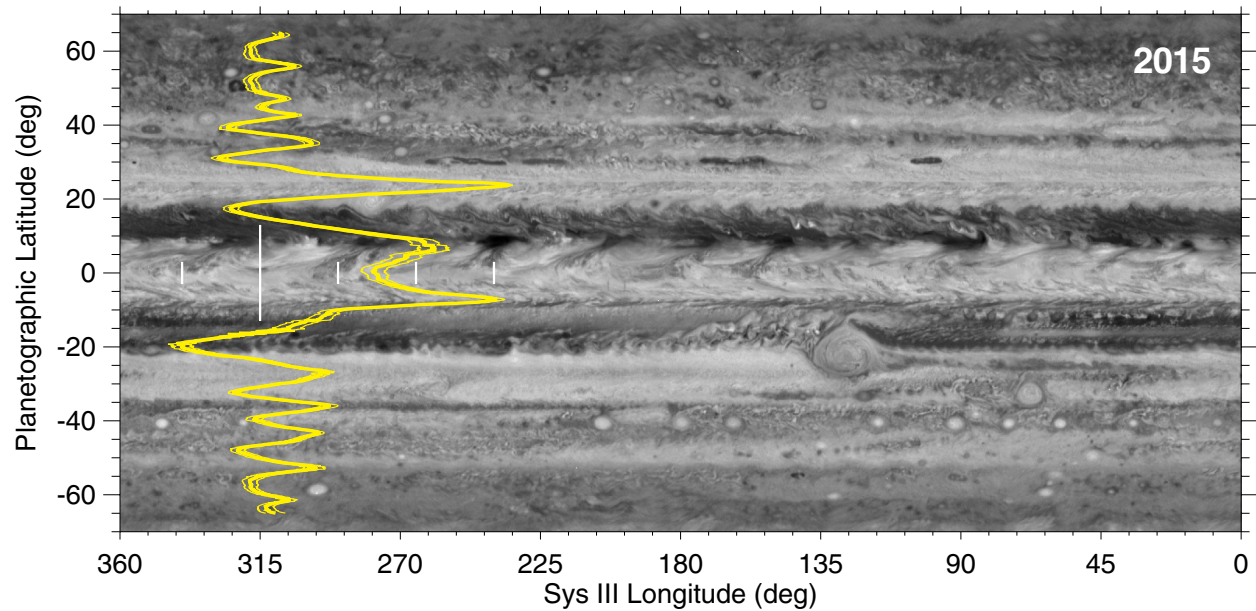


Figure 2.3: As Figure 1 except for 2015.

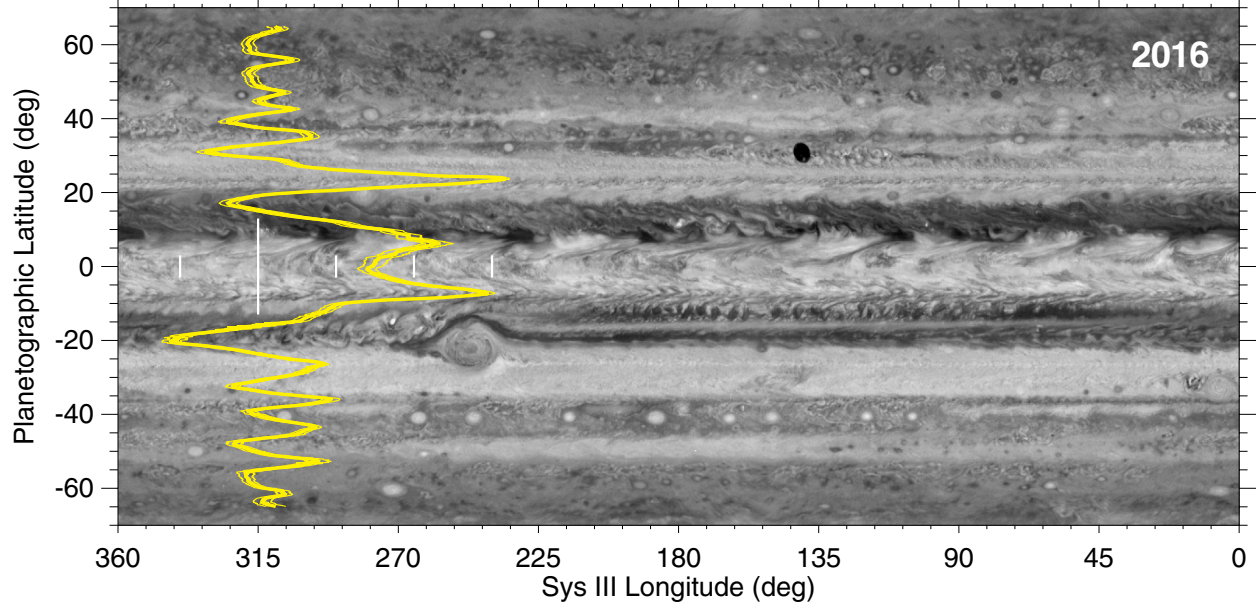


Figure 2.4: As Figure 1 except for 2016.11 (OPAL).

 $R(\theta, v) =$

$$\sum_{(I_k, I'_k)} \sum_{\theta'=\theta-\Delta\theta}^{\theta+\Delta\theta} \left[\frac{\langle I_k I'_k \rangle - N_{k,k'} \langle I_k \rangle \langle I'_k \rangle}{\sqrt{(\langle I_k^2 \rangle - N_{k,k'} \langle I_k \rangle^2) (\langle I_k'^2 \rangle - N_{k,k'} \langle I'_k \rangle^2)}} \right] \quad (2.1)$$

The function above is dependent on the mean and variance of an image, and the cross-correlation of the unshifted image I_k with the shifted image I'_k . These are defined below:

$$\langle I_k I'_k \rangle (\theta, v) = \frac{1}{N_{k,k'}} \sum I_k(\theta, \phi_i) I'_k(\theta, \phi_i) \quad (2.2)$$

$$\langle I_k \rangle (\theta, v) = \frac{1}{N_{k,k'}} \sum I_k(\theta, \phi_i) \quad (2.3)$$

$$\langle I_k^2 \rangle (\theta, v) = \frac{1}{N_{k,k'}} \sum I_k^2(\theta, \phi_i) \quad (2.4)$$

These quantities sum over $N_{j,k}$, which is the number of overlapping pixels between image the pair of images I_j and I'_k at a given θ and v .

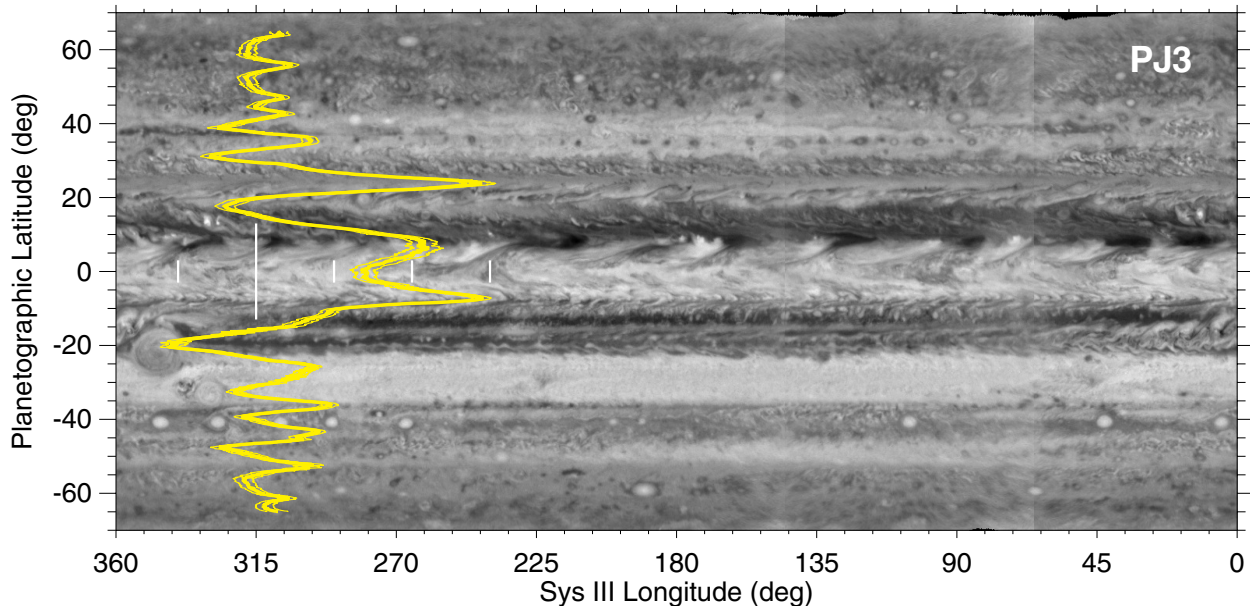


Figure 2.5: As Figure 1 except for 2016.95 (*Juno* PJ3).

To compute the above correlations, we first crop each individual map to $\pm 40^\circ$ longitude of the central meridian and $\pm 72^\circ$ latitude to limit effects near the limb. We then mask out the Great Red Spot and Oval BA in images where these features are present. Large vortices do not move with the background flow on Jupiter, and have internal velocities that would interfere with our accurate measurement of zonal velocities. This chosen masking is, admittedly, arbitrary. Future implementations may improve on this by first calculating all the residuals from the unmasked data with ACCIV (see Section 3.2), then using the data themselves to flag significant non-zonal flows, and finally re-running the analysis with all areas masked out where the residuals are flagged for exceeding a set threshold. This process would be more time-consuming, but it should reduce the global mean uncertainty.

We also limit our computations to pairs of images that are taken within 5 – 15 hours of each other, corresponding to 0.5 – 1.5 Jupiter rotations. If the time difference between images is too short, the correlation given in (2.1) will be large for the sampled velocities since the displacements in the advected image will remain close to the reference image. Too long a time offset and correlations will be small at all sampled velocities, as inherent morphological changes arise and displacements from non-zonal velocities grow. Correlations are computed for velocities within $\pm 50 \text{ m s}^{-1}$ in 0.5 m s^{-1} intervals of a reference zonal wind profile, taken from Cassini maps published in Porco et al. (2003). Finally, we compute (2.1) by summing over all latitudes within $\pm \Delta\theta$ of the given latitude θ . For our zonal velocities, $\Delta\theta = 0.25^\circ$ which amounts to summing over 11 rows of pixels, five on either side of the given latitude. Summing over multiple latitudes eliminates correlations produced by spurious and prominent structures at any single latitude, producing a ‘smooth’ zonal wind profile. This

latitude-summing procedure and reference zonal wind profile are identical to that used in Asay-Davis et al. (2011).

Uncertainties

Uncertainties in some previous works have made use of temporal fluctuations (Limaye (1986, 1989); García-Melendo and Sánchez-Lavega (2001)). Specifically, when multiple zonal wind profiles can be derived from data taken close in time, the RMS temporal variation among the profiles was taken as the estimate of the uncertainty in the mean profile. RMS differences between profiles contain differences due to both random errors as well as systematic errors, including temporal evolution on the timescale of the separation between individual profiles. But since a major motivation for determining uncertainties is to be able to quantify real temporal change, it would be beneficial to define uncertainties that are independent of temporal variation.

To estimate the precision of our derived zonal wind profiles, we use correlation uncertainties, as defined in Asay-Davis et al. (2011). The error estimation involves first advecting individual maps to a common time point, using the derived zonal wind profile from the 1D method. If the derived profile were perfectly accurate, then these advected maps would all be identical. In reality, the advected maps differ, due to a combination of effects: scale differences between discrete features and jet widths, temporal evolution of cloud tracers, random and periodic longitudinal departures from zonal flow, meridional flow, temporal variation on short timescales, vertical wind shear, noise in image data, navigation errors in mapping the data, and astrometric distortion of the images. The combined effect of these error terms can then be estimated by measuring the displacements between the individual advected maps. We measure displacements using Correlation Image Velocimetry, or CIV (Fincham and Spedding (1997); Fincham and Delerce (2000)). Displacements are then converted to velocities by dividing by the interval between advected maps. The specific implementation of CIV employed was the ACCIV code, described in Asay-Davis et al. (2011), which includes a statistical filter for rejecting outliers in the velocity field.³

The velocity vectors found by correlating advected maps are residuals from the mean flow. We combine and smooth velocity residual vectors from all map pairs to create residual maps. These maps constrain the velocity uncertainty. We define zonal wind profile uncertainty at a given latitude as the RMS average of the velocity residuals at that latitude. Residual maps also reveal dynamical features such as vortices, turbulence, and waves. Correlations cannot be accurately measured at the edges of the maps, which we arbitrarily restricted to latitudes closer than 72 degrees from the equator to limit the effects of viewing geometry distortion and loss of contrast due to greater slant path through Jupiter’s hazes.

Uncertainties in the zonal wind profiles are shown as thin yellow lines in Figures 2.1–2.5. Tabular text files containing each zonal wind profile from this paper (with uncertainties) are available in the supplemental Material of the online article (Tollefson et al., 2017). The

³ACCIV is available online at <https://github.com/xylar/acciv>.

supplemental files also list the number of 2D correlations found at each latitude as part of the uncertainty estimate; very few 2D correlations were found at latitudes north of 69.1°N or south of 69.1°S. Velocity residuals are shown in Figure 2.6 for the 2016.11 data set. Residual plots for the other data sets are available in the online Supplemental Materials Figures S1-S4. The middle panel of each subfigure shows north-south velocity residuals, while the lower panel shows east-west residuals. The top panel shows all residuals overlaid on the global albedo map, with the zonal wind profile shown for comparison at top right. We identify two sources of error that may contribute to the residuals. First is navigational uncertainties, which we estimate as around 0.10° per frame. The second is errors that arise from the correlation calculation. This source of uncertainty is partitioned into: the dynamics of discrete features, like vortices, that drift with respect to the zonal flow; variations in velocity with longitude; variations in velocity with latitude, including deviations within the 11 pixel window as well as North-South velocities; and the effects of limb-darkening. It is harder to determine the magnitude of each of these sources. Figure 2.6 shows compact dipoles (pairs of red/blue or orange/blue velocity residuals) which are characteristic of vortices. The presence of these velocity signatures at a particular latitude will increase the standard deviation of velocities at that latitude, so vortices affect the zonal wind uncertainties. For example, a series of cyclonic vortex signatures between 50°–60°S (labeled “Cyclone Alley” in Fig. 2.6) produces locally high zonal wind uncertainties, as discussed in Sec. 2.5.

High-Level Science Products (HLSP) are also available at the MAST archive hosted by Space Telescope Science Institute. Calibrated global maps associated with the OPAL program are available at the OPAL HLSP page.⁴ Calibrated global maps and zonal wind profiles associated with the WFCJ program, synchronized with Juno perijove passes, will be available at the WFCJ HLSP page.⁵ All zonal wind profiles at the WFCJ HLSP page will be derived using the procedures described here, and global maps will be constructed as described in Simon et al. (2015).

2.4 Results

In the following section we plot our derived zonal wind profiles and compare differences between pairs of profiles. We define the uncertainty in the zonal velocity difference between two profiles at a particular latitude as:

$$RMS_{\text{Total}} = \sqrt{RMS_1^2 + RMS_2^2} \quad (2.5)$$

RMS_1 and RMS_2 are the the correlation velocity uncertainties defined in the previous section. Differences greater than RMS_{Total} are significant. Comparisons between a number

⁴The OPAL archive page at MAST has the DOI 10.17909/T9G593, and can be accessed at <http://archive.stsci.edu/prepds/opal/>.

⁵The WFCJ archive page at MAST can be accessed at <http://archive.stsci.edu/prepds/wfcj/>.

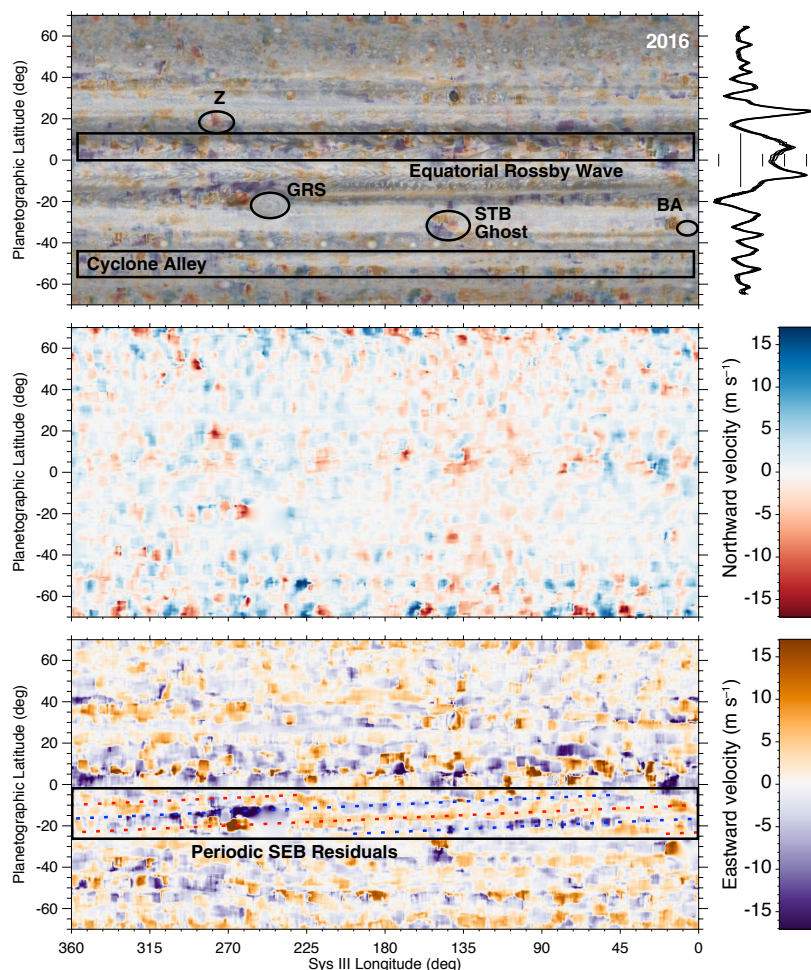


Figure 2.6: Residual non-zonal velocities are used to calculate uncertainties, but they also highlight dynamical features. Top panel: All velocity residuals are overlaid on the 2016.11 albedo map from Fig. 2.4. The GRS and Oval BA were masked out of the 2D correlation retrieval, so their areas are blank. The smaller anticyclone Oval Z, as well as a cyclone known as the STB Ghost are clearly visible in the residual maps. A band near 55°S is marked by strong velocity residuals; we mark this as “Cyclone Alley.” Residuals are also very high near 9°N , where an equatorially-trapped Rossby wave produces a series of $5\text{-}\mu\text{m}$ hot spots and plumes. Middle panel: Meridional velocity residuals are shown on their own. Vortices indicated in the top panel show up here as east-west dipoles. Bottom panel: Zonal velocity residuals are shown on their own. Vortices indicated in the top panel show up here as north-south dipoles. A periodic pattern of alternating residuals is seen between the equator and 20°S , with zonal wavenumber 1 (red and blue dotted lines are overlotted as guides to the eye). Residual maps for the other epochs are available in the Supplemental Materials of Tollefson et al. (2017). Similar phenomena are seen on these maps.

of derived ZWPs are presented in Figures 2.7–2.8. For each comparison, two ZWPs are plotted against each other on the left (blue and green curves in the online version of this article), with differences between them shown on the right as a black curve, bounded by the uncertainty envelope in red. Figure 2.7 compares zonal wind profiles at multiple epochs, while Figures 2.8 and 2.9 are used to evaluate the effects of differences in our methodology (see below).

Temporal change

Figure 2.7 shows comparisons of the 2016.11 mean ZWP to the mean ZWP’s for each other data set (here, ‘mean’ is the average zonal wind speed over all longitudes and frames, in contrast to the other two sets below). The most significant differences in the jet peak speeds occur around 24°N , 8°N , 6°S , 26°S , and 50°S . The zonal wind differences and uncertainties, averaged over $\pm 65^{\circ}$, are shown in Table 3. We also include the 2008 ZWP from HST/WFPC2 data (Asay-Davis et al. (2011)) for comparison. On a global basis, the zonal winds are constant ($\langle \Delta \rangle < \langle \sigma \rangle$), but the few significant changes are highly interesting. We define $\langle \sigma \rangle$ as the globally averaged uncertainty between two epochs, equal to the latitudinal-average RMS_{Total} and $\langle \Delta \rangle$ as the globally averaged difference in the zonal winds in two epochs.

WFC3 provides an improvement in velocity measurement precision compared to WFPC2. Diagonal elements of Table 3 give the uncertainties of each individual ZWP. Average uncertainties measured with WFC3 (years 2009–2016) are considerably lower than the 11 m s^{-1} reported in Asay-Davis et al. (2011) for 2008, based on WFPC2 data. Several instrument-related differences between WFPC2 and WFC3 can be linked to the improvement. WFC3 provides a detector format that allows the full disk of Jupiter to be imaged in every frame, leading to better navigation accuracy than WFPC2, where the high-resolution PC1 chip was too small to capture the full disk. There may be a small improvement due to angular resolution, since the $0.039''$ pixel size of WFC3 is a 15% improvement over the $0.046''$ WFPC2 pixel size (McMaster et al. (2008)). A significant improvement can be seen between uncertainties in 2009 (7.6 m s^{-1}), compared to uncertainties at the later 2012, 2015, and 2016.11 epochs ($5\text{--}6 \text{ m s}^{-1}$). All of these epochs had comparable spatial resolution. This improvement in uncertainties is partially due to improved knowledge of WFC3’s geometric distortion, which is corrected to a precision of about $0.001''$ (Kozhurina-Platais (2014)). The 2009 data were acquired using the quad filter FQ643N, which (unlike the full-frame filters used in 2012–2016) never received updates to its distortion corrections.

Figure 2.7 compares the resulting ZWPs for each epoch. We find significant temporal variability near latitudes of 24°N , 8°N , 6°S , 26°S , and 50°S . Many of these variable regions correspond to non-zonal flow, such as regions with large vortices and the 5-micron hot spots. While we mask out the Great Red Spot, global waves emitting from this vortex still affect the flow. This is reasonable, since the activity of vortices and the dark projections varies with longitude, and we expect these signatures to appear in the ZWP derivations.

The latitude with the greatest uncertainties (widest part of the red envelope) falls in the region of the 8°N 5-micron hot spots. Zonal velocities are notoriously difficult to obtain in

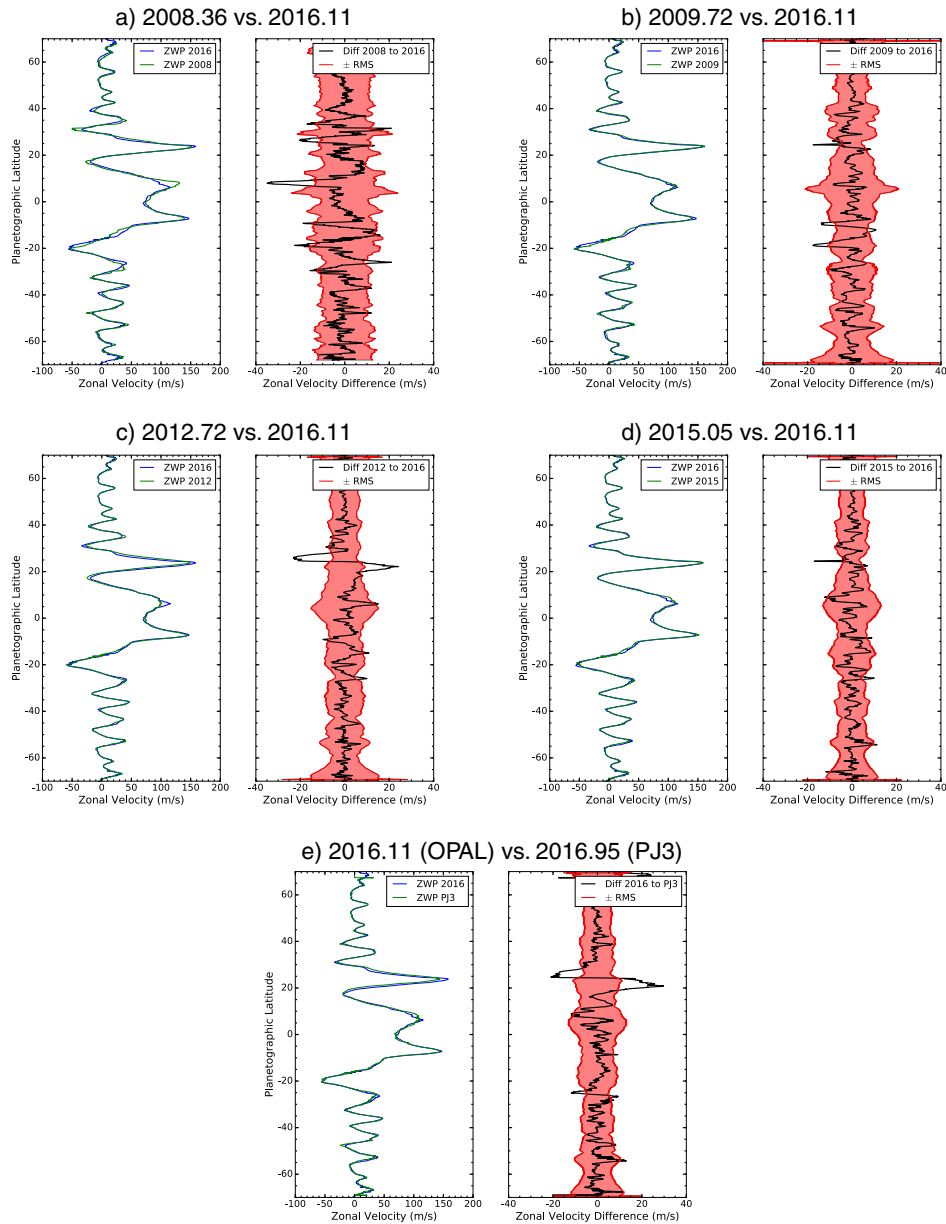


Figure 2.7: Left: Jupiter's derived ZWP from 2008–2016 compared to the 2016.11 ZWP. Right: The difference between the compared ZWPs (black line) and RMS Total (Eq. (2.5), red area). Differences outside the red region are significant. In all figures, the black line is the 2016.11 ZWP minus the ZWP of the compared epoch.

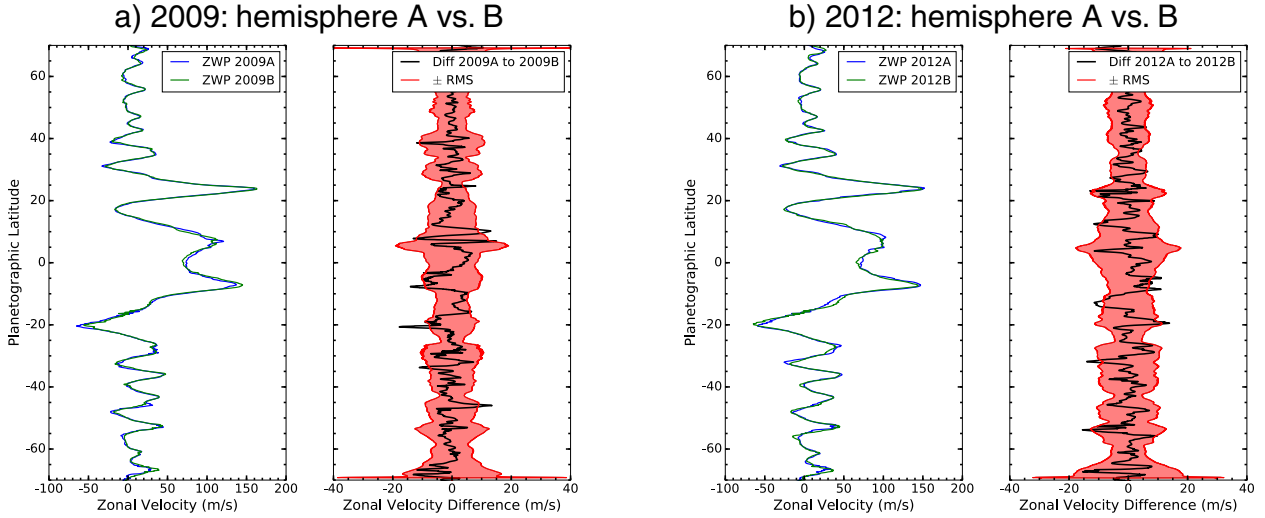


Figure 2.8: As Figure 2.7 except comparing Hemispheres A and B in the 2009 and 2012 epochs.

this area since the hot spots do not move with the local flow (Ortiz et al. (1998); García-Melendo et al. (2011); Asay-Davis et al. (2011); Choi et al. (2013)). Asay-Davis et al. (2011) manually tracked this area and found large RMS deviations. This is suggestive of wave activity or changes in the cloud optical depth, indicative of vertical wind shear. Results from global method analyses are difficult to interpret due to these local variations. The large velocity residuals here are marked “Equatorial Rossby Wave” in Fig. 2.6.

Effect of restricted longitude range

The 2009 observations were taken with two hemispheres observed about 4 days apart, in an attempt to increase HST scheduling flexibility. To investigate whether this observation design affected the resulting ZWP, we performed an analysis of the 2012 data in a similar fashion, constructing two different ZWPs from separated hemispheres. The two hemispheres for 2009 are shown in Fig. 2.1, and for 2012, horizontal bars in Fig. 2.2 show the longitude ranges used for each separate hemisphere analysis.

Figure 2.8a compares differences in the zonal winds between hemispheres A and B in 2009, and Fig. 2.8b compares the two 2012 hemisphere profiles. Very few significant differences (black curves protruding from red envelopes) are seen at either epoch. In the 2012 dataset, there is a significant difference in the location of the “kink” in the cyclonic shear zone near 15°S, and at both epochs, there are differences in the peak of the strongest westward jet at 20°S (see also Sec. 2.5).

Table 2.4 summarizes the latitude-averaged results from the two-hemisphere analyses. As with Table 2.3, the diagonal of the table gives mean correlation uncertainties $\langle\sigma\rangle$ for each individual ZWP measurement. Uncertainties from all WFC3 analyses, whether global

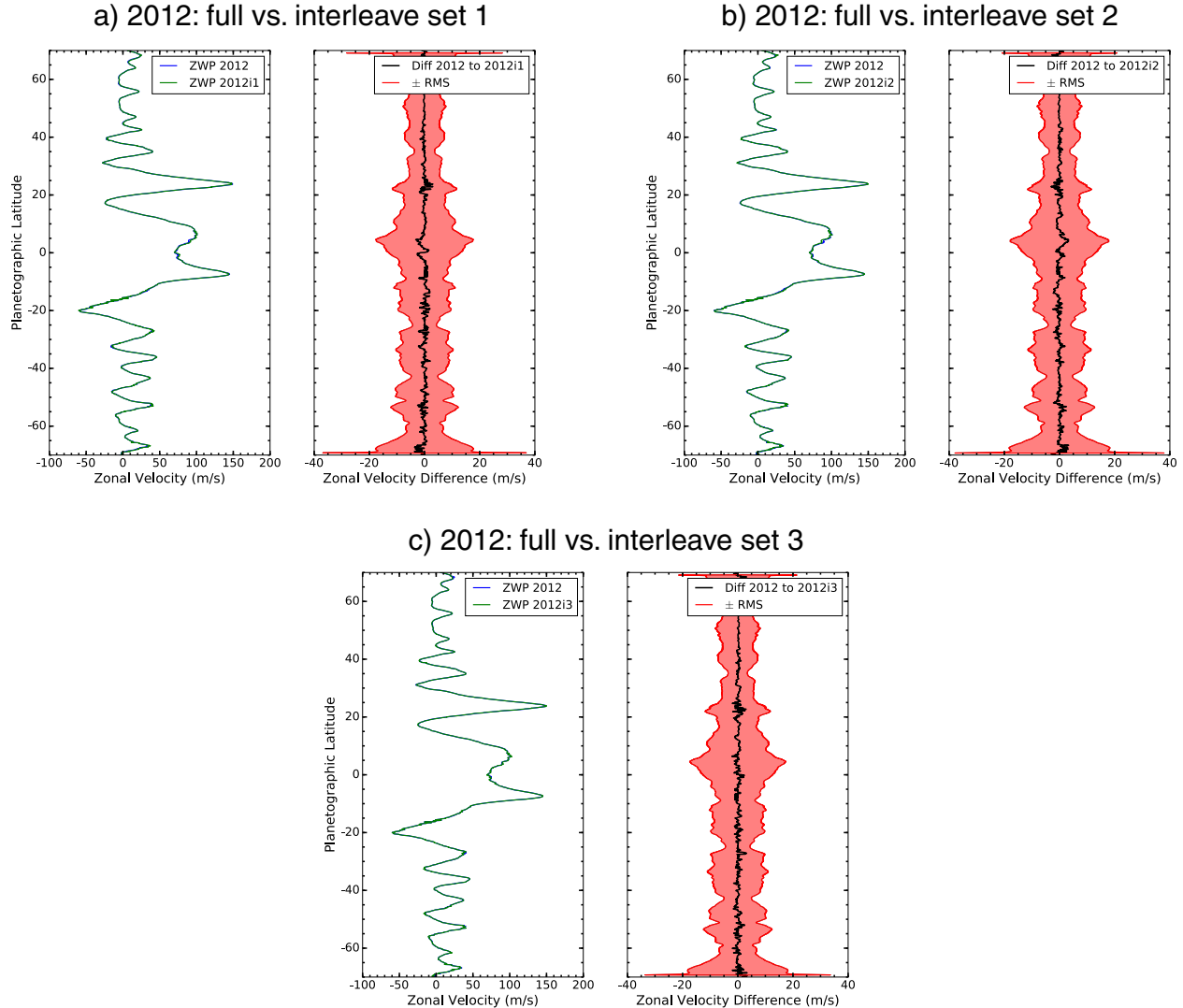


Figure 2.9: As Figure 2.7 except comparing the interleaved 2012 sets.

or single-hemisphere, all fall in the $5\text{-}6 \text{ m s}^{-1}$ range. Differences between 2009A/2009B profiles, and between 2012A/2012B profiles are in the 3 m s^{-1} range, just like the differences between global profiles in 2009, 2012, 2015, and 2016 (Table 2.3). These results suggest that a ZWP derived from data covering a single hemisphere may be just as accurate as results from data with full global coverage. Surprisingly, Table 2.4 suggests that precision is also not decreased by using hemispherical rather than global data: $\langle\sigma\rangle_{2012B} < \langle\sigma\rangle_{2012global} < \langle\sigma\rangle_{2012A}$, and $\langle\sigma\rangle_{2009global}$ is greater than either $\langle\sigma\rangle_{2009A}$ or $\langle\sigma\rangle_{2009B}$. The comparison between these hemispherical and global uncertainties gives some insight into the length scale of longitudinally variable flow; the variation is most likely dominated by length scales significantly shorter than a hemisphere. Indeed, studies of the OPAL 2015 and 2016 data focused on

longitudinal variation (Johnson et al., 2018) identified longitudinal variation with horizontal scales of around 50° , based on wind profiles based on data spanning only 30° of longitude, even shorter than our hemispherical (180°) tests.

Effect of sampling cadence

Enough individual frames were obtained in 2012 to compare the ‘mean’ retrieval to retrievals based on interleaved subsets of the data. The interleaved subsets were obtained by taking every third frame from the 2012 data set, resulting in timing differences on the order of 10 min (see Table 2.2). Each subset had 20 frames, roughly comparable to the number of frames used in the 2015 and 2016 analyses. These interleaved 2012 subsets span the same longitudinal and temporal range, allowing effects on the ZWP due to instrumental or navigational errors to be isolated.

Figure 2.9 compares the mean 2012 profile to each interleaved set. The zonal wind differences are small, $< 5 \text{ m s}^{-1}$ over the full latitude range, and $< 1 \text{ m s}^{-1}$ in the globally-averaged sense (Table 2.5). Due to very similar longitudinal and temporal coverage of these three interleaved datasets, differences in the ZWPs should be due only to random errors from sources such as navigation uncertainty or detector distortion. Values of mean ZWP differences $\langle \Delta \rangle < 1 \text{ m s}^{-1}$ imply that such random errors are very small compared to other uncertainty terms.

Comparisons between the full retrievals, single-hemisphere retrievals, and interleaved 2012 subset retrievals suggest that the dominant error in ZWP measurements is longitudinal variability. Because the 2012 interleaved data sets span the same range of longitudes, they are not sensitive to this source of error, and their differences are smaller than 1 m s^{-1} on average. But the length scale of this longitudinal variability must be shorter than 180° , because there is no significant increase in $\langle \sigma \rangle$ between the 2012 hemispherical and global ZWPs.

Some constraints can also be placed on temporal variation. Differences and uncertainties between 2012A and 2012B retrievals, which were observed within the same 24-hour span, are very similar in magnitude to the differences in 2009A and 2009B retrievals, which were taken about 4 days apart. If temporal variability on the scale of 100 hours were significant, then the 2009 and 2012 dual-hemisphere results should show some significant differences, perhaps including significantly higher uncertainties or differences in the 2009A/2009B case.

The mean correlation uncertainty is higher for the full 2009 profile ($\langle \sigma \rangle = 7.63 \text{ m s}^{-1}$) than for the full 2012 profile (5.79 m s^{-1}). However, $\langle \sigma \rangle$ is in the range of $5\text{--}6 \text{ m s}^{-1}$ for all the single-hemisphere cases. If the difference between the 2009 and 2012 $\langle \sigma \rangle$ values is entirely due to real physical effects, then it suggests a timescale of variation that is on the order of a few days, but long enough to go undetected in the 2012 data spanning only a couple of Jupiter rotations. A caveat to this finding is that there was a potentially significant difference in how the mean 2009 and 2012 profiles were constructed. For 2012, we constructed a mean profile based on global data. For 2009, this approach was impossible because correlations

are unreliable over a time span of 4 days, so we averaged the ZWPs from the A and B hemispheres.

2.5 Discussion

Periodogram analysis

We added the WFC3 ZWPs to the set of WFPC2 and Voyager profiles analyzed in Simon-Miller and Gierasch (2010), updating the Lomb-Scargle periodogram analysis (Fig. 2.10). The combined dataset allows a much finer temporal resolution in short (< 8 yr) periods. The current analysis combines prior ZWPs derived using a discrete feature tracking (local) method, with the WFC3 ZWPs derived using the 1D correlation (global) method. After more WFC3 zonal wind profiles are measured in the future, there will be sufficient data to determine whether combining data based on different retrieval methods affects the results. However, where the false alarm probability is low, several latitudes show signs of periodic variation, similar to those in (Simon-Miller and Gierasch, 2010):

Within a few degrees of the equator, variation is suggested with a period of 6.7 years, and possibly at the longest period of 13.8 years. Similar signals were evident in the analyses of Simon-Miller and Gierasch (2010) and Simon-Miller et al. (2007), though with lower confidence; the data used in Simon-Miller et al. (2007) did not have enough temporal coverage to accurately constrain periods. The long-period equatorial variability is intriguingly close to the 11.9-year seasonal period. Because of the nature of the Lomb-Scargle periodogram retrieval, the long period signals have underestimated false alarm probabilities, as there are not yet enough datasets to demonstrate repeatability at the longest timescale. However, the 6.7-yr period could correspond to the first overtone of the seasonal frequency. As shown in Fig. 8 of Simon-Miller and Gierasch (2010), there is some indication that tropospheric mesoscale wave features could be tied to the seasonal cycle, and if so, similar changes might be expected in the tropospheric winds.

Peaks also appear at 5 years at 18°N and 7°S , as Simon-Miller and Gierasch (2010). Stratospheric temperatures derived from infrared observations show a strong low-latitude periodicity at about 4.5 years, known as the Quasi-Quadrennial Oscillation (QO), which should produce observable signals in the tropospheric zonal wind speeds if resulting temperature anomalies propagate down to the cloud tops (e.g. Leovy et al. (1991); Simon-Miller et al. (2007)). However, the only periodogram peaks near this period are tightly focused in latitude at 18°N and 7°S , and could be tied to other features, such as the wave pattern at 7°S . The analogous equatorial oscillation in the Earth's atmosphere, the Quasi-Biennial Oscillation (QBO), varies from 20 to 26 months, and sometimes fails to fully form at lower altitudes, or pauses. In other words, the Earth's QBO is not exactly periodic and does not always fully propagate, so it is possible that the approximately 5-year wind variability seen at Jupiter's equator is also related to this cycle. The best option for distinguishing between these possibilities is the expansion of the regular WFC3 zonal wind time series, which should

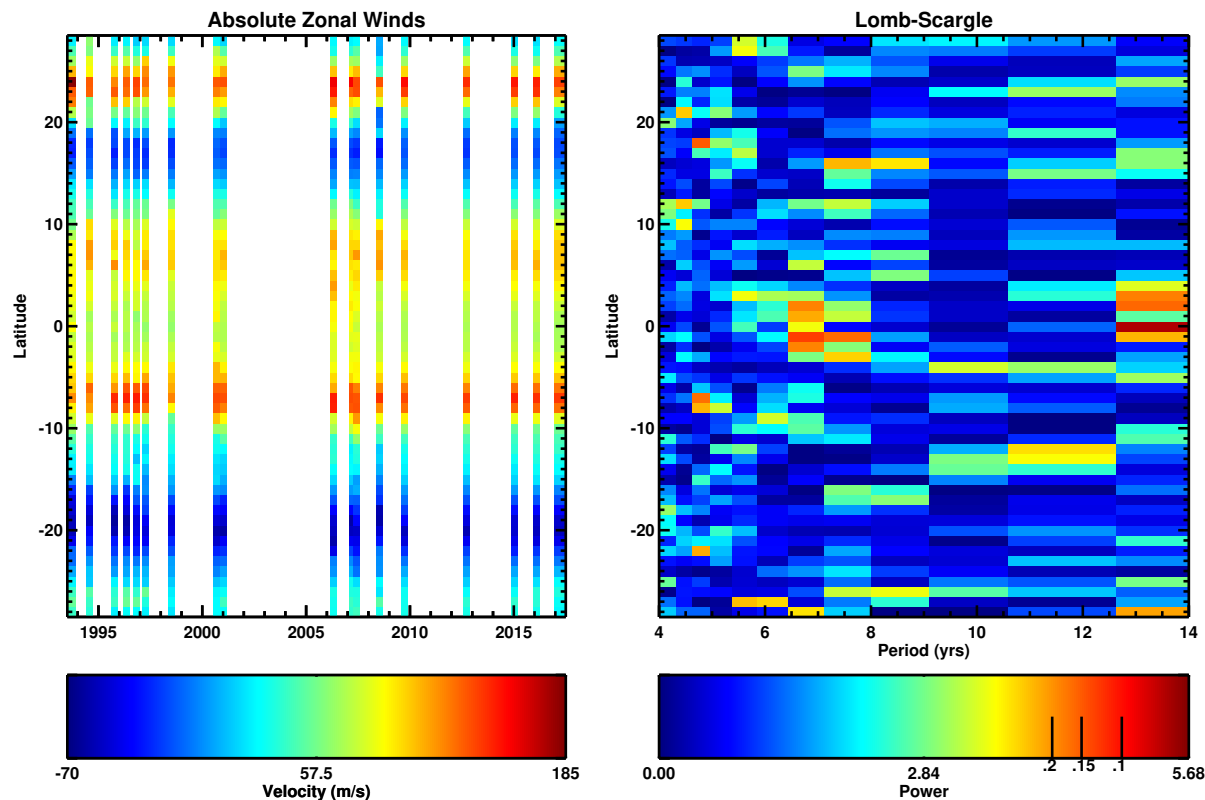


Figure 2.10: Left: Time series of low-latitude zonal winds from WFC3 (2009–2016), combined with zonal winds measured from Voyager (not shown) and HST/WFPC2 data (Simon-Miller and Gierasch, 2010), with speeds corresponding to color values. Right: Corresponding Lomb-Scargle periodogram. False alarm probabilities of 20%, 15% and 10% are shown as vertical ticks on the color bar. The periodogram color bars span over the derived period mid-points, and correspond to periods of 4.2, 4.5, 4.8, 5.2, 5.6, 6.1, 6.7, 7.5, 8.5, 9.7, 11.4 and 13.8 yrs

more accurately determine whether a seasonal signal or equatorial oscillation is present or not; these can be much more tightly constrained with this combined dataset, compared with prior analyses.

There is no significant periodicity at the latitude of 24°N , where the highest-magnitude wind speed changes are found. This point is discussed further in Sec. 2.5.

Non-zonal features in the velocity residual maps

The 1D correlation method determines the average zonal flow in Jupiter's atmosphere. This method provides no direct information about flows different of this background. The residuals in Figure 2.6 indicate compact dipoles in north-south and east-west velocities where

vortices are present in the 2016.11 data. Residual maps for the other epochs (Supplemental Materials of Tollefson et al. (2017)) show similar vortex signatures.

A chain of such features, marked “Cyclone Alley” in Fig. 2.6, results in locally high mean zonal wind uncertainties near 55°S . These locally high uncertainties produce noticeable protrusions in the red envelopes in Figs. 2.7–2.9 near 55°S . Cyclone Alley in our velocity residual maps coincides with where the Galileo imaging experiment found the highest density of lightning strikes per unit area (Little et al. (1999); 52.5°S planetocentric latitude in their Table II is equivalent to 56.1°S planetographic latitude in our figures). Cyclones can be bordered by turbulent regions around their main bodies (resulting in ‘frilly’ looking structures). Levin et al. (1983) concluded that water cloud particles are the most likely medium for Jupiter’s lightning generation, based on estimates of electrical conductivity for the different jovian cloud materials, as well as mass loading values that are consistent with values in more recent work by Wong et al. (2015a). Thus, evidence of cyclones and lightning near 55°S suggests that the vortices could vertically extend to pressures associated with the water cloud layer between 5–8 bar (Weidenschilling and Lewis (1973); Wong et al. (2008); Bjoraker et al. (2015)).

The large, turbulent, convectively active region to the northwest of the GRS (the “GRS wake”) displays a consistent signature in the velocity residuals, at all epochs. The residual wind blows to the northwest in the northern section of the GRS wake, and to the southeast in the southern section, and thus corresponds to divergent flow at the cloud top level. Although divergent flow has been known to characterize individual convective supercells in this region, which themselves generate both cyclonic and anticyclonic eddies (Gierasch et al., 2000), our residual maps indicate that the entire region is characterized by large-scale divergence.

A persistent feature in the ZWPs at the same latitude as the GRS wake (within the SEB) is a “kink” in the meridional wind shear in the 10° – 15°S range. It might seem plausible that the kink may be associated with the GRS wake, since its velocity residual is so large. The 2009 and 2012 two-hemisphere analyses test this hypothesis, since at each epoch, the GRS wake was present in only one of the hemispheres. Indeed, for 2012, significant differences (15 – 18 m s^{-1}) are present around the kink (Fig. 2.8). The kink is much weaker (smaller changes in meridional shear) in the hemisphere that does contain the GRS wake.

For 2009, a significant difference is not seen, consistent with the absence of a turbulent GRS wake at that time; convective activity had stopped and the SEB was quiescent and whitening (Fletcher et al., 2011). Conversely in 2008, the wind speed in the kink was particularly slow, and convective activity was present at most longitudes at this time (see Fig. 1 of Asay-Davis et al. (2011)). There seems to be a correlation between large-scale convective activity and slower zonal wind speeds near 10 – 15°S . One caveat is that gaps in the temporal sampling of our 2009 dataset degraded the sensitivity to velocities near 270°W , just to the west of the GRS (Supplemental Figure S1, Velocity Residuals for 2009 in Tollefson et al. (2017)).

An additional velocity feature is present at these latitudes for the 2016.11 data, but not for any other epoch. This feature consists of a diagonal streak of eastward velocity residuals (Fig. 2.6) that corresponds to a thin, zone-like linear cloud feature in the albedo

map (Fig. 2.4). Longitudinally, the velocity residual feature and the albedo feature both alternate in sign, with one complete cycle around the planet (zonal wavenumber 1), possibly an example of the GRS and its turbulent wake reflecting large-scale waves back toward the equator (Simon-Miller et al., 2012). When similar albedo features are present (2009 and 2016.95 epochs), they maintain a similar slope in latitude/longitude, yet the velocity residual features appear to be aligned strictly east-west. This may be an effect of the much coarser resolution of velocity residual maps compared to albedo maps. The planetary-scale linear albedo feature may be at a different altitude than the surrounding clouds, but the feature is much weaker in CH_4 -band (889-nm) images than in the deep-sensing red wavelengths used in this study. The nature of this feature, and its corresponding velocity residuals, remains elusive.

Velocity fields derived from HST/WFC3 observations will provide valuable comparisons with a wide range of observations taken by the NASA *Juno* spacecraft, as well as other supporting observations from the ground. In particular, JunoCam will measure winds in some polar images with time separations on the order of an hour, which could be directly cross-validated with our wind profiles if the data extend to latitudes lower than 70° . Infrared global imaging sequences at $4.8 \mu\text{m}$ acquired by *Juno*’s JIRAM instrument can be used to measure the wind field with potential sensitivity to deeper tracers⁶, potentially revealing vertical wind shear in combination with data from HST. Repeated spacecraft passes over Jupiter at different longitudes will enable MWR, the Microwave Radiometer (Janssen et al., 2017), to sample deep composition in and out of discrete features such as the Great Red Spot and $5\text{-}\mu\text{m}$ hot spots. Horizontal wind fields from HST observations will complement the inferences on vertical motions derived from these MWR measurements. Ground-based stratospheric temperatures retrieved during the mission can be used to derive stratospheric winds via the thermal wind equation (Fletcher et al., 2016), using contemporaneous wind profiles as a lower boundary condition rather than wind fields measured over a decade before. Both the wind profiles and the optical maps themselves are also useful for comparison with spectrally-resolved microwave maps to be obtained during the *Juno* mission. These maps measure variability in NH_3 concentration, a tracer of vertical motion (de Pater et al., 2016).

Year-to-year differences

Figure 2.11 plots our calculated year-to-year differences of Jupiter’s equatorial jet peaks, including Cassini (Porco et al. (2003)) and HST WFPC2 data (Asay-Davis et al. (2011)). The long-term trend confirms that the jet peaks are stable (although they may vary significantly year-to-year). The most activity is seen at Jupiter’s strong eastward jet at 24°N . This jet has been intensely studied over several decades and with a variety of instruments, including: the Voyager era (Maxworthy (1984)), ground based CCD and HST/WFPC2 images (García-Melendo et al. (2000)) and most recently, from JunoCam and ground-based observations (Sánchez-Lavega et al. (2017)). However, predicting the amplitude and period of variations

⁶See <https://photojournal.jpl.nasa.gov/catalog/PIA21036>

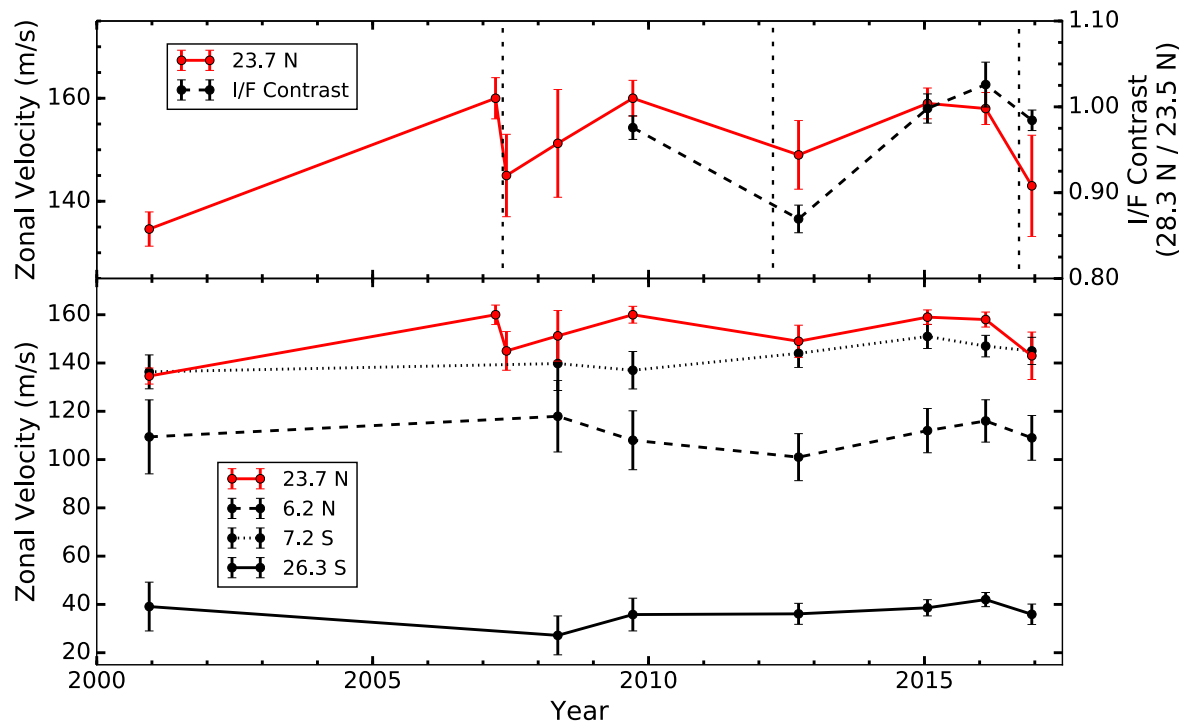


Figure 2.11: Bottom: Equatorial jet peak velocities (m s^{-1}) vs. year. Top: 24N jet peak velocities (solid red line) and I/F contrast (dashed black line) vs. year. Vertical dashed lines indicate the time of an NTB plume outbreak.

in this jet peak has remained elusive to date. Figure 2.12 plots the ZWP around the Northern Temperate Belt (NTB) jet peak for each epoch. The biggest decreases in jet speed follow eruptions of massive convective outbreaks, which result in a decrease from about 160 m s^{-1} to 147 m s^{-1} (Sánchez-Lavega et al. (2008)). The jet peak also appeared to widen and slow by 50 m s^{-1} between the Voyager era and the period 1994–1997, which may be a result of 1990 disturbance in the NTB (García-Melendo et al. (2000)). These outbreaks imply significant vertical wind shear between the visible cloud deck and deeper levels, with sporadic coupling of the layers driven by convective release of internal heat. Three such drops in the jet speed are shown in the top panel of Figure 2.11: in 2007 after a well-documented convective outbreak in the North Temperate Belt (NTB), in 2012, and at the end of 2016. The 2012 speed drop followed another such outbreak that was very poorly imaged because it happened near solar conjunction (Rogers and Adamoli (2012)). The roughly 5-year interval between these events suggested a third possible event in 2017, but an outbreak was observed slightly earlier in October 2016 in infrared imaging by the NASA IRTF, shown in Figure 2.13

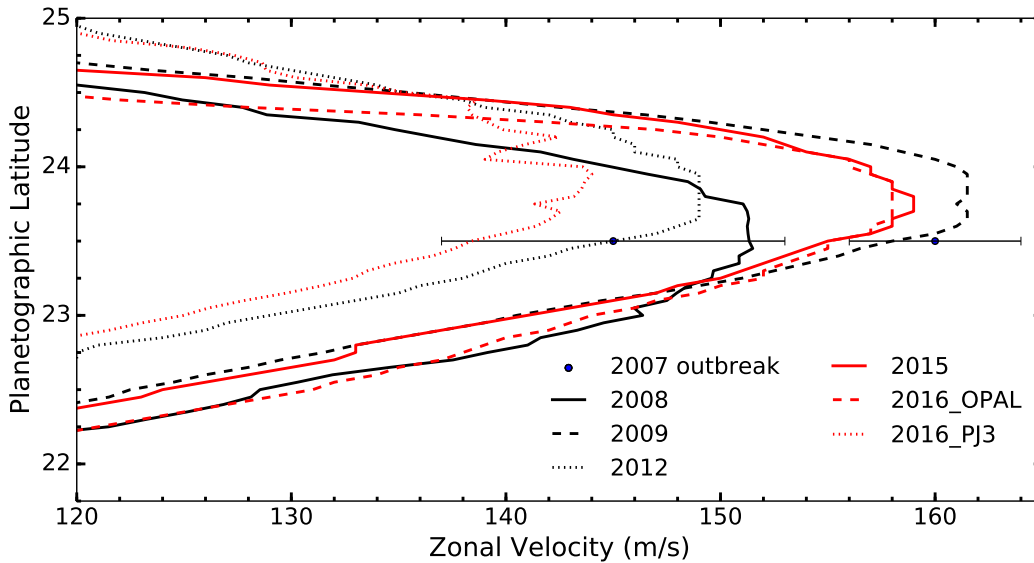


Figure 2.12: Zoomed in ZWPs highlighting the changes in the NTB jet peak speed over the past decade. 2008–2012 data are shown in black lines and 2015–2016 data with red lines. The points from the 2007 plume outbreak come from Sánchez-Lavega et al. (2008).

and available for view at <http://junoirtf.space.swri.edu> (Rogers (2016)). The 2016.95 ZWP, acquired roughly two months after the onset of this latest outbreak, show another dramatic drop in jet speed, from 160 m s^{-1} to 144 m s^{-1} . The difference in the latitude of the NTB jet peaks in 2008 and 2016.11 are also modestly significant based on estimates of the uncertainty in the navigation procedure ($\sigma \sim 0.10^\circ$ per frame).

The dissipation of NTB outbreaks is also associated with albedo changes in this region. The top panel of Figure 2.11 shows the I/F contrast between the jet peak and the region directly to the north. There is a correlation between this contrast and the zonal velocity, with the 2012 jet speed drop correlated with a darkening of the NTB near 28°N . The darkening is also apparent comparing Fig. 2 to e.g., Fig. 1. This pattern is consistent with neutral, pre-plume conditions where the region is bright (seen from Voyager), followed by a chaotic disturbance and rapid darkening during and shortly after plume eruption observed via ground-based telescopes and HST (Sánchez-Lavega et al. (1991, 2008, 2017)). Barrado-Izagirre et al. (2009) also monitored the brightness distribution as the 2007 NTB disturbance developed, verifying changes in the slope of the brightness power spectra as well as an increase in dark cloud patches post-plume that may be consistent with Rossby wave dispersion. However, the I/F contrast following the October 2016 plume outbreak only modestly decreased, suggesting that the response to the outbreak is more rapid in the velocity field than in the cloud albedo. An unprecedented high cadence of microwave observations, with Juno’s Microwave Radiometer (Janssen et al. (2017)) and ground-based VLA

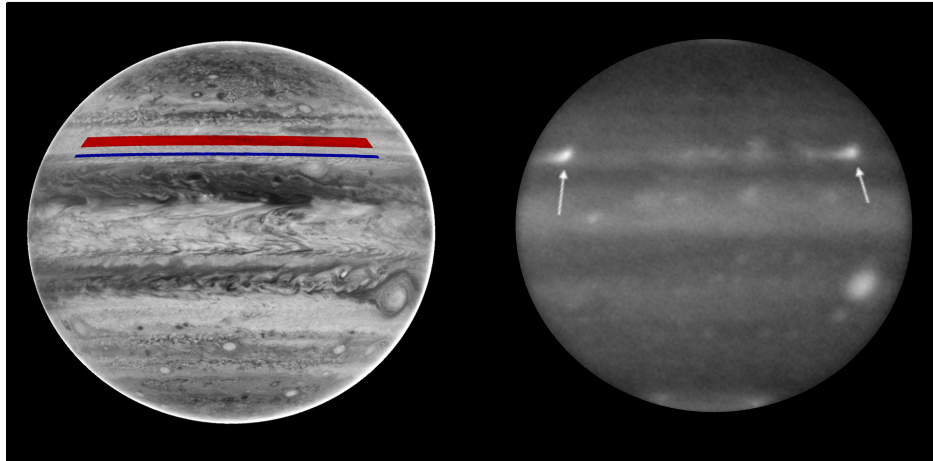


Figure 2.13: Left: Image corrected for limb darkening shows area used to calculate the I/F contrast in Figure 2.11; the red region is centered around 28.3°N and the blue around 23.5°N . Right: Near-infrared image of the NTB plume outbreak on 19 Oct 2016, taken with SpeX (Rayner et al. (2003)) at the NASA IRTF. Plumes are indicated with arrows.

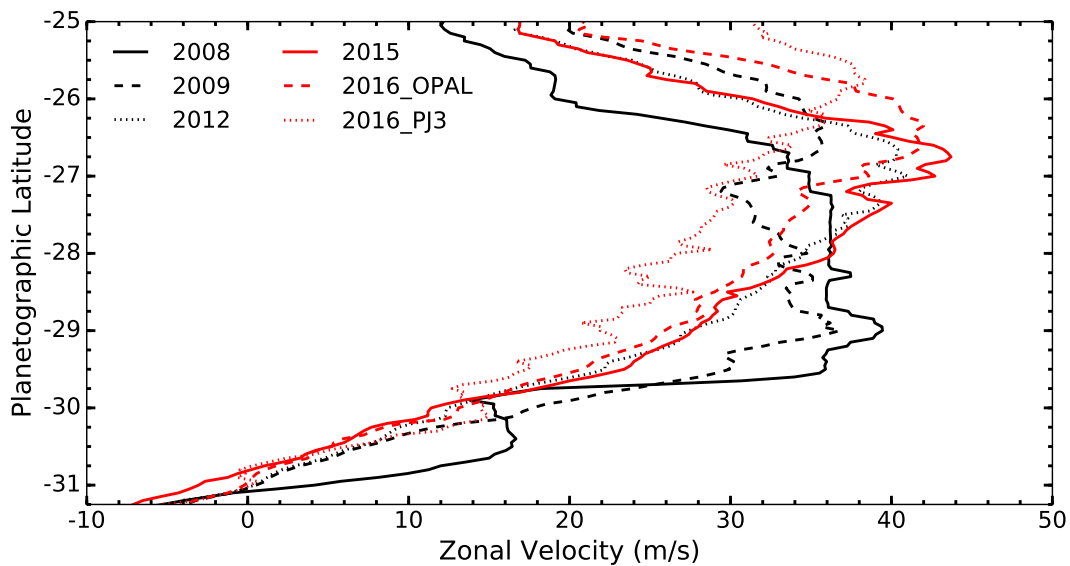


Figure 2.14: As figure 2.12 but zoomed over the STB.

data (de Pater et al. (2016)), will help determine whether there are also sub-cloud changes in volatile concentrations before and after the 2016 outbreak.

The South Temperate Belt (STB) also exhibits significant ZWP variations between some epochs. Figure 2.14 plots the STB ZWP for each epoch. The variation in this region

consists mainly in the presence or absence of a sub-peak at 29°S, and we find that it appears to correlate with the presence of a dark STB segment at 29–32°S. The 29°S sub-peak was present in 2008, 2009, and 2012 (hemisphere A), where such a STB segment was present, and not in 2012 (hemisphere B) nor 2016, where the STB segment was absent. In 2015, the 29°S sub-peak was not visible in the global ZWP, despite the presence of a short STB segment 19 degrees long just west of oval BA; however, the map of residuals (see Supplemental Materials Figures S3, velocity residuals for 2015, in Tollefson et al. (2017)) shows a strong eastward anomaly at 29°S precisely alongside this segment (and indeed, rapid circulation around the segment). These results confirm the report of Rogers et al. (2013), who likewise inferred that the 29°S sub-peak was conspicuous only in sectors containing a dark STB segment, from both HST and ground-based data in 2009 and 2012. Methods which do not smear the longitudinal velocity should be considered when determining the true flow in the STB region.

2.6 Conclusion

We present five epochs of WFC3 HST Jupiter observations and zonal wind analysis from 2009–2016. We used the 1D correlation method for velocity extraction (Asay-Davis et al. (2011)). The derived 2016 zonal wind fields are the most timely for comparison to NASA *Juno* observations in late 2016 (PJ1 and PJ3).

We find that the zonal winds are globally stable on Jupiter throughout these epochs with some exceptions. The largest uncertainty in the wind field is found to be when vortices or hot spots are present. These phenomena do not follow the background flow, and thus increase the uncertainty of the extracted zonal velocity. This agrees with analysis from Asay-Davis et al. (2011). Vortices with the strongest deviations from the mean flow can be identified in our residual maps (Fig. 2.6) as paired N/S or E/W velocities. Future studies of Jupiter’s zonal winds may construct similar maps to identify vortex features, including global Rossby waves resulting from vortex dynamics.

By deriving zonal winds from subsets of data—interleaved or covering only single hemispheres rather than all longitudes—we are able to isolate longitudinal variability as the dominant source of uncertainty in zonal wind retrievals. WFC3’s slightly finer pixel scale and larger field of view, compared to WFPC2, result in a roughly factor of two reduction (from 10 m s⁻¹ to 5–6 m s⁻¹) in uncertainty over our previous HST-based wind profile calculated with the same methods from Asay-Davis et al. (2011).

We also find variations in the 24°N jet peak velocity from 2009–2012. Specifically, the 2012 jet peak velocity is about 10 m s⁻¹ slower than the 2009 and 2015 velocities. A 2012 plume outbreak, while not directly observed, is consistent with global changes to the albedo in the NTB. Brightness and velocity variations pre- and post-plume outbreak were also seen during other plume outbreaks on Jupiter (Sánchez-Lavega et al. (1991, 2008)). A recent plume outbreak was observed in late 2016 with IRTF. Continued monitoring of the NTB with *Juno*’s Microwave Radiometer, ground-based telescopes, and amateur observations will

be crucial for understanding the workings of these highly energetic storms, and their role in coupling the visible cloud deck with deeper atmospheric layers.

2.7 Acknowledgements

Based on observations made with the NASA/ESA Hubble Space Telescope, obtained from the Data Archive at the Space Telescope Science Institute, which is operated by the Association of Universities for Research in Astronomy, Inc., under NASA contract NAS 5-26555. These observations are associated with programs listed in Table 2.2. Support for programs 11559, 13937, 14334, and 14661 was provided by NASA through a grant from the Space Telescope Science Institute. This work has also been supported in part by NASA under the NASA Earth and Space Science Fellowship program Grant NNX16AP12H to UC Berkeley. For observations shown in Fig. 2.13, the authors thank Tom Momary, Tommy Greathouse, and Leigh Fletcher, Visiting Astronomers at the Infrared Telescope Facility, which is operated by the University of Hawaii under contract NNH14CK55B with NASA. The authors wish to recognize and acknowledge the very significant cultural role and reverence that the summit of Mauna Kea has always had within the indigenous Hawaiian community. We are most fortunate to have the opportunity to conduct observations from this mountain.

Timespan (years)	Facility	Appx. Sub-observer Resolution (km/pixel)	Method	References
1979	Voyager 1 & 2 ISS	100	Local	Ingersoll et al. (1981)
			Local	Limaye et al. (1982)
			Global	Limaye (1986)
1995–2000	HST WFPC2	140	Global	García-Melendo and Sánchez-Lavega (2001)
2000	Cassini	120	Global	Porco et al. (2003)
			Local	Li et al. (2004)
			Local	Li et al. (2006)
2007	HST WFPC2	160	Global	Cheng et al. (2008)
2008	HST WFPC2	160	Global	Asay-Davis et al. (2011)
2011	PVOL/IOPW	380	Global	Barrado-Izagirre, N. et al. (2013)
2009–16	HST WFC3	130	Global	This work

Table 2.1: Compilation of derived Zonal Wind Profiles for Jupiter. ‘Global’ describes either the 1D or 2D correlation methods, while ‘Local’ describes feature tracking.

Data set	Filter	Date	UT Times							
Epoch: 2009.72 PI: I. de Pater Proposal ID: 11559	FQ643N	09-18	13:13:10	13:16:15	13:31:45	13:55:42	13:58:47			
			14:49:40	14:52:45	15:08:13	15:32:07	15:35:12			
			22:49:13	22:52:18	23:01:37	23:04:42	23:32:17			
		09-19	23:35:22	02:01:02	02:04:07	02:13:26	02:16:31	02:43:36		
			02:46:41	09-22	11:31:52	11:34:57	11:50:25	12:14:20	12:17:25	
		13:07:45	13:10:50		13:26:18	13:50:14	13:53:19			
		14:43:39	14:46:44		15:02:12	15:26:08	15:29:13			
		21:07:12	21:10:17		21:19:36	21:22:41	21:50:17			
		09-23	21:53:22	00:18:58	00:22:03	00:31:22	00:34:27	01:02:03		
			01:05:08							
		Epoch: 2012.72 PI: G. Schneider Proposal ID: 13067	F763M	09-19	23:43:20	23:50:39	23:57:58			
				09-20	00:05:17	00:23:28	01:19:04	01:26:23	01:33:42	
					01:41:01	01:59:12	02:54:47	03:02:06	03:09:25	
03:16:44	03:34:55				04:30:29	04:37:48	04:45:07			
04:52:26	05:10:37				06:06:13	06:13:32	06:20:51			
06:39:07	06:46:26				07:41:57	07:49:16	07:56:35			
09:17:40	09:24:59				09:32:18	10:53:24	11:00:43			
11:08:02	12:29:08				12:36:27	12:43:46	14:04:51			
14:12:10	14:19:29				14:27:21	15:40:35	15:47:54			
15:55:13	16:02:32				17:16:19	17:23:38	17:30:57			
17:38:16	17:57:00				18:52:02	18:59:21	19:06:40			
19:13:59	19:32:43				20:27:46	20:35:05	20:42:24			
20:49:43	21:07:54									
Epoch: 2015.05 PI: A. Simon Proposal ID: 13937	F631N				01-19	02:16:48	02:56:55	03:52:18	04:32:25	05:27:49
						06:07:56	07:03:19	07:43:26	08:38:49	09:18:56
		10:14:19	10:54:26	11:49:50		12:29:57	15:00:50			
		15:41:02	16:36:21	17:16:33		18:11:51	18:52:03			
		19:47:22	20:27:34	21:22:56		22:03:08	22:58:22			
		23:38:34								
		Epoch: 2016.11 PI: A. Simon Proposal ID: 14334	F631N	02-09		09:41:57	10:07:03	11:17:21	11:42:27	12:53:20
13:18:26	14:28:43				14:53:49	16:04:07	16:29:13			
17:39:32	18:04:38				19:14:56	19:40:02	20:50:21			
21:15:32	22:25:45				22:50:56					
02-10	00:01:08			00:26:19	01:36:32	02:01:43	03:11:21			
	03:36:32			04:46:45	05:11:56					
	Epoch: 2016.95 ¹ PI: M.H. Wong Proposal ID: 14661			F631N	12-11	08:01:08	08:24:51	10:50:45	11:35:55	12:26:07
						13:11:17	14:01:29	14:46:39	15:36:51	16:22:04
12-12	18:47:00	21:02:21	21:57:44	22:43:03	23:33:07					
	00:18:26	01:11:57	02:52:12	04:42:53	06:29:57					
		07:53:12	09:05:55							

Table 2.2: The epochs and filters used to derive Jupiter's ZWP in this study.

Year	2016.95	2016.11	2015	2012	2009	2008
2016.95	$\langle\sigma\rangle = 5.7$	$\langle\Delta\rangle = 3.6$ $\langle\sigma\rangle = 7.6$	$\langle\Delta\rangle = 3.6$ $\langle\sigma\rangle = 7.6$	$\langle\Delta\rangle = 3.2$ $\langle\sigma\rangle = 8.2$	$\langle\Delta\rangle = 4.1$ $\langle\sigma\rangle = 9.5$	$\langle\Delta\rangle = 5.9$ $\langle\sigma\rangle = 12.7$
2016.11		$\langle\sigma\rangle = 4.9$	$\langle\Delta\rangle = 2.3$ $\langle\sigma\rangle = 7.0$	$\langle\Delta\rangle = 3.3$ $\langle\sigma\rangle = 7.6$	$\langle\Delta\rangle = 2.9$ $\langle\sigma\rangle = 9.1$	$\langle\Delta\rangle = 5.1$ $\langle\sigma\rangle = 12.3$
2015			$\langle\sigma\rangle = 5.0$	$\langle\Delta\rangle = 3.2$ $\langle\sigma\rangle = 7.7$	$\langle\Delta\rangle = 2.9$ $\langle\sigma\rangle = 9.2$	$\langle\Delta\rangle = 4.9$ $\langle\sigma\rangle = 12.3$
2012				$\langle\sigma\rangle = 5.8$	$\langle\Delta\rangle = 3.5$ $\langle\sigma\rangle = 9.7$	$\langle\Delta\rangle = 5.1$ $\langle\sigma\rangle = 12.7$
2009					$\langle\sigma\rangle = 7.6$	$\langle\Delta\rangle = 4.4$ $\langle\sigma\rangle = 13.6$
2008						$\langle\sigma\rangle = 11.2$

Table 2.3: Year-to-year comparisons of the mean ZWPs. $\langle\sigma\rangle$ is the average uncertainty, equal to the latitudinal-average RMS_{Total} if the comparison is between two different years (values off the main diagonal). Along the diagonal, the reported $\langle\sigma\rangle$ is the average uncertainty for that year (equal to RMS_1). Similarly, $\langle\Delta\rangle$ is the average difference between two years. The units are m s^{-1} .

Year	2012	2012A	2012B	2009	2009A	2009B
2012	$\langle\sigma\rangle = 5.8$	$\langle\Delta\rangle = 1.9$ $\langle\sigma\rangle = 8.4$	$\langle\Delta\rangle = 1.7$ $\langle\sigma\rangle = 7.7$	$\langle\Delta\rangle = 3.5$ $\langle\sigma\rangle = 9.7$		
2012A		$\langle\sigma\rangle = 6.1$	$\langle\Delta\rangle = 3.1$ $\langle\sigma\rangle = 8.0$			
2012B			$\langle\sigma\rangle = 5.0$			
2009				$\langle\sigma\rangle = 7.6$	$\langle\Delta\rangle = 1.5$ $\langle\sigma\rangle = 9.4$	$\langle\Delta\rangle = 1.5$ $\langle\sigma\rangle = 9.3$
2009A					$\langle\sigma\rangle = 5.4$	$\langle\Delta\rangle = 2.9$ $\langle\sigma\rangle = 7.6$
2009B						$\langle\sigma\rangle = 5.1$

Table 2.4: As Table 3, except comparing the 2009 and 2012 averaged ZWPs with those derived from the individual hemispheres A and B (defined in Figure 1 and 2).

Year	2012	2012i1	2012i2	2012i3
2012	$\langle\sigma\rangle = 5.8$	$\langle\Delta\rangle = 0.5$ $\langle\sigma\rangle = 8.1$	$\langle\Delta\rangle = 0.5$ $\langle\sigma\rangle = 8.1$	$\langle\Delta\rangle = 0.5$ $\langle\sigma\rangle = 8.2$
2012i1		$\langle\sigma\rangle = 5.6$	$\langle\Delta\rangle = 0.9$ $\langle\sigma\rangle = 8.0$	$\langle\Delta\rangle = 0.8$ $\langle\sigma\rangle = 8.1$
2012i2			$\langle\sigma\rangle = 5.6$	$\langle\Delta\rangle = 0.8$ $\langle\sigma\rangle = 8.1$
2012i3				$\langle\sigma\rangle = 5.8$

Table 2.5: As Table 3, except comparing the 2012 averaged ZWP with each individual interleaved set (i1,i2,i3).

Chapter 3

Vertical Wind Shear in Neptune's Upper Atmosphere Explained with a Modified Thermal Wind Equation

We present observations of Neptune taken in H-(1.4-1.8 μm) and K'-(2.0-2.4 μm) bands on the nights of July 3, 2013 and August 20, 2014 from the 10-m W.M. Keck II Telescope using NIRC2 coupled to the Adaptive Optics (AO) system. We track the positions of ~ 100 bright atmospheric features over a 4-5 hour window on each night to derive zonal velocities and wind profiles.

Our results deviate from the smooth Voyager zonal wind profile from Sromovsky et al. (1993), often by 100-200 m/s, and often by 3-10 times their estimated uncertainties. Besides what appears to be a random dispersion, probably due to a mix of unaccounted for measurement errors, eddy motions, vertical wind shear, and wave-generated features that don't follow the mass flow, there is also a systematic deviation that is wavelength dependent. The H-band profile is best described with a 73–106 m/s shift towards the east for a retrograde flow (i.e., a lessening of the retrograding velocities) from the Voyager profile at the equator. The K'-band profile is consistent with Voyager on both nights.

Comparing H and K' contribution functions and K'/H intensities suggests equatorial H-band features are, on average, deeper than K'-band features. The H-band equatorial features also have greater eastward (less negative) velocities than K'-band features. Differences in zonal wind speed with depth at constant latitude and time imply vertical wind shear. Assuming the average variations in the zonal wind profiles result from wind shear over 3–5 scale heights, we predict vertical wind shears between -1.0 and -2.2 m/(s·km) at the equator (increasing with height).

The standard thermal wind equation and meridional thermal profile for Neptune given by Voyager/IRIS spectra predict wind shear of the wrong sign relative to the observations. We consider two effects that reconcile this inconsistency. First, we calculate the meridional temperature gradients at pressures outside the Voyager/IRIS narrow sensitivity window required to match our predicted wind shears. Second, we generalize to a thermal wind equation

that considers global methane variations and re-derive the temperature structure needed to match the observed wind shear. If methane is uniformly distributed or weakly-varying, the equator must be 2–15 K cooler than the mid latitudes below 1 bar. If methane is strongly-varying, the equator can be 2–3K warmer than the mid latitudes below 1 bar, qualitatively consistent with observed temperature contrasts. These findings may imply a stacked-celled circulation pattern in Neptune's troposphere and lower stratosphere.¹

3.1 Introduction

The zonal wind velocities of the giant planets are obtained by tracking bright cloud features in their atmospheres. Sromovsky et al. (1993) created a zonal wind profile for Neptune by constructing a fit to measurements of position and velocity of discrete cloud features by Limaye and Sromovsky (1991) from Voyager 2 images taken in visible wavelengths. Derived velocities were averaged in latitudinal bins and fit to a fourth-order polynomial to create a smooth zonal wind profile, also referred to as the canonical profile. This profile revealed Neptune's atmospheric winds are extremely strong, despite Neptune receiving minimal solar insolation. Equatorial wind speeds reach up to 400 m/s, some of the fastest in the solar system.

Cloud tracking studies have shown significant deviations from Neptune's canonical wind profile. Limaye and Sromovsky (1991) saw deviations on the order of 50 m/s, particularly in clouds around the vicinity of a Great Dark Spot (GDS) and at Northern latitudes between 25° - 30° N. Sromovsky et al. (1993) found dispersion in cloud velocities from their constructed canonical profile. Hammel and Lockwood (1997) also saw dispersion of velocities in narrow latitude strips from 1995 HST maps. Sromovsky et al. (2001b,c) tracked features in 1996 data and found general agreement with the canonical profile apart from features close to a dark spot. These findings suggest Neptune's clouds are not all passive tracers for the background winds, but may also be evidence of wind shear, wave propagation from the presence of vortices, such as the GDS, or other local phenomena.

Recent fits to the zonal wind profile using near-infrared imaging data show shifts relative to the canonical profile, in addition to the dispersion of clouds at a given latitude noted by earlier studies. Fitzpatrick et al. (2014) tracked dozens of bright atmospheric features using Keck AO images in the H-band and found that a profile with a ~ 180 m/s eastward shift from the canonical profile at the equator best matched the data. Martin et al. (2012) also observed many cloud features in the H-band ($1.6\mu\text{m}$) that appeared to not move with the canonical profile, with differences reaching as large as 500 m/s. Interestingly, Fitzpatrick et al. (2014) also tracked features in K'-band ($2.2\mu\text{m}$) images and found that the derived profile was consistent with the Voyager profile. They suggested that the eastward shift in the H-band profile from the K'-band and Voyager profiles could be due to temporal changes or a wavelength/depth effect.

¹This work has been previously published in *Icarus* (Tollefson et al., 2018) and has been reproduced with permission from all co-authors.

However, the exact mechanisms that drive the dispersion and profile shifts in the zonal winds of Neptune remain largely unresolved. Martin et al. (2012) observed wave-like behavior in the east-west motions of several cloud features with periods close to the 7.2 hr period of the principal semi-diurnal tides from Triton. They suggested that future observations look at the effect of tidal forcing from Triton on the velocities of Neptune's cloud features. Recent *Kepler* observations did not find signals in photometric light curves corresponding to the periods of Neptune's major moons, disproving this idea (Simon et al. (2016)). Fitzpatrick et al. (2014) used radiative transfer models to determine the approximate altitudes of clouds and concluded that the differences between their observed wind profiles in H- and K'-bands were too large in magnitude and in the opposite direction than what could be explained by vertical wind shear. Evidence of large north-south velocities in feature motions may be due to vortices or various wave mechanisms but the exact cause of zonal wind variability is unknown.

A major drawback to the studies conducted by Martin et al. (2012) and Fitzpatrick et al. (2014) is that they either: imaged at one wavelength, so that differences in wind speed versus atmospheric depth cannot be seen; or performed cloud tracking at two wavelengths on different nights so that the two can not be directly compared. With these issues in mind, we perform analyses similar to Martin et al. (2012) and Fitzpatrick et al. (2014) to test the vertical wind shear hypothesis for zonal wind dispersion on Neptune. We first present observations of Neptune taken in the H-(1.4-1.8 μm) and K'-(2.0-2.4 μm) bands on each of the nights of July 3, 2013 and August 20, 2014 and derive zonal wind profiles for each band by tracking the motions of bright cloud features. We remark on observed differences between the H- and K'-band profiles in the equatorial region, leading us to reconsider vertical wind shear as being important, as we observe differences in speeds for features at the same latitudes and time. We then discuss the applicability of the thermal wind equation to model vertical wind shear in Neptune's troposphere and lower stratosphere from the equator to mid-latitudes. Finally, we examine the physical consequences of vertical wind shear in terms of Neptune's global circulation.

3.2 Data

Observations and Data Reduction

We observed Neptune's atmosphere on July 3, 2013 and August 20, 2014 UT from the Keck II Telescope on Mauna Kea, Hawaii at Near-Infrared (NIR) wavelengths. H- (1.4-1.8 μm) and K'- (2.0-2.4 μm) band images were taken on both nights with the narrow camera of the NIRC2 instrument coupled to the Adaptive Optics (AO) system. The detector is a 1024×1024 array with a scale of 0.009942 arcsec/pixel in this view (de Pater et al. (2006)).

A total of 75 images were taken in each band on July 3, 2013 from 10:48 - 15:09 (UT); 100 images were taken in each band on August 20, 2014 from 08:13 - 13:30 (UT). An integration time of 60 seconds was used for all images. This provides the best compromise of high

signal to noise while minimizing feature smearing and avoiding over-saturating the detector. Moreover, short integration times allow many images to be taken over the observation period and ensure the identification of the same features in successive images. Images were taken in sets of five and alternated between the H- and K'-bands, corresponding to a ~ 15 minute separation between image sets in a single band.

Images were reduced using standard infrared reduction techniques of sky subtraction, flat fielding, and median-value masking to remove bad pixels. We estimate $< 1\%$ of the total number of pixels are bad, more than half of which are confined to one quadrant of the detector. Care was taken to image Neptune away from this quadrant. Each image was corrected for the geometric distortion of the array using the 'dewarp' routines provided by P. Brian Cameron², who estimates residual errors at ≤ 0.1 pixels.

We photometrically calibrated images using the Elias standard stars (Elias et al. (1982)) HD162208 on July 3, 2013 and HD1160 on August 20, 2014 and converted them to units of I/F, defined as (Hammel et al. (1989)):

$$\frac{I}{F} = \frac{r^2 F_N}{\Omega F_\odot} \quad (3.1)$$

Here, r is the ratio of Neptune's to Earth's heliocentric distance in A.U., πF_\odot is the Sun's flux density at Earth's orbit, F_N is Neptune's observed flux density, and Ω is the solid angle subtended by a pixel on the detector.

Imaging Results

Figure 3.1 shows calibrated images of Neptune at the beginning and end of each observing night and in each band. Because there were problems in the optical alignment of the AO system on the night of August 20, 2014, we did not achieve expected (diffraction-limited) resolution. This resulted in limited feature tracking capabilities for these images. Our viewing is limited to latitudes south of $+50^\circ$ due to the sub-Earth latitude of -27 deg..

Cloud features can be seen in both bands on both nights and their general characteristics agree with previous observations (e.g. Sromovsky et al. (2001a); Max et al. (2003); Martin et al. (2012); Fitzpatrick et al. (2014)). The brightest clouds stretch along several constant latitude bands centered at the mid-latitudes. On July 3, 2013, we see the largest bright feature centered at about 40°N . By August 20, 2014, this feature had disappeared or migrated to the dark side of the planet. Instead, we see two bright features in the Southern hemisphere centered at roughly 40°S . In the H-band, we also see a feature at Neptune's south pole, seen since the Voyager era (e.g. Smith et al. (1989); Limaye and Sromovsky (1991); Luszcz-Cook et al. (2010); Fitzpatrick et al. (2014); de Pater et al. (2014)). No features are seen immediately south of the equator.

Figures 3.2a and c show single images of Neptune that have been produced by combining the set of July 3, 2013 H- and K'-band images, respectively, using a procedure described in

²<http://www2.keck.hawaii.edu/inst/nirc2/forReDoc/postobserving/dewarp/nirc2dewarp.pro>

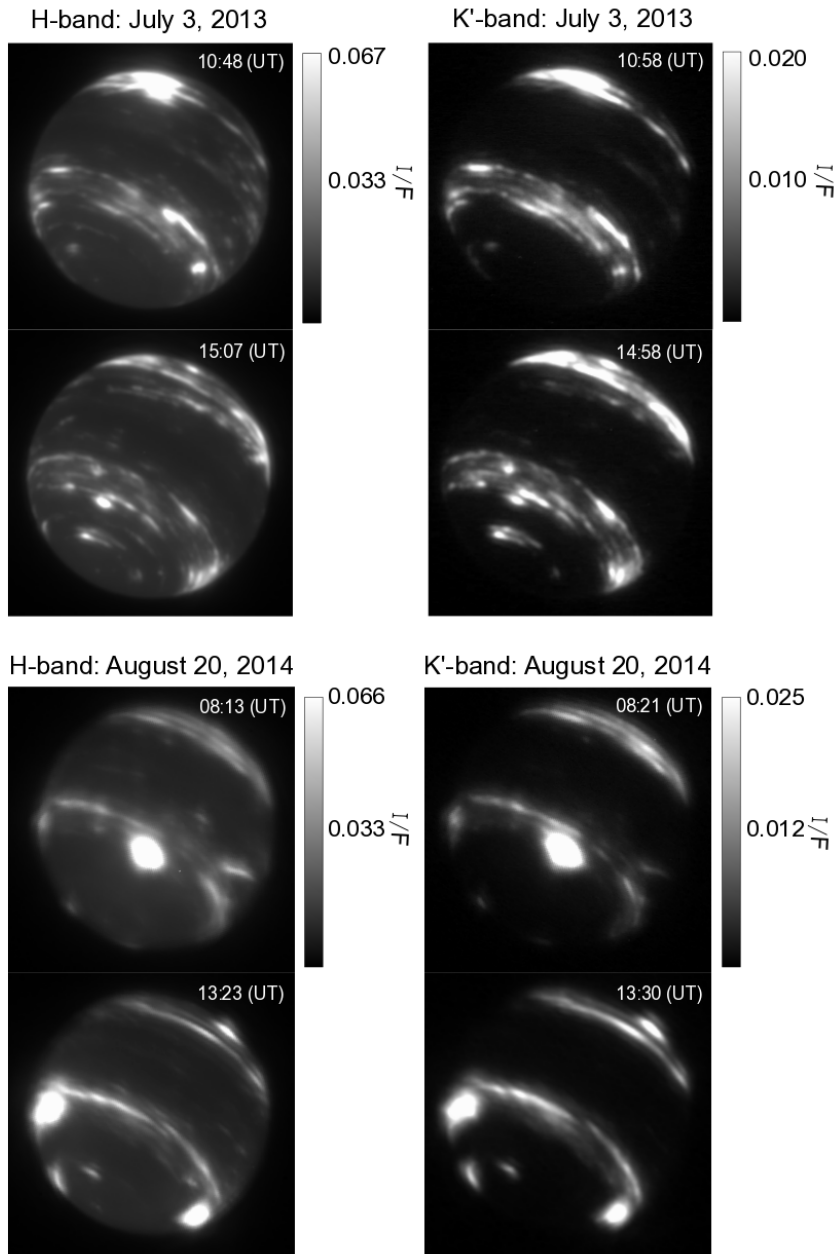


Figure 3.1: Images of Neptune taken in the H- (left columns) and K'- (right columns) taken on July 3, 2013 (top) and August 20, 2014 (bottom). The first and last images taken of Neptune on a given night are shown for each band. Images are in units of I/F with a colorbar given on the right of each image set.

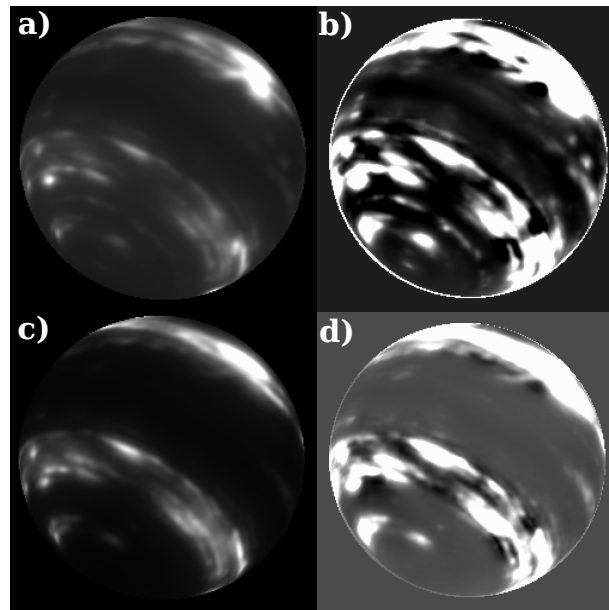


Figure 3.2: Images of Neptune in the H-band (top row) and K'-band (bottom row) on July 3, 2013 using the image combination method described in Fry et al. (2012). Figures a) and c) show the unaltered image while b) and d) show an enhanced, high-pass filtered version. Subtle equatorial features and banding can be made out due to the increased S/N ratio.

Fry et al. (2012). The image combination increases the S/N ratio of the images by employing a pixel brightness averaging method and correcting for feature motions induced by rotation and the canonical zonal wind profile. We did not make such images for August 20, 2014 due to the poor AO performance. Figures 3.2b and d are Figures 3.2a and c passed through a high-pass filter by subtracting a median-smoothed image. Banding at the equator can be made out as well as several subtle features. More features can be identified around the equator in the H-band compared to the K'-band.

Image Navigation and Projection

Accurate navigation and feature tracking requires precise determinations of Neptune's center in each image. An offset of even one pixel in the image centering can dramatically alter an image's projection and the determination of feature locations. This is seen in Figure 4 of Martin et al. (2012), which shows the errors due to a shift in the center of the disk in a map projection. We derive image centers by fitting the observed positions of three moons to their orbits as generated by the Rings Node of NASA's Planetary Data System (<http://pds-rings.seti.org/>) with a χ^2 minimization routine using a method developed by Luszcz-Cook et al. (2010) and used by Fitzpatrick et al. (2014). The error in image center was estimated by the variance in observed orbit to modeled orbit modified by a factor of the reduced χ^2 .

The estimated mean uncertainty of the center in both the H- and K'-band images on each night is between 0.1 - 0.2 pixels in x and y coordinates.

The accuracy of this procedure can be judged in Figure 3.3. Shown are the mean images of the aligned image stacks in each band on July 3, 2013. Each averaged image was passed through a high-pass filter by subtracting a median-smoothed image. This allows the individual orbits of Despina, Galatea, and Larissa to be resolved. Overlain on each image are the Rings Node moon orbits, which align well with the observed orbits after image alignment and navigation.

Images are then projected onto a rectangular grid and averaged over the five frames within each image set, with the rotation rate of the planet removed (about 16.11 hr, or $1.86^\circ/5$ min). Generally, the zonal drift rates are smaller ($< 0.65^\circ/5$ min) than the angular resolution at disk center ($\sim 2.4^\circ$). Hence, averaging images does not significantly smear features, but increases the signal-to-noise and allows fainter features to be distinguished. Averaging sets of data yielded 15 images in both bands on July 3, 2013 and 20 images in both bands on August 20, 2014.

3.3 Atmospheric Feature Tracking

The velocities of cloud features act as tracers for atmospheric wind velocities. Figure 3.4 is a rectangular projection of Figures 3.2a and c and shows candidate features identified for tracking. Features which are bright and morphologically stable over ~ 1 hour are candidates for tracking. Moreover, a feature must be distinct in longitude and latitude to be considered for tracking. In both bands, trackable features are most common at the mid-latitudes. Near the equator, both bands are relatively dark, with slightly more trackable features in H-band compared to K'-band.

The procedure for extracting wind velocities from feature positions is described in detail in Sromovsky et al. (2012). To summarize, from the projected, averaged images we produce strips of images in a fixed latitude range stacked in a vertical time series. An example of this image stack is given in Figure 3.5. For each visible feature, a reference image is chosen and centered around a target box containing the feature and a region outside it. Target boxes are placed in all other image strips based on the Voyager canonical longitudinal drift rates for Neptune and their positions are adjusted to maximize the cross-correlation between the feature signals in the reference target box and those in the other images. The centers of each box are the predicted longitude and latitude of the feature in each image. Figure 3.6 gives an example output of this method, which plots the predicted centers and correlation for each time slice of one feature.

Measured longitudes and latitudes vs. time were fit to straight lines with weighted regressions. Errors in position are given as the RMS deviation from a straight line. We repeat this procedure for dozens of features. In Figures 3.7 and 3.8 we plot the longitude position of selected tracked features versus time. Plots for all features can be found in the online Supplementary Materials 2 (Tollefson et al., 2018). While most features, within

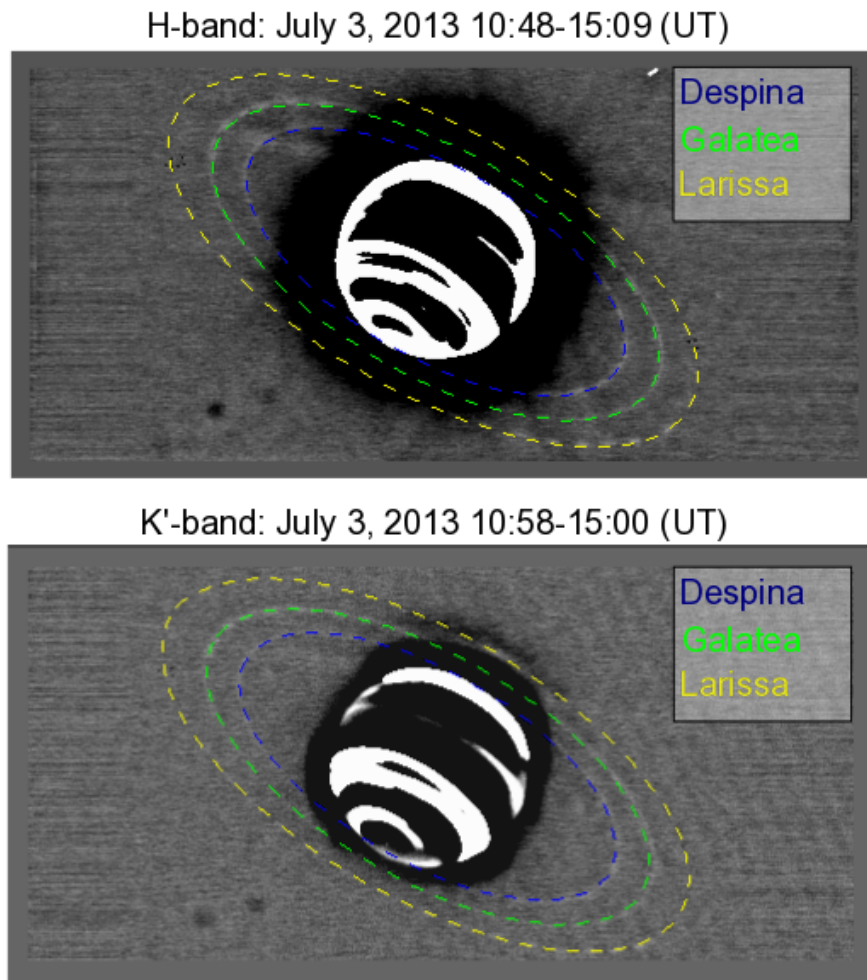


Figure 3.3: Mean averaged, high-pass filtered images of the aligned image stacks taken on July 3, 2013 in the H- (top) and K'- (bottom) bands. The colored dashed lines are the Ring Nodes orbits of three Neptunian moons (Despina, Galatea, and Larissa) and were used to determine the center of Neptune for navigation purposes. The path of each moon is seen as faint gray ellipses in these combined image stacks. The NASA orbits overlay the moon positions in the aligned images nicely, suggesting adequate navigation.

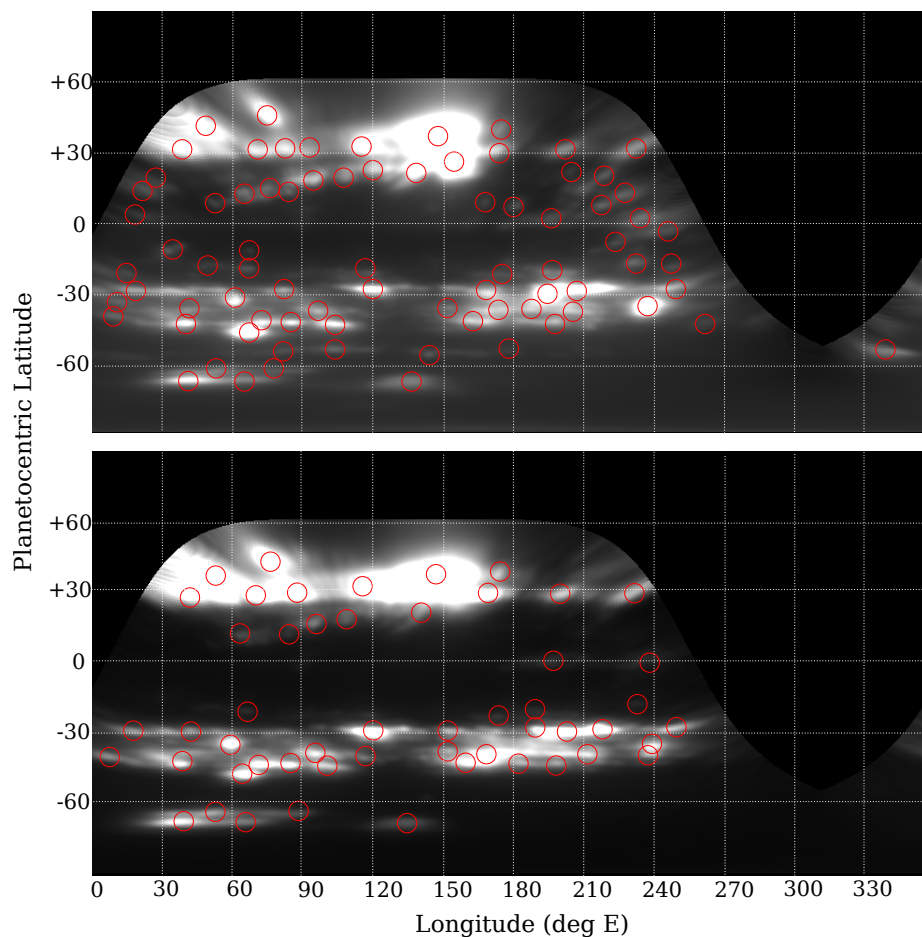


Figure 3.4: Rectangular projections of Figures 3.2a (H-band; top) and 3.2c (K'-band; bottom). Red circles are potential trackable features.

their estimated error, follow the drift rates expected by the canonical profile, many deviate significantly. Differences from the anticipated drift rate could be real or due to measurement errors and will be further discussed in later sections. Tables 1–4 in the online Supplementary Materials 1 summarize all tracked feature information.

3.4 Results

Zonal Wind Profiles

Longitudinal and latitudinal drift rates are transformed into zonal and meridional velocities by the following equations for planetocentric latitudes (Sromovsky et al. (2001b)):

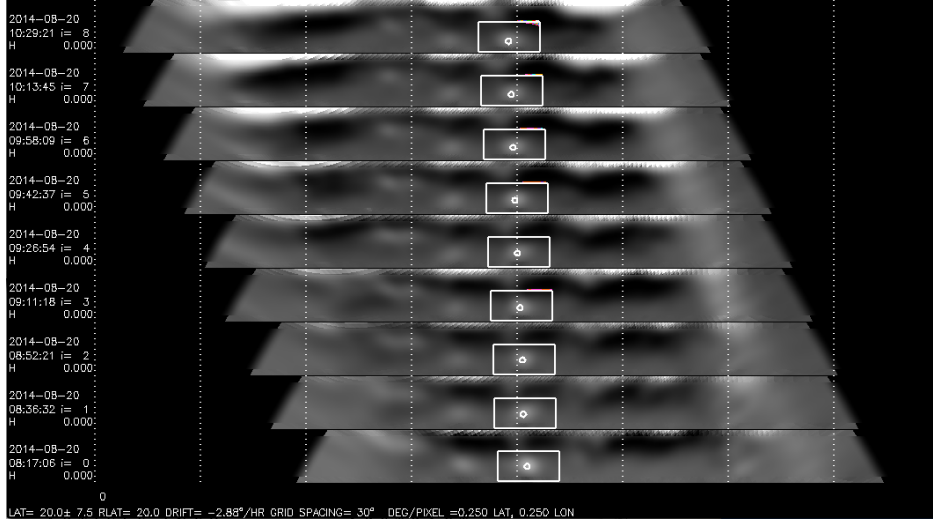


Figure 3.5: Example deprojected image strips at a fixed latitude range ($20^\circ \pm 7.5^\circ\text{N}$) stacked vertically by time since the initial observation. Each image strip is an average of a set of five images. Vertical white lines mark 30° increments in longitude. An example target feature of the tracking method is outlined in each box and its center is the result of maximizing the cross-correlation between image sets.

$$V_{\text{lon}} = \frac{R_{\text{eq}}}{\sqrt{1 + \frac{R_{\text{eq}}^2}{R_{\text{pol}}^2} \tan^2 \theta}} \frac{d\phi}{dt} \quad (3.2)$$

$$V_{\text{lat}} = \frac{R_{\text{pol}}^2}{R_{\text{eq}}} \left(\frac{1 + \frac{R_{\text{eq}}^4}{R_{\text{pol}}^4} \tan^2 \theta}{1 + \frac{R_{\text{eq}}^2}{R_{\text{pol}}^2} \tan^2 \theta} \right)^{\frac{3}{2}} \frac{d\theta}{dt} \quad (3.3)$$

Here, V is the wind speed in m/s, R_{eq} and R_{pol} are the equatorial and polar radii of Neptune, equal to 2.4766×10^7 m and 2.4342×10^7 m respectively (Lindal (1992)). $d\theta/dt$ and $d\phi/dt$ are the derived zonal and meridional drift rates (rad/s). Velocities for each feature are then plotted as a function of latitude and fit to a fourth-order polynomial symmetric about the equator. Neptune rotates from west to east, in the same direction as Earth, and eastward winds are taken to be positive. Thus the equatorial winds on Neptune are retrograde, blowing opposite to the direction of the planet's rotation, unlike Jupiter and Saturn, where equatorial winds are eastward and prograde. Comparisons to our profiles in both bands and the canonical profile are shown in Figures 3.9 and 3.10. Table 1 lists the parameters of each fitted polynomial and their widths of uncertainty.

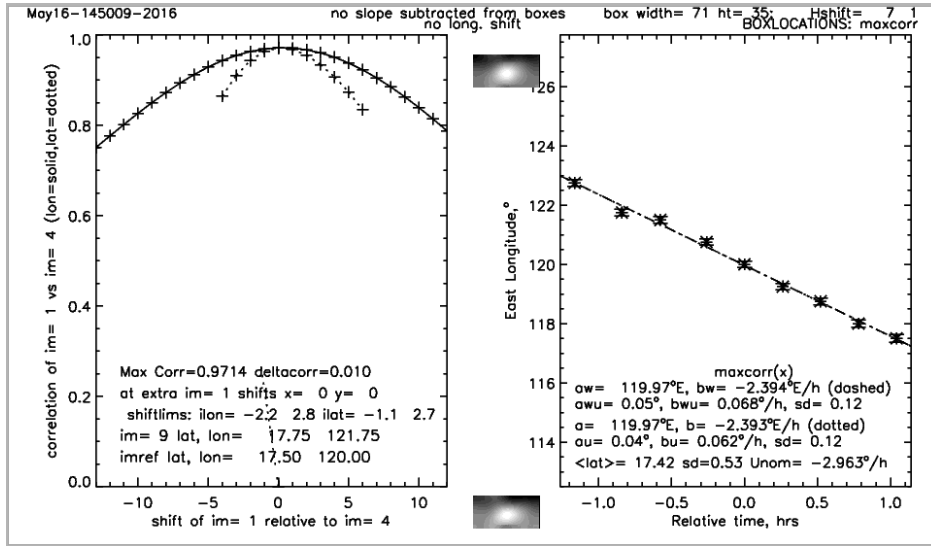


Figure 3.6: The output of the feature tracking method showing the predicted longitude positions (right) from maximizing the cross-correlation between image slices (left) for one particular feature (see Figure 3.5). Left: The solid lines are the correlation between longitudinal positions and the dashed lines are the correlation between latitudinal positions. Right: the black dots are the predicted longitude based on maximizing the correlation between image slices. The dash-dot line is a line of best fit through the black (correlation) points. The selected feature at the initial and end frames is shown in the center.

Poly. Profile	a (m/s)	b	c
Voyager	-398 ± 12	$1.88\text{E-}1 \pm 1.40\text{E-}2$	$-1.20\text{E-}5 \pm 3.00\text{E-}6$
H-band 2013	-325 ± 16	$1.58\text{E-}1 \pm 2.20\text{E-}2$	$-1.21\text{E-}5 \pm 4.67\text{E-}6$
K'-band 2013	-415 ± 42	$2.35\text{E-}1 \pm 5.34\text{E-}2$	$-2.23\text{E-}5 \pm 1.14\text{E-}5$
H-band 2014	-292 ± 29	$1.45\text{E-}1 \pm 4.91\text{E-}2$	$-1.18\text{E-}5 \pm 1.11\text{E-}5$
K'-band 2014	-433 ± 56	$2.40\text{E-}1 \pm 7.88\text{E-}2$	$-2.73\text{E-}5 \pm 1.90\text{E-}5$
Leg. Profile	a	b	c
H-band 2013	-159	462	37
K'-band 2013	-134	601	-127
H-band 2014	-95	359	76
K'-band 2014	-147	474	13

Table 3.1: Parameters in the fits to tracked zonal wind velocities. The fits are 4th-order polynomials given by: $V = a + b\theta^2 + c\theta^4$ (top half). For comparison, profiles generated from 4th-order Legendre polynomial fits given by: $V = a + b(3\mu^2 - 1)/2 + c(35\mu^4 - 30)/8$ where $\mu = \sin \theta$, are also shown (bottom half). The equatorial velocities derived from the Legendre polynomials are all well within the 2-sigma uncertainty given by the generic polynomial fits.

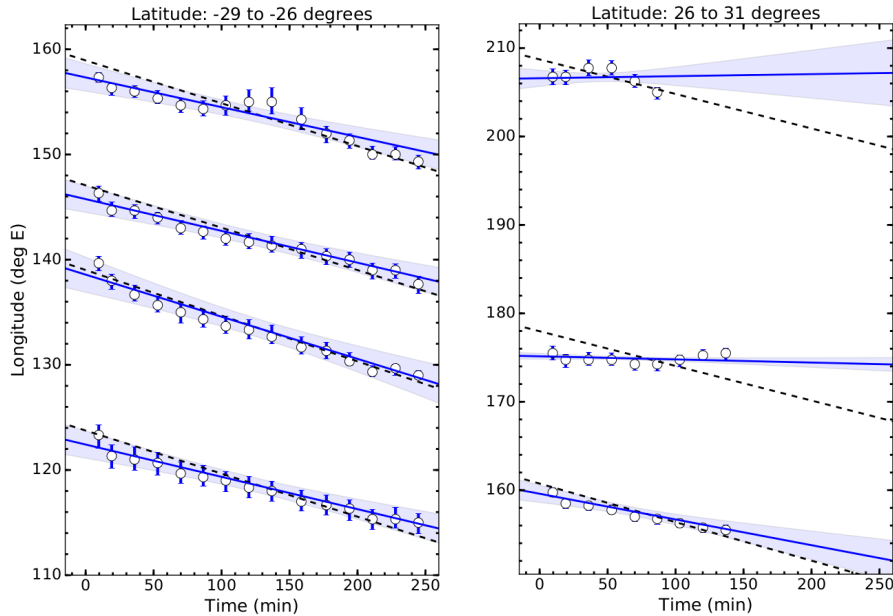


Figure 3.7: Selected feature tracking results in the H-band from July 3, 2013. Each data point is a feature’s derived longitude since the initial observation. The blue lines are lines of best fit to the data. The blue shaded region is the 1σ error in the fit. The dashed black line is the longitude path the feature would follow according to the canonical profile. The majority of tracked features follow the canonical profile (left figure), but some deviate significantly (right figure). Plots for all features can be found in Supplementary Materials 2.

A significant, large spread in the individual derived zonal velocities is observed at constant latitudes on both nights. This is most prominent at the equator and mid-latitudes in both bands, with differences in feature velocities reaching as high as 500-600 m/s. Moreover, there is a pronounced difference between the derived H and K’ zonal wind profiles near the equator. At the equator on July 3, 2013, the deviation in the H-band wind speeds compared to those derived by the Voyager fit is 73 ± 16 m/s. The difference between the H- and K’-bands on this night at the equator is 90 ± 45 m/s. This shift persists in the August 20, 2014 observations. There is a 93 ± 29 m/s deviation between the H-band and canonical profile and a 141 ± 63 m/s difference between the H- and K’-bands on this night. There is no significant difference between the K’-band and Voyager profile on either night. The difference between the H-band and Voyager profiles qualitatively agree with Fitzpatrick et al. (2014), although their H-band velocities are best described by a profile shifted toward positive velocities by 180 ± 50 m/s. The dispersion of our new results falls within the wide range seen in previous publications. Spreads in feature velocity were first seen in measurements of the motions of small clouds in Voyager 2 data, particularly around the GDS and Dark Spot 2 (Smith

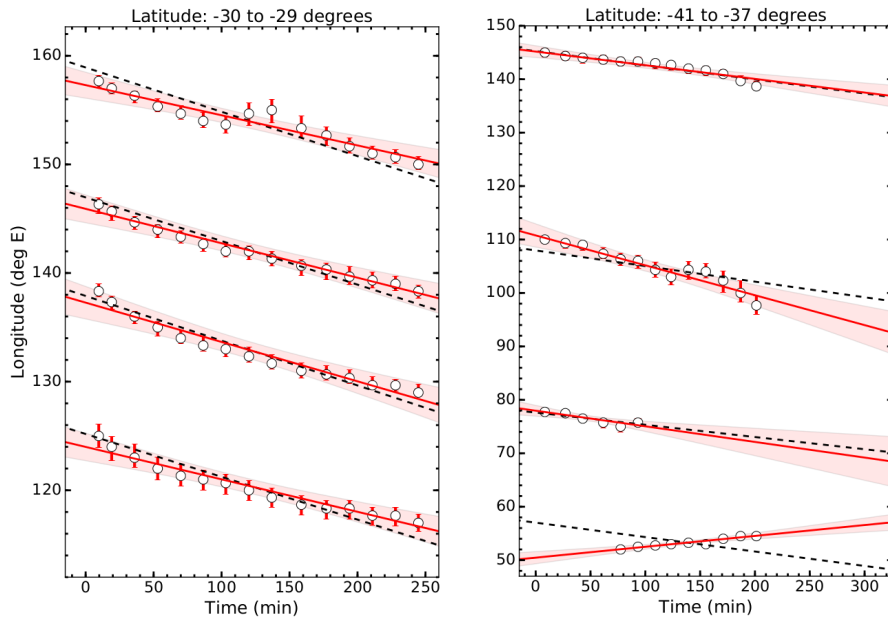


Figure 3.8: As figure 5 except for the K'-band. The red lines are lines of best fit to the data. The red shaded region is the 1σ error in the fit. The dashed black line is the longitude path the feature would follow according to the canonical profile. The majority of tracked features follow the canonical profile (left figure), but some deviate significantly (right figure).

et al. (1989); Limaye and Sromovsky (1991)). Martin et al. (2012) found large spreads in zonal velocities at constant latitudes in Keck AO H-band observations. Comparatively, at the southern low- and mid-latitudes, the Voyager data show much less dispersion from the canonical profile than the results of Martin et al. (2012). Fitzpatrick et al. (2014) also observed significant deviation in H-band features at the equator and southern-mid latitudes compared to the Voyager profile, with differences reaching as high as ~ 500 m/s.

Spurious data affect the fit. Such data could be due to a number of factors including features near the edge of Neptune's circumference becoming smeared from projection, changes in cloud morphology, limb-brightening, navigation errors, and errors in the position extraction procedure. Several features also move in oscillatory patterns (as in Martin et al. (2012)) and limited tracking times may not capture a feature's full period of motion. Similar effects were seen on Uranus due to inertial oscillations (Sromovsky and Fry (2005)). Figures 3.9 and 3.10 show the individual feature velocities and their 1σ errors alongside the zonal wind profiles. Each feature's plot symbol is proportional to its tracking time. Features tracked over the entire observing period generally have smaller errors than those tracked in only a few images and tend to lie closer to their band's zonal wind profile. Thus, the spread in feature velocities at a fixed latitude is partially a result of their limited tracking time

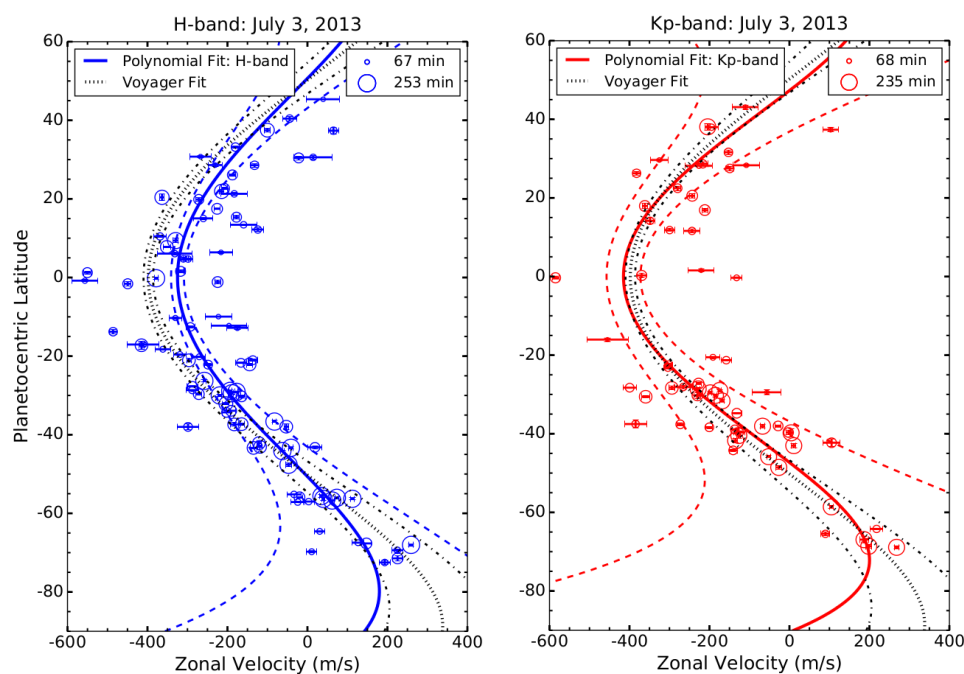


Figure 3.9: Eastward zonal wind velocities of tracked features in the H- and K'-band on July 3, 2013. Individual features are plotted as circles with their marker size proportional to the length of time the feature was tracked. The shortest and longest times are given in the top right corner. The Voyager profile is shown in a dotted black line with the width of uncertainty in a dot-dash black line. Our polynomial fit to the H-band is shown with a blue solid line (left image) while the fit to the K'-band is in red (right image). Their widths of uncertainty are in dashed blue and red lines respectively. There is significant positive deviation in the H-band wind speeds at the equator compared to those derived by the Voyager fit by 73 ± 16 m/s. The K'-band velocities agree well with the Voyager profile.

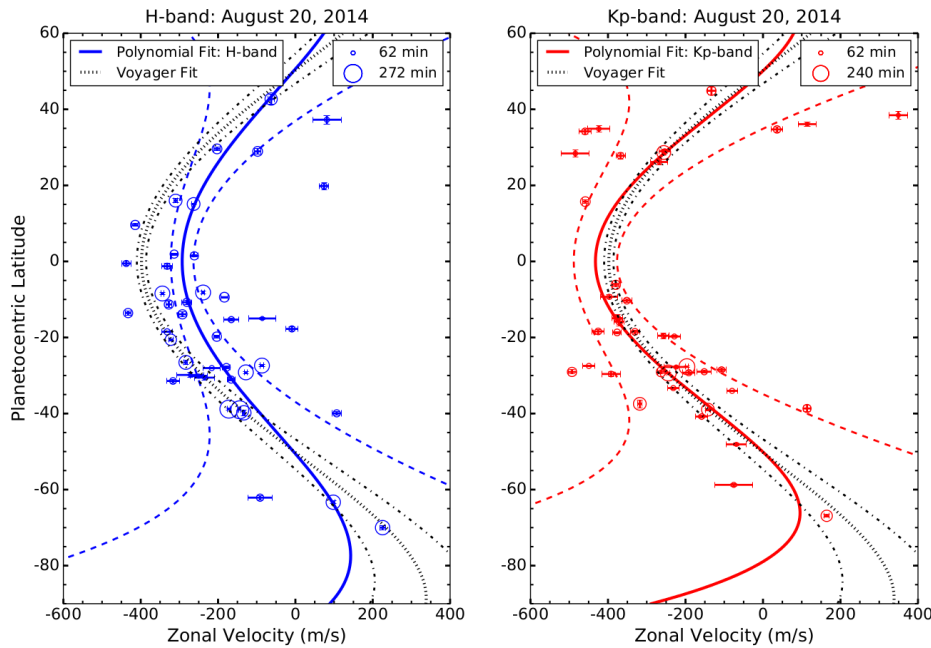


Figure 3.10: Same as figure 3.9 except for August 20, 2014. The Voyager profile is shown in a solid black line with the width of uncertainty in a dashed black line. Our polynomial fit to the H-band is shown with a blue solid line while the fit to the K²-band is in red. Again, there is a significant positive shift in the H-band zonal velocities at the equator compared to those derived by Voyager by 93 ± 29 m/s.

and measurement errors. Figures 3.11 and 3.12 show features which have velocity errors less than 30 m/s and were tracked in at least 10 images (~ 2.5 hours). These features are usually bright and morphologically stable and are likely to follow the zonal flow. Spreads in feature velocities up to ~ 200 m/s at constant latitudes are still seen on both nights and both bands, although this is far less than the spread of 500-600 m/s seen with the full set of tracked features. This suggests that large, bright features are less dispersed from the derived zonal profile. It is also true that such features are less susceptible to tracking errors, which might also account for much of their reduced dispersion. This is consistent with Martin et al. (2012), who also found that the brightest features usually agreed with the canonical profile. However, we still find that the H- and K'-bands zonal wind profiles still differ by more than 1σ at the equator. The H-band and canonical profiles also differ by 2σ at the equator.

The meridional wind velocities for each tracked feature are plotted in Figures 3.13 and 3.14. Globally, the latitudinal velocities are consistent with zero. But, a few features have latitudinal velocities as large as 100–200 m/s. The zonal velocity of these features tend to significantly deviate from the canonical profile, suggesting they are driven by mechanisms

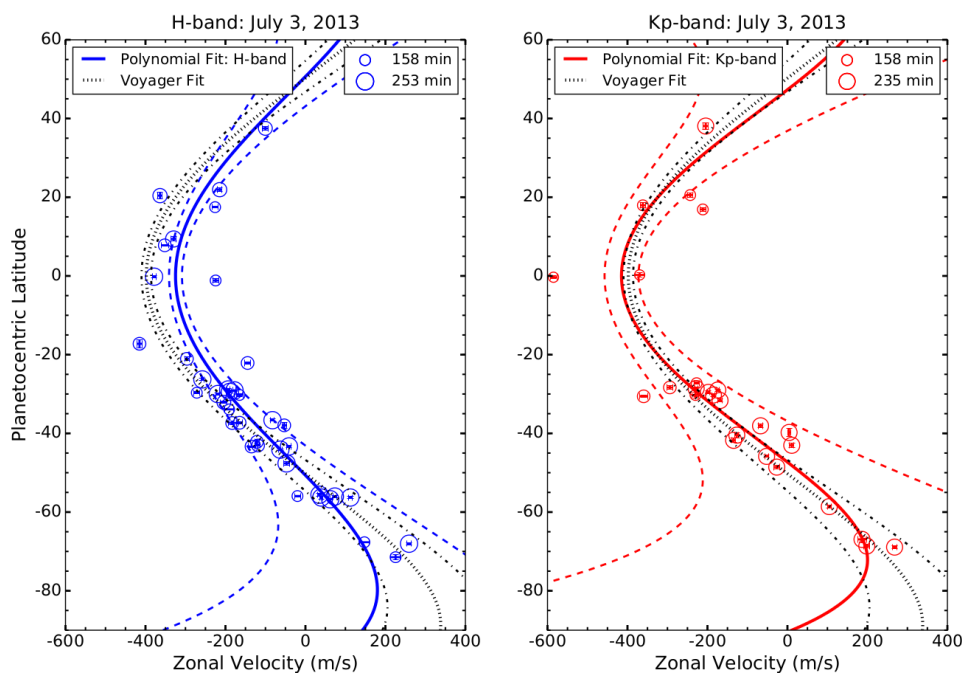


Figure 3.11: Same as figure 3.9 but only including features tracked in at least 10 images and with errors < 30 m/s.

that produce motion in both directions, such as vortices or wave mechanisms. This behavior was found by Sromovsky et al. (2001) in HST observations, where several features near the same longitude as a dark spot, but widely scattered in latitude, were accurately measured (within 10–20 m/s) to have meridional wind speeds around 100 m/s, and zonal winds that deviated from the canonical profile by over 200 m/s, while the vast majority of their tracked clouds had insignificant meridional motions and very small deviations from the canonical profile. However, our features with this behavior also have large errors and are not tracked for very long. As previously mentioned, the centers and velocities of features that are faint, ephemeral, or close to the limb, are difficult to constrain.

Trends in Feature Depth and Velocity

The derived H and K' profiles give a crude 3D look into Neptune's upper atmosphere since these bands probe different altitudes. We hypothesize that the equatorial shift in the H-band profile is due to deep features. Our data are spectrally limited so accurate cloud top pressures can not be determined. However, the K'-to-H I/F ratio indicates whether features are deeper or shallower relative to one-another: the deeper a cloud is in the atmosphere, the greater the expected H-band intensity relative to the K'-band intensity. We compute the maximum

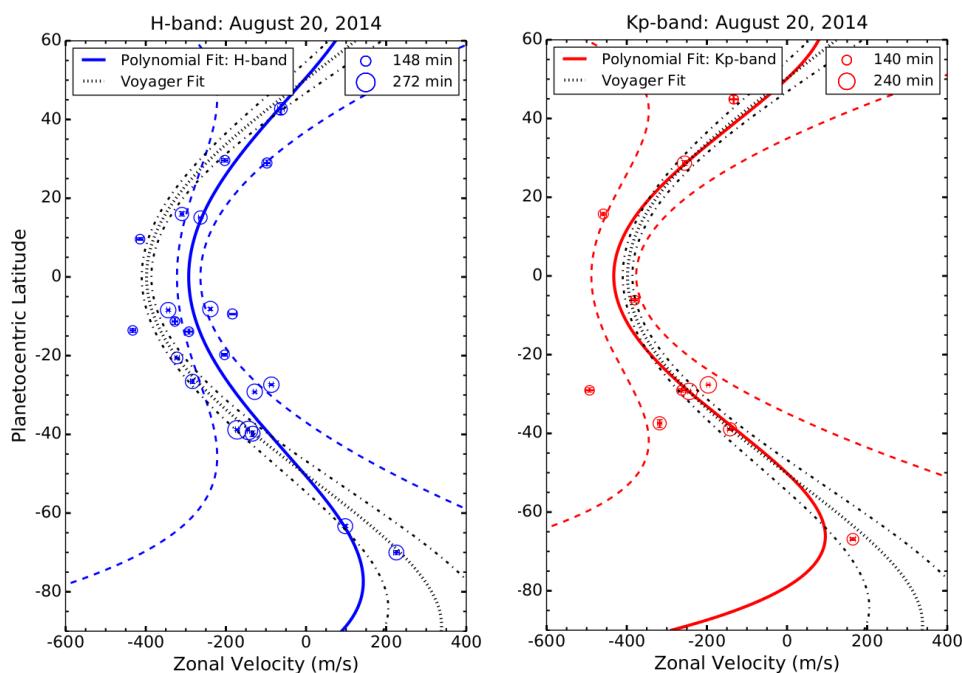


Figure 3.12: Same as figure 3.12 but only including features tracked in at least 10 images and with errors < 30 m/s.

allowed K' -to- H I/F ratio for each 2013 H-band feature and compare this to their latitude and zonal velocity (see Table 5 in Supplementary Materials 1). Uncertainties are estimated as 20% of I/F, from the uncertainty in the photometry. Figure 3.15 plots the maximum K' -to- H I/F ratio vs. latitude of each H-band feature. We find equatorial features ($\pm 20^\circ$) have smaller K'/H intensities than those at mid-latitudes, suggesting they are deeper. This is consistent with Fitzpatrick et al. (2014), who found that clouds at equatorial latitudes are uniformly deeper (~ 0.5 bar) than those at northern mid-latitudes (~ 0.1 bar). Numerous authors also find northern features at the highest altitudes (Sromovsky et al. (2001b); Gibbard et al. (2003); Luszcz-Cook (2012); de Pater et al. (2014)), generally in the stratosphere at the ~ 10 mbar level, although exact pressures vary due to spectral limitations, instrument sensitivity at different altitudes, and model assumptions. Luszcz-Cook et al. (2010) compared observed and modeled K'/H and K'/J intensities to determine upper altitudes for south polar features and found that a K'/H ratio of 10% gave a minimum cloud top pressure of 0.4 bar. Features seen in H but not K' may also be deep, with pressures greater than 1 bar. A notable example of this is the south polar feature, observed in H-band but not in K' , located at 1.6 bar (de Pater et al. (2014)). We tracked 29 and 20 H-band features in our 2013 and 2014 observations, respectively, that were equatorward of 20° N/S, but only 10 (in 2013) and 11 (in 2014) K' -band features in this same region. Taken altogether, we argue that the H-band

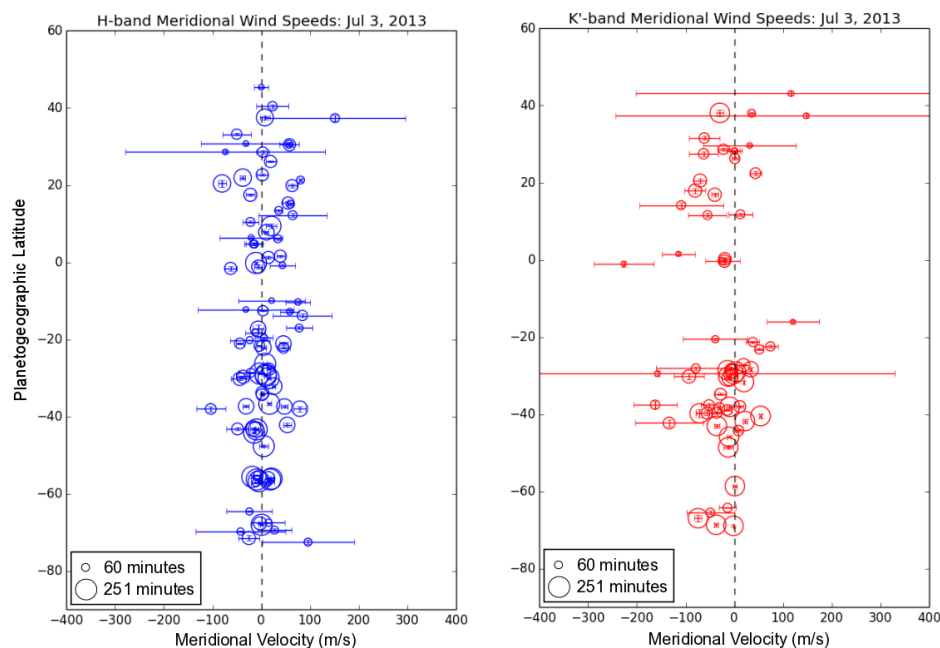


Figure 3.13: Meridional velocities of tracked features on July 3, 2013 with the H-band in blue on the left and the K'-band in red on the right. Circle size is proportional to tracked time with the shortest and longest times in the bottom left corners. The black dashed line marks zero and visually shows that the velocities are not too different from zero.

zonal wind profile represents features which are, on average, deeper than those given in the K'-band profile at low latitudes.

Figure 3.15 plots the zonal velocity difference from the derived K'-profile vs. latitude for each 2013 H-band features. The difference between the H- and K'-band profiles (from Fig. 3.9) is overplotted. Positive values indicate velocities eastward (less negative) relative to the K'-profile. The largest deviations from the K' profile are around the equator, where features have low K'/H intensities and are probably deep. The deviations in zonal velocity of features at the southern midlatitudes lie closer to zero and are mostly within the uncertainty of the K' profile fit. This is consistent with our hypothesis: the shift in H-band profile may be driven by a handful of deep features around the equator.

Previous studies have also shown that the brightest H-band features are typically at greater depths (pressures) than the brightest K'-band features (Gibbard et al. (2003); Luszcz-Cook (2012); de Pater et al. (2014)). This is consistent with our expectations from radiative transfer modeling. Figure 3.16 shows the contribution functions for each filter in three different atmospheric models, illustrating the range of depths from which the H- and K'-reflectivity may arise. In all three cases, the gas opacity is dominated by H₂ collision-

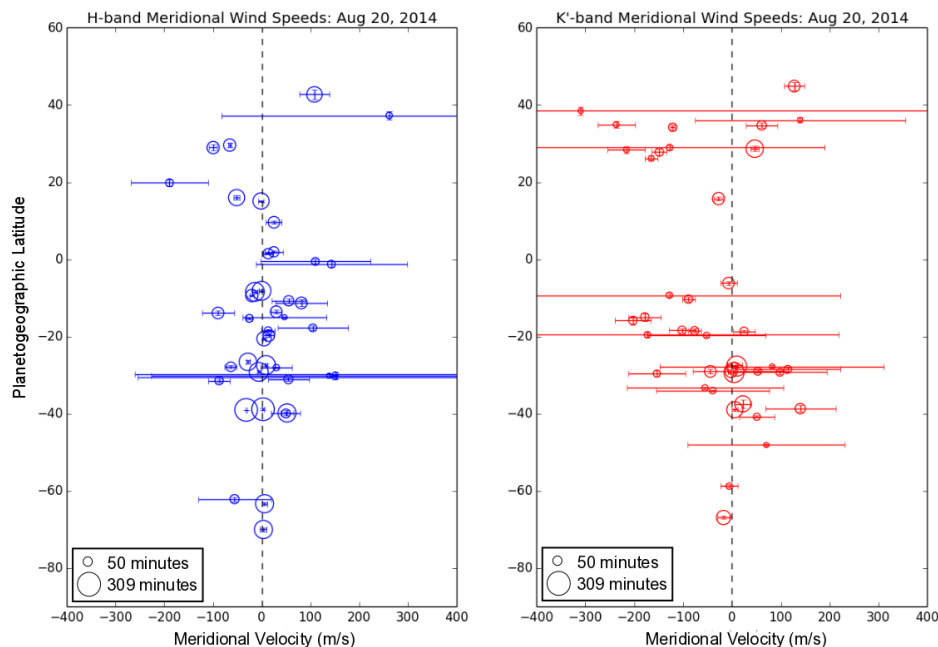


Figure 3.14: As figure 3.13 except for August 20, 2014.

induced absorption and CH_4 absorption. All models include a vertically thin cloud at 3 bar with a $1.6 \mu\text{m}$ optical depth of 0.5; models b) and c) contain additional aerosols in the upper troposphere/stratosphere, as described in the figure caption. For the purposes of our models in the following sections, we assume that the H-band features are located at 1–2 bar, while K'-band features are located between 10–100 mbar.

3.5 Interpreting Differences in The H and K' Zonal Wind Profiles

The major caveat to current and past zonal wind profiles is that they are merely best fits to the data. These fits do not pick up any fine scale structure in the zonal winds. Moreover, the profiles represent features driven by a number of possible mechanisms, including shear, wave phenomena, or other local dynamics. Dispersion is partly due to faint, ephemeral features, whose exact centers and velocities may be difficult to pinpoint. Thus, explaining all variations in zonal velocity from these profiles is difficult, if not impossible, to do.

We also note that our following models assume that the derived zonal flow is set at a constant pressure level. However, tracked features are not necessarily at the same altitude. For instance, northern mid-latitude features appear at the highest altitudes on Neptune (Sro-

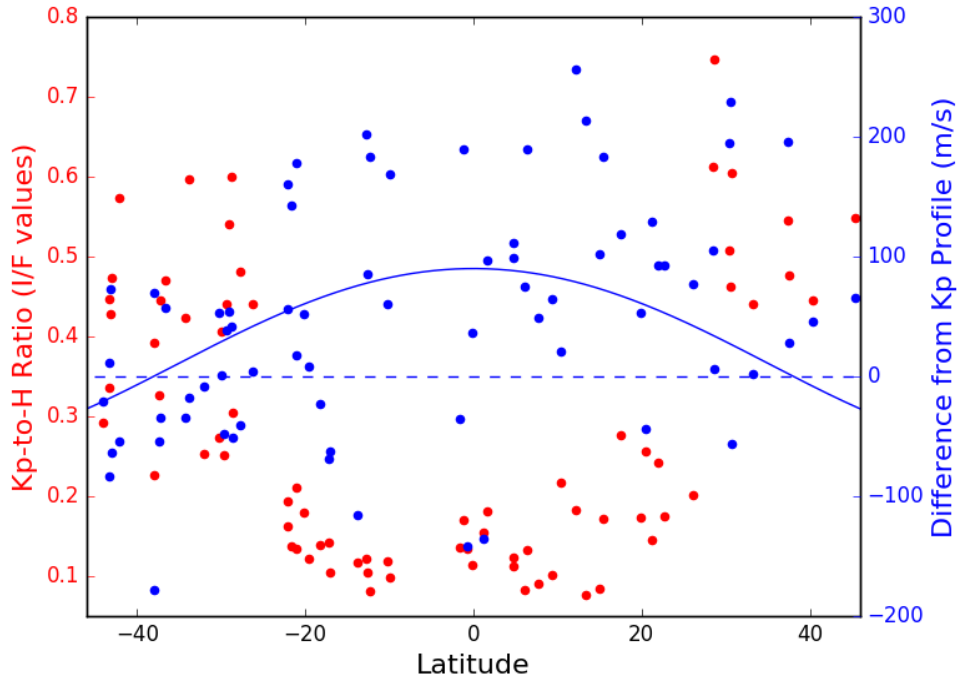


Figure 3.15: Derived K'-to-H I/F ratios vs. latitude (red) and zonal velocity deviation from the K' profile vs. latitude (blue) for 2013 H-band features. Shown are features between $\pm 45^\circ$. Positive values in velocity variation are eastward (less negative) relative to the K'-profile. Overplotted is the difference between the H and K' profiles (solid blue line) and the zero velocity difference (dashed blue line). Features in the equatorial region ($\pm 25^\circ$) have smaller K'/H intensities and larger velocity variations than those at mid-latitudes. This suggests that the shift in the H profile from the K' and canonical profiles is partly due to deep features.

movsky et al. (2001b); Gibbard et al. (2003); Luszcz-Cook (2012); Fitzpatrick et al. (2014); de Pater et al. (2014)). Irwin et al. (2016) analyzed VLT/SINFONI H-band observations made in 2013 and found bright, deep seated clouds ($P > 1$ bar) in the southern mid-latitudes and 'intermediate' clouds ($300 < P < 400$ mbar) in the near-equatorial region. Moreover, features at constant latitudes may have different altitudes. de Pater et al. 2014 saw NIR clouds in the southern mid-latitudes at two levels: in the stratosphere from 0.02 – 0.03 bar and at altitudes below 0.3 bar ($P > 0.3$ bar). Luszcz-Cook (2012) observed similar altitude variations in Keck OSIRIS data.

With these limitations in mind, we only attempt to explain the mean ~ 100 m/s eastward offset in the equatorial region in the H profile from the canonical and K' profiles. This difference seems real (greater than 2σ) and persistent, seen in 2009 (Fitzpatrick et al. (2014)) and now in both our 2013 and 2014 observations. Fry and Sromovsky (2004) also show that

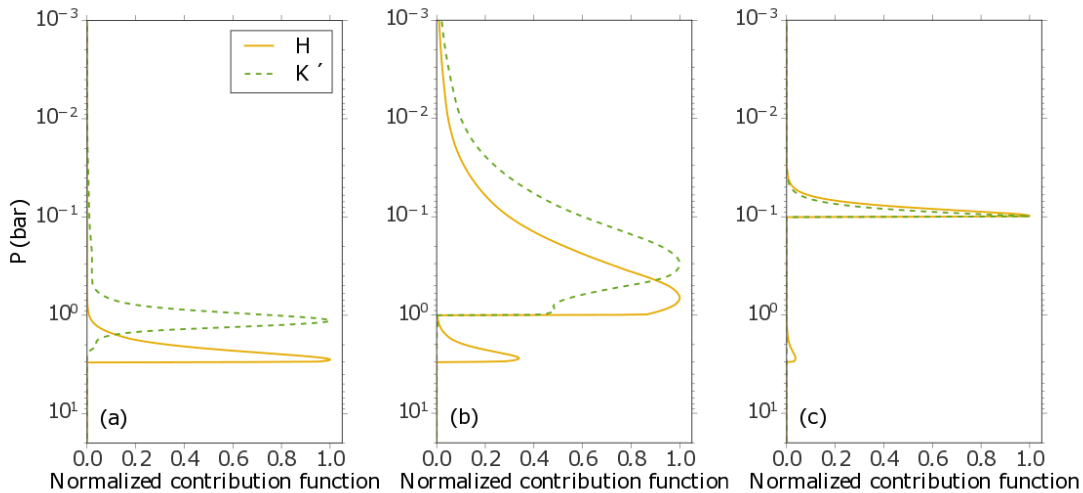


Figure 3.16: Normalized H-band (solid orange line) and K-band (green dashed line) contribution functions for three different model atmospheres, illustrating the range of depths from which the H- and K'- reflectivity may arise. In all three cases, gas opacity is contributed by collision-induced absorption of H₂ with H₂, He, and CH₄; and by CH₄ absorption. Details of the atmosphere models may be found in Luszcz-Cook et al. (2015). The three models differ only in the assumed distribution of aerosols: all three models include a vertically thin cloud at 3 bar with a 1.6-micron optical depth of 0.5. In model (a), the atmosphere is clear aside from this 3-bar cloud. In model (b), there is an additional haze (scale height equal to that of the gas) between 1 bar and 1 mbar, with total 1.6-micron optical depth of 0.5. Model (c) includes the 3-bar cloud and an additional vertically thin cloud at 0.1 bar, also with a 1.6 micron optical depth of 0.5. Single scattering albedo and asymmetry factors are 0.75 and 0.7, respectively for all aerosol particles.

H-band wind results from 202 cloud measurements taken in 2003 and 2004 images also fall below the canonical profile at low latitudes. Based on the K'/H intensity trends and previous NIR studies, we interpret the H-band profile in the equatorial region as the “average” zonal velocity of features which are mostly: 1) deep (greater than 1 bar), and 2) have velocities shifted $\sim +100$ m/s from the K'-profile. Likewise, we interpret the K'-band profile in the equatorial region as the “average” zonal velocity of features which are mostly: 1) located in stratosphere (around ~ 10 mbar), and 2) have velocities shifted ~ -100 m/s from the H-profile. Differences in the zonal winds with depth at constant latitude and time is evidence of vertical wind shear in Neptune's troposphere and stratosphere. Our derived profiles suggest a wind shear around -100 m/s over several scale heights at the equator (increasing with height).

The Voyager results of Sromovsky et al. (1993) also provide evidence of vertical wind shear. Their Figure 15 shows that three major long-lived cloud features, including the GDS,

Scooter, and the Second Dark Spot, all move in the same direction as the canonical profile, but with reduced speed. If these major features are more deeply rooted than the small clouds on which the canonical profile is based, and there is spectral evidence that this is true for Scooter, then it would appear that this is another example of the magnitude of wind speeds increasing (becoming more westward) with altitude. Based on Voyager 2/IRIS temperature retrievals alone, this produces the wrong sign of vertical wind shear in the thermal wind equation, as explained below.

Modeling Vertical Wind Shear at the Equator with the Thermal Wind Equation

In this section, we will examine the plausibility of vertical wind shear modeled with the thermal wind equation as an explanation for the observations. The largest and most meaningful differences (i.e. smallest uncertainty) between the H- and K'-band zonal wind profiles occur at the equator. In the following text, we discuss the applicability of the thermal wind equation to Neptune and how it may be extended to the equator under certain conditions, despite the Coriolis force vanishing there. Using plausible depths for the H- and K'-band profiles, discussed in the previous section, we then show that integrating the thermal wind equation does not reproduce the predicted vertical wind shear at the equator. Finally, we discuss the importance of methane variability in modeling the vertical wind shear and how it can reconcile the inconsistency between the observed wind shear and the thermal wind equation. We stress that these results are speculative since they rely on assumptions about the symmetric structure of the zonal wind and temperature fields as well as the exact pressures of H- and K'-band features.

The standard thermal wind equation is:

$$f_0 \sin \theta \frac{\partial u}{\partial r} = -\frac{g}{r_0 T} \frac{\partial T}{\partial \theta}, \quad (3.4)$$

where $f_0 \equiv 2\Omega_0$ is the Coriolis parameter at the North Pole, rather than the local Coriolis parameter. We define: r_0 as the radius of the planet, T as the temperature, $\partial T/\partial \theta$ as the latitudinal-temperature gradient as constant pressure P , g as the gravity in the \hat{r} direction, and u is the zonal (longitudinal) velocity. Table 2 lists the relevant values for these variables

Although the standard thermal wind equation is used in many planetary atmospheric applications and is derived in many texts, c.f., Pedlosky (1987), it is limited in its use due to the divergence of the Coriolis force near the equator. Marcus et al. (2019) derive an equatorial thermal wind equation (EQTWE) which provides a relationship between the vertical wind shear and the horizontal temperature gradients that is valid at and near the equator:

$$f_0 \frac{\partial u}{\partial r} = -\frac{g}{r_0 T} \frac{\partial^2 T}{\partial \theta^2} \quad (3.5)$$

A similar result was noted as equation 8.2.2 in Andrews et al. (1987). This equation is derived by assuming $\partial T/\partial \theta \equiv 0$ and taking L'Hôpital's rule of the standard thermal wind

Variable	Description	Value
Ω	Rotation rate of Neptune (rad/s)	1.09E-4
g	Gravitational acceleration (m/s ²)	11.15
r_0	Neptune's equatorial radius (m)	2.4766E7
H	Scale height (km)	19.1 below 500 mbar 51.8 above 500 mbar
T	Temperature (K)	
u	Zonal velocity (m/s)	
θ	Latitude (rad)	
z	Radial distance into atmosphere (m)	

Table 3.2: List of variables and their values (if constant) used in the thermal wind equation.

equation in the limit as $\theta \rightarrow 0$. One problem with using L'Hôpital's rule in this fashion is that it creates a singularity at the equator if $\partial T/\partial\theta \neq 0$ there. The EQTWE derived by Marcus et al. (2019) does not require mirror-symmetric flow and does not produce this singularity.

It is seen by inspection that integrating both (3.4) and (3.5) upward will not reproduce the observed H and K²-band equatorial differences. As the zonal winds become more negative (westward) with altitude (H-band to K²-band), $du/dr < 0$. This implies that the meridional temperature gradient and its second derivative at the equator to mid latitudes must be positive. However, this is inconsistent with derived temperature profiles of Neptune's troposphere from Voyager/IRIS spectra in Figure 3.17, which show that the equator and poles are warm and the mid-latitude are cool and $\partial^2 T/\partial\theta^2 < 0$ at the equator. (Fletcher et al. (2014)).

In the next two sections, we discuss two reasons that could reconcile the inconsistency between the derived zonal wind profiles and temperature profile. First, we discuss whether the assumed temperature profile is correct. Second, we examine the impact non-ideal gas behavior has on the thermal wind equation. In particular, we focus on the latter (our preferred) explanation in the subsequent discussion.

Temperature Profile Incorrect?

Our temperature data come from inbound Voyager/IRIS maps, which are only sensitive to the 70-800 mbar range ((Conrath et al., 1991; Fletcher et al., 2014)). Temperatures above and below these pressures are smooth relaxations to an *a priori* profile based on the mean stratospheric temperature and the profile from Moses et al. (2005). So, while average global temperatures are known throughout the upper atmosphere, the meridional trends are more uncertain outside 70-800 mbar. This can be seen in the data itself. In Figure 3.18 we plot sample inbound temperature data with error bars inside and outside the 70-800 mbar

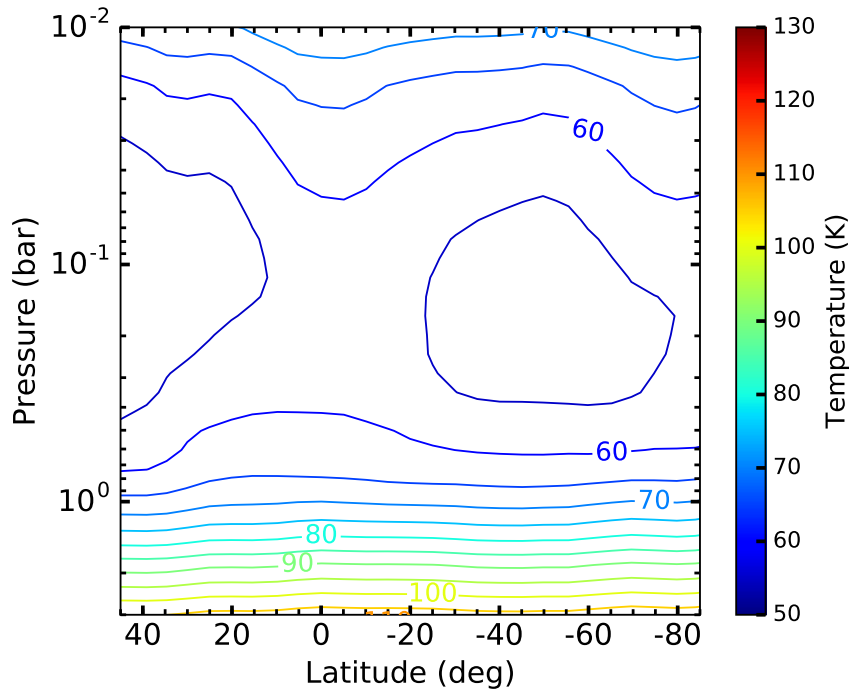


Figure 3.17: Temperature contours from inbound Voyager/IRIS spectra Conrath et al. (1991); Fletcher et al. (2014). This profile was used to determine the meridional temperature gradient.

range. At pressures outside this range, the uncertainties become larger, approaching the temperature difference between the equator and mid-latitudes. We can not confidently infer whether the equator is warmer or colder than the mid-latitudes outside 70-800 mbar from the current data alone.

We now explore whether meridional variations in temperature outside the well-constrained 70-800 mbar pressure range could cause wind shear consistent with the difference between our H and K' observations. We break this calculation into two steps.

First, we calculate the wind shear du/dr between the depth of the K'-band profile down to 1 bar. We do this by using the temperature profile given by the Voyager/IRIS spectra (Fig. 3.17) to determine the expected zonal wind profile at 1 bar assuming the K'-profile is at a set pressure level. Since the depth of the K' features are not precisely constrained, we test a range of pressures from 10 to 100 mbar. The value du/dr is the difference in the zonal winds between the extrapolated profile at 1 bar and the H-band, which we also set to a variety of pressures between 1.0 - 2.4 bar, 2.4 bar being the location of a commonly assumed optically thick bottom cloud (Irwin et al. (2011)). Altitude changes are calculated assuming hydrostatic equilibrium with a scale height of 19.1 km in the troposphere and lower stratosphere, a value obtained from de Pater et al. (2014). Voyager/IRIS derived meridional

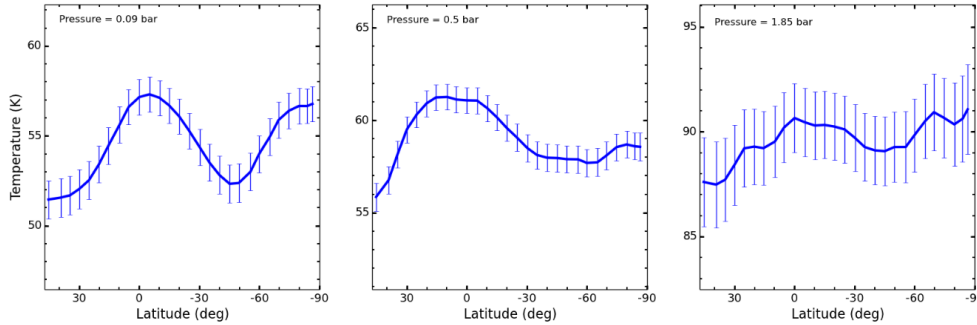


Figure 3.18: Meridional temperatures and errors at constant pressure from Fletcher et al. (2014). The first two images show Voyager/IRIS temperature retrievals that are within its sensitivity range (70 - 800 mbar). The latter figure is a temperature profile extrapolated from Voyager/IRIS results by the application of the smooth relaxation to an *a priori* profile. In this case, the uncertainty is substantial.

temperatures are sampled every 5° latitude, which is too sparse to reliably numerically differentiate. To circumvent this issue, we fit a symmetric profile to the temperature data:

$$T(\theta) = \sum_{n=0}^N a_n \cos(n\theta) \quad (3.6)$$

One problem with this assumption is evidence of seasonal variations in Neptune's atmospheric brightness that could cause differences in hemispheric temperatures (Sromovsky et al. (2003); Hammel and Lockwood (2007)). Fletcher et al. (2014) and de Pater et al. (2014) estimate random uncertainty in the Voyager/IRIS temperatures to be 1-2 K in the troposphere, increasing to 2-4 K in the mid-stratosphere. The temperature difference predicted from Voyager/IRIS between hemispheres at constant latitude is close to or within this error, so our chosen temperature profile is consistent with meridional symmetry. We now evaluate the derivative of (3.6) divided by $\sin \theta$:

$$\frac{1}{\sin \theta} \frac{\partial T}{\partial \theta} = -\frac{1}{\sin \theta} \sum_{n=1}^N n a_n \sin(n\theta) \quad (3.7)$$

$$= -\sum_{n=1}^N n a_n [\sin(n\theta) / \sin \theta] \quad (3.8)$$

It can be shown that the ratio of sines in the summation is:

Pressure (bar)	N	l^1 -norm	l^2 -norm
0.1	2	16.6724	14.4143
0.1	4	11.3805	8.1870
0.1	6	10.8843	7.0204
0.1	8	14.1867	10.2813
0.01	2	41.0348	81.8547
0.01	4	26.0158	39.5551
0.01	6	25.6478	37.7382
0.01	8	28.2277	39.3755

Table 3.3: Examples of the errors in the temperature fit to that derived from Voyager/IRIS spectra as a function of pressure and fit degree N. The l^1 -norm is the sum of the absolute difference between the observed and modeled data and the l^2 -norm is the sum of the squares of these differences.

$$\sin(n\theta)/\sin\theta = \begin{cases} 2[\cos((n-1)\theta) + \cos((n-3)\theta) + \dots + \cos(3\theta) + \cos(\theta)] & : n \text{ even} \\ 2[\cos((n-1)\theta) + \cos((n-3)\theta) + \dots + \cos(4\theta) + \cos(2\theta) + 1/2] & : n \text{ odd} \end{cases}$$

We substitute the above expression and equations (3.6) and (3.7) into equation (3.4) to obtain a numeric thermal wind equation.

One problem with this formulation is that the coefficient a_N with the highest order will contribute the most to the derivative at lower latitudes. To mitigate this effect, we must fit the temperature to as low an order as possible while maintaining a reasonable fit. Table 3 compares various errors of the fit to the observed temperature data as a function of pressure and fitting degree. We choose to use $N = 4$ which is the lowest order that provides a reasonable fit to the temperature data.

Second, we solve for the meridional temperature structure needed to reproduce the vertical wind shear between the 1 bar zonal wind profile (calculated in the first step) and that at the pressure of the H-band profile. This is done by integrating (3.4) and (3.5) and solving for $T(\theta, P)$. We choose 1 bar as the upper limit to the constructed temperature profiles for two reasons: 1) From de Pater et al. (2014), the equatorial H-band features not seen in K' must be below 1 bar; 2) If we placed our limit at the edge of the Voyager/IRIS range, unphysical discontinuities in the temperature structure would arise. Placing the limit at 1 bar allows reasonable 'smoothing' in the temperature structure between 800 mbar and 1 bar.

Away from the equator, we solve for the meridional temperature structure with the standard thermal wind equation where we integrate this equation with respect to a reference latitude θ_0 at a particular pressure P :

$$2\Omega \int_{\theta_0}^{\theta} \sin \theta' \frac{du(\theta', P)}{dr} d\theta' = -\frac{g}{r_0} \int \frac{1}{T(\theta, P)} dT, \quad (3.9)$$

and then solve for $T(\theta, P)$:

$$\log \left(\frac{T(\theta, P)}{T_0(P)} \right) = -\frac{2\Omega r_0}{g} \int_{\theta_0}^{\theta} \sin \theta' \frac{du(\theta', P)}{dr} d\theta'. \quad (3.10)$$

Here, $T_0(P)$ is the temperature at θ_0 . The extrapolated zonal wind profile at 1 bar from the K'-band profile can be fit to a fourth-order polynomial in degrees latitude, as was done with the H- and K'-band profiles. So, the total vertical wind shear can be written as³:

$$\frac{\partial u}{\partial r} = p_0 + p_1 \cdot \theta^2 + p_2 \cdot \theta^4 \quad (3.11)$$

Note that θ is converted from degrees to radians for the purposes of integration. Furthermore, this procedure assumes du/dr is constant with pressure (although still a function of latitude) so the resultant temperature structure will represent an 'average' profile. p_0, p_1 , and p_2 do not depend on latitude (though they depend on the pressure the K'-band is placed). Equation (9) becomes:

$$\log \left(\frac{T(\theta, P)}{T_0(P)} \right) = -\frac{2\Omega r_0}{g} \int_{\theta_0}^{\theta} \sin \theta' \frac{du(\theta', P)}{dr} d\theta' \quad (3.12)$$

$$= -\frac{2\Omega r_0}{g} \int_{\theta_0}^{\theta} \sin \theta' (p_0 + p_1 \theta'^2 + p_2 \theta'^4) d\theta' \quad (3.13)$$

The integral on the right-hand side of can be solved analytically via repeated integration-by-parts. The final solution, written for brevity, is:

$$\log \left(\frac{T(\theta, P)}{T_0(P)} \right) = -\frac{2\Omega r_0}{g} (p_0 \cdot t_0 + p_1 \cdot t_1 + p_2 \cdot t_2) \quad (3.14)$$

$$T(\theta, P) = T_0(P) \cdot \exp \left[-\frac{2\Omega r_0}{g} (p_0 \cdot t_0 + p_1 \cdot t_1 + p_2 \cdot t_2) \right] \quad (3.15)$$

³We use fourth-order polynomial fits in latitude to the vertical wind shear, instead of Legendre polynomials in $\sin \theta$ for two reasons. First, while the solution to Laplace's equation on a sphere are expressed in terms of Legendre polynomials in $\sin \theta$ (and are used to fit the zonal wind profile for Uranus in Sromovsky et al. (2009)), this is only especially necessary close to the poles, whereas we are doing a local expansion near the equator. Second, we feel it best to use fourth-order fits in latitude since this is the most common fit in the literature to the zonal wind profiles for Neptune. In the Appendix 3.8, we show an example demonstrating that using a Legendre expansion does not change the qualitative interpretation of the temperature profile from the equator to mid-latitudes.

where:

$$\begin{aligned} t_0 &= -\cos \theta \\ t_1 &= 2\theta \sin \theta - (\theta^2 - 2) \cos \theta \\ t_2 &= 4\theta(\theta^2 - 6) \sin \theta - (\theta^4 - 12\theta^2 + 24) \cos \theta \end{aligned}$$

At and near the equator, we use the EQTWE to solve for the thermal profile. Assuming the same model for the vertical wind shear (3.35), the EQTWE becomes a second-order differential equation in θ :

$$T'' = c \cdot p(\theta)T, \quad (3.16)$$

where $p(\theta) = p_0 + p_1\theta^2 + p_2\theta^4$ and $c = -f_0r_0/g$. Letting T to be symmetric about the equator:

$$T = \sum_{n=0}^{\infty} a_{2n}\theta^{2n}. \quad (3.17)$$

Then:

$$T'' = \sum_{n=1}^{\infty} a_{2n}(2n)(2n-1)\theta^{2n-2} \quad (3.18)$$

Change the limits on (3.18):

$$T'' = \sum_{n=0}^{\infty} a_{2n+2}(2n+2)(2n+1)\theta^{2n}. \quad (3.19)$$

Plug these expansions into (3.16):

$$\sum_{n=0}^{\infty} a_{2n+2}(2n+2)(2n+1)\theta^{2n} = c \cdot p(\theta) \sum_{n=0}^{\infty} a_{2n}\theta^{2n} \quad (3.20)$$

$$\sum_{n=0}^{\infty} (a_{2n+2}(2n+2)(2n+1) - a_{2n}c \cdot p(\theta))\theta^{2n} = 0 \quad (3.21)$$

The above implies that the relation within the parentheses equals zero for all powers of θ . The only complication is that $p(\theta)$ also include powers of θ . The recurrence relation for the constants are below:

$$a_2 = a_0 \frac{c \cdot p_0}{2} \quad (3.22)$$

$$a_4 = a_2 \frac{c \cdot p_1}{12} \quad (3.23)$$

$$a_6 = a_4 \frac{c \cdot p_2}{30} \quad (3.24)$$

$$a_{2n+2} = a_{2n} \frac{c}{(2n+2)(2n+1)} \quad (3.25)$$

a_0 is the equatorial temperature. As an example, set $a_0 = 80\text{K}$ and plug in relevant values of the constants for Neptune. Then (4) becomes:

$$T = 80 + 28.7\theta^2 - 13.4\theta^4 - 0.1\theta^6 + \dots \quad (3.26)$$

To summarize, we have calculated the thermal structure below 1 bar by solving both the standard and equatorial thermal wind equations. The later is valid at and near the equator while the former is valid away from it. Assuming an equatorial temperature of 80K, we find that the difference between the modeled temperatures resulting from these two models is 0.5K at $\pm 20^\circ$ and 0.2 K at $\pm 15^\circ$. The reason the temperature solution given in (3.15) is almost equal to the solution given by (3.26) near the equator is that (3.15) is symmetric about the equator (t_0, t_1 , and t_2 are all even functions). Thus, in the limit as θ goes to 0, the solutions appear similar near the equator due to L'Hôpital's rule.

Figure 3.19 shows a contour plot of a temperature profile in Neptune's troposphere that matches the observed H- and K'-band wind profiles through the thermal wind equation. The Voyager/IRIS temperature retrievals are plotted for pressures less than 800 mbar. The temperature solution required to match the observed equatorial vertical wind shear is shown for pressures greater than 1 bar. We choose the reference latitude θ_0 to be the equator and $T_0(P)$ to be the mean global temperature (given by the smooth relaxation to the *a priori*) at P . In this example, we assumed the K'-band profile corresponds to 10 mbar and the H-band profile represents the 1.3 bar layer. This solution predicts 10–15 K temperature differences between the equator and mid-latitudes below 1 bar. In cases where the H- and K'-band features are further apart in altitude, we predict amplitudes of around 5–10 K at $P > 1$ bar. Requiring these large temperature contrasts has an effect on the IRIS flux and will worsen the quality of the spectral fits. This can be avoided if the H-band profile is moved further outside the IRIS sensitivity window, say $P > 2$ bar. In this case, the quality of the spectral fit is unaffected, but this may result in unrealistic depths for H-band features.

The predicted temperature profile is largely a function of the expected wind shear. Figure 3.19 represents an altitude change over 4 scale heights. In cases where the H- and K'-band features are further apart, the temperature contrasts are decreased. If the zonal winds change more rapidly with increasing altitude, larger meridional temperature gradients are needed to match the predicted vertical wind shear. If vertical wind shear is not uniform throughout the atmosphere, then the amplitude of temperature variability will change. For instance, if du/dr changes more rapidly below 1 bar than above it, then there is a larger total integral of $dT/d\theta$ between the H-band and 1 bar. This would decrease the latitudinal gradient needed to produce the expected vertical wind shear and could result in temperature contrasts more compatible with expected IRIS spectral fits.

Revisiting the Thermal Wind Equation

The standard thermal wind equation is derived from the vorticity equation in part by assuming the ideal gas law for a single-component gas: $P = \rho RT$. This involves replacing the horizontal gradient of the density with the horizontal temperature gradient. Therefore in

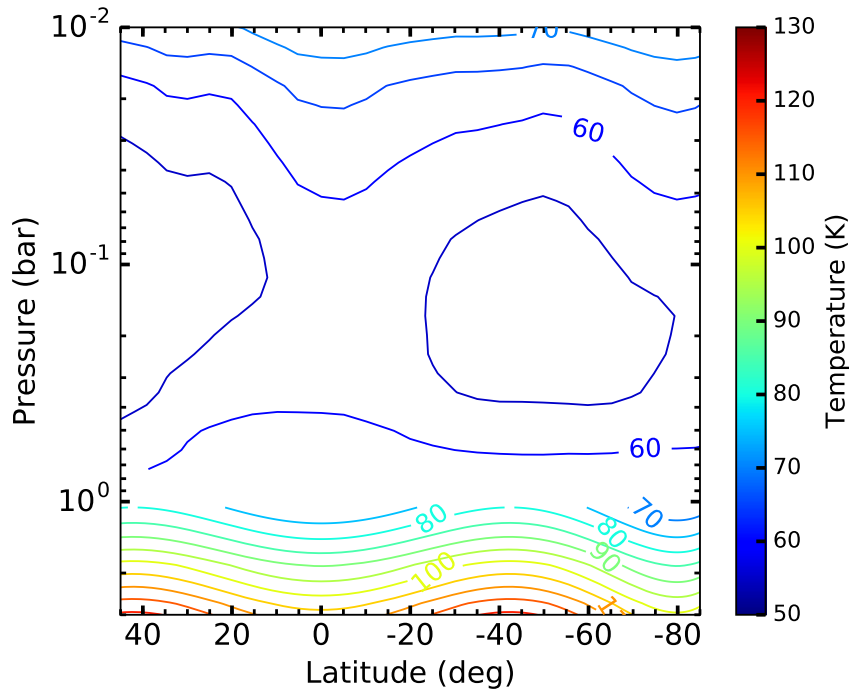


Figure 3.19: An example of the derived temperature profiles below 1 bar needed to produce the expected zonal wind differences between the H-and K'-bands. At a given pressure, the temperature at the equator was set to the mean global temperature. This is superimposed with the Voyager/IRIS temperature retrievals above 800 mbar. The region between 800 mbar to 1 bar region is left blank (without a temperature solution) to emphasize that a smooth transition between the the solution profile and the Voyager/IRIS profile is needed to avoid nonphysical boundaries. For this example, the H-band profile was set at 1.3 bar and the K'-band profile at 10 mbar. In all tested solutions, the required difference between the equatorial and mid-latitude temperatures falls between 5-15 K.

a multi-component atmosphere, the thermal wind equation is not correct because the atmosphere's density gradient is due to spatial variations in temperature and in the composition. The later no longer makes the gas constant 'constant' spatially, but turns it into a function of the densities of the components. Generally, in the Earth's atmosphere, the correction to the thermal wind equation is not large because the molar mass of water (the most significant contributor to density variations in the atmosphere) is small compared to the atmosphere's mean molar mass. However the mean molar mass of the atmosphere of Neptune (and the other giant gas planets) is small compared to the molar mass of gases such as methane that cause spatial density variations. If this effect is large enough to produce significant variations in the meridional density, the thermal wind equation (3.4) will be altered. We define the *virtual temperature* T_v as the temperature at which a dry atmosphere has the same density

and total pressure as an atmosphere with an additional component (Sun et al. (1991)):

$$T_v = \left(1 + \frac{1-\epsilon}{\epsilon} \frac{q}{1+q}\right) T \approx \left(1 + \frac{1-\epsilon}{\epsilon} q\right) T \quad (3.27)$$

Here, $q = \rho_c/\rho_d$ is the mass mixing ratio between the extra constituent and dry air and $\epsilon = m_c/m_d$ is the ratio of the molar mass of methane to the molar mass of dry air. For Neptune with methane as the main trace gas, $m_c/m_d \approx 6.96$ and the virtual temperature is:

$$T_v = (1 - 0.856q) T \quad (3.28)$$

Contrast this with Earth, where water vapor is the main condensible; $m_c/m_d \approx 0.622$ and the virtual temperature is:

$$T_v = (1 + 0.608q) T \quad (3.29)$$

The atomic mass of methane is larger than that of dry air on Neptune, while the atomic mass of water vapor is smaller than dry air on Earth. Thus, the virtual temperature will be smaller than the actual temperature on Neptune, while the virtual temperature is larger on Earth. An equator enhanced in methane (and with larger q) compared to mid-latitudes will, therefore, have a cold virtual temperature relative to the mid-latitudes. If the density gradient induced by methane abundance variations is large enough, it may explain the sign of Neptune's apparent vertical wind shear.

Sun et al. (1991) use the concept of virtual temperature to derive a more general thermal wind equation. We similarly generalize equation (3.4) by using virtual temperature:

$$f \frac{\partial u}{\partial r} = -\frac{g}{r_0 T_v} \frac{\partial T_v}{\partial \theta} [P, \phi] \quad (3.30)$$

Defining $C = (1 - \epsilon)/\epsilon$, Sun et al. (1991) shows that:

$$f \frac{\partial u}{\partial z} = -\frac{g}{r_0 T} \frac{\partial T}{\partial \theta} - \frac{g}{r_0} \frac{C}{1 + Cq} \frac{\partial q}{\partial \theta} \quad (3.31)$$

Equation (3.31) is identical to equation (7) of Sun et al. (1991), which we refer to as the thermal and compositional wind equation. Their study investigated the effect of horizontal variations in molar mass on vertical wind shear in Neptune and Uranus. They found that methane depletion at high latitudes compared to low latitudes produced vertical wind shear with opposite sign to vertical wind shear produced by thermal gradients. If the gradient in molar mass is large enough to overcome the thermal term, the zonal wind speed will become more negative with increasing altitude, consistent with our observations.

Similar to the previous section, we ask what temperature gradient is needed below 1 bar if molar mass gradients also contribute to the vertical wind shear. Karkoschka and

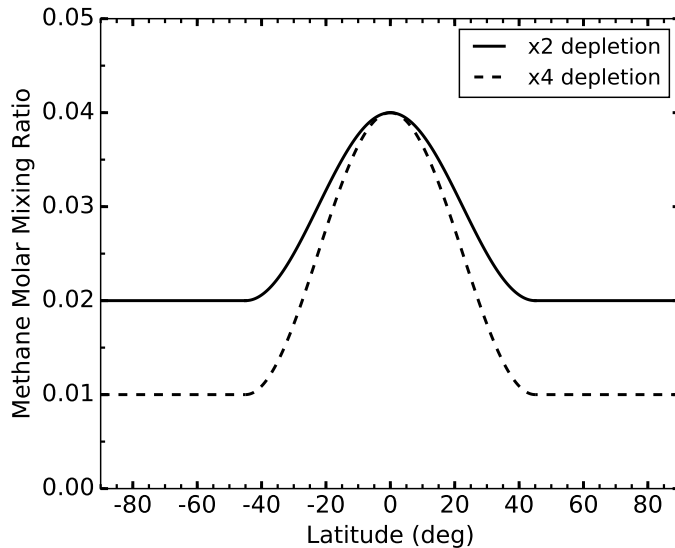


Figure 3.20: Plot of our methane model, given by equations (22) and (23).

Tomasko (2011) found evidence of methane depletion between 1.2 and 3.3 bar at the mid-latitudes in data acquired by the Hubble STIS spectrograph. They derived a methane molar mixing ratio of 0.04 (0.28 mass mixing ratio) at the equator and a $\sim 3\times$ depletion at mid-latitudes. Luszcz-Cook et al. (2013) found brightness variations in spatially-resolved millimeter maps of Neptune, suggestive of meridional opacity variations. Their models were consistent with mmassesethane from 1–4 bar depleted by $2\times$ at mid-latitudes and by $8\times$ at the poles compared to nominal values at the equator (0.044 molar mixing ratio). Luszcz-Cook et al. (2016) also find methane variations consistent with Karkoschka and Tomasko (2011). We assume methane is the major source of molar mass variations and that these variations are confined to altitudes below 1 bar but do not otherwise depend on the pressure. We also assume the variation is hemispherically symmetric in order to extend the general thermal wind equation to the equator. Our model reflects the findings of Karkoschka and Tomasko (2011) and is similar to their Figure 8: methane is enriched at the equator, smoothly decreasing to 45°S and remaining constant out to the poles. The model for the methane mass mixing ratio is expressed below:⁴

$$q(\theta) = \begin{cases} q_0 \cos(4\theta) + q_1 & : \quad |\theta| \leq 45 \\ q_1 - q_0 & : \quad |\theta| > 45 \end{cases}$$

⁴Among many functions we could choose to represent the methane gradient, we picked $\cos(4\theta)$ since its derivative is zero at 45° . This produces a smooth transition in the methane abundance from low-latitudes and high-latitudes, where methane abundance is constant as in Karkoschka and Tomasko (2011).

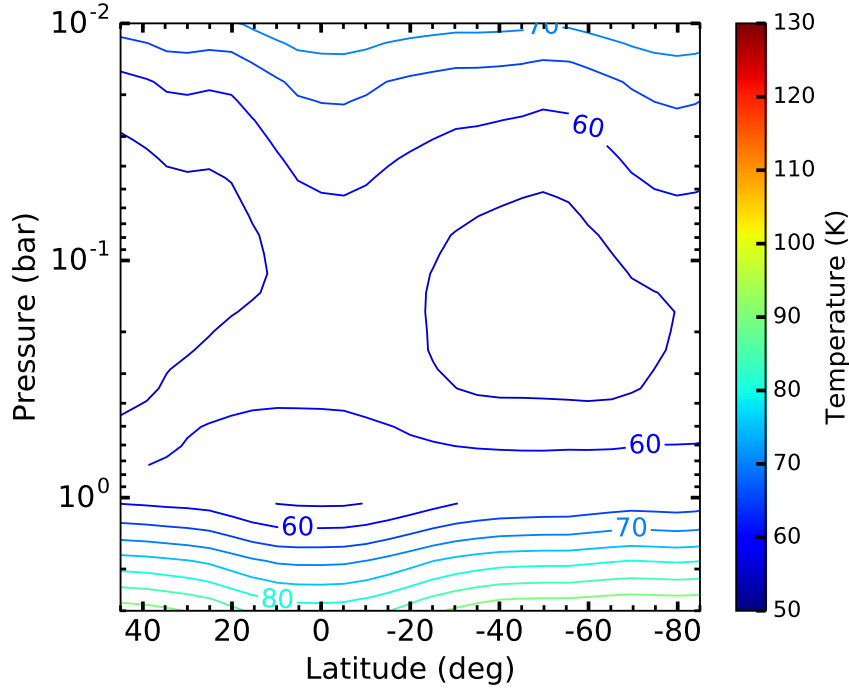


Figure 3.21: As Figure 3.17, except plotting the virtual temperature below 1 bar, assuming $\times 2$ depletion in methane at mid-latitudes and the poles. The virtual temperature is given by equation (3.28) and demonstrates the impact of methane gradients. A cold virtual temperature at the equator is produced, which is consistent with the expected sign of vertical wind shear.

Figure 3.20 plots our methane model assuming $\times 2$ and $\times 4$ depletion at the mid-latitudes to poles assuming an equator with a molar mixing ratio of 0.04. Figure 3.21 plots the virtual temperature assuming this model for the methane mixing ratio. The molecular mass variation due to methane will change the thermal contribution to the observed vertical wind shear. The new equation to solve is:

$$2\Omega \sin \theta \frac{\partial u}{\partial r} = - \left. \frac{g}{r_0 T} \frac{\partial T}{\partial \theta} \right|_P - \left. \frac{g}{r_0} \frac{C}{1 + Cq} \frac{\partial q}{\partial \theta} \right|_P, \quad (3.32)$$

where we integrate this equation to solve for $T(\theta, P)$:

$$-\frac{g}{r_0} \int \frac{1}{T(\theta, P)} dT = 2\Omega \int_{\theta_0}^{\theta} \sin \theta' \left[\frac{du(\theta', P)}{dr} + \frac{g}{r_0} \frac{C}{1 + Cq} \frac{\partial q}{\partial \theta'} \right] d\theta', \quad (3.33)$$

$$\log \left(\frac{T(\theta, P)}{T_0(P)} \right) = - \frac{2\Omega r_0}{g} \int_{\theta_0}^{\theta} \sin \theta' \left[\frac{du(\theta', P)}{dr} + \frac{g}{r_0} \frac{C}{1 + Cq} \frac{\partial q}{\partial \theta'} \right] d\theta' \quad (3.34)$$

Like before, we assume the vertical wind shear and molar mass term can be fit to fourth-degree polynomials:

$$\frac{\partial u}{\partial r} + \frac{g}{r_0} \frac{C}{1 + Cq} \frac{\partial q}{\partial \theta} = p_0 + p_1 \cdot \theta^2 + p_2 \cdot \theta^4 \quad (3.35)$$

Integrate as before to solve for the temperature profile below 1 bar. The derived temperature profile taking methane variations into account is shown in Figure 3.22. Our examples illustrate how important the meridional methane distribution is on the derived temperature solutions. In the first case, where methane is depleted by $2\times$ at mid-latitudes and poles compared to the equator, we obtain an equator 2–3K colder than the mid-latitudes. In the second case, where methane is depleted by $4\times$ at the mid-latitudes compared to the equator and poles, we obtain an equator 2–3K warmer than the mid-latitudes. This is qualitatively consistent with the warmer equatorial temperatures observed at $P < 1$ bar by Voyager/IRIS (e.g. Conrath et al. (1998)) and ground-based observations (Fletcher et al. (2014)).

An important caveat to this analysis is that it assumes methane does not condense. Ices are 1000-fold denser than gases and the ideal gas law is no longer applicable. Our model occurs in the heart of methane's condensation region so these results should be viewed with caution. Nonetheless, the above work demonstrates the necessity of including compositional gradients in models of Neptune's winds. Future models will need to consider all phases of methane and other heavy species deeper down to accurately calculate Neptune's density profile.

In summary, the meridional temperature structure needed to replicate Neptune's equatorial zonal wind shear depends heavily on the gaseous methane distribution below 1 bar. If methane abundance is globally uniform or weakly varying, then a cold equator relative to the mid-latitudes is needed to explain the vertical wind shear. If methane abundance changes greatly, then a warm equator is permitted.

Thermal infrared spectra from Cassini/CIRS observations have been used to derive temperature fields for the stratosphere and troposphere of Jupiter and Saturn and allow us to compare our derived temperatures for Neptune's troposphere. Below ~ 100 –700 mbar, both planets have a cool equator with peak meridional contrasts ~ 2 –10 K (see Fig. 2 of Simon-Miller et al. (2006) and Fig. 2 of Fletcher et al. (2010)). Zonal wind speeds of Jupiter's deep troposphere were extracted from the Doppler Wind Experiment at 6°N and show an increase in the velocity with depth below 1 bar (Atkinson et al. (1998)). This is consistent with a positive latitudinal temperature gradient (i.e. cool equator) since the wind shear is negative. Numerical simulations of off-equatorial jets in Jupiter's and Saturn's upper atmosphere reproduce similar results (Fig. 1 of Liu and Schneider (2015)). However, wind shear near 5-micron hotspots is likely to be complex, because dynamics are affected by a planetary-scale wave in addition to zonal-mean gradients (Showman and Dowling (2000)). Neptune's measured tropospheric temperatures are the opposite to that described on Jupiter and Saturn (i.e., a warm equator instead), but this work could hint at a cool 'Jupiter-like' equator at depths > 1 bar provided a flatter methane distribution. More precise constraints

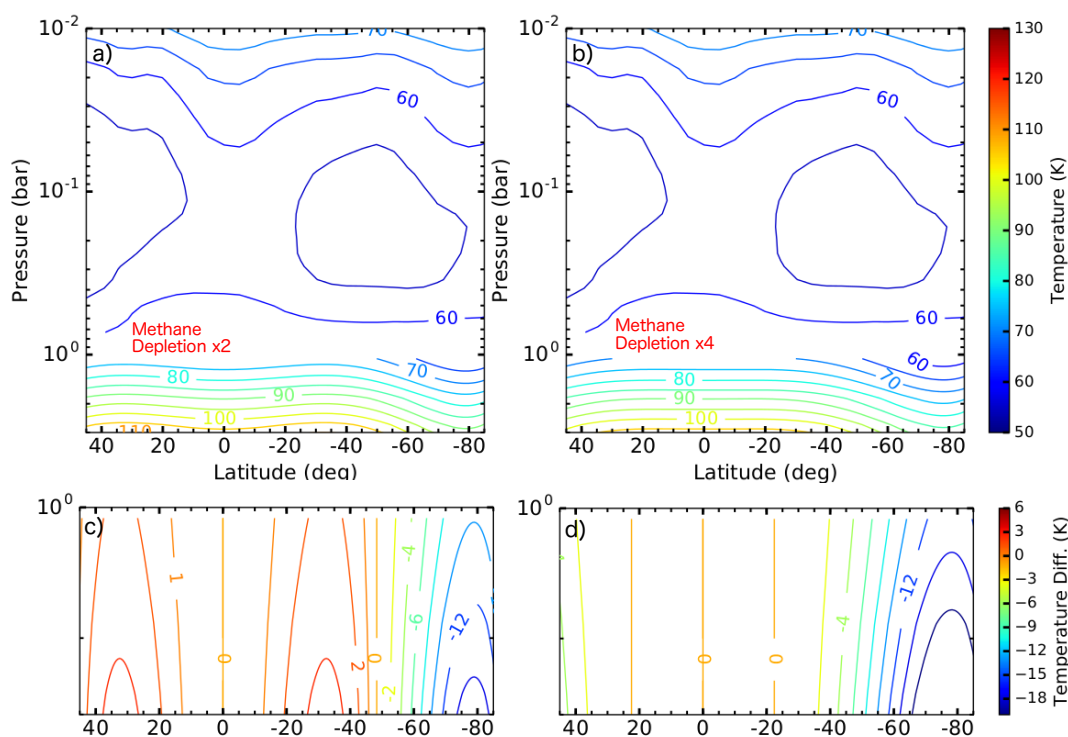


Figure 3.22: As Figure 3.19, but considering meridional methane variations in the thermal wind equation. a) Methane abundance depleted by 2 \times at mid-latitudes and poles (molar mixing ratio 0.02) compared to the equator (molar mixing ratio 0.04). b) Methane abundance depleted by 4 \times at mid-latitudes and poles (molar mixing ratio 0.01) compared to the equator and (molar mixing ratio 0.04). c) and d) show how the derived meridional temperatures deviate from the equatorial temperature along isobars, between 1–3 bar. c) corresponds to a) and d) to b). The low methane depletion (2 \times) case predicts an equator 2–3K cooler than the mid-latitudes. Higher depletion (4 \times) yields an equator 2–3K warmer than the mid-latitudes. These examples highlight how the meridional methane distribution affects the temperature gradient. In both cases, the H-band profile was set at 1.3 bar and the K'-band profile at 10 mbar.

on Neptune's methane profile and extent of zonal flow are needed to determine if Neptune's temperature field is similar to the other jovian planets. Considering the energetics of flow in future models will also be important for relating Neptune's zonal winds, temperature field, and composition.

Global Circulation

Multi-wavelength observations have been crucial for determining Neptune's global circulation pattern. De Pater et al. 2014 analyzed near-infrared cloud activity, temperature patterns, ortho/para H₂ ratios, and measurements of mid-infrared and radio temperature brightness to construct a hemispherically symmetric circulation pattern where air rises above the mid-latitudes and sinks at the equator and poles. Their single-layer circulation is broadly extended, ranging from the stratosphere down to ~ 40 bar, and could explain most, though not all, observations at wavelengths spanning a range from the visible to 6 cm. If methane abundances are uniform or weakly varying, our data are indicative of a more complicated circulation between the equator and mid-latitudes. Below 1 bar, an equator colder than the mid-latitudes is needed to produce the predicted vertical wind shear. This scenario is consistent with air rising and cooling as it adiabatically expands at the equator while air subsides and warms due to adiabatic compression at the mid-latitudes. Such a circulation pattern is consistent with data that do not agree with the single-cell circulation in de Pater et al. (2014). Butler et al. (2012) constructed 1-cm radio maps of Neptune from data obtained with the Expanded Very Large Array (EVLA) and found weak brightness enhancements at the southern mid-latitudes, as well as strong enhancements over the pole and equator. Karkoschka and Tomasko (2011) found evidence of methane depletion between 1.2 and 3.3 bar at mid-latitudes in data acquired by the Hubble STIS spectrograph. Regions of low methane abundance and opacity indicate downwelling. Conversely, high abundances and opacities suggest upwelling. Moreover, methane-rich air will cool and condense as it rises at the equator. This may explain the presence of deep-seated H-band features. An example two-celled model that is consistent with these observations is given in Figure 3.23. This modifies the model given by de Pater et al. (2014) below 1 bar to an unknown depth. A three-cell circulation pattern has been proposed for Uranus to explain polar methane depletion and cloud activity at the mid-latitudes (Sromovsky et al. (2014)). Stacked circulation cells above and below the clouds of Saturn may explain spatial distributions of chemical tracers measured by Cassini/VIMS (Fletcher et al. (2011)). Neptune's atmosphere may be similarly complex.

On the other hand, if methane abundances vary significantly, a warm equator can still reproduce our observed vertical wind shear. Such a temperature profile would be consistent with both: 1) the single-cell circulation model suggested by de Pater et al. (2014), and 2) direct measurements of the temperature field. Although the de Pater et al. (2014) model explained a broad range of observations, observed variations in methane abundance are not explained by this circulation model. It is likely that an elaborate circulation model is needed to explain all known observations of Neptune's upper atmosphere. Neptune's circulation

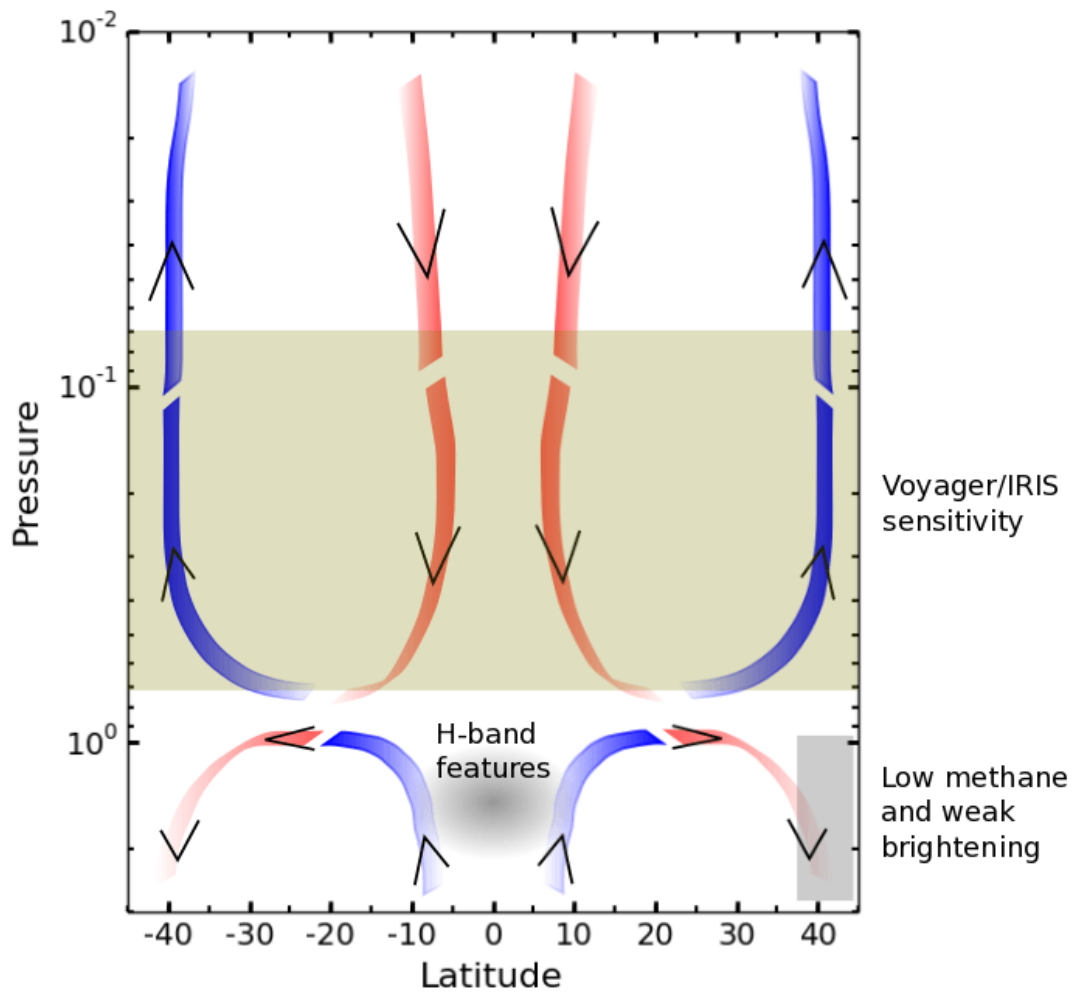


Figure 3.23: Schematic of our proposed circulation model between 10 mbar and 3 bar from the equator to mid-latitudes. The colored bands and arrows indicate the direction of circulation, blue indicating cool, rising air, and red warm, sinking air. Each cell forms a closed loop, continuing outside the range shown in the figure. The depth of circulation below 1 bar is unknown. The yellow band highlights the range of Voyager/IRIS sensitivity. The equatorial clouds seen in the H-band but not the K'-band are indicated as a gray circle. The mid-latitude region of methane depletion and weak brightening from Karkoschka and Tomasko (2011) and Butler et al. (2012) is represented by a gray rectangle.

pattern may contain finer latitudinal and vertical structure than we can determine from currently available data.

3.6 Conclusion

We tracked the longitude-latitude positions of dozens of bright features in Neptune's atmosphere from Keck AO images on July 3, 2013 and August 20, 2014 in the H- and K'-bands. From their positions and length of time tracked, we derived zonal and meridional velocities and constructed zonal wind profiles for each band and night.

Our main conclusions are:

1. The motions of many individually tracked cloud features are significantly different than the zonal wind speeds predicted by the canonical profile from Sromovsky et al. (1993). This dispersion is most prominent from the equator to mid-latitudes, reaching as high as 500-600 m/s, and is seen on both nights. A few features have meridional velocities as large as 100-200 m/s. These features also tend to have the largest zonal velocity deviations from the canonical profile, suggesting they are driven by mechanisms like vortices or wave phenomena as these produce motion in both directions. Generally, features with the largest velocity variations (in both directions) have large RMS errors and are tracked for a short time. These features are usually ephemeral, faint, or near the planetary limb, meaning their centers are hard to constrain. Velocity variations also persist in low-error, long-tracked features, although the magnitude of variability is muted.

2. There are significant differences in the zonal wind profiles between the H-band and K'-band on both nights. This is most prominent at the equator, where the H profile is best described by a profile shifted eastward by 90 ± 45 m/s on July 3, 2013 and 141 ± 63 m/s on August 20, 2014. There is little difference between the K'-band zonal wind profiles and the canonical profile. 2013 H band features have smaller Kp/H I/F ratios at the equator than the mid-latitudes. The exquisite quality of our July 3, 2013 images reveal numerous equatorial features in the H-band that are not present in K'-band. This suggests those features are located below 1 bar. Taken all together, this is consistent with the idea that the mean eastward velocity shifts in the H profile are driven by deep-seated features. Differences in velocity with depth are evidence of vertical wind shear.

3. If the shift in the H profile is real and indicative of vertical wind shear, we predict shears between -1.0 to -2.2 m/(s·km) at the equator, assuming H and K' features typically differ in altitude by 3–5 scale heights. Previous studies have dismissed vertical wind shear as an explanation for the variability between the H-band and canonical profile, claiming that thermal winds would decay (be less negative) with increasing altitude and produce the opposite of what is observed. However, this analysis relied on Voyager/IRIS temperature retrievals that are only sensitive between 70–800 mbar, outside the pressures we expect the H-band to see at the equator. Using a formulation that extends the thermal wind equation to the equator (Marcus et al. (2019)), we derived the meridional temperature profiles that are needed below 1 bar to match our predicted vertical wind shear. Neglecting density effects

due to variation in methane concentration, we find that the equator must be colder than the midlatitudes by 5–15 K to explain the observations, although this range can be lowered if wind shear is not uniform throughout the atmosphere. This is similar to tropospheric temperature profiles derived from mid-infrared observations and numerical simulations of Jupiter' and Saturn's atmosphere. Colder temperatures at the equator are consistent with upwelling and are not consistent with the de Pater et al. (2014) single-layer model's equatorial downwelling.

4. We used the generalized thermal-compositional wind equation (Sun et al. (1991)) to account for density variations that result from latitudinally fluctuating methane abundances. We used this equation to re-derive the temperature structure below 1 bar needed to match expected methane variations and vertical wind shear. If methane is weakly-depleted at the mid-latitudes ($2\times$ depletion), an equator 2–3 K colder than the mid-latitudes is consistent with our inferred wind shear. This could be explained by adiabatic cooling and methane enrichment at the equator due to upwelling, but it is inconsistent with the de Pater et al. (2014) single-layer circulation with equatorial downwelling. If methane is strongly-depleted at mid-latitudes ($4\times$ depletion), an equator 2–3K warmer than the mid-latitudes is consistent with our inferred wind shear. Equatorial warming combined with methane enrichment is not consistent with either the single-layer de Pater et al. (2014) model, or the double-layer model in Fig. 23. It is, however, consistent with observed measurements of Neptune's temperature field. We emphasize the importance of including these density variations future models, as condensation regions or phase changes result in large density changes.

5. Our results suggest a global circulation pattern more complicated than the single-celled, vertically broad model described by de Pater et al. (2014). Stacked circulation cells may explain observed methane variations and our derived temperature profiles. However, we can not reconcile all observations of Neptune's upper atmosphere with this model. Latitudinally and vertically complex circulation cells may be needed to explain the dynamics of Neptune's atmosphere.

Multi-wavelength observations of Neptune are required to fully understand the degree of vertical wind shear and true circulation pattern in the troposphere. Cloud tracking with spectral information would verify whether features with different speeds are in fact at different depths. Radio wavelengths are sensitive to H_2S variations in Neptune's atmosphere below 1 bar. Longitudinally-resolved radio maps of Jupiter have recently been produced with the upgraded VLA (de Pater et al. (2016)). Similar maps of Neptune's deep atmosphere would trace variations in the H_2S abundance and determine regions of sinking (low H_2S) and rising (high H_2S) air. This would provide a check for the stacked-celled circulation hypothesis.

3.7 Acknowledgements

The data presented were obtained at the W.M. Keck Observatory, which is operated as a scientific partnership among the California Institute of Technology, the University of California and the National Aeronautics and Space Administration. The Observatory was

made possible by the generous financial support of the W.M. Keck Foundation. This work has been supported in part by the National Science Foundation, NSF Grant AST-0908575 and AST-1615004 to UC Berkeley and by NASA Headquarters: under the NASA Earth and Space Science Fellowship program Grant NNX16AP12H to UC Berkeley, and Grant NNX23AG56G under NASA Planetary Atmospheres to UC Berkeley. The authors wish to recognize and acknowledge the very significant cultural role and reverence that the summit of Mauna Kea has always had within the indigenous Hawaiian community. We are most fortunate to conduct observations from this mountain.

3.8 Appendix

In this appendix, we show an alternate model for the vertical wind shear: $\partial u / \partial r$ used in Section 5.1.1 equation (3.35). We assume that the vertical shear can be expanded in even 4th-order Legendre polynomials:

$$\frac{\partial u}{\partial r} = p_0 + p_1 \frac{1}{2}(3\mu^2 - 1) + p_2 \frac{1}{8}(35\mu^4 - 30\mu^2 + 3), \quad (3.36)$$

where $\mu = \sin \theta$. Legendre polynomials may be preferred to the 4th-order polynomials used in Section 5.1.1 since the former are solutions to Laplace's equation on the sphere and are valid expansions at the poles. Now solve for the temperature profile:

$$\log \left(\frac{T(\theta, P)}{T_0(P)} \right) = - \frac{2\Omega r_0}{g} \int_{\theta_0}^{\theta} \sin \theta' \frac{du(\theta', P)}{dr} d\theta' \quad (3.37)$$

$$= - \frac{2\Omega r_0}{g} \int_{\theta_0}^{\theta} \sin \theta' \left(p_0 + p_1 \frac{1}{2}(3\mu^2 - 1) + p_2 \frac{1}{8}(35\mu^4 - 30\mu^2 + 3) \right) d\theta' \quad (3.38)$$

The integral on the right-hand side of can be solved analytically via repeated integration-by-parts. The final solution, written for brevity, is:

$$\log \left(\frac{T(\theta, P)}{T_0(P)} \right) = - \frac{2\Omega r_0}{g} (p_0 \cdot t_0 + p_1 \cdot t_1 + p_2 \cdot t_2) \quad (3.39)$$

$$T(\theta, P) = T_0(P) \cdot \exp \left[- \frac{2\Omega r_0}{g} (p_0 \cdot t_0 + p_1 \cdot t_1 + p_2 \cdot t_2) \right] \quad (3.40)$$

where:

$$t_0 = - \cos \theta$$

$$t_1 = \frac{1}{8} (\cos(3\theta) - 5 \cos \theta)$$

$$t_2 = \frac{1}{384} (-21 \cos(5\theta) + 55 \cos(3\theta) - 114 \cos \theta)$$

As before, this result be easily extended to the equator. In the following table, we compare the latitudes of the local maximal/minimal temperatures using this model and the model given in Section 5.1.1; we assume, for sake of example, an equatorial temperature of 80K.

Sect. 5.1.1 model	Appendix model
0 deg - 80.0K	0 deg - 80K
38.3 deg - 85.9K	33.5 deg - 84.4K
78.2 deg - 72.2K	70.5 deg - 76.0K

The qualitative analysis is the same between these models - the equator is colder than the mid-latitudes. The peak mid-latitude temperatures differ by 1.5K. While the model in Section 5.1.1 has a more extreme temperature change and is probably less accurate at high-latitudes, we do not consider this region in our analysis of Neptune's tropospheric temperature profiles since the zonal wind profile is wildly uncertain there - very few features are tracked in this region. Thus, the model presented in Section 5.1.1 is good enough as a base analysis - future work may explore better methods to model vertical wind shear on Neptune. We point out that analogous calculations can be used in the model presented in Section 5.1.2.

Chapter 4

Neptune’s Latitudinal Variations Viewed with ALMA

We present spatially resolved millimeter maps of Neptune between 95 and 242 GHz taken with the Atacama Large Millimeter/submillimeter Array (ALMA) in 2016 – 2017. The millimeter weighting functions peak between 1 and 10 bar on Neptune, lying in between the altitudes probed at visible/infrared and centimeter wavelengths. Thus, these observations provide important constraints on the atmospheric structure and dynamics of Neptune.

We identify seven well-resolved latitudinal bands of discrete brightness temperature variations, on the order of 0.5 – 3K in all three observed ALMA spectral bands. We model Neptune’s brightness temperature using the radiative transfer code Radio-BEAR and compare how various H₂S, CH₄, and *ortho/para* H₂ abundance profiles can fit the observed temperature variations across the disk. We find that observed variations in brightness temperature with latitude can be explained by variations in the H₂S profile that range from sub- to super-saturations at altitudes above the 10-bar pressure level, while variations in CH₄ improve the quality of fit near the equator. At the south polar cap, our best fit model has a depleted deep atmospheric abundance of H₂S from 30 to only 1.5 times the protosolar value, while simultaneously depleting the CH₄ abundance. This pattern of enhancement and depletion of condensable species is consistent with a global circulation structure where enriched air rises at the mid-latitudes (32° – 12°S) and north of the equator (2° – 20°N), and dry air descends at the poles (90° – 66°S) and just south of the equator (12°S–2°N). Our analysis finds more complex structure near the equator than accounted for in previous circulation models.

4.1 Introduction

Millimeter continuum observations of Neptune provide a valuable bridge between visible/infrared studies of the cloud tops and above ($P < 1$ bar) and deeply probing centimeter maps ($10 < P < 40$ bar). Visible and near-infrared (NIR) imaging from *Voyager*, the Hubble

Space Telescope (HST), and Keck have shown bright methane cloud activity at Neptune’s mid-latitudes and comparatively dark regions and/or hazes at the equator and poles (Limaye and Sromovsky, 1991; Sromovsky et al., 2001b; Martin et al., 2012; Fitzpatrick et al., 2014; Tollefson et al., 2018). Mid-infrared (MIR) images and spectra have been used to obtain zonal-mean temperature profiles which show that the equator and south pole are warmer than the southern mid-latitudes in the upper troposphere and stratosphere (Conrath et al., 1991; Orton et al., 2007; Fletcher et al., 2014). Centimeter maps obtained with the Very Large Array (VLA) probe well below Neptune’s cloud deck and indicate the presence of dry (low-opacity) air at the south pole (e.g., Butler et al., 2012; de Pater et al., 2014). Taken together, observations of the deep troposphere and upper atmosphere are broadly consistent with a global circulation pattern where air enriched with trace gases rises at the mid-latitudes, adiabatically cools and condenses to form clouds, dries out, and descends at the poles and equator (Conrath et al., 1991; de Pater et al., 2014). Millimeter observations probe altitudes in between those seen in the above maps, $1 < P < 10$ bar, making such observations vital for bridging the pressures viewed in the visible/infrared and centimeter, and for improving our overall understanding of Neptune’s atmospheric structure and dynamics. In particular, millimeter continuum observations are sensitive to variations in composition, including variations in trace condensable species such as H_2S and CH_4 . Like the centimeter, millimeter observed variations in these trace gases reflect atmospheric motions; depleted, low-opacity regions (enriched, high-opacity) are consistent with downwelling (upwelling) air.

The opacity of Neptune’s continuum at millimeter observations is dominated by collision-induced absorption of H_2 (CIA) with hydrogen, helium, and methane. Trace gases, such as H_2S , PH_3 , and NH_3 also contribute to the overall opacity. Since millimeter observations of these gases probe Neptune’s troposphere between 1 and 10 bar, individual lines are highly pressure-broadened, appearing as broad ‘continuum’ bands in the millimeter spectrum. As a result, it is difficult to differentiate between these opacity sources since clear line features cannot be detected.

On previous millimeter maps, Neptune’s disk was spatially resolved and regions of enhanced or diminished brightness temperatures could be distinguished. Using the Combined Array for Research in Millimeter-wave Astronomy (CARMA), Luszcz-Cook et al. (2013) imaged Neptune in the far wings of the CO (2 – 1) line (230.538 GHz). In their longitudinally-averaged maps, they found brightness temperatures increased by 2 – 3 K from 40°N to the south pole. Since their observations were taken far (~ 5 GHz) from the CO (2 – 1) line center, this emission is primarily from sources forming the ‘quasi-continuum’. Assuming an adiabat in the troposphere, the authors showed that variations in the brightness temperature at the south pole could be explained by a 30% decrease in opacity at $P > 1$ bar. If variations in opacity would occur at altitudes only below 4 bar, the opacity needed to be decreased by a factor of 50. Hence, brightness variations at a particular wavelength are coupled to the pressure at which the opacity changes, itself dependent on the opacity source. Luszcz-Cook et al. (2013) could explain the latitudinal variations in brightness temperature as latitudinal gradients in any or all of: H_2S , CH_4 , and/or *ortho/para* H_2 . However, due to their limited wavelength coverage, they were unable to disentangle the true contribution to the brightness

Table 4.1: Summary of observations.

ALMA Band	Configuration	UT Date	Flux Calibrator	Bandpass Calibrator	T_{Source}^a
Band 3	C40-8	2017-07-27	J0006-0623	J2246-1206	726
Band 4	C40-7	2016-10-07	J2258-2758	J2246-1206	1701
Band 6	C40-7	2016-10-24	J2258-2758	J2246-1206	1032

^a Total science time on Neptune, in seconds

from each candidate source.

In this paper, we present millimeter maps of Neptune taken with the Atacama Large Millimeter/Submillimeter Array (ALMA). ALMA provides the wavelength coverage, sensitivity, and resolution needed to constrain Neptune’s opacity sources accurately across the disk. In Section 2, we present ALMA observations taken in three bands over the millimeter wavelength range (1–3 mm). The observed brightness temperature distribution is compared to model maps produced with the radiative-transfer code Radio-BEAR, described in Section 3. We generate a model for the latitudinally-varying H₂S and CH₄ abundance profiles that agree with the observations in each band in Section 4. In Section 5, we compare these results to other profiles of Neptune’s trace gases and summarize how our findings impact our understanding of the dynamics and evolution of Neptune’s upper atmosphere.

4.2 Observations

Data

We observed Neptune with ALMA, which is an interferometer located in the Atacama desert in northern Chile. A total of 66 high-precision antennas form the array: fifty-four 12m and twelve 7m. The arrangement of these antennas defines the angular resolution and maximum resolvable angular scale of the data. The tightest packed configuration, where the antennas are up to 150 m apart, allow large, faint objects to be observed. Extended arrangements, where the antennas are 16 km apart, provide a more detailed look. Our Neptune observations were taken between 2016 – 2017 in Bands 3, 4, and 6, between 95 – 250 GHz (1–3 mm). For each band, we selected the antenna configuration which allowed us to resolve Neptune and simultaneously see Neptune’s entire (2.3” diameter) disk. A typical resolution was 0.3” using ~ 40 12-m antennas. We observed in four spectral windows in continuum mode covering Neptune’s continuum spectra within each band. Table 4.1 summarizes the observations while Table 4.2 outlines the correlator and spectral setup.

Calibration and Imaging

The obtained visibility data were reduced and calibrated in the Common Astronomical Software Application (CASA) version 5.1. We applied the standard ALMA pipeline to

Table 4.2: Summary of correlator setup, spectral windows, and synthesized beams.

ALMA Band	Center Frequency (GHz)	Center Wavelength (mm)	Channel Width (MHz)	Total Bandwidth ^a (MHz)	Beam Size (arcsec ²)	Position Angle ^b (degrees)
Band 3	95.012	3.155			$0.45'' \times 0.33''$	281.5°
	96.970	3.092	15.625	2000	$0.44'' \times 0.33''$	282.1°
	107.000	2.802			$0.40'' \times 0.30''$	282.9°
	109.000	2.750			$0.39'' \times 0.29''$	282.9°
Band 4	135.986	2.205			$0.38'' \times 0.28''$	23.0°
	137.924	2.174	15.625	2000	$0.38'' \times 0.28''$	24.8°
	147.986	2.026			$0.35'' \times 0.26''$	22.7°
	149.986	1.999			$0.35'' \times 0.26''$	24.3°
Band 6	223.982	1.338			$0.31'' \times 0.25''$	64.3°
	225.982	1.327	15.625	2000	$0.32'' \times 0.24''$	61.8°
	239.981	1.249			$0.30'' \times 0.23''$	64.0°
	241.981	1.239			$0.29'' \times 0.23''$	63.6°

^a Each spectral window has the same total bandwidth, consisting of 128 channels with the same channel width.

^b Defined as north through east.

perform flagging (bad edge channels, shadowed antennas, and poor quality data), bandpass and flux calibration, and gain-time solutions. Table 4.1 lists our calibrator sources. Finally, we applied three iterations of self calibration on our Neptune data to remove short-term phase variability caused by fast atmospheric fluctuations (Brogan et al., 2014). The first iteration used the entire observation range while the second and third used 350-second and 60-second intervals.

The multi-frequency synthesis mode in CASA *tclean* was used to transform the visibility data into image maps. We used natural weighting and restricted clean to a circular mask that is roughly the size of Neptune’s diameter plus twice the beam size. The natural weighting scheme gives equal weight to all baseline samples while the uniform weighting scheme gives equal weight to each spatial frequency. Since there are ‘naturally’ more short baselines than long baselines, natural weighting preserves the peak sensitivity while uniform weighting reduces the peak sensitivity as the short baselines have been weighted less. In our testing, we found that uniform and intermediate weightings produced artificial speckles on the disk and large scale structures in the sky. Natural weighting limits these artifacts since the sensitivity is highest, but sacrifices some angular resolution since the long-baselines are under-weighted relative to the uniform scheme. Despite this, we still resolve roughly one-seventh of Neptune’s disk. We also subtracted a limb-darkened model from the data to speed up the deconvolution process and reduce imaging artifacts. The number of clean iterations varied from 1000-2000, stopping once the noise within the planetary disk reached the noise in the sky.

Our resulting maps are 512×512 pixels² with a cell size of $0.02''$. This cell size follows a common rule-of-thumb, which is to make the cell size roughly $1/10$ the size of the synthesized beam. The planetary disk appears elliptically elongated due to convolution with the synthesized beam. This beam resembles a Gaussian with full-width at half maxima and position angles given in Table 4.2.

Error estimation

The error in our maps is calculated by averaging over four regions of the sky with boxes equal to the diameter of Neptune and taking the root-mean-square (RMS). RMS values range from $0.1 - 0.6\text{K}$. Table 4.3 lists our estimated errors in each band. This RMS does not include systematic effects, such as errors in the bandpass or flux calibration. The ALMA Calibrator Source Catalogue lists errors in the calibrator’s flux estimate being about 5% or less in each band so we use this as an estimate for the absolute error in our disk-averaged temperature data (Section 5.1).

4.3 Models

2D model maps of Neptune’s disk were created using our radiative transfer (RT) code Radio-BEAR described in de Pater et al. (2019)¹. Given an atmospheric composition and

¹This code is available at: <https://github.com/david-deboer/radiobear>.

Table 4.3: Summary of observed and modeled millimeter disk-averaged brightness temperatures.

Center	Frequency (GHz)	Observed Flux Density ^a (Jy)	Observed T_b^a (K)	Nominal T_b^b (K)	Noise ^c (K)	Factor ^d
95.012		3.4 ± 0.2	126.6 ± 6.3	119.9	0.1	0.945
96.970		3.5 ± 0.2	126.0 ± 6.3	119.4	0.1	0.950
107.000		4.1 ± 0.2	120.5 ± 6.0	116.7	0.2	0.975
109.000		4.1 ± 0.2	118.8 ± 6.0	116.1	0.3	0.975
135.986		5.9 ± 0.3	108.5 ± 5.4	109.0	0.3	1.010
137.924		6.1 ± 0.3	108.0 ± 5.4	108.5	0.2	1.010
147.986		6.7 ± 0.3	104.3 ± 5.2	105.7	0.2	1.020
149.986		6.8 ± 0.3	104.5 ± 5.2	105.1	0.3	1.025
223.982		13.3 ± 0.7	93.4 ± 4.7	94.8	0.4	1.020
225.982		13.5 ± 0.7	93.0 ± 4.7	94.7	0.4	1.025
239.981		15.1 ± 0.8	93.1 ± 4.7	93.4	0.6	1.010
241.981		15.3 ± 0.8	92.8 ± 4.6	93.2	0.6	1.010

^a The listed errors are the absolute errors, estimated at 5% from the calibrators.

^b The nominal model assumes a dry adiabat with trace gases enhanced by $30\times$ the protosolar value.

^c Random errors defined as the RMS on the sky.

^d This factor is used to scale the observed brightness temperature to match the nominal model to within the estimated noise.

thermal structure (described below), we calculate the RT-derived brightness temperatures of the planet on each location on the planet.

Radio-BEAR assumes that the atmosphere is in local thermodynamic equilibrium, where the temperature is calculated from deep in the atmosphere upwards assuming a dry or wet adiabat such that the temperature at 1 bar matches 71.5 K, that derived by *Voyager* radio occultation measurements (Lindal, 1992). At altitudes above 1 bar, we use the temperature profile from Fletcher et al. (2010). The temperature, pressure, and altitudes are related to each other through hydrostatic equilibrium. In all of our latitude-varying models (Sections 4.2 and 4.3), we assume that the temperature-pressure profile follows a dry adiabat in the troposphere. Cases of a wet adiabat are presented in the context of the disk-averaged brightness temperature in section 4.1. Our models also allow the abundance profiles of H₂S, CH₄ and ortho/para H₂ to vary, as discussed below.

Neptune’s trace gases H₂S, CH₄, H₂O, and NH₃ in the deep atmosphere are assumed to be enhanced by 30× their protosolar values² in our nominal model, apart from ammonia gas as 30× protosolar values for NH₃ are inconsistent with previous microwave disk-averaged temperatures (de Pater and Massie, 1985; de Pater et al., 2014). At higher altitudes, these gases follow the saturated vapor pressure curve with 100% relative humidity. Clouds expected to form under thermochemical equilibrium on Neptune include: an aqueous ammonia solution (H₂O-NH₃-H₂S) topped with water ice, ammonium-hydrosulfide (NH₄SH), and H₂S- and CH₄-ice (Weidenschilling and Lewis, 1973). To form the NH₄SH cloud, H₂S and NH₃ are reduced in equal molar quantities until the product of their partial pressures reaches the equilibrium constant of the reaction forming NH₄SH. Once equilibrium is reached, only H₂S will remain to form clouds since there is practically no NH₃ gas remaining above the NH₄SH cloud. A tentative detection of H₂S spectral features near 1.58 μm in Neptune’s troposphere implies that the deep bulk S/N ratio is greater than one (Irwin et al., 2019). The cloud density might affect microwave measurements (de Pater et al., 1991; de Pater and Mitchell, 1993). However, little is known about the cloud density on Neptune and the millimeter weighting functions peak at altitudes above the aqueous and ammonium-hydrosulfide clouds (see Fig. 4.1). Clouds have also been shown to not affect the microwave opacity on Jupiter (de Pater et al., 2019). Therefore, we ignore the effect of cloud opacity and focus on the gas opacity in our models.

The gas opacity of Neptune’s millimeter spectrum is dominated by H₂S and the collision-induced absorption (CIA) of H₂ (we include: H₂-H₂, H₂-He, H₂-CH₄). NH₃ and H₂O affect the spectra at wavelengths longer than 10 cm; NH₃ would have a larger impact at millimeter wavelengths if its abundance within Neptune were larger (see Fig. 4 of Luszcz-Cook and de Pater (2013)). The effect of PH₃ in the millimeter is most prominent at the (1 – 0) absorption line at 266.9 GHz. The width of this line is ~ 20 GHz due to pressure broadening, meaning the wings of this absorption feature will have a small effect on the highest frequency data. However, this effect is well within the estimated noise of the maps so we do not add

²We use the protosolar values from Asplund et al. (2009): C/H₂ = 5.90E-4; N/H₂ = 1.48E-4; O/H₂ = 1.07E-3; S/H₂ = 2.89E-5.

this gas in our models.

The *ortho/para* H₂ fraction also influences Neptune’s millimeter brightness temperature, by modifying both the adiabatic lapse rate and the gas opacity (Trafton, 1967; Wallace, 1980; de Pater and Massie, 1985; de Pater and Mitchell, 1993). The ratio of ortho to para hydrogen in equilibrium depends on temperature; however, fast vertical mixing could bring the ratio of ortho and para states of hydrogen away from equilibrium and towards a “normal” ratio of 3 parts ortho to 1 part para. In this paper, we assume “intermediate” H₂ proposed by Trafton (1967) and used by e.g., Luszcz-Cook et al. (2013): the ortho and para states of hydrogen (which define the CIA opacities) are set to the equilibrium value at the local temperature, while the specific heat is set to that of ‘normal’ hydrogen. For further explanation of intermediate hydrogen, see e.g., Massie and Hunten (1982). Luszcz-Cook et al. (2013) find that assuming a normal hydrogen fraction rather than equilibrium fraction significantly increases the opacity and lowers the brightness temperature by 5 – 6K in their 1.2-mm model maps.

We generate 2D model maps of Neptune as follows: at the center frequencies of each spectral window, we calculate the RT-derived brightness temperatures of the planet on 9455 points on the disk and interpolate between these points to obtain the same resolution as our CASA imaged maps (0.02”). We then convolve each RT-map with an elliptical gaussian model of the synthesized beam. Our nominal model can be summarized as follows: 1) Neptune’s trace gases are enhanced to 30× their protosolar value, except NH₃ which is 1× protosolar; 2) ‘intermediate’ *ortho/para* H₂ (i.e., equilibrium *ortho/para* H₂; specific heat close to that of normal H₂); 3) the temperature-pressure profile follows a dry adiabat in the troposphere. Figure 4.2 plots the temperature-pressure and abundance profiles for the nominal model. In the following section, we compare these beam-convolved model maps to the observed disk-averaged brightness temperatures and latitudinal brightness variations.

4.4 Results

In the following subsections, we investigate the distribution of Neptune’s observed brightness temperature. First, we look at the disk-averaged brightness temperature and compute a variety of RT models using dry and wet adiabats and different enhancements of the deep abundance of trace gases. From these results, we present our nominal model (the same as that described at the end of Section 3), which fits both our ALMA and 2003 VLA disk-averaged temperatures simultaneously. Second, we subtract our nominal model from the data to produce residual maps. These maps show seven distinct latitudinal bands across Neptune’s disk. In the final subsections, we find abundance profiles of H₂S, CH₄, and *ortho/para* H₂ which fit the observed brightness variations in each latitudinal band. As an example of how we do this, we first look at Neptune’s south polar cap, where previous VLA studies constrained the deep abundance of H₂S. This provides a good litmus test for our model and fitting routine. We then move on to the rest of Neptune’s disk and show that we can fit the observed brightness temperature distribution at all latitude bands by varying the

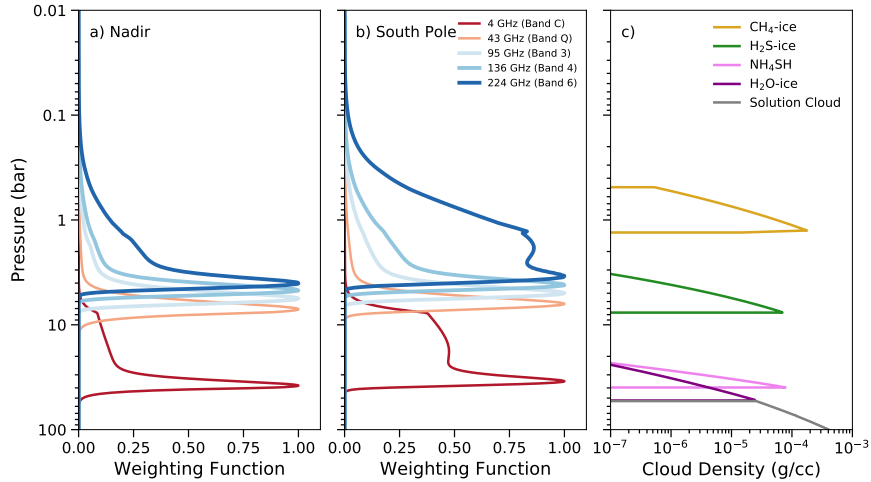


Figure 4.1: Normalized weighting functions at: a) nadir and b) the south pole, compared to the expected clouds expected to form on Neptune (c). The weighting functions at nadir and the south pole are both computed using the nominal abundance profile depicted in Figure 4.2. Weighting functions are shown for representative frequencies in each ALMA band: 95 GHz (3.155 mm, Band 3), 136 GHz (2.205 mm, Band 4), and 224 GHz (1.338 mm, Band 6), as well as selected VLA frequencies: 4 and 43 GHz (6.2 cm and 0.7 cm, respectively). Note that the VLA frequencies probe significantly deeper into Neptune’s atmosphere than the ALMA frequencies. The rightmost plot shows the density of different clouds expected to form on Neptune under thermochemical equilibrium.

abundances of the aforementioned species.

Disk-Averaged Brightness Temperatures

We calculate Neptune’s disk-averaged brightness temperature from the ALMA data in two ways. First, we sum the flux density contained within the planetary disk convolved with the model beam. Second, we fit the u-v short-spacing amplitude with a Bessel function and obtain an estimate of the zero-spacing flux density. Both results agree to well within the absolute calibration errors. We report the average of these two methods in Table 4.3. Since Neptune blocks the cosmic microwave background (CMB), its true brightness temperature is higher than observed in the radio. In all of our millimeter observations, we correct for the CMB by following the procedure laid out in Appendix A of de Pater et al. (2014).

Figure 4.3 plots our observed radio disk-averaged brightness temperatures on top of RT model spectra. In this plot, we show the effect of varying the deep abundance enhancement of trace gases (H₂S, CH₄, H₂O, and NH₃) relative to their protosolar values and consider both wet and dry lapse rates. We find that the nominal model: 30× enhancement with a dry

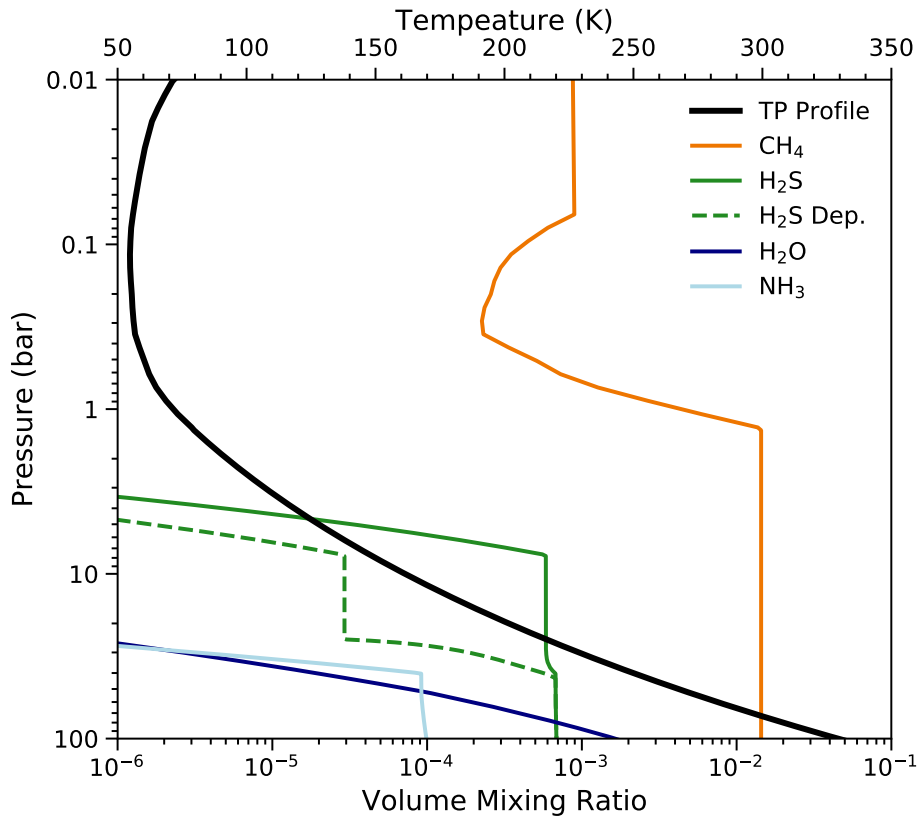


Figure 4.2: Temperature and abundance profiles of trace gases whose deep atmospheric abundances are enhanced by $30\times$ their protosolar value, apart from NH_3 which is $1\times$ (solid lines). In the troposphere, the temperature follows a dry adiabat. These profiles define the nominal model. The dashed line is the H_2S depleted profile that best fits Neptune’s south pole from 2003 VLA data (de Pater et al., 2014).

lapse rate, agrees very well with both the ALMA millimeter and the 2003 VLA centimeter data from de Pater et al. (2014). Models with temperatures following wet lapse rates are too cold relative to these data. We acknowledge, though, the following shortcomings in our models. First, these models are highly degenerate. Gas abundances are seldom at 100% humidity and so a profile with a wet adiabat where the gases are sub-saturated may result in high enough brightness temperatures to match the data. Second, our models do not account for the cooling (heating) of the atmosphere from adiabatic expansion (compression) at latitudes where the air is rising (sinking). Finally, apart from the dry and wet adiabat, we do not consider latitudinal variations in temperature. Conrath et al. (1998) and Orton et al. (2007) see 2 – 3 K latitudinal temperature variations between 50 – 100 mbar. These temperature variations are similar in strength to those we see in our residual maps (Fig. 4.4), particularly in Band 6. Luszcz-Cook et al. (2013) created temperature profiles matching the

2 – 3 K variations described in Conrath et al. (1998) and Orton et al. (2007) at altitudes above 1 bar. These temperature-varying models reduced the overall χ^2 in their fit to 1.2 mm continuum data. However, we expect similar profiles to have only a modest effect in Band 6, where the contribution functions peak at the highest altitudes (but still below 1 bar, see Fig. 4.1), and little effect in Bands 3 and 4, which probe pressures much higher than where temperature variations are seen in the infrared. Below 1 bar, the temperature profile should strictly follow an adiabat, regardless of latitude. In summary, while we do not consider temperature variations in our analysis, we do not expect them to be the primary cause of the observed brightness temperature distribution.

Latitudinal Brightness Temperature Variations

In Figure 4.4, we show residual maps of Neptune in the first spectral window of each ALMA band. Since the absolute calibration is imperfect, each map is scaled by a factor such that the observed disk-averaged temperature matches the nominal model (see Table 3). As a result, our main assumption in this analysis is that Neptune’s disk-average matches the nominal model. Deviations from this model result in the latitudinal structure evident in the residuals. This structure is due to changes in the brightness temperature that we assume to be due to variations in the opacity. The dark areas at the southern mid-latitudes and in the northern equatorial region are interpreted as probing higher, colder altitudes due to enhancements in absorbers. Conversely, the south pole appears bright in the radio due to opacity depletions, allowing the deeper, warmer layers to be probed.

Planetary coordinates are computed for each pixel on the disk using ephemeris data from JPL Horizons, with the center pixel equaling the sub-observer latitude and longitude. Latitudes are reported in planetographic coordinates. We identify seven bands on Neptune that correspond to discrete changes in the temperature structure: 90°S–66°S, 66°S–55°S, 55°S–32°S, 32°S–12°S, 12°S–2°N, 2°N–20°N, northward of 20°N. Each latitude bin is well-resolved, covering at least the total area of the ALMA beam, and is in planetographic coordinates. In Figure 4.5, we plot the average temperature difference between the data and nominal model per spectral window and band. Differences that are twice the RMS noise reported in Table 3 are significant.

Neptune’s South Polar Cap

The ALMA residual maps show clear warming on Neptune at latitudes southward of -66°. This region is Neptune’s south polar cap and has been detected as a hot spot in the radio (Butler et al., 2012; Luszcz-Cook et al., 2013; de Pater et al., 2014) and in the mid-infrared (Hammel et al., 2007; Orton et al., 2007). de Pater et al. (2014) found a best fit to their VLA data to the hot spot by defining a ‘plateau’ of constant low opacity from 66°S to the south pole, depleting H₂S to 1.5× the protosolar value (or 5% their nominal 50× model) above 43 bar (i.e., above the NH₄SH cloud). The deep CH₄ abundance is also depleted to 1.5× the protosolar value in their model (equivalently, a 0.072% volume mixing ratio), but itself

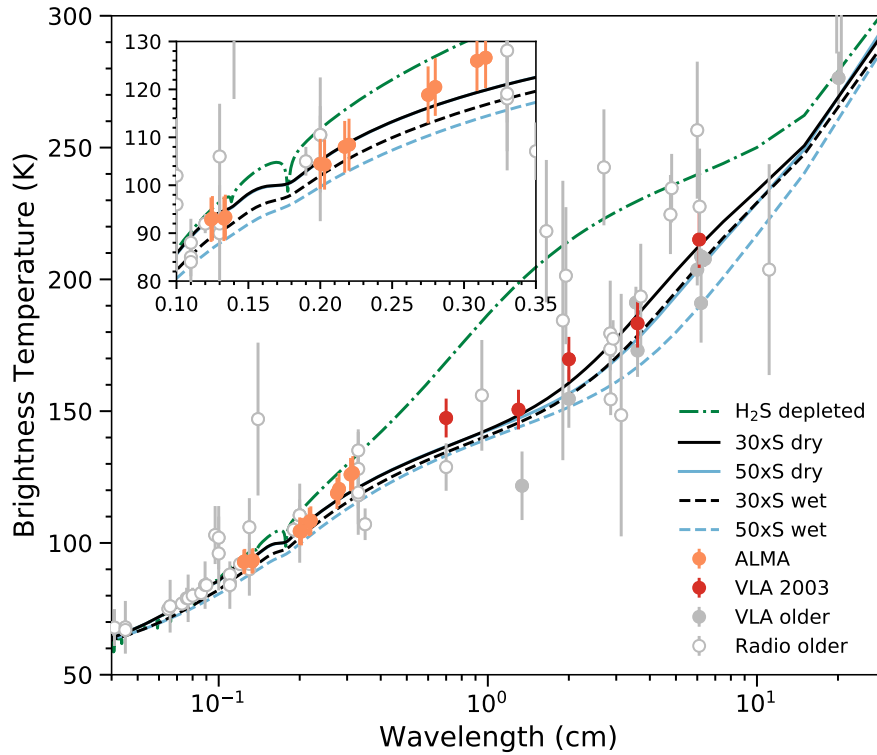


Figure 4.3: Disk-averaged brightness temperatures of Neptune. The ALMA data are plotted as orange points, with 5% absolute errors estimated from the calibrators. In addition, VLA 2003 data are plotted in red (de Pater et al., 2014), along with older VLA data in gray (de Pater et al., 1991) and older single dish radio data in open circles (de Pater and Richmond, 1989). Overplotted are model spectra which vary the deep abundance of H_2S , CH_4 , and H_2O ($30\times$ and $50\times$ their protosolar values in black and light blue respectively), and compare dry and wet lapse rates (solid and dashed lines, respectively). A model for Neptune’s south polar hot spot which depletes H_2S above 43 bar is also shown in the dot-dash green line (de Pater et al., 2014).

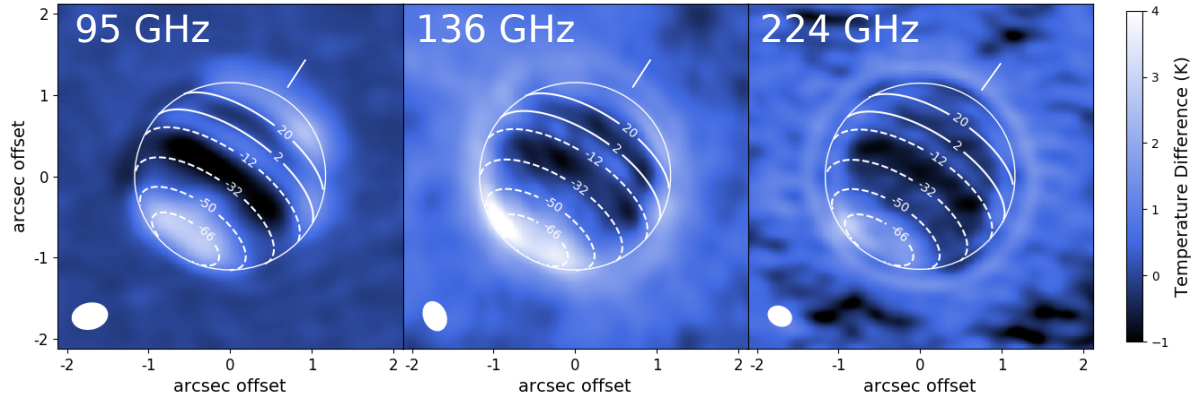


Figure 4.4: ALMA residual maps where the beam-convolved nominal model has been subtracted from the data. Contour lines delineate the latitude transitions between bands. Dark bands represent cold brightness temperatures relative to the model, while bright bands are warmer than the model. The FWHM of the beam is indicated in white in the bottom left of each map.

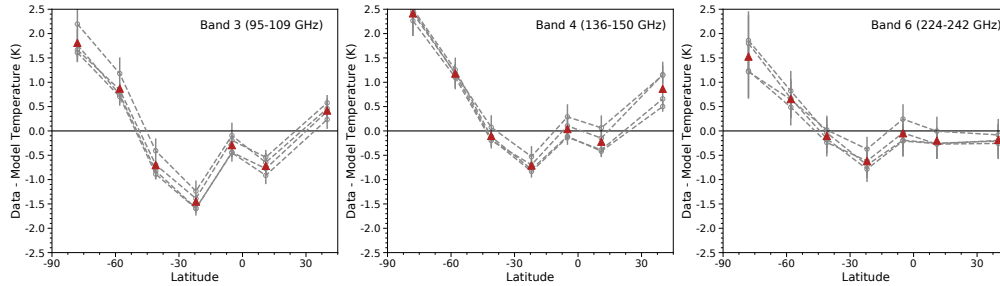


Figure 4.5: Residual temperatures comparing the data to the beam-convolved nominal model versus latitude (Band 3 left, Band 4 middle, Band 6 right). Points are plotted at the central latitude in the seven identified bins. The four gray dashed lines are the residual temperatures for each of the four spectral windows in a band. Red triangles are the average residual over each spectral window. The residuals in each latitude bin are calculated by averaging over each pixel within 60° of the sub-observer longitude. Error bars are the image noise divided by the square-root of the number of ALMA beams that fit into the corresponding bin.

is not a source of opacity at cm-wavelengths and so this study did not attempt to constrain the south pole CH_4 content (although methane does affect the adiabat and opacity due to CIA). Luszcz-Cook et al. (2013) found that the high southern latitudes in their CARMA 1.3-mm map were consistent with the VLA model. In Figure 4.2, we show this depleted profile and in Figure 4.6 we compare the bin-averaged residual brightness temperatures for the ALMA observations and the de Pater VLA depleted model. We find good agreement in Band 6, which covers the frequency of the CARMA map, however the model is too bright at lower frequencies. Luszcz-Cook et al. (2013) found that the high southern latitudes in their CARMA data could be matched if CH_4 were depleted to 0.55%, while keeping H_2S at the nominal value. A comparison of our data with this CH_4 depleted model is also shown in Figure 4.6. Once again, the Band 6 data agree with the 1.3-mm map of Neptune presented in Luszcz-Cook et al. (2013) to within their estimated uncertainties. However, the model is too cold to match the new low frequency data.

A better fit at low frequencies is obtained by setting the deep atmospheric CH_4 abundance to 0.55% and by depleting H_2S to $1.5\times$ protosolar from 43 bar up to the saturated vapor pressure curve. The H_2S abundance follows the saturated vapor pressure curve below 4.5 bar; for $P < 4.5$ bar, H_2S is subsaturated down to 5% of the saturated vapor curve. This adjusted profile is plotted in Figure 4.7 and the temperature residuals are shown in Figure 4.6. We emphasize that some subsaturation is needed in order to fit the data well. Since the millimeter is most sensitive to the pressures where H_2S saturation occurs, all models in which H_2S profiles follow the saturated vapor pressure curve appear indistinguishable in terms of their contributions to the overall opacity and all under-predict the brightness temperatures in this region. Therefore, even models significantly depleting the deep abundance of H_2S will have temperatures that are too cold at the south pole and will resemble the residuals in Figure 4.5.

With this new depleted model for Neptune’s south polar hot spot, we can fit the VLA, CARMA, and ALMA data simultaneously. This is because the VLA cm-data probe pressures deeper than our alterations at the H_2S saturation curve and we have not changed the deep H_2S abundance estimated from de Pater et al. (2014) nor the deep CH_4 abundance determined by Luszcz-Cook et al. (2013). The CARMA maps have larger uncertainties (2 – 4 K) than our maps presented here, and so depleting both H_2S and CH_4 is consistent with those data.

Constraining Neptune’s Variations with Latitude

From Figures 4.4 and 4.5, it is clear that the magnitude of temperature variations across Neptune’s disk varies with wavelength. In the millimeter, these variations are caused by altering the abundance of trace gases: H_2S and CH_4 , or changing the fraction of *ortho/para* H_2 . Figure 4.8 compares the millimeter-spectrum of the nominal model to that of models depleted in trace gases. These plots show that the spectral shape varies with both wavelength and composition. Models where the H_2S profile follows the saturated vapor pressure curve differ little from the nominal model, no matter the abundance alterations in the deep

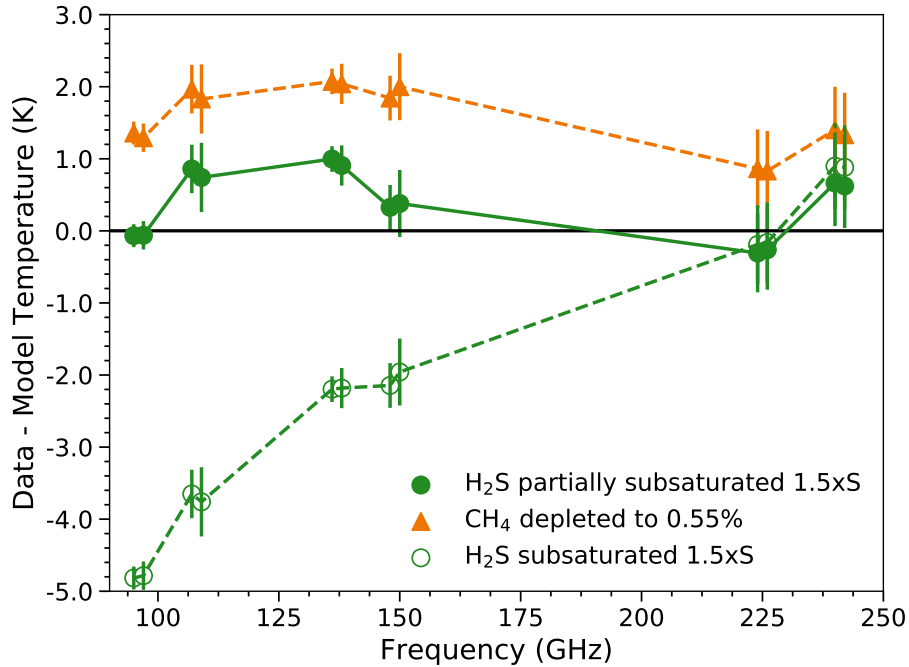


Figure 4.6: Residuals of the south polar data minus each of three different models, as described in Section 4.3. The dashed green line represents the residuals for the data compared with the model assuming H₂S subsaturation to 5% of its nominal value, as suggested by the VLA cm data in de Pater et al. (2014). The orange dashed line and orange triangles are residuals to the south pole region in a model which only depletes CH₄ to 0.55%, holding the other trace gases to their nominal values. The solid green line represents the residuals for the data compared with a model in which H₂S is partially subsaturated. This model depletes H₂S to 1.5×S above 43 bar before following the saturation vapor pressure curve up to 4.5 bar and becoming subsaturated at higher altitudes (see Figure 4.7 for a plot of this profile). Simultaneously, CH₄ is depleted to 0.55% in the deep atmosphere. This is our preferred model and is consistent with the observations of de Pater et al. (2014) and Luszcz-Cook et al. (2013).

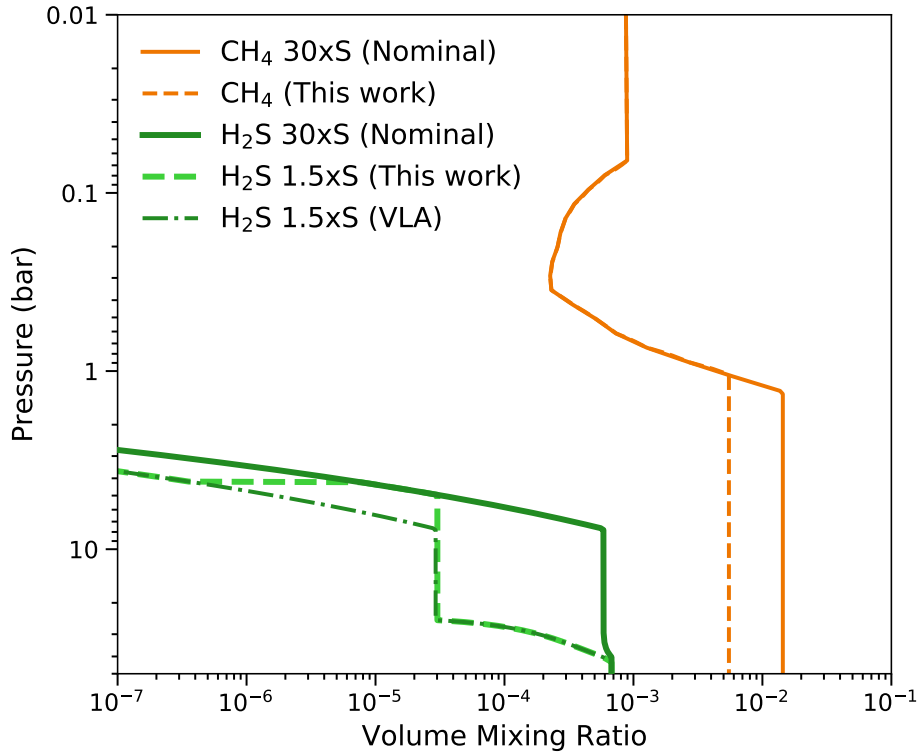


Figure 4.7: H_2S (green) and CH_4 (orange) abundance profiles. Models depleting one or both of these gases are used to explain radio brightness enhancements at Neptune’s South Pole. The $30\times\text{S}$ nominal profiles are shown as solid lines. The H_2S model fitting VLA measurements depletes H_2S down to 5% ($1.5\times\text{S}$) of the nominal profile at $P < 43$ bar; this profile is plotted as a dot-dash green line (de Pater et al., 2014). Our models for the H_2S and CH_4 profile, which simultaneously fits the ALMA, CARMA, and VLA measurements, are plotted as dashed lines. Note that in our H_2S profile, H_2S partially follows the saturation pressure curve, and follows the subsaturated profile of de Pater et al., 2014 higher than 4.5 bar.

troposphere. This is because the ALMA bands probe altitudes above 10 bar, where H₂S saturation begins, meaning changes in the constant deep abundance profile are undetected. On the other hand, models which subsaturate H₂S significantly increase the brightness temperature at short frequencies. The Band 6 (high frequencies) contribution functions peak between 1 – 5 bar while Band 3 (low frequencies) probes between 5 – 10 bar, altitudes close to where H₂S begins saturation. Thus, subsaturating H₂S results in a larger loss of opacity at low frequencies than the frequencies which probe higher altitudes, meaning low frequencies are able to probe deeper, warmer layers. In contrast, depleting CH₄ results in uniform increases across the millimeter. Substituting normal hydrogen for equilibrium hydrogen decreases the brightness temperature by 4K in Band 6 and less than 2K in Band 3. These differences with wavelength enable us to disentangle the effect of each constituent on the observed brightness temperatures in each spectral band.

In the following subsections, we present models where we vary a single constituent: H₂S, CH₄, or *ortho/para* H₂, while holding the others at their nominal value. We find the profiles which best match the data in each latitude bin for a single band. Then, we compare how well this matches the data in the other spectral bands. This gives a sense of how important the varied constituent is in producing model temperatures for each observation. Following this procedure, we present our best model fits to all three spectral bands where every parameter is allowed to vary. Table 4.4 describes how the constituent profiles change over all latitude and models.

The significance of our results within a particular latitude bin is computed with the reduced χ^2 :

$$\chi^2 = \frac{1}{M - N} \sum_{m=0}^{M-1} \frac{\delta T_m^2}{\sigma_m^2}, \quad (4.1)$$

where δT_m is the difference between the data and model brightness temperature at each spectral window m , σ_m is the image noise (see Table 3) divided by the square root of the number of beams that fit within the particular latitude bin. $M - N$ is the number of degrees of freedom in the model. We calculate the probability p that this value of the reduced χ^2 , or a larger one, could arise by chance given $M - N$. We take the number of degrees of freedom to be eight: twelve spectral windows (M) minus four free parameters (N): the deep abundances of H₂S and CH₄, the *ortho/para* H₂ fraction, and the scaling factor assumption. For eight degrees of freedom, $p < 0.05$ when the reduced $\chi^2 > 15.5$. Therefore, models with reduced $\chi^2 > 15.5$ are unlikely to occur due to random chance and are inconsistent with the observations. Table 4.5 summarizes the various fits to the data across each latitude range.

Varying H₂S

We first consider variations in H₂S that best match the Band 3 latitude variations. For each latitude band other than the south pole, we produce a grid of models in which the H₂S mixing ratio above 43 bar (the NH₄SH cloud) is set from 5 – 30× solar in 5×S steps. The profile then follows the saturation curve up to 4.5 bar, and is either depleted above 4.5 bar

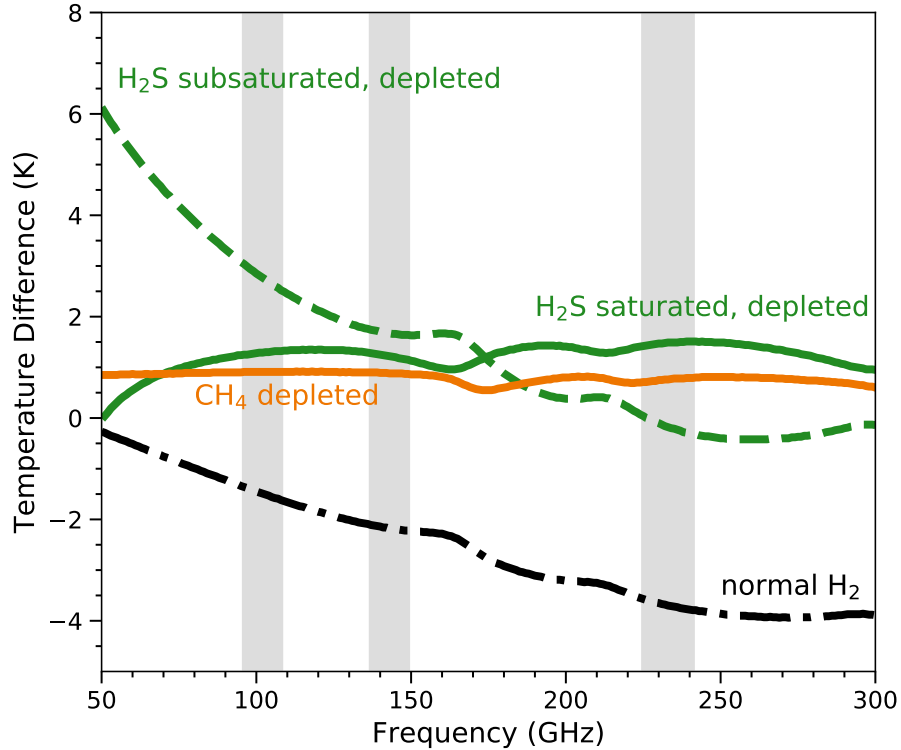


Figure 4.8: A comparison of models of Neptune’s spectrum to gauge how different opacity sources affect the brightness temperature across millimeter wavelengths. Plotted is the disk-averaged brightness temperatures for various models with the nominal model subtracted. The orange model depletes CH_4 to $15\times$ the protosolar value (0.72%) below saturation and the follows saturated vapor pressure curve above (as in the dashed-orange line in Fig. 4.7). The solid green model depletes H_2S to $15\times$ the protosolar value ($3.52\text{E-}4$ mixing ratio) in the deep atmosphere, but follows the saturation curve. The dashed green model depletes H_2S similarly, but subsaturates H_2S by the same fraction (similar to the dashed green profile in Figure 4.2). The black dot-dash model substitutes opacity by normal hydrogen for equilibrium hydrogen. Gray rectangles indicate the ALMA bands (Bands 3, 4, and 6 left-to-right).

or supersaturated to a higher altitude. We choose 4.5 bar as this transition pressure as this matches the data at the south pole best. For supersaturated models, the H_2S abundance is set to the constant deep atmospheric value until 5 – 7 bar, testing a grid of models in 0.25 bar steps. At altitudes above 3 bar (the high-altitude limit of H_2S cloud formation), the H_2S profile follows the saturation curve. At pressures in between 3 bar and 5 – 7 bar, the abundance is assumed to be linear in log-log space. For the south pole, we do not produce new model fits but continue to use the model from Section 4.3, which is depleted to a much higher depth to be consistent with VLA observations. The deep CH_4 abundance is held to its nominal value of 1.44% ($30\times$ S) and equilibrium H_2 is assumed. Figure 4.9 plots example H_2S profiles used in these fits.

From the residuals plotted in Figure 4.10, there is general good agreement between the data and model in each band, apart from 12°S – 2°N where the model in Bands 4 and 6 is too warm compared to the data. This suggests the need to enhance CH_4 or add normal H_2 in this area.

Varying CH_4

In order to determine if variations in CH_4 may effect the brightness temperature, we find CH_4 profiles which fit Band 6 to within the error bars of the average residual of the four spectral windows. The H_2S abundance is held at the nominal $30\times$ S profile and equilibrium H_2 is assumed. CH_4 is either enhanced or depleted from the nominal volume mixing ratio (1.44% or $30\times$ S), below the saturation curve. We create a grid of models in mixing ratio step-sizes of 0.36% (or $7.5\times$ S), testing deep abundances between 0.55 – 4.4%, the limits considered in Luszcz-Cook et al., 2013.

The residuals in each band are plotted in Figure 4.11. Bands 3 and 4 do not fit a CH_4 -varying only model well, implying H_2S must vary as well.

Varying *ortho/para* H_2

In these fits, we consider the fraction of equilibrium H_2 to normal H_2 needed to match the Band 6 brightness temperatures. Since normal H_2 decreases the brightness temperature, adding normal H_2 to latitudes with positive temperature residuals (like the south pole) is implausible. Figure 4.12 plots the temperature residuals in each band. We find that a hydrogen mixture of 90% equilibrium hydrogen and 10% normal hydrogen can explain the Band 6 data between 32°S – 12°S , with equilibrium H_2 used everywhere else. However, the other ALMA spectral bands fail to fit the data from 32°S – 12°S . This result is expected based on the spectral analysis in figure 4.8, showing the minimal effect normal hydrogen has in Band 3. For the best fit model, we therefore do not consider normal hydrogen. We emphasize however that our results do not preclude a small fraction of normal H_2 , on the order of $\leq 10\%$, existing at the pressures probed by ALMA. This is consistent with findings from *Voyager* IRIS measurements (Conrath et al., 1998; Fletcher et al., 2014. These studies

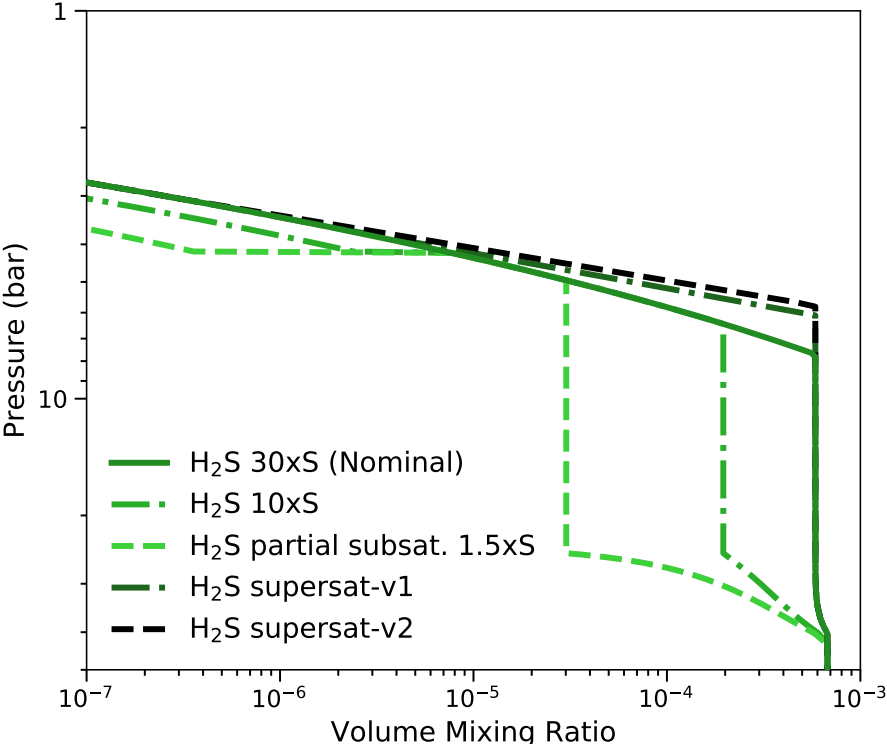


Figure 4.9: Examples of H₂S abundance profiles used to best fit the ALMA data. The light green dashed line and solid green line are the same profiles as depicted in Fig. 4.7. The dark green and black dashed and dot-dashed lines are supersaturated profiles (abbreviated supersat-v1 and supersat-v2).

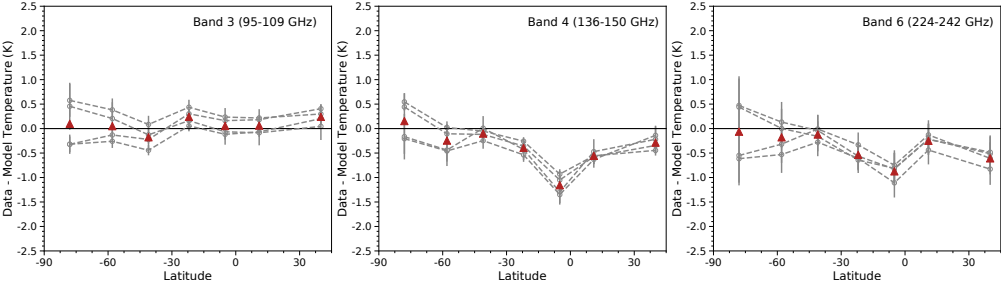


Figure 4.10: Residual temperatures comparing the data to the beam-convolved nominal model versus latitude, as in Fig. 4.5, allowing H₂S (only) to vary with latitude to best-match the Band 3 data.

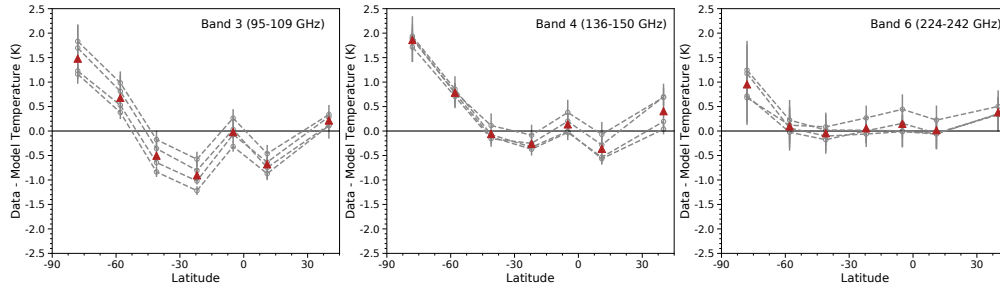


Figure 4.11: As Fig. 4.10, but allowing only CH_4 to vary with latitude. We find CH_4 profiles that match the Band 6 data and compare these with the Band 3 and Band 4 data.

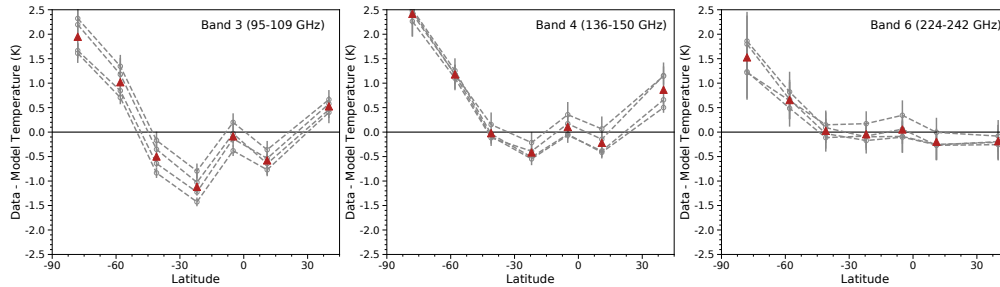


Figure 4.12: As Fig. 4.10, but allowing only the fraction of equilibrium H_2 to vary with latitude. We find H_2 profiles that match the Band 6 data and compare these with the Band 3 and Band 4 data.

find that the para H_2 fraction deviates from its expected equilibrium values on the order of 2 – 5% between 0.01 – 1 bar.

Best Fit Model

The first row in Table 4.4 describes the H_2S and CH_4 profiles that provide a best fit to the data in all ALMA bands in each latitudinal bin. Figure 4.13 plots colormaps of the best fit profiles versus latitude. Figure 4.14 plots the temperature residuals in each band, showing that an excellent fit is obtained at all latitudes. In general, we find that bright regions in the residual maps require depleting H_2S and sometimes CH_4 (down to $\sim 0.6 - 1.1\%$), while dark regions require supersaturating H_2S and enhancing the deep CH_4 abundance ($\sim 2.2 - 2.9\%$) to fit the data in every band.

Comparison to Karkoschka and Tomasko, 2011

Karkoschka and Tomasko (2011) determined methane mixing ratios from the HST/STIS spectrograph data between 300 – 1000 nm across Neptune's disk. Their results are consistent with a constant deep methane mixing ratio of $4 \pm 1\%$ at $P > 3.3$ bar. However, between

1.2 – 3.3 bar, they argued that the methane mixing ratio was depressed by a factor of ~ 3 at Neptune’s mid-latitudes compared to the equator. Not only is their deep methane mixing ratio significantly higher than our best fit models (ranging between 0.6 – 2.9%), but their observed trend in the methane abundance across Neptune’s disk differs from ours. We find high methane mixing ratios relative to the nominal model between 32°S–12°S and 2°N–20°N, and low abundances from 90°S–66°S and 12°S–2°N. The ALMA Band 6 contribution functions peak at $P < 4$ bar, so we expect some signature of the opacity from 1.2 – 3.3 bar to appear in our results.

In order to test the models presented in Karkoschka and Tomasko (2011) to our data, we compare how the H₂S abundance must change to fit the data in every band. Between 32°S–20°N, we use the Karkoschka and Tomasko (2011) methane profile at 6°S; elsewhere, we use their 45°S model (see their Figs. 10 and 14)³. The one exception is at the south pole cap, 90°S–66°S, where we use our best fitting profile since the deep H₂S abundance is fairly well constrained in VLA data.

Since the Band 6 data have the most overlap with the analysis in Karkoschka and Tomasko (2011) in terms of altitude, we find the H₂S profiles at each latitude that fit Band 6 well, assuming their adopted CH₄ profiles and equilibrium H₂. Our results are plotted in Figure 4.15 and a full description of the model and corresponding statistics is listed in Tables 4.4 and 4.5. We can find H₂S profiles which result in generally good agreement between the model and data only from 90°S–50°S and northward of 20°N. In this case, the disk-averaged H₂S abundance is $\sim 10\times S$. Luszcz-Cook and de Pater (2013) computed the disk-averaged brightness temperature assuming a $10\times S$ model, showing that the brightness temperature is too high in this case compared to most of the radio data (see also Fig. 4.3). Therefore, our data are not consistent with the Karkoschka and Tomasko (2011) methane profiles. We address this in the following section.

4.5 Discussion

Neptune’s South Polar Cap

Our ALMA millimeter observations provide a glimpse of Neptune’s atmosphere situated between the deep troposphere in centimeter maps ($P \geq 10$ bar) and the upper troposphere and stratosphere in the visible and infrared. The constraints on the trace gases are useful to infer the dynamics of Neptune’s atmosphere. Of particular interest is Neptune’s south pole, whose high temperatures were first published by Hammel et al. (2007) with images taken with the Gemini north telescope at 7.7 μ m and 11.7 μ m. They suggested these bright regions are due to enhancements in ethane and methane. Orton et al. (2007) imaged atmospheric line-

³The methane profiles in Karkoschka and Tomasko (2011) are constructed by increasing the methane mixing ratio at a constant rate below 1.2 bar: ~ 0.15 bar/% at 6°S and ~ 0.6 bar/% at 45°S. There is a transition region using intermediate rates from 20°S–45°S. A 4% deep mixing ratio is assumed. For $P < 1.2$ bar, methane follows the saturation vapor pressure curve.

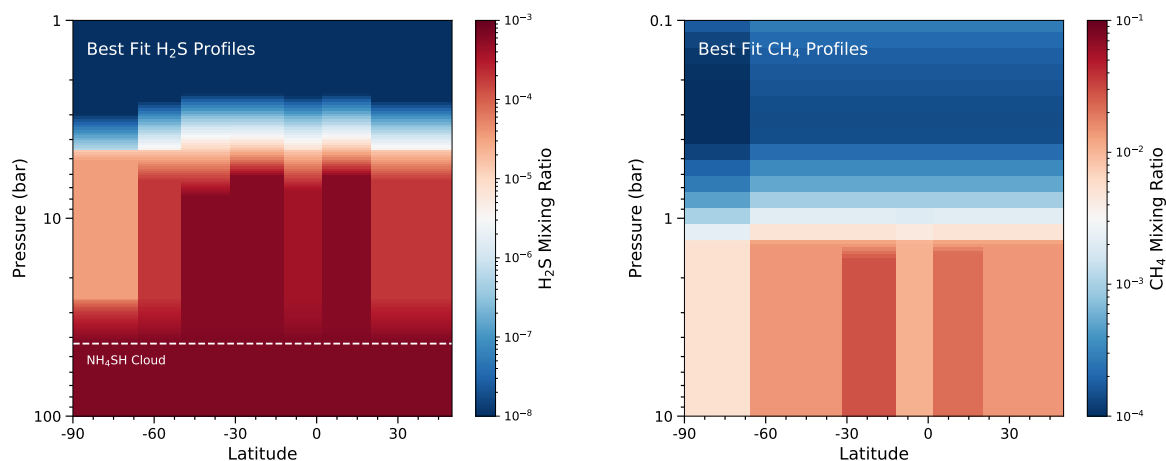


Figure 4.13: Left: Best fit H_2S vertical profiles versus latitude. Right: Best fit CH_4 vertical profiles versus latitude. These profiles are the same as those listed in the first row of Table 4.4. The colors represent volume mixing ratios, with high abundances in red and low abundances in blue. Note the different pressure and mixing ratio scales between the two figures.

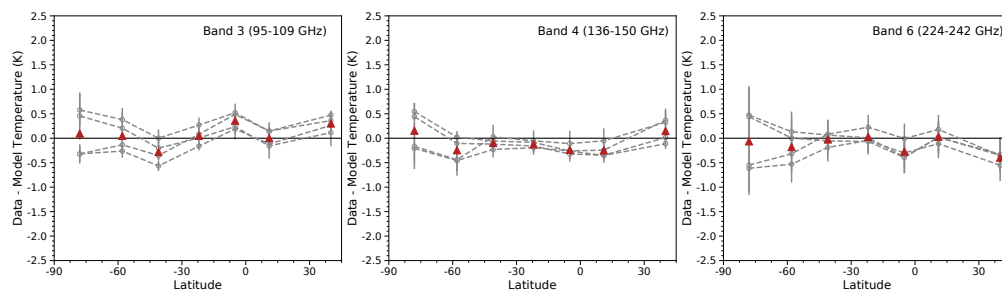


Figure 4.14: As Figure 4.10, but using the best fit H_2S and CH_4 profiles.

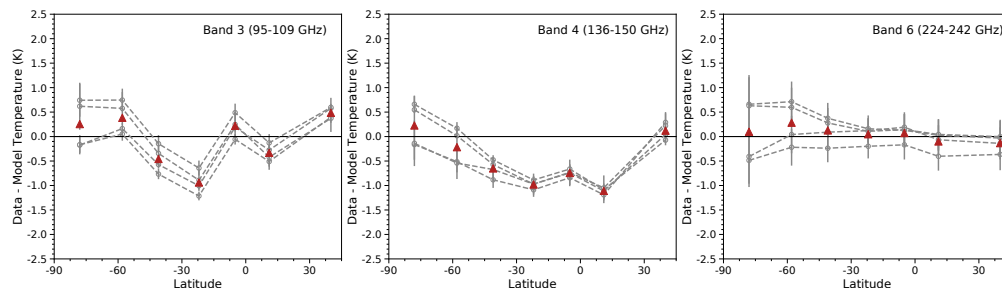


Figure 4.15: As Figure 4.5, but using the CH_4 profiles from Karkoschka and Tomasko, 2011 and finding the H_2S profiles that best match Band 6.

Table 4.4: Model names and their constituent profiles in each latitude bin that give a best fit to the data.

Model Name	90°S–66°S	66°S–55°S	55°S–32°S	32°S–12°S	12°S–2°N	2°N–20°N	20°N–50°N
Best Fit	H ₂ S 1.5×S	H ₂ S 10×S	H ₂ S 30×S	H ₂ S supersat-v1	H ₂ S 20×S	H ₂ S supersat-v1	H ₂ S 10×S
	CH ₄ 0.55%	CH ₄ 1.44%	CH ₄ 1.44%	CH ₄ 2.88%	CH ₄ 1.08%	CH ₄ 2.16%	CH ₄ 1.44%
	H ₂ equil.	H ₂ equil.	H ₂ equil.	H ₂ equil.	H ₂ equil.	H ₂ equil.	H ₂ equil.
Vary H ₂ S Only	H ₂ S 1.5×S	H ₂ S 10×S	H ₂ S 30×S	H ₂ S supersat-v2	H ₂ S 3×S	H ₂ S supersat-v2	H ₂ S 3×S
	CH ₄ 0.55%	CH ₄ 1.44%	CH ₄ 1.44%	CH ₄ 1.44%	CH ₄ 1.44%	CH ₄ 1.44%	CH ₄ 1.44%
	H ₂ equil.	H ₂ equil.	H ₂ equil.	H ₂ equil.	H ₂ equil.	H ₂ equil.	H ₂ equil.
Vary CH ₄ Only	H ₂ S 30×S	H ₂ S 30×S	H ₂ S 30×S	H ₂ S 30×S	H ₂ S 30×S	H ₂ S 30×S	H ₂ S 30×S
	CH ₄ 0.55%	CH ₄ 0.55%	CH ₄ 1.44%	CH ₄ 2.88%	CH ₄ 1.44%	CH ₄ 1.44%	CH ₄ 0.55%
	H ₂ equil.	H ₂ equil.	H ₂ equil.	H ₂ equil.	H ₂ equil.	H ₂ equil.	H ₂ equil.
Vary H ₂ Only	H ₂ S 30×S	H ₂ S 30×S	H ₂ S 30×S	H ₂ S 30×S	H ₂ S 30×S	H ₂ S 30×S	H ₂ S 30×S
	CH ₄ 0.55%	CH ₄ 1.44%	CH ₄ 1.44%	CH ₄ 1.44%	CH ₄ 1.44%	CH ₄ 1.44%	CH ₄ 1.44%
	H ₂ equil.	H ₂ equil.	H ₂ 90% equil.	H ₂ equil.	H ₂ equil.	H ₂ equil.	H ₂ equil.
KT2011 ^a CH ₄	H ₂ S 1.5×S	H ₂ S 5×S	H ₂ S 15×S	H ₂ S 15×S	H ₂ S 10×S	H ₂ S 10×S	H ₂ S 5×S
	CH ₄ 0.55%	CH ₄ 45S	CH ₄ 45S	CH ₄ 6S	CH ₄ 6S	CH ₄ 6S	CH ₄ 45S
	H ₂ equil.	H ₂ equil.	H ₂ equil.	H ₂ equil.	H ₂ equil.	H ₂ equil.	H ₂ equil.

^a KT2011 refers to Karkoschka and Tomasko, 2011. CH₄ 45S and 6S refer to their adopted methane profiles at those latitudes in their Figs.

Model Name	90°S-66°S	66°S-55°S	55°S-32°S	32°S-12°S	12°S-2°N	2°N-20°N	20°N-50°N
Best Fit	3.4	2.9	6.8	2.0	8.1	4.1	6.2
Vary H ₂ S Only	3.4	2.6	3.2	14.8	46.4	13.0	7.5
Vary CH ₄ Only	55.8	20.7	16.5	56.7	2.3	25.5	7.3
Vary H ₂ Only	95.8	48.0	16.1	85.6	2.8	17.2	29.0
KT2011 CH ₄ Only	3.9	4.3	28.9	100.4	20.9	50.3	8.8

Table 4.5: Reduced χ^2 values versus latitude bin per model. Bold values are significant at the $p \leq 0.05$ level, meaning the model at those latitudes is inconsistent with the observations.

free thermal emission of Neptune with the Very Large Telescope in 2006, finding temperature excesses of 10 – 11K and 3 – 5K near, but not at, Neptune’s south pole at $17.6\mu\text{m}$ and $18.7\mu\text{m}$ respectively. These authors suggested that seasonal warming around Neptune’s south pole could explain why the stratospheric abundance of methane is larger than expected; cold temperatures should result in methane condensing and becoming trapped below the tropopause. However, warm polar temperatures may allow methane gas to escape upward into the stratosphere and diffuse across the globe.

Warm brightness temperature measurements at high-latitudes are persistent throughout radio maps. de Pater et al. (2014) found temperature enhancements from 8–30K in VLA 1.3–6.2 cm maps, where sensitivities peak between 5 – 50 bar. EVLA 1-cm maps show enhancements of similar magnitudes southward of 70°S (Butler et al., 2012). Luszcz-Cook et al. (2013) see southern high-latitude enhancements of 2 – 3K compared to the northern mid-latitudes in 1.2 mm CARMA maps. Our ALMA maps show average enhancements of 2 – 3K in Bands 3 and 4, with sensitivities peaking at $P > 1$ bar, and 1 – 2K in Band 6, whose sensitivities peak at 1 bar. Iino and Yamada (2018) analyzed ALMA flux calibration data of Neptune at 646 GHz (0.46 mm), peaking at 0.6 bar, and ruled out a detection of the south polar hot spot greater than 2.1K compared to the background. Combined, these data suggest that the magnitude of the south polar brightness enhancements decreases with increasing altitude. This trend is likely due to the temperature-pressure profile, which is mostly isothermal between 0.1 – 1 bar. This picture also appears dynamically distinct from that described in Orton et al. (2007), who predicted upwelling air to explain methane and ethane enrichment in the stratosphere. In the radio, brightness enhancements are consistent with low-opacity (dry) air so deeper warmer layers are probed. The air is likely subsiding, after having been dried out at other latitudes. The subsiding air causes adiabatic warming, which is sensed in the mid-IR (e.g., Fig. 16 in de Pater et al. (2014)). Persistent cloud activity surrounding Neptune’s south pole may be indicative of vigorous convection and evidence of a south polar vortex (Luszcz-Cook et al., 2010), analogous to the polar activity seen on Saturn (Fletcher et al., 2008; Dyudina et al., 2008). Such a system could explain the observed temperature, ethane and methane enhancements in the mid-IR, polar cloud features seen with *Voyager* and Keck, and high brightness temperatures in the radio.

Recent findings by Irwin et al. (2019) find a tentative detection of an H_2S spectral signature between $1.57 - 1.58\mu\text{m}$ on Neptune with Gemini-North/NIRS. They find that the signature is stronger at southern latitudes than at the equator, with H_2S abundances around 3 ppm and 1 ppm respectively at the top of Neptune’s H_2S cloud deck: 2.5 – 3.5 bar. This broadly agrees with our suite of proposed H_2S profiles (Fig. 9), where H_2S is depleted to an abundance of 1 ppm between $\sim 2.5 - 4$ bar. The exception is our model for the south polar cap, which has less H_2S at the relevant altitudes than predicted by Irwin et al. (2019). In order to match their results, we would have to lower the altitude where H_2S follows the saturated vapor pressure curve (to $P > 4.5$ bar) so that the abundance from 2.5 – 3.5 bar could be increased to 1 ppm. Moreover, their retrieved H_2S abundances are most consistent with models which deplete the deep abundance of CH_4 at the southern high-latitudes relative to the equator. This agrees with our results and Karkoschka and Tomasko (2011).

Neptune’s Mid-Latitudes and Equator

Moving northward, our ALMA maps show that latitudes spanning $32^\circ - 12^\circ\text{S}$ and $2^\circ - 20^\circ\text{N}$ are colder than the background by $\sim 0.5 - 1.5\text{K}$ in all three bands. This difference can only be explained at all wavelengths with models which both increase the deep CH_4 abundance to $\sim 2.2 - 2.9\%$ and supersaturate the H_2S profile. This is consistent with upwelling, adiabatically cooling plumes, and the observed distribution of prevalent bright cloud activity in this latitude range seen in the visible and near-IR. Karkoschka and Tomasko (2011) find that methane is well-mixed in the deep-atmosphere, with an abundance of $4 \pm 1\%$. In addition, they find that methane is depleted by a factor of 3 at the southern mid-latitudes compared to the equatorial region between 1.2 and 3.3 bar. This pressure range contributes the most to the opacity in Band 6, wavelengths where we also see the lowest temperature contrasts. If we assume their horizontal methane profiles, our models are too cold to match the ALMA data, due to their high methane abundance. A corresponding global decrease in the H_2S abundance to $\sim 10\times\text{S}$ must be made in order to decrease the total opacity and increase the brightness temperature so that the Band 6 data and model agree. However, decreasing the global H_2S abundance has the side effect of dramatically increasing the brightness temperatures in Bands 3 and 4, particularly near the equator. In Band 4, these profiles fit the equatorial regions poorly, yet agree at these latitudes in Band 3. For Band 4 to match here, the H_2S abundance would have to be increased to account for a 1 K difference. However, the Band 3 model temperatures would be decreased by at least this same amount, putting it outside a two-sigma fit to the data. Moreover, model disk-averaged brightness temperatures assuming a $10\times\text{S}$ H_2S abundances are too warm compared to the ALMA and 2003 VLA data (Fig. 4.3).

Our results are more consistent with Baines et al. (1995), who predict disk-averaged deep-atmosphere methane molar fractions of $2.2^{+0.5}_{-0.6}\%$. Karkoschka and Tomasko (2011) remark that the two studies use different haze and cloud profiles and relative humidities. Correcting for these factors lowers their deep-atmosphere methane mixing ratio to within the error bars cited in Baines et al. (1995). In addition, Karkoschka and Tomasko (2011) note that a significant contribution to their error bars is due to systematic variations in their center-to-limb profiles in the methane bands. Their model is too bright at disk center and too cold at the limb. Lowering the methane mixing ratio and using different values for the (poorly known) methane and hydrogen absorption coefficients would improve their fit. Alternatively, a high deep methane mixing ratio may be possible if methane is subsaturated, which we did not consider in our models. Subsaturated models will produce warmer brightness temperatures while increasing the deep methane mixing ratio will produce colder temperatures. As a result, these effects will partially cancel and combined may produce a more reasonable fit. There may also be uncertainties in the millimeter spectral line parameters that are not accounted for here. Laboratory measurements of H_2S absorption in the millimeter are extremely limited and not at Neptune’s tropospheric conditions (Joiner et al., 1992). Updated measurements of the trace gas absorption lines under cold, ice giant conditions would improve, and perhaps reconcile, models of these multi-wavelength observations.

While we disagree with the deep methane mixing ratio computed by Karkoschka and Tomasko (2011), we find general agreement with their observed latitude trends. Both our study and theirs find enhancements in trace gases from $32^\circ - 12^\circ\text{S}$ and $2^\circ - 20^\circ\text{N}$, depletion from $90^\circ - 50^\circ\text{S}$ and north of 20°N , and intermediate values from $50^\circ - 32^\circ\text{S}$. Our sole inconsistency is from $12^\circ\text{S}-2^\circ\text{N}$, where we also depleted trace gases. However, at these latitudes, Karkoschka and Tomasko (2011) lowered the tropospheric haze optical depth compared to the surrounding latitudes. If their haze optical depth was increased here, we would expect them to need to decrease the methane abundance from $12^\circ\text{S}-2^\circ\text{N}$ to fit their data. Luszcz-Cook et al. (2016) also investigated methane profiles in cloud free regions of Neptune with the OSIRIS integral field spectrograph in the H and K broad bands. These data probe altitudes higher than ALMA and HST/STIS and so are insensitive to the deep troposphere methane abundance. These authors saw tentative evidence of meridional variations in the methane profile, qualitatively consistent with Karkoschka and Tomasko (2011), but remarked that their parameterizations could not fully characterize the true shape of the methane profile since they were only sensitive to $P < 2.5$ bar.

In the equatorial region, our ALMA residual maps show clear latitudinal structure undetected in prior radio studies of Neptune. North of the equator, we detect low brightness temperatures that are consistent with supersaturating H_2S and a slight increase in the deep CH_4 abundance. In the visible and near-IR, Neptune’s equatorial region is quiescent, lacking bright cloud activity compared to the dramatic stormy mid-latitudes. However, there is evidence of more cloudy activity just north of the equator than south of it, agreeing with our finding of CH_4 enrichment from $2^\circ - 20^\circ\text{N}$ and depletion from $12^\circ\text{S}-2^\circ\text{N}$. Figure 4.16 shows a histogram counting the number of bright cloud features versus latitude from *Voyager*, the Hubble Space Telescope, and H-band Keck maps which were tracked in five papers: Limaye and Sromovsky (1991); Sromovsky et al. (2001b); Martin et al. (2012); Fitzpatrick et al. (2014); Tollefson et al. (2018). By eye, there appears to be a clear correlation between our ALMA defined latitude bands and latitudes where the number of features transitions from low-to-high or vice-versa, particularly in the *Voyager* data. This suggests that the banded structure seen by ALMA from 1 – 10 bar exists up to the visible cloud deck. Specifically, at the central latitudes within the $12^\circ\text{S}-2^\circ\text{S}$ band, there is a persistent scarcity of activity observed over a 30 year period. In contrast, features are seen regularly between $2^\circ\text{S}-20^\circ\text{N}$, suggesting a larger source of condensible methane. This agrees with our best fit model which depletes CH_4 to $\sim 1.1\%$ in the cloud-free latitudes and enriches it to $\sim 2.2\%$ in the cloud-prevalent latitudes. The enhancement of methane in this region is consistent with a moist convective origin of a recently discovered large bright storm centered at 2°N (Molter et al., 2019). Moreover, this model may explain inconsistencies between the thermal wind equation and observed vertical wind shear measurements. Fitzpatrick et al. (2014) and Tollefson et al. (2018) detected vertical wind shear at Neptune’s equator by tracking bright cloud features in the H- and K’-bands with Keck, with the K’-band probing higher altitudes with features that have, on average, stronger retrograde velocities than features seen in the H-band. Tollefson et al. (2018) showed that the equator must be methane-rich and warm compared to mid-latitudes if the thermal wind equation holds.

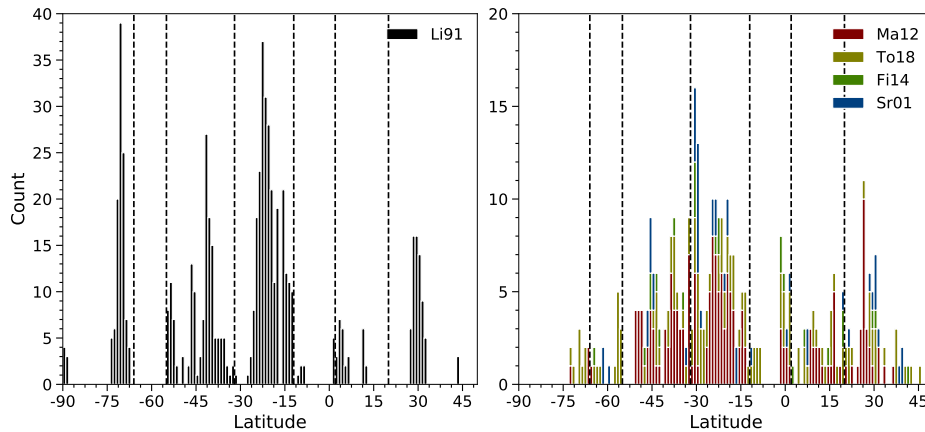


Figure 4.16: Histogram counting the number of tracked bright cloud features versus latitude. Dashed lines delineate the latitude bands used in the modeling of the ALMA data and correspond to variations in the residual brightness temperature. Counts are in one-degree latitude bins and latitudes have been converted to planetographic coordinates. Since the *Voyager* data would otherwise dominate the count and perceived trend, these data are split apart, showing the *Voyager* counts on the left and post-*Voyager* counts on the right. These data come from five papers, labeled as follows: Li91 - Limaye and Sromovsky, 1991; Ma12 - Martin et al., 2012; To18 - Tollefson et al., 2018; Fi14 - Fitzpatrick et al., 2014; Sr01 - Sromovsky et al., 2001b.

The thermal profile inferred from MIR observations, the horizontal distribution of clouds, and observed regions of enriched/depleted air all relate to vertical circulation motions. Based on multi-wavelength observations, de Pater et al. (2014) suggest a vertically extended, hemispheric symmetric double-cell pattern with upwelling at the mid-latitudes and downwelling at the equator and poles from the stratosphere down to the deep troposphere (~ 40 bar). The ALMA, HST/STIS, and OSIRIS results suggest more detailed circulation, particularly near the equator. Our analysis is consistent with the prediction of vertically extended cells, going from the stratosphere down to ~ 40 bar, since there is a clear alignment between the ALMA detected latitudinal bands and the observed distribution of cloud features. However, we argue that the equatorial region is more intricate than what was outlined by de Pater et al. (2014), with upwelling from 2°N – 20°N and downwelling from 12°S – 2°N . A narrower circulation cell than predicted by de Pater et al. (2014) centered just south of the equator would partially explain the differing predictions between these studies. Figure 4.17 gives a sketch of our proposed global circulation pattern.

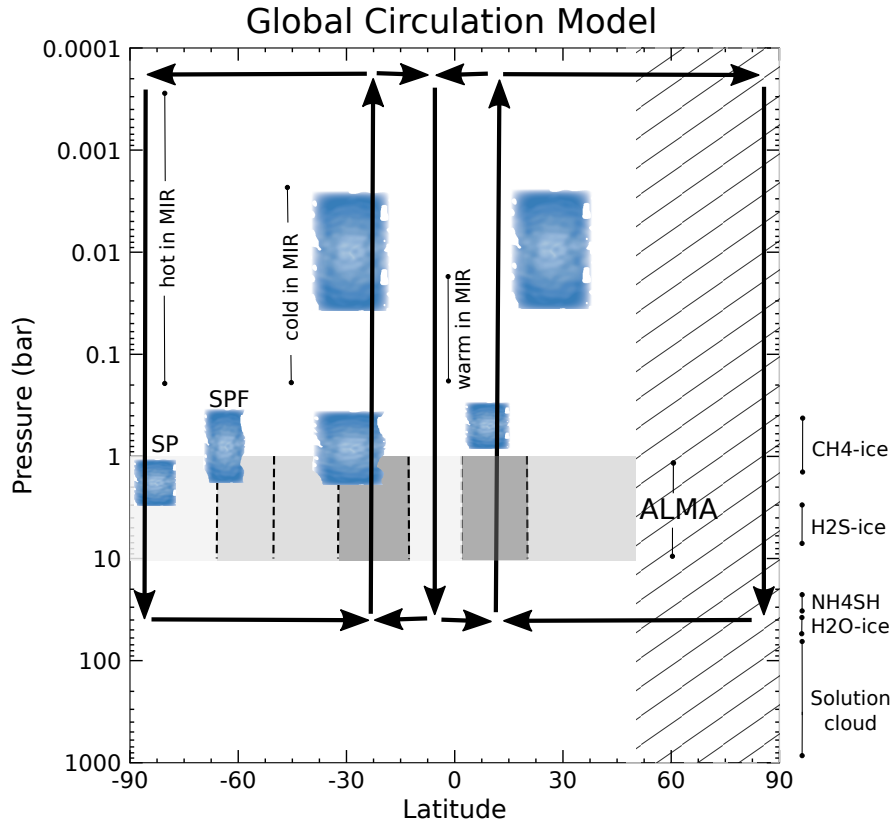


Figure 4.17: Schematic of Neptune’s global circulation inferred from ALMA observations, adapted from Fig. 21 in de Pater et al. (2014). Black arrows outline the circulation pattern, which extends from the stratosphere down to 40 bar. The biggest change from the sketch in de Pater et al. (2014) is our circulation cells are narrowed near the equator and we prefer a subsiding region which is just south of the equator (aligning with the 12°S–2°N range seen in our residual map), instead of hemispheric symmetric cells. The gray rectangle between 1 – 10 bar shows the sensitivity of the ALMA spectral bands (see Fig. 1). Dark-gray (off-white) rectangles are the latitude ranges where the residual brightness temperature is colder (warmer) than the background (see Fig. 4.4). At these latitudes, both H₂S and CH₄ are enriched (depleted) (see Table 5). The light-gray rectangles are latitude ranges where the residual brightness temperature is similar to the background. Here, H₂S and CH₄ equal their nominal value, or only H₂S is depleted. The locations of Visible/NIR clouds are illustrated with blue vertical patches. Most clouds are seen at the mid-latitudes (peak cloud counts are centered near 25°S and 30°N, see Fig. 15) and are seen high in the atmosphere (e.g., those tracked in de Pater et al. (2014)). However, clouds just north of the equator are also seen and are deeper in the atmosphere (de Pater et al. (2014), Tollefson et al. (2018), and Fig. 15). Neptune’s south polar feature (SPF) and south polar (SP) cloud are also placed. Marked cloud layers (CH₄-ice, H₂S-ice, NH₄SH, H₂O-ice, Solution Cloud) on the right are assumed to be independent of latitude (see Fig. 1). Also indicated are where high and low temperatures are measured in the MIR (Fletcher et al. 2014). Poleward of ~ 50°N, seeing is cut off in all observations as Neptune’s north pole is tilted away from the observer (rectangular diagonal hatches). Downwelling motions are assumed at Neptune’s north pole in order to complete the circulation diagram.

4.6 Conclusion

Spatially resolved millimeter maps of Neptune are presented in three ALMA bands, spanning 95 – 242 GHz. These maps have unprecedented sensitivities in the millimeter, ranging between 0.1 – 0.6K, and resolutions down to 0.3”, roughly one-eighth of Neptune’s diameter. The observed emission is mainly modulated by the opacity due to H₂S absorption, CIA of H₂ with H₂, He, and CH₄, and *ortho/para* H₂. We used the radiative transfer code Radio-BEAR to vary the abundance profiles of these gases in order to model the brightness temperature across Neptune’s disk. Our main conclusions are as follows:

1. The disk-averaged brightness temperature of Neptune in the millimeter and centimeter matches a model where: the temperature-pressure profile follows a dry adiabat; H₂S, CH₄, and H₂O are enriched by 30× their protosolar values, while NH₃ is held at 1× its protosolar value; intermediate H₂ is assumed. This is referred to as the ‘nominal’ model.
2. Subtracting the nominal beam-convolved model from the data shows clear brightness temperature variations across Neptune’s disk. We identify latitudes in between significant transitions in the brightness temperature: 90° – 66°S, 66° – 55°S, 55° – 32°S, 32° – 12°S, 12°S–2°N, 2° – 20°N, and northward of 20°N. These bands are at least the size of the ALMA synthesized beam and are apparent in all maps. Relative to the nominal model, brightness enhancements of 1 – 3K are seen at 90°S–66°S and 66°S–55°S. Negative temperature residuals between 0.5 – 1.5K are seen from 32° – 12°S and 2° – 20°N. These bands align with regions transitioning from high or low counts in the number of cloud features versus latitude, suggesting that the banded structure we see in the ALMA data exists up at the visible cloud deck. As a result, these identified latitudinal bands may be indicative of a zonal wind profile that is more complex than hitherto considered.
3. At the south polar cap, our best fit model depletes the deep atmospheric abundance of both H₂S to 1.5× the protosolar value and CH₄ to 0.55% (11.5×S). This is consistent with models fitting VLA and CARMA data (de Pater et al., 2014; Luszcz-Cook et al., 2013). Between 55° – 32°S and northward of 20°N, our best fit models deplete H₂S to 10×S while keeping CH₄ at the nominal value of 1.44% (30×S). From 32° – 12°S and 2°N–20°N, H₂S is supersaturated and the deep abundance of CH₄ is enriched to 2.2 – 2.9% (45 – 60×S). From 12°S–2°N, we deplete H₂S to 10× protosolar and CH₄ to 1.1% (22.5×S). Warm brightness temperatures relative to the nominal model are consistent with dry, subsiding air. Conversely, cold brightness temperatures are consistent with moist, rising air. Our results are, therefore, consistent with an intricate global circulation system that extends from the cloud deck to deep in the atmosphere.

These ALMA maps are evidence of a more complex zone and belt structure that may be yet unresolved in the zonal wind field. An ice-giant probe and high-resolution spacecraft

imaging characterizing the zonal wind structure in detail would help settle any inconsistencies between Neptune's velocity, thermal, and compositional profiles.

4.7 Acknowledgements

The authors wish to thank Arielle Moullet for helping with the data reduction and imaging process. This work has been supported in part by the National Science Foundation, NSF Grant AST-1615004 to UC Berkeley and by NASA Headquarters: under the NASA Earth and Space Science Fellowship program Grant NNX16AP12H to UC Berkeley.

Chapter 5

Neptune’s Latitudinal Variations Viewed with VLA

5.1 Introduction

The millimeter images of Neptune presented in Chapter 4 are the first spatially-resolved, high sensitivity look of the planet in the millimeter. The millimeter wavelengths are sensitive to between 1 – 10 bar. This is in contrast to the visible and near-infrared wavelengths, which interact with Neptune’s high-lying methane clouds and hazes, limiting the view into the atmosphere to pressures above ~ 1 bar. Thus, ALMA observations bridge the gap between Neptune’s stratosphere and troposphere. In particular, the latitudinal brightness distribution seen from clouds and hazes in the visible and near-infrared was also seen in these ALMA maps, suggesting Neptune’s vertical structure was rather extended. In the millimeter, cold/dark regions correspond to increases in opacity sources, namely Neptune’s trace gases: H_2S and CH_4 . Tollefson et al. (2019) found that dark latitude bands required super-saturating H_2S and increasing the CH_4 abundance relative to the ‘nominal’ profiles, which assume enhancements of these species by $30\times$ their protosolar values.

Centimeter wavelengths probe Neptune deeper than the millimeter: $100 < P < 1$ bar. de Pater et al. (2014) observed Neptune with the Very Large Array (VLA) at centimeter wavelengths and found that the disk-average properties of their maps agreed with the nominal profiles. In addition, they analyzed brightness enhancements at Neptune’s south polar cap, finding that their models had to deplete the abundance of H_2S down to ~ 40 bar in order to match the observed brightness temperature. However, this study did not investigate brightness variations at other latitudes, as the sensitivity and resolution were not good enough to detect significant variations apart from at the south polar cap.

In 2011, plans to modernize the VLA were completed. This expansion improved the continuum sensitivity by 5-to-20-fold and increased the wavelength coverage and bandwidth. This expansion prompted a program to re-look at Neptune with the upgraded VLA at centimeter wavelengths. Here, we report on a preliminary analysis of these observations. In

Table 5.1: Summary of observations.

Wavelength (cm)	Frequency (GHz)	Band	Beam Size (arcsec ²)	Position Angle ^a
0.9	32.958	Ka	0.12 × 0.12	0.06
2.0	14.880	Ku	0.25 × 0.25	0.12
3.0	9.869	X	0.35 × 0.26	1.07
5.1	5.861	C	0.56 × 0.45	0.96
9.7	3.096	S	0.98 × 0.79	0.93

^a Defined as north through east.

Section 5.2, we present longitudinally-smearred maps of Neptune taken with the expanded VLA in 2015 between 0.9 – 9.7 cm. Combining these data with VLA 2003 and ALMA observations of Neptune, we then use a Markov chain Monte Carlo (MCMC) implementation of Radio-BEAR to obtain retrievals of the abundances of Neptune’s trace gases in the deep atmosphere. In Section 5.5, we briefly compare our findings to other results.

5.2 Observations

Data

We observed Neptune with the expanded VLA, an interferometer located in Socorro, New Mexico, at UTC 1 and 2 September, 2015. Maps were obtained at wavelengths of 0.9 cm (Band Ka), 2.0 cm (Band Ku), 3.0 cm (Band X), 5.1 cm (Band C), and 9.7 cm (Band S) in the ‘A’ configuration. The VLA consists of 27 antennas grouped into three arms of nine antennae to form a ‘Y’-shape. Every four months, the configuration is changed by moving the antennae along tracks. The A configuration is the VLA’s most extended; the length of each arm is ~ 21 km, forming a maximum baseline of ~ 36 km. The maximum baseline is inversely related to the angular resolution and beam size, meaning variations across Neptune’s disk are most pronounced in the A configuration. Neptune was observed on two days, each for 7 hours in scans of 5 minutes per wavelength. Table 5.1 lists a summary of our observations.

Calibration and Imaging

Data reduction was done using the VLA calibration pipeline. This initial processing flags and removes bad data. The flux density was calibrated to the standard J2246-1206 using the MIRIAD software package (Sault et al., 1995). In addition, self-calibration was performed to correct for short-term variability in the phases caused by fast atmospheric fluctuations. This was done by fitting a limb-darkened disk to Neptune that best matched the observations. The limb-darkened temperature profile is represented by the peak brightness temperature T_b multiplied by $\cos^k \theta$, where θ is the emission angle and k is a limb-darkening constant.

Values for T_b and k were found at each wavelength such that the difference between the limb-darkened model disk and observations were minimized.

Our final longitudinally-smearred images of Neptune are shown in Figure 5.1.

Error estimation

The error in our VLA maps is calculated by averaging over four regions of the sky with boxes equal to the diameter of Neptune and taking the root-mean-square (RMS). RMS values range from 0.4 – 2.0K. Table 5.2 lists our estimated errors in each band. This RMS does not include systematic effects, such as errors in the bandpass or flux calibration. Uncertainties in the flux density are estimated from 3 – 5% or less in each band so we use this as an estimate for the absolute error in our disk-averaged temperature data.

5.3 Modeling

We generate models of Neptune’s brightness temperature using the radiative transfer (RT) code Radio-BEAR described in de Pater et al. (2019)¹. We use the same basic atmospheric setup (temperature profiles, cloud structure, and composition) described in Chapter 4 Section 4.3. However, since centimeter wavelengths probe deeper into Neptune’s atmosphere than the millimeter, our models now consider the impact of NH₃. As shown in Figure 4.1, these VLA observations probe between 1 – 100 bar, meaning they are sensitive to the NH₄SH cloud. This cloud is formed by the following reaction:



The equilibrium constant K of this reaction is governed by (Lewis, 1969):

$$\log_{10} K = \log_{10}(p_{\text{H}_2\text{S}} \cdot p_{\text{NH}_3}) = -4715.0/T + 14.83, \quad (5.2)$$

where $p_{\text{H}_2\text{S}}$ and p_{NH_3} are the partial pressures of H₂S and NH₃ and T is the temperature at pressure P . If the deep molar fractions of H₂S and NH₃ are $X_{\text{H}_2\text{S}, 0}$ and $X_{\text{NH}_3, 0}$, their abundance at pressure P will be depleted by some fraction $0 \leq \xi \leq 1$ of the NH₃ deep abundance (assuming $X_{\text{H}_2\text{S}, 0} > X_{\text{NH}_3, 0}$):

$$X_{\text{H}_2\text{S}} = X_{\text{H}_2\text{S}, 0} - \xi X_{\text{NH}_3, 0} \quad (5.3)$$

$$X_{\text{NH}_3} = X_{\text{NH}_3, 0} - \xi X_{\text{NH}_3, 0} \quad (5.4)$$

Using Eq. (5.2), we obtain the abundances of NH₃ and H₂S by solving the following quadratic equation for ξ for given P , T , $X_{\text{H}_2\text{S}, 0}$ and $X_{\text{NH}_3, 0}$:

¹This code is available at: <https://github.com/david-deboer/radiobear> .

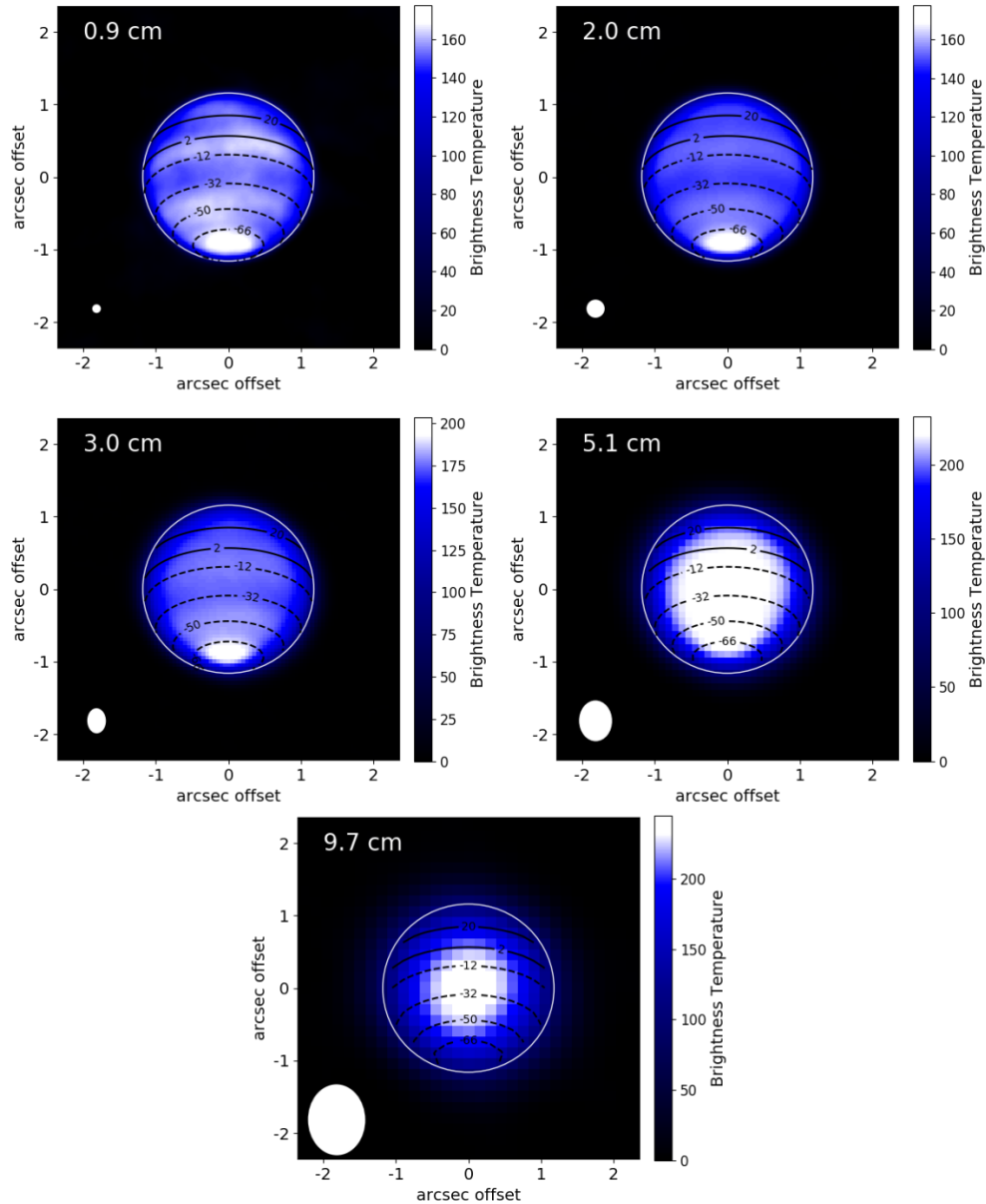


Figure 5.1: Longitudinal-smear maps of Neptune taken with the expanded VLA. The color scale has been chosen to enhance the brightness contrasts across the disk. Contour lines delineate the latitude transitions between bands, set by the ALMA maps in Chapter 4. Neptune's disk is outlined with a white ellipse. The FWHM of the beam is indicated in white in the bottom left of each map. Neptune has been rotated so that its north pole is pointing up in each image.

$$\log_{10}(P^2 X_{\text{H}_2\text{S}} X_{\text{NH}_3}) = -4715.0/T + 14.83 \quad (5.5)$$

$$P^2 X_{\text{H}_2\text{S}, 0} X_{\text{NH}_3, 0} \left(1 - \xi \frac{X_{\text{NH}_3, 0}}{X_{\text{H}_2\text{S}, 0}}\right) (1 - \xi) = 10^{-4715.0/T + 14.8} \quad (5.6)$$

Our forward models allow the deep abundances of H_2S , NH_3 , and CH_4 to vary. We define ‘deep’ as pressures below the NH_4SH and aqueous solution cloud formation ($P > 100$ bar). For the purposes of these preliminary retrievals, we do not consider the effect of the aqueous solution cloud in the forward models, but it is accounted for in the nominal models. We also vary the relative humidities of CH_4 and H_2S at the formation of their respective ice clouds (see Fig. 5.2).

Retrievals

In Chapter 4, we compared the ALMA data to forward models of Neptune’s atmosphere. From these forward models, we obtained deep abundances of H_2S and CH_4 that fit the latitudinally-varying brightness temperatures. A downside to this approach is that we can only rule out models which are improbable from χ^2 -statistics, meaning we do not retrieve uncertainties on our final results. In order to estimate uncertainties in our model parameters, we couple our Radio-BEAR models to Markov Chain Monte Carlo (MCMC) simulations via a python implementation of the Goodman and Weare (2010) ensemble sampler called *emcee* (Foreman-Mackey et al., 2013). *emcee* has been used by Luszcz-Cook et al. (2016) in near-infrared analyses of Neptune’s hazes and its usage is described in detail therein. We use their same log-likelihood gaussian function and uniform/log-uniform priors.

We also compare retrievals for different model atmospheres using the Deviance Information Criterion (DIC, Spiegelhalter et al. (2002)). DIC penalizes models with both poor goodness-of-fit and number of free parameters. The difference between DIC values can be used to determine the more preferred model, with differences greater than 10 favoring the model with the lower DIC score. The use of the DIC is also described in more detail in Luszcz-Cook et al. (2016).

5.4 Results

Disk-Average Profiles

We calculate Neptune’s disk-average brightness temperature by summing over the flux density contained within the planetary disk convolved with an area three times the size of the model beam. Since Neptune blocks the cosmic microwave background (CMB), its true brightness temperature is higher than observed in the radio. In all of our millimeter observations, we correct for the CMB by following the procedure laid out in Appendix A of de Pater et al. (2014). A 5% error arising from uncertainties in the calibration is assumed. These

Table 5.2: Summary of observed and modeled millimeter disk-averaged brightness temperatures.

Center Frequency (GHz)	Facility	UT Date	Observed T_b^a (K)	Nominal T_b^b (K)	Noise ^c (K)
3.096	VLA	02-Sep-2015	238.6 ± 11.5	233.3	1.3
4.915	VLA	28-Jun-2003	215.1 ± 10.8	–	–
5.861	VLA	01-Sep-2015	214.3 ± 10.9	197.7	0.6
8.328	VLA	27-Jun-2003	183.3 ± 9.2	–	–
9.869	VLA	01-Sep-2015	177.2 ± 8.9	174.9	0.4
14.880	VLA	01-Sep-2015	153.3 ± 7.7	162.9	0.7
14.990	VLA	26-Jun-2003	169.7 ± 8.5	–	–
23.061	VLA	11-Oct-2003	150.6 ± 7.5	–	–
32.958	VLA	01-Sep-2015	158.1 ± 7.9	149.1	2.0
42.827	VLA	12-Oct-2003	147.4 ± 7.4	–	–
95.012	ALMA	07-Jul-2017	126.6 ± 6.3	123.1	0.1
96.970	ALMA	07-Jul-2017	126.0 ± 6.3	122.4	0.1
107.000	ALMA	07-Jul-2017	120.5 ± 6.0	118.9	0.2
109.000	ALMA	07-Jul-2017	118.8 ± 6.0	118.2	0.3
135.986	ALMA	08-Oct-2016	108.5 ± 5.4	109.4	0.3
137.924	ALMA	08-Oct-2016	108.0 ± 5.4	108.8	0.2
147.986	ALMA	08-Oct-2016	104.3 ± 5.2	105.9	0.2
149.986	ALMA	08-Oct-2016	104.5 ± 5.2	105.2	0.3
223.982	ALMA	24-Oct-2016	93.4 ± 4.7	92.2	0.4
225.982	ALMA	24-Oct-2016	93.0 ± 4.7	92.0	0.4
239.981	ALMA	24-Oct-2016	93.1 ± 4.7	90.1	0.6
241.981	ALMA	24-Oct-2016	92.8 ± 4.6	89.9	0.6

^a The listed errors are the absolute errors, estimated at 5% from the calibrators.

^b The model brightness temperatures from the best-fitting wet adiabat MCMC retrievals.

^c Random errors defined as the RMS on the sky.

results are combined with measurements of Neptune’s disk-average brightness temperature from VLA 2003 (de Pater et al., 2014) and ALMA (Tollefson et al., 2019) to form our set of data used in MCMC retrievals. A summary of this data set is given in Table 5.2.

For our retrievals, we allow the deep abundances of H_2S , NH_3 , and the relative humidity of H_2S to vary. We do not consider CH_4 here as its effect on the opacity is small compared to the other species, and in terms of brightness temperature, is smaller than the systematic absolute calibration error. Moreover, adding additional free parameters slows the burn-in phase of *emcee*. The effect of CH_4 will be explored when comparing variations in Neptune’s latitudinal bands, where only the random errors (estimated by the RMS on the sky) matter.

We perform retrievals on wet and dry adiabats constructed assuming a ‘nominal’ $30\times$ solar deep abundance for the trace gases, apart from NH_3 which is $1\times$ solar. The temperature profiles for both the wet and dry adiabats are plotted in Figure 5.2. Figure 5.3 plots the abundances of Neptune’s trace gases assuming $30\times$ enrichment for H_2S and CH_4 and $1\times$ enrichment for NH_3 . The adiabatic profiles are affected by the composition of Neptune’s

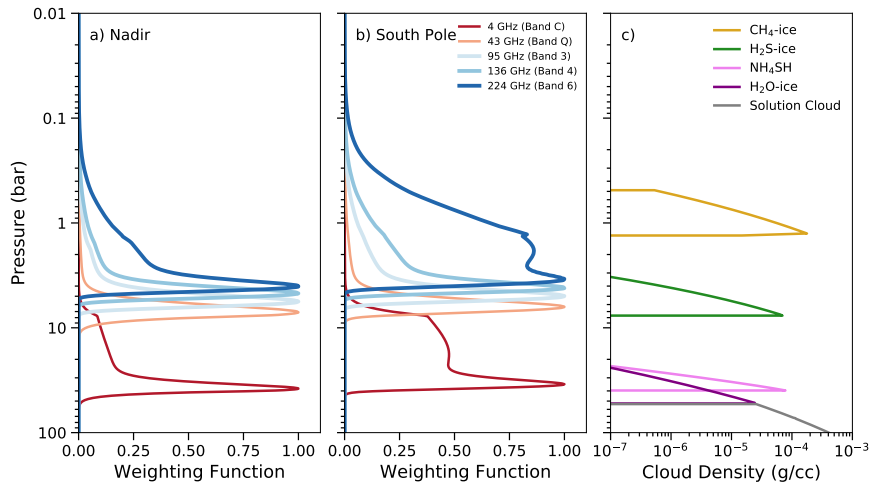


Figure 5.2: Normalized weighting functions at: a) nadir and b) the south pole, compared to the expected clouds expected to form on Neptune (c). The weighting functions at nadir and the south pole are both computed using the nominal abundance profile depicted in Figure 4.2. Weighting functions are shown for representative frequencies in each ALMA band: 95 GHz (3.155 mm, Band 3), 136 GHz (2.205 mm, Band 4), and 224 GHz (1.338 mm, Band 6), as well as selected VLA frequencies: 4 and 43 GHz (6.2 cm and 0.7 cm, respectively). Note that the VLA frequencies probe significantly deeper into Neptune’s atmosphere than the ALMA frequencies. The rightmost plot shows the density of different clouds expected to form on Neptune under thermochemical equilibrium.

atmosphere due to latent heat release. However, the ultimate effect on the temperature is not significantly changed by our retrieved abundances and does not change our conclusions.

In Figure 5.4, we show the results of the MCMC retrievals for Neptune’s disk-average brightness temperature. Table 5.4 lists the ‘best-fitting’ parameters, defined as the 50th percentile of the probability distribution after burnin and their uncertainties, defined as the 16th and 84th percentiles. In both the wet and dry adiabat models, there is significant positive correlation between the deep NH₃ and H₂S abundances. This is expected based on the NH₄SH cloud chemistry; retrievals with larger than normal NH₃ require additional H₂S to be removed during the NH₄SH reaction. If the H₂S abundance is not larger, the model brightness temperatures would be too cold near the NH₄SH cloud layer as the additional, unreacted NH₃ would increase the opacity. At higher altitudes, the depleted H₂S would result in models which are too warm. The dry adiabat results in marginally larger abundances of H₂S throughout the upper atmosphere due to the need to increase the opacity in order to offset the higher temperatures. However, both the H₂S and NH₃ profiles are consistent to within the retrieved uncertainties between the wet and dry models. The DIC for the wet and dry adiabats are also quite similar, implying that neither model does a superior job at

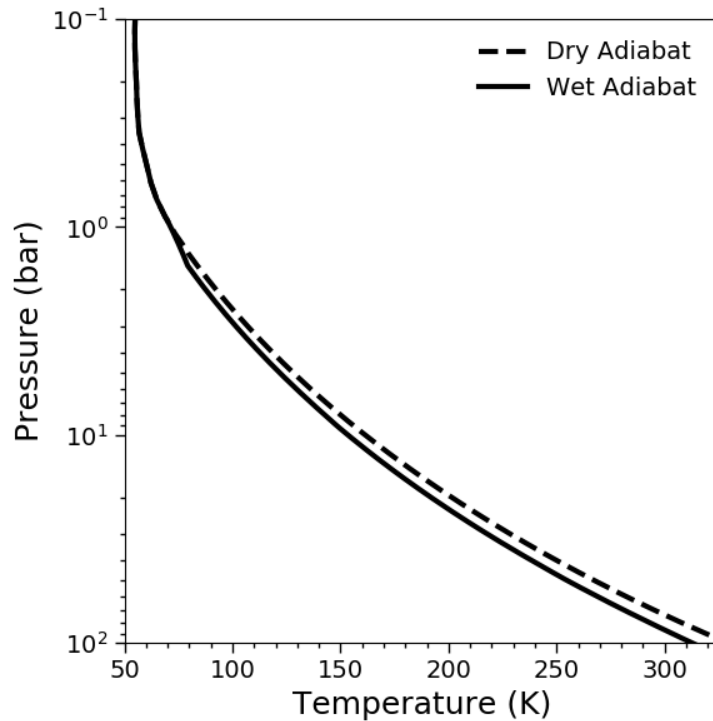


Figure 5.3: Temperature profiles for wet and dry adiabats assuming the ‘nominal’ abundances.

Model	H ₂ S	log ₁₀ NH ₃	H ₂ S Rel. Hum.	DIC
Wet Adibat	1.02 ^{+0.54} _{-0.26}	-0.71 ^{+1.20} _{-1.39}	0.10 ^{+0.09} _{-0.05}	135.46
Dry Adibat	1.37 ^{+0.48} _{-0.30}	-1.34 ^{+1.62} _{-2.25}	0.38 ^{+0.23} _{-0.17}	136.15

Table 5.3: MCMC fit results for the disk-average models. The ‘best-fit’ model is the 50th percentile of the distribution and values given in the error bars correspond to the 16th and 84th percentiles. The H₂S and log₁₀ NH₃ parameters are multipliers to their nominal deep values. For example, a value of 1.0 for H₂S corresponds to 30× the protosolar abundance while 2.0 corresponds to 60×.

fitting the data.

Figure 5.5 plots abundance profiles based on the MCMC retrieved parameters for the wet adiabat model. Figure 5.6 plots the brightness temperature data and the retrieved spectrum for the wet adiabat model. This later plot verifies that our MCMC retrieved parameters describe the data well. The retrieved profiles are consistent with the nominal models in Figure 4.2 apart from the need to subsaturate H₂S. If H₂S were not subsaturated, the spectrum between 10 – 100 GHz would be too cold. The NH₃ abundance is not well

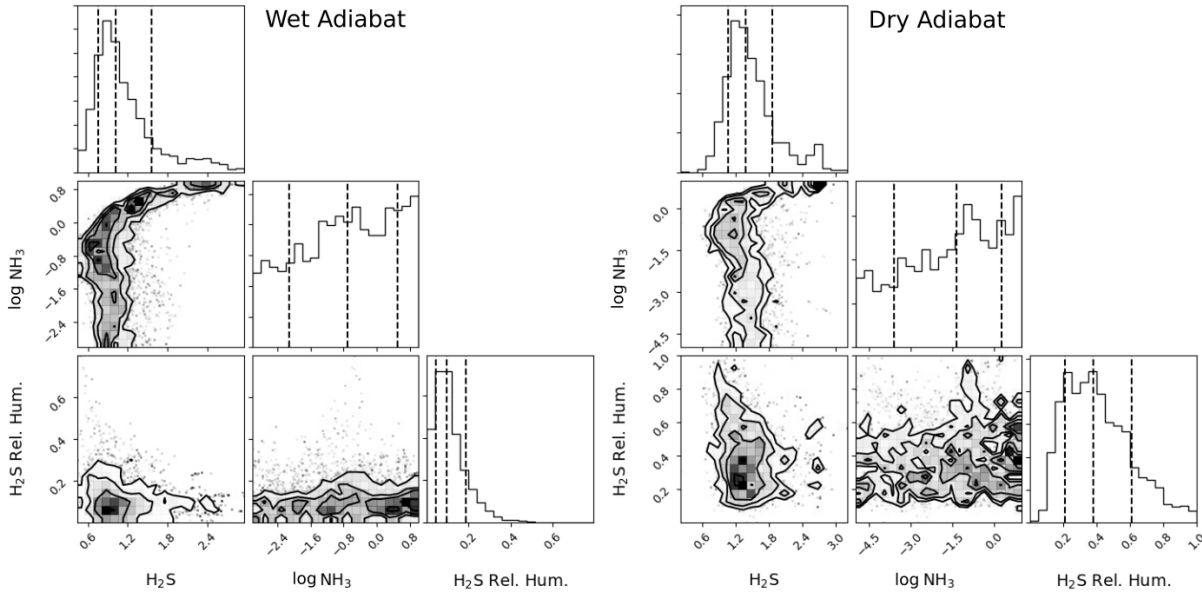


Figure 5.4: Corner plots of MCMC retrieved parameters for Neptune’s disk-average spectrum assuming a wet (left) or dry (right) adiabat. The scatter plots show the sampled distribution of each walker at each iteration after burnin for pairs of parameters. The histograms plot the probability distribution for each parameter, labelled on the x-axis. The H_2S and $\log_{10} \text{NH}_3$ parameters are multipliers to their nominal deep values (again, where deep is defined as pressures below the NH_4SH and aqueous solution cloud formation). The dashed lines delineate the 16th, 50th, and 84th percentiles of the distribution. Note the large degree of correlation and deviation from a multivariate normal distribution.

constrained, as only the longest wavelengths (lowest frequencies) probe deep enough to be sensitive to deep NH_3 (see Fig. 5.2).

12°S – 32°S Profiles

The latitude band between 12°S – 32°S is dark in both the VLA maps presented here (Fig. 5.1) and ALMA residual maps (Fig. 4.4). Low brightness temperatures imply increased sources of opacity from Neptune’s trace gases. Data for Neptune’s latitudinal variations are not available in the VLA 2003 maps.

Since we are interested in brightness variations across Neptune’s disk, we ‘zero-out’ the uncertainty in the brightness temperature due to the calibration by scaling each pixel in our maps such that the scaled map’s disk average temperature equals that of the best-fitting disk-average RT model. We obtain the band’s disk-average temperature by averaging over all pixels that are within 60 degrees of the sub-observer longitude between 12°S – 32°S. The new uncertainty is therefore the RMS due to random fluctuations on the sky (see Table 5.2

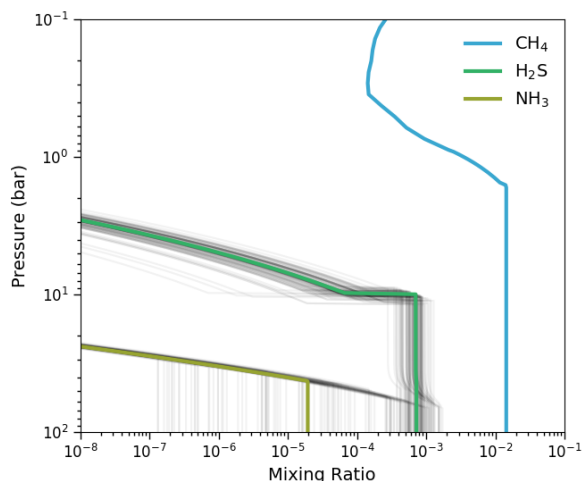


Figure 5.5: MCMC retrieved abundance profiles for the disk-average wet adiabat model. The solid color lines are the 'best-fit' model, representing the 50th, percentile of the retrieved probability distribution. 100 random profiles from the retrieved distribution are also plotted as light gray lines. The CH_4 profile was not varied, but is shown here for reference.

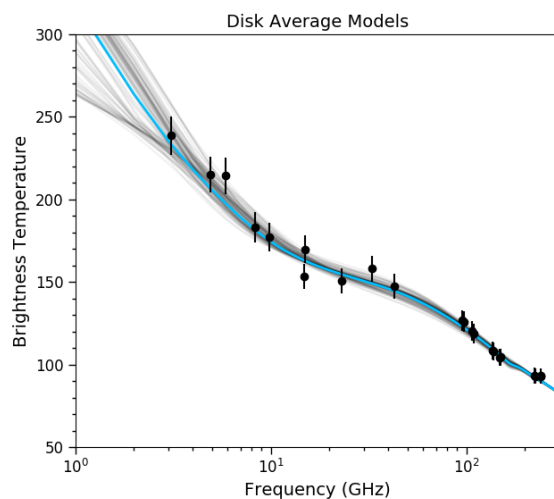


Figure 5.6: Disk-average temperatures and MCMC retrieved spectra for the wet adiabat model. The black scatter points are data from this work, de Pater et al. (2014), and Tollefson et al. (2019), with assumed 5% errors due to uncertainties in the calibration. The best-fit retrieved spectrum is the solid blue line. 100 random retrieved spectrum are also plotted as light gray lines.

divided by the square root of the number of beams that fit within the sampled region. We do this for both the wet and dry models.

One issue with RT models of particular regions on Neptune is that we cannot account for the PSF. Convolving the disk with the PSF results in a blurring of the disk, meaning the sampled temperature within a particular latitude bin is dependent on the background temperature and that of neighboring bins. This effect is hard to model while conducting MCMC as convolving the whole disk with the PSF is slow and the model composition of the surrounding latitudes must be simultaneously known. We circumvent this issue in two steps. First, we generate RT disks of the best-fitting disk-average models and then determine the brightness temperature within the region of interest with and without convolving the disk with the PSF. We then scale each MCMC retrieved model by the ratio of these values to obtain a model brightness temperature which approximates the effect of the PSF. This model temperature is fed into the *emcee* likelihood function. We emphasize that this effect is smallest near the center of the disk (i.e., the latitude bands considered in this section) and largest near the limb. Second, we add an error term to account for the uncertainty introduced by this approach,

$$\sigma_T^2 = \sigma_{RMS}^2 + \sigma_{PSF}^2, \quad (5.7)$$

where σ_T is the total error term used by *emcee* to calculate the likelihood function, σ_{RMS} is the random error on the sky divided by the square root of the number of beams that fit within the sampled region, and σ_{PSF} is the error introduced by RT-modeling for not accounting for the PSF. In our MCMC retrievals, we define an additional free parameter, σ , that is proportional to σ_{PSF} :

$$\sigma_{PSF} = \sigma \cdot T_{\text{data}} \cdot S, \quad (5.8)$$

where T_{data} are the data and S is the product of the beam’s semi-major and semi-minor axes. This relation is physically reasonable since both small (large) temperatures and small (large) beam sizes mean that there is a smaller (larger) absolute difference between the PSF-convolved and unconvolved models. We make the prior distribution of σ \log_{10} -uniform since we do not know the magnitude of this parameter.

The other free parameters for the MCMC retrievals are the deep abundances of H_2S , NH_3 , and CH_4 , and the relative humidities of H_2S and CH_4 . The new uncertainties described above are smaller than the systematic uncertainties, meaning we are potentially sensitive to CH_4 .

In Figures 5.7 and 5.8, we show the results of the MCMC retrievals for Neptune’s brightness temperature between 12°S – 32°S . Table 5.4 lists the best-fitting parameters and their uncertainties. Like the disk-average results, neither the wet and dry models are preferred over the other based on their DIC score. In both models, the best fits require more H_2S deep in the troposphere and at saturation than the nominal model. However, neither the NH_3 nor the CH_4 abundances are well-constrained. Only significant enrichment of CH_4 can be ruled-out, corresponding to values greater than $\sim 1.6\times$ the nominal abundance ($\sim 48\times$ solar or 2.3% molar mixing ratio).

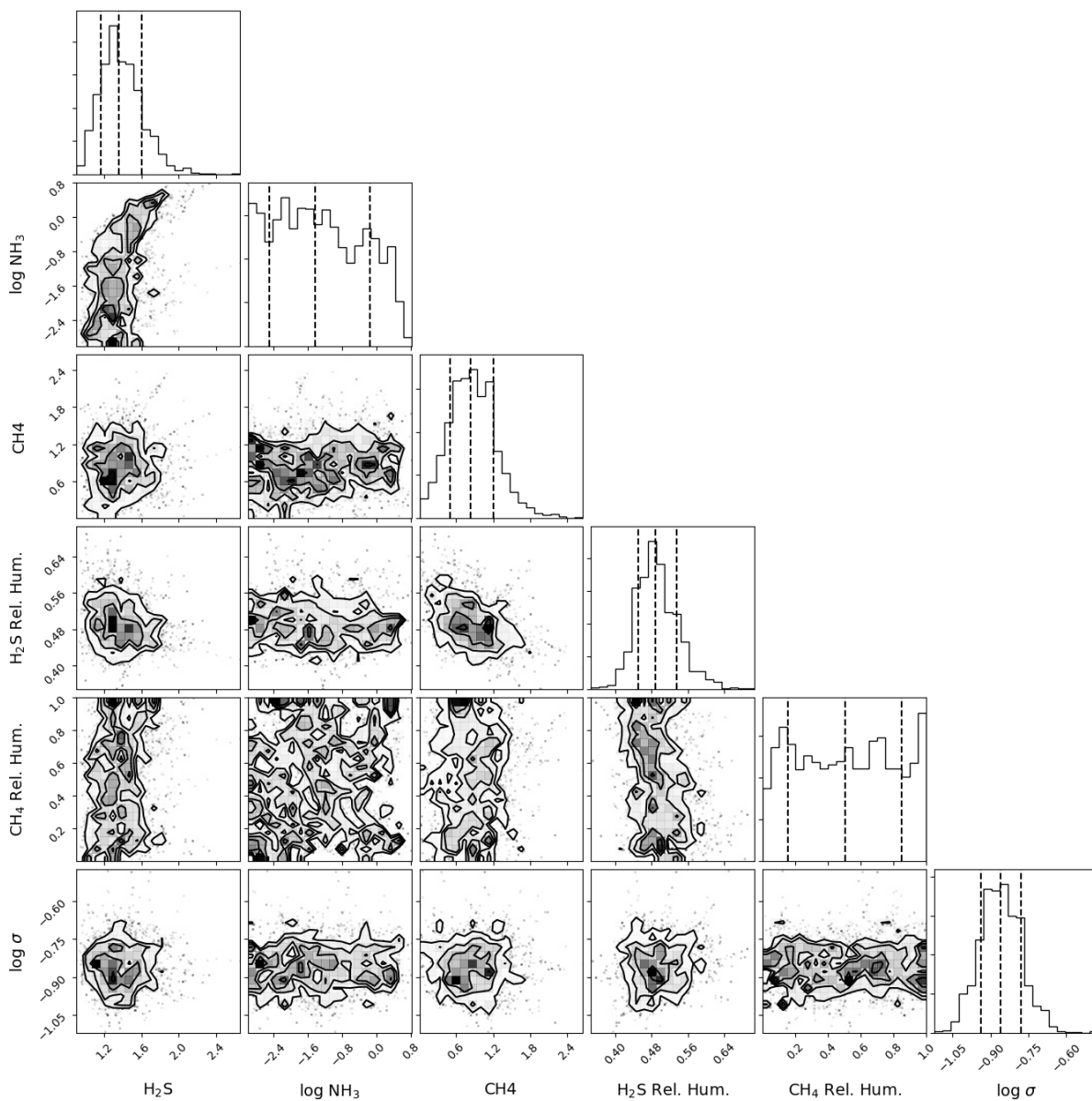


Figure 5.7: As Fig. 5.4, except these retrievals are for models of Neptune's brightness temperature between $12^\circ\text{S} - 32^\circ\text{S}$ assuming a wet adiabat.

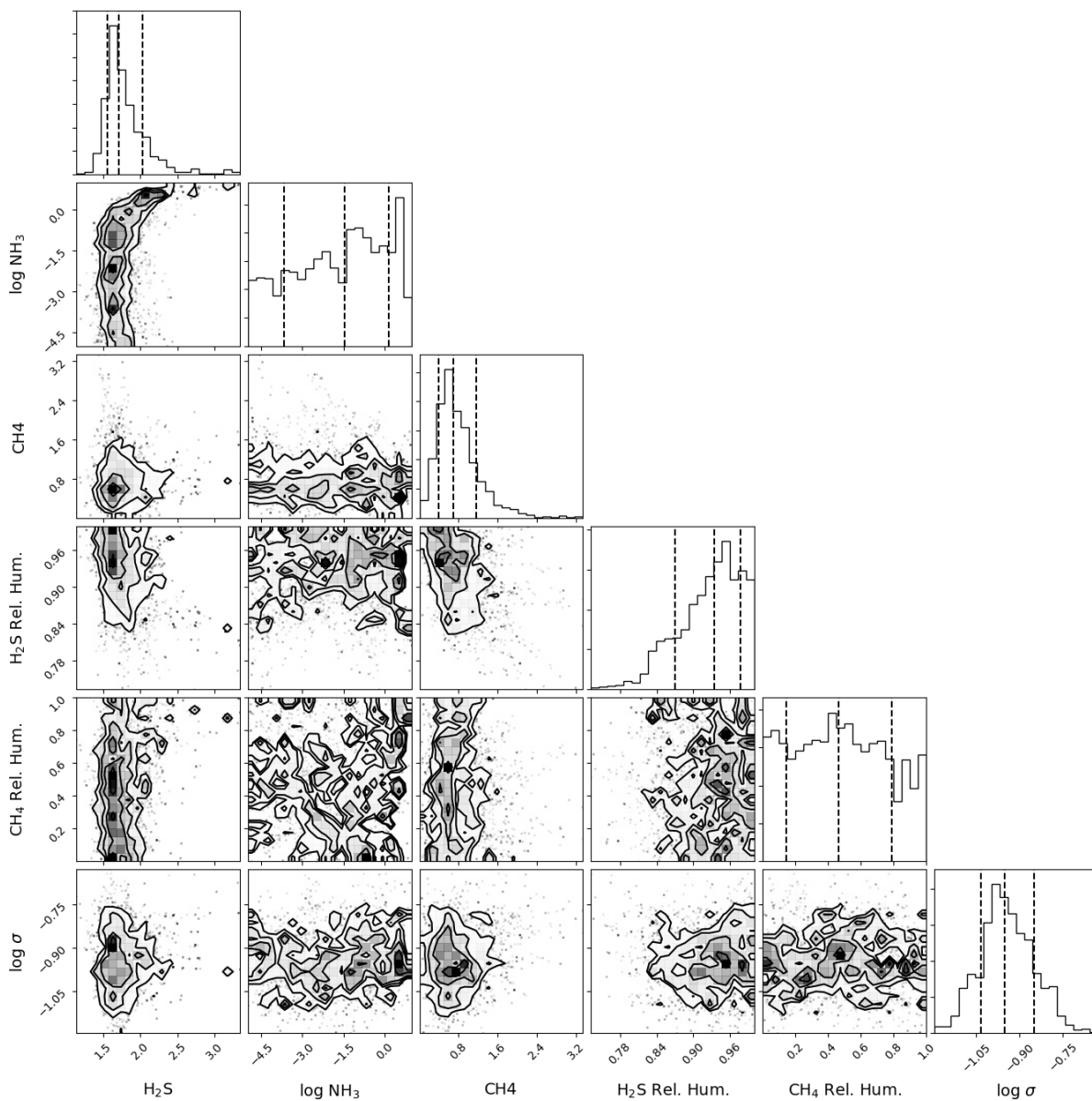


Figure 5.8: As Fig. 5.4, except these retrievals are for models of Neptune's brightness temperature between 12°S – 32°S assuming a dry adiabat.

Model	H ₂ S	log ₁₀ NH ₃	CH ₄	H ₂ S Rel. Hum.	CH ₄ Rel. Hum.	log ₁₀ σ	DIC
Wet Adiabatic	1.36 ^{+0.24} _{-0.19}	-1.43 ^{+1.28} _{-1.06}	0.83 ^{+0.37} _{-0.33}	0.49 ^{+0.05} _{-0.04}	0.50 ^{+0.35} _{-0.35}	-0.86 ^{+0.08} _{-0.08}	69.77
Dry Adiabatic	1.71 ^{+0.32} _{-0.15}	-1.47 ^{+1.63} _{-2.21}	0.70 ^{+0.47} _{-0.29}	0.93 ^{+0.04} _{-0.06}	0.46 ^{+0.32} _{-0.32}	-0.95 ^{+0.10} _{-0.08}	65.57

Table 5.4: As Table 5.4, except these fit results are for models of Neptune's brightness temperature between 12°S – 32°S.

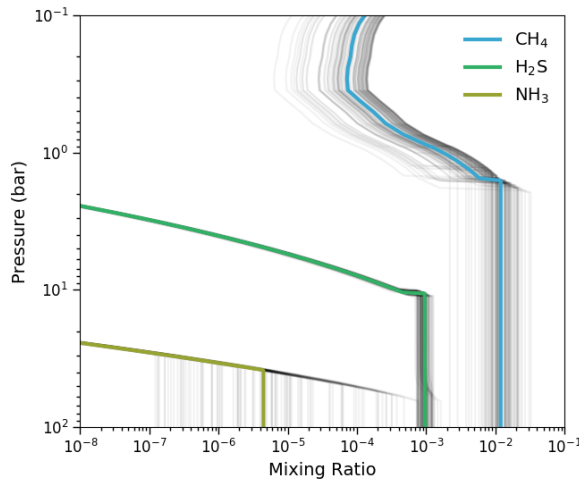


Figure 5.9: As Figure 5.5, except between 12°S – 32°S. The CH₄ deep abundance and relative humidity are also allowed to vary.

The best-fit values for σ_{PSF} are similar in magnitude to the difference, δ , between the convolved and unconvolved disk-average models within this latitude range. This suggests that σ_{PSF} is an adequate representation for the PSF in RT modeling coupled with *emcee*. For example, in the wet adiabat model at 9.7 cm, the best-fitting value of σ_{PSF} equals 22.2 K, compared to $\delta = 29.6$ K. At 0.9 cm, $\sigma_{PSF} = 0.3$ K and $\delta = 0.03$ K. Differences between σ_{PSF} and δ are due to the disk-average model not being an accurate representation of the latitude range of interest, σ_{PSF} not being a full prescription of the effect of the PSF, and/or σ_{PSF} accounting for other uncertainties not described here.

Figure 5.9 plots abundance profiles based on the MCMC retrieved parameters for the wet adiabat model. Figure 5.10 plots the brightness temperature data and the retrieved spectrum for the wet adiabat model. This later plot verifies that our MCMC retrieved parameters describe the data well.

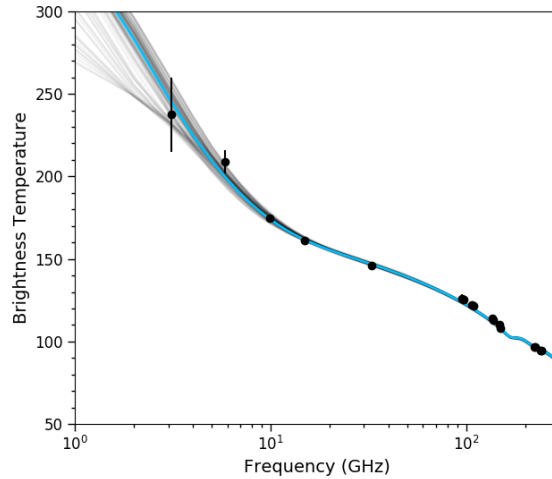


Figure 5.10: As Figure 5.6, except between $12^{\circ}\text{S} - 32^{\circ}\text{S}$. Moreover, data from VLA 2003 are not used here since brightness variations within this latitude bin are not reported. Error bars are equal to σ_T based on the best-fitting value of $\log_{10} \sigma$. The error bars are roughly the same size as the data points at frequencies higher than 10 GHz.

5.5 Discussion and Conclusion

We present preliminary maps and analysis of spatially-resolved maps of Neptune taken with the upgraded VLA between 0.9 – 9.7 cm on 1-2 September, 2015. At the longest wavelengths, clear bands of brightness temperature variations can be discerned. These bands align with those seen in 2016 – 2017 ALMA maps presented in Tollefson et al. (2019). Cold latitudes correspond to increased sources of opacity, mainly due to the enrichment of Neptune’s trace gases: H_2S , CH_4 , and NH_3 . Conversely, warm latitudes are due to depletion of these same gases. We couple the radiative transfer code Radio-BEAR to *emcee* in order to retrieve probability distributions for Neptune’s composition profiles. Our final results are in reference to our ‘nominal’ model: the deep abundances of Neptune’s trace gases are enhanced by $30\times$ their protosolar value, apart from NH_3 which is $1\times$ protosolar. The nominal model also assumes 100% relative humidity. We consider nominal models with temperature profiles governed by both wet and dry adiabats.

1. We combine these VLA data with that from ALMA (Tollefson et al., 2019) and VLA 2003 (de Pater et al., 2014) to analyze Neptune’s disk-average properties. The best-fitting deep abundances are consistent with the nominal model. However, H_2S is strongly subsaturated at the formation of the H_2S -ice cloud ($8 < P < 3$ bar). Neither a dry nor wet adiabatic profile is preferred. There is a strong correlation between the deep H_2S and NH_3 abundances when the amount of NH_3 exceeds its nominal value. This is due to the formation of the NH_4SH cloud.

2. We also use these VLA maps with the ALMA maps to model the cold brightness temperatures between $12^{\circ}\text{S} - 32^{\circ}\text{S}$. For a wet adiabat, the best-fit for the deep H_2S abundance is about $40_{-5}^{+8} \times$ the protosolar value and $\sim 50\%$ relative humidity. For a dry adiabat, the best-fit for the deep H_2S abundance is about $50_{-3}^{+11} \times$ the protosolar value and $\sim 93\%$ relative humidity, meaning H_2S almost exactly follows the saturation curve. Thus, H_2S is enriched relative to the nominal and disk-average models within this latitude band. NH_3 is not well-constrained, but like in the disk-average results, NH_3 abundances larger than $1 \times$ protosolar correlate with high amounts of H_2S (greater than $60 \times$ protosolar). This enrichment is consistent with upwelling air and the circulation sketch shown in Fig. 4.17.

The retrieved deep abundance of CH_4 for the wet and dry models are $25_{-10}^{+11} \times$ and $21_{-9}^{+14} \times$ the protosolar value, respectively. In terms of the molar mixing ratio, this is $1.20_{-0.48}^{+0.53}\%$ and $1.00_{-0.42}^{+0.69}\%$. The retrieved uncertainties are within the bounds reported in Baines et al. (1995), who obtain methane molar fractions of $2.20_{-0.60}^{+0.50}\%$. However, our results are lower than seen in the ALMA maps alone. This can be explained by the the enrichment of H_2S relative to the nominal model - Tolleson et al. (2019) did not allow the deep H_2S abundance to exceed $30 \times$ protosolar and only assumed a dry adiabat. We also differ from Karkoschka and Tomasko (2011), who assume methane abundances of $4 \pm 1\%$ for $P > 3.3$ bar. In fact, our reported uncertainties rule out CH_4 abundances larger than $\sim 2.4\%$. For further discussion regarding the differences between these models, revisit Chapter 4.

Since our RT models do not convolve the model disk with the PSF, we introduce an additional 'PSF-error' parameter that is added to the total uncertainties. The retrieved values for this parameter result in errors that are similar in magnitude to the difference between convolving and not convolving a model disk assuming disk-average properties within this latitude region. Future work will test the robustness of this approach close to the limb, where the effect of the PSF is most prominent. We will then look at the other latitude bins and test how deep abundance variations go.

Chapter 6

Conclusion and Future Work

Neptune is the least well-studied planet in our Solar System, being the furthest planet from the Sun and having only been visited up close by *Voyager 2*. However, advances in ground-based instrumentation and the launch of the *Hubble Space Telescope* have allowed Neptune to be regularly observed in detail. I have combined multi-wavelength observations of Neptune to constrain the bulk properties and dynamic patterns within its upper atmosphere. I helped develop theory that extends the thermal wind equation to the equator, connecting observed wind, temperature, and composition profiles. I also used radiative transfer code to retrieve model spectra of Neptune’s radio brightness temperature as a function of temperature and composition.

6.1 Jupiter and Neptune in the Visible and Near-Infrared

The zonal wind profile is one of the most important planetary properties. Through the thermal wind equation, vertical changes in the zonal wind velocity are related to the horizontal temperature and composition fields. Tracking the motions of bright features is one of the ‘easier’ observations to analyze, not requiring knowledge of spectroscopy, photometry, or radiative transfer. However, its application is powerful due to its relationship with local density variations. This is especially useful on Neptune - no probe has plunged into its atmosphere to extract these properties *in situ* and mapping its temperature field is limited to the stratosphere and upper troposphere with mid-infrared observations. But the thermal wind equation and zonal wind profile are used on all planets to indirectly calculate these properties at and below the visible cloud decks.

I analyzed five epochs of WFC3 HST Jupiter observations to derive zonal wind profiles from 2009 – 2016 (Chapter 2). Velocities were extracted using a 1D correlation method (Asay-Davis et al. (2011)). The derived 2016 zonal wind fields are the most timely for comparison to NASA *Juno* observations in late 2016 (PJ1 and PJ3). I find that Jupiter’s zonal winds are globally stable apart from periodic small changes on the order of 10 m/s. These

differences are most prominent in the presence of large scale vortices, which do not follow the background flow and thus increase the uncertainty of the extracted velocity, and at the Northern Temperate Belt (NTB), where the jet peak velocity varies in conjunction with periodic plume outbreaks (Sánchez-Lavega et al. (1991, 2008), Chapter 2). The albedo at visible wavelengths also darkens, suggesting that material, normally unseen, is dredged upward due to these plumes. If plumes are a signature of deeper activity, the decrease in velocity we see at the NTB during outbreaks may be evidence of vertical wind shear. To confirm this, observations of plume outbreaks must be coordinated with measurements that probe deeper into Jupiter. The high cadence of microwave observations with Juno’s Microwave Radiometer (Janssen et al. (2017)) and ground-based VLA data (de Pater et al. (2016)) would help determine the depth of the plume outbreak in late 2016, thereby constraining the extent of vertical wind shear and changes in the volatile density in the deeper atmosphere. Recently, ALMA maps of Jupiter show evidence of a plume at the SEB at multiple wavelength, indeed a sign of dredged up material.

To date, only the Galileo probe has directly measured vertical wind shear on any giant planet, when it descended into a Jupiter 5- μm hot spot located just North of the equator (Atkinson et al., 1998; Young, 2003). However, since the geostrophic balance breaks down near the equator, the thermal wind equation can not be applied at this hot spot. I worked with Philip J. Marcus to derive a new thermal wind equation applicable at the equator which was used to re-analyze the Galileo probe findings (Marcus et al. (2019), Appendix A). This new equation has wide spread applications in planetary science.

The equatorial region of Neptune is one example of the power of this new equatorial thermal wind equation. I observed Neptune with the Keck NIRC2 instrument in the near-infrared (NIR) H- and Kp-band filters at two epochs from 2013 to 2014 (Chapter 3). The NIR detects reflected sunlight bouncing off cloud tops and hazes in the upper atmosphere. I tracked the motions of hundreds of bright cloud features, deriving a zonal wind profile for both filters and epochs. This approach is different than the Jupiter method described in Chapter 2, as global correlations are impossible on Neptune due to worse resolution and lack of discernible features other than the few bright clouds. The extracted velocities are highly dispersed, meaning clouds at similar latitudes can move at dramatically different speeds. Similar dispersion was seen in *Voyager* results (Limaye and Sromovsky, 1991), suggesting Neptune’s clouds are more turbulent and not completely passive tracers of the background dynamics. However, I found that the average equatorial velocity was about 100 m/s slower in the H-band profile than the Kp-band profile on both epochs. This difference persisted even when the profiles were generated by averaging over low-error, long-monitored tracked clouds. Since the Kp-band is more sensitive to methane absorption, it probes higher in the atmosphere than the H-band, meaning the extracted zonal wind profiles are at two different altitudes. Fitzpatrick et al. (2014) found similar velocity differences between filters, but could not rule out temporal variability as a cause. My images were taken in both filters on the same night, meaning I could confirm velocity differences with depth, i.e. vertical wind shear, at Neptune’s equator.

I then used the new equatorial thermal wind equation to reconcile the observed vertical

wind shear with Neptune’s methane and temperature profiles. At pressures deeper than 1 bar, methane must be enriched at the equator relative to the mid-latitudes to match the observed Voyager/IRIS temperatures (Fletcher et al., 2014). This may be evidence of stacked circulation, Hadley-like, cells within Neptune. Below 1 bar, methane-rich air rises at the equator (forming deep H-band clouds); above 1 bar, methane dry-air sinks (where only a quiescent dark haze is seen in the Kp-band). This circulation disagrees with that presented in de Pater et al. (2014), who favor a single cell, vertically extended from the stratosphere down to 40 bar, with dry air sinking at the equator. Its likely that our simplistic assumptions regarding Neptune’s latitudinal structure and zonal wind profile are incorrect - in Chapters 4 and 5, I show maps of Neptune with distinct latitudinal variations in the brightness temperature. This banding structure is prominent near the equator, challenging the notion that the methane abundances and circulation pattern are uniform there.

Like Jupiter’s plumes and hot spots, Neptune’s dark spots are a window into the deeper atmosphere that is normally obscured at visible and near-infrared wavelengths. Two new dark spots have been recently spotted with HST, dubbed SDS-2015 and NDS-2018, for ‘Southern Dark Spot discovered in 2015’ and ‘Northern Dark Spot discovered in 2018’ (Wong et al., 2018; Simon et al., 2019). Both these spots and the *Voyager* dark spots move eastward relative to the background zonal wind profile, just like the H-band equatorial profile is eastward relative to the Kp-band profile. Moreover, dark spots are believed to originate deep in the atmosphere (similar to upwelling convective plumes on Jupiter), meaning dark spots may be a reliable tracer of the deeper winds and therefore the deep temperature and density structure via the thermal wind equation. Upcoming programs to look at NDS-2018 with HST, Gemini/Alopeke, Keck/OSIRIS, and ALMA have been proposed. NDS-2018 is massive, nearly the size of the Great Dark Spot, making it a prime target for coordinated ground-based imaging in both the radio and visible. If successful, this multi-wavelength campaign will map out the vertical structure of this dark spot and Neptune’s surrounding atmosphere in unprecedented detail.

6.2 Neptune in the Radio

Radio wavelengths probe pressures deeper than the methane clouds and hazes prominent in the visible and near-infrared. As a result, millimeter and centimeter continuum observations are sensitive to the deep abundances of Neptune’s trace gases: H_2S , NH_3 , and CH_4 . Knowing their quantities is crucial, as they reveal the formation environment of Neptune within the early outer Solar System. Moreover, abundance variations across Neptune’s disk are related to circulation patterns, indicating how material and energy are transported and distributed upward from the interior. This in turn relates to the thermal formation and evolution of the planet. I used the Atacama Large Millimeter/Submillimeter Array (ALMA) and expanded Very Large Array (VLA) to observe Neptune in the millimeter and centimeter (Chapters 4 and 5). Prior radio observations saw brightness variations across Neptune’s disk (Butler et al., 2012; Luszcz-Cook et al., 2013; de Pater et al., 2014). However, specific abun-

dance profiles could not be extracted (apart from at Neptune’s bright south pole) due to the comparatively poor sensitivity and lack of wavelength coverage. Our radio maps are the first to achieve the sensitivity, resolution, and wavelength coverage required to simultaneously extract the abundance profiles of H_2S , CH_4 , and NH_3 across Neptune’s disk.

I use MCMC retrievals coupled to the radiative transfer code Radio-BEAR to model Neptune’s brightness temperature in the radio. Neptune’s disk-average temperatures from 1 mm to 10 cm are consistent with both dry and wet adiabats with $30\times$ enhancements in the deep H_2S , CH_4 and H_2O abundances relative to their protosolar values, with deep NH_3 equalling its protosolar value. I generate uniform 2D model disks (the ‘nominal’ model) of Neptune using this disk-average profile.

In both the ALMA and VLA maps, I identified seven distinct latitudinal bands with discrete transitions in the brightness temperature. Residual maps are formed by subtracting the nominal model disk. Regions with negative residual temperatures are cold and enriched in trace species, while positive residuals are warm and depleted. The most prominent enhancements are from $32^\circ - 12^\circ\text{S}$, where H_2S must either be enriched to $30 - 60\times$ protosolar and/or supersaturated in order to produce the observed brightness temperatures. The CH_4 enhancements up to $60\times$ protosolar (or 2.88% mixing ratio) are consistent with the observations, although the spread of retrieved values for CH_4 is large. Supersaturated H_2S and enriched CH_4 are also consistent with a narrow dark band from $2^\circ - 12^\circ\text{N}$. At Neptune’s bright south polar cap (poleward of 66°S), the best fitting model has a depleted deep atmospheric abundance of H_2S , down to only 1.5 times the protosolar value - simultaneously the CH_4 abundance is depleted to 0.55%. This is consistent with findings within de Pater et al. (2014) and Luszcz-Cook et al. (2013).

The observed pattern of enhancement (dark temperatures) and depletion (bright temperatures) of condensable species is consistent with a global circulation structure where enriched air rises at the mid-latitudes ($32^\circ - 12^\circ\text{S}$) and north of the equator ($2^\circ - 20^\circ\text{N}$), and dry air descends at the poles ($90^\circ - 66^\circ\text{S}$) and just south of the equator ($12^\circ\text{S} - 2^\circ\text{N}$). I showed that this distribution aligns with regions of cloud formation - more bright clouds have been seen and tracked at latitudes corresponding to dark brightness temperatures in the radio. The equator in particular is more complex than accounted for in previous circulation models. The detection of a dark band north of the equator in the radio maps is compatible with the conclusions reached in my zonal wind analysis.

While the general makeup of Neptune has been quantified in the 30 years since *Voyager*, some basic elements like phosphorous in the form of phosphine (PH_3) have not been found. Despite not being detected in either ice giant, PH_3 is believed to be an important source of microwave opacity. PH_3 is a disequilibrium species in the gas giants. In the deep atmosphere, PH_3 should oxidize to form P_4O_6 and dissolve in water (Fegley and Prinn, 1986). In the upper atmosphere, PH_3 is photolyzed and subsequent photochemical reactions may form P_4 or complex polymers and compounds (Fletcher et al., 2009). Thus, phosphine must be uplifted rapidly from deep in the atmosphere to exist, making it useful as a passive tracer for both vertical and horizontal motions. Its use as a dynamic proxy would let us test our hypothesized circulation schematic. ALMA has the required sensitivity and bandpass sta-

bility needed to detect the broad PH_3 (1-0) rotation line from 245 – 275 GHz, allowing us to constrain the phosphorous abundance in ice giant interiors for the first time.

The impending launch of the James Webb Space Telescope (JWST) will mark a new era in planetary science. Spectroscopic measurements from JWST will characterize exoplanetary atmospheres in unprecedented detail. Bridging our understanding of these objects starts with the techniques and analysis developed to study the bodies within our own Solar System.

Appendix A

A Derivation of the Equatorial Thermal Wind Equation

In this section, I present a derivation of the new Equatorial Thermal Wind Equation (EQTWE)¹.

The derivation of the EQTWE begins with Euler's equation in spherical coordinates, rotating around the z -axis with angular velocity Ω_0 . The first half of this derivation follows the derivation of the usual thermal wind equation (TWE) which we briefly remind the reader of below. We feel it is important to include this reminder as it outlines the assumptions and fractional errors that go into the EQTWE. Taking the curl of Euler's equation gives the vorticity $\boldsymbol{\omega}$ equation. Upon taking the dot product of the vorticity equation with $\hat{\phi}$, we obtain the following equation (which required no assumptions to be made):

$$\begin{aligned}
 \frac{\partial \omega_\phi}{\partial t} &+ (v \cdot \nabla) \omega_\phi + v_\phi (\omega_r - \omega_\theta \tan \theta) / r \\
 &- (\boldsymbol{\omega} \cdot \nabla) v_\phi - \omega_\phi (v_r - v_\theta \tan \theta) / r \\
 &+ (\nabla \cdot v) \omega_\phi \\
 &= \hat{\phi} \cdot \frac{\nabla \rho \times \nabla P}{\rho^2} + f_0 \frac{\partial v_\phi}{\partial z},
 \end{aligned} \tag{A.1}$$

At this point, two assumptions are made. First, hydrostatic equilibrium $\nabla P \simeq -g\rho\hat{r}$, so that $\nabla \rho \times \nabla p$ could be replaced with $g\rho\hat{r} \times \nabla \rho$, and so that the azimuthal component of $\nabla \rho \times \nabla p$ could be approximated as $-\frac{g\rho}{r} \frac{\partial \rho}{\partial \theta}$. The exact form of this approximation, including its fractional errors, is below:

¹Presented here is an adaption of the derivation of the Equatorial Thermal Wind Equation, previously published in *Icarus* (Marcus et al., 2019). This has been produced with permission from all co-authors.

$$\hat{\phi} \cdot (\nabla \rho \times \nabla P) = -\frac{g\rho}{r} \frac{\partial \rho}{\partial \theta} \bigg|_P \left(1 - \frac{f_0^2 r \cos^2 \theta}{4g} \right) \left[1 + O \left(\frac{DV_\phi^2}{gL_\phi^2}, \frac{DV_\theta^2}{gL_\theta^2}, \frac{DV_\phi V_\theta}{gL_\phi L_\theta} \right) \right], \quad (\text{A.2})$$

For the giant gas planets, these fractional error terms are small because the vertical scale height D is much smaller than the extent of the horizontal flow. Therefore, we shall drop these fractional errors from the remainder of a derivation below.

The second assumption is that changes in the flow are slow in time so that $\partial/\partial t \simeq 0$. It can be shown that using just these two assumptions, we obtain the following:

$$\begin{aligned} & -f_0 \frac{\cos \theta}{r} \frac{\partial v_\phi}{\partial \theta} + (v \cdot \nabla) \omega_\phi + v_\phi (\omega_r - \omega_\theta \tan \theta)/r \\ & - \frac{\omega_\phi}{r \cos \theta} \frac{\partial v_\phi}{\partial \phi} - \omega_\phi (v_r - v_\theta \tan \theta)/r \\ & - \frac{v_\phi \tan \theta}{r} \frac{\partial v_\phi}{\partial r} - \frac{1}{r \cos \theta} \frac{\partial v_\phi}{\partial r} \frac{\partial v_\theta}{\partial \phi} \\ & - \frac{1}{r^2} \frac{\partial v_\phi}{\partial \theta} \left[v_\phi - \frac{1}{\cos \theta} \frac{\partial v_r}{\partial \phi} \right] \\ & + (\nabla \cdot v) \omega_\phi \\ & = -\frac{g'}{r\rho} \frac{\partial \rho}{\partial \theta} \bigg|_P + f_0 \sin \theta \frac{\partial v_\phi}{\partial r}. \end{aligned} \quad (\text{A.3})$$

Here, we define the reduced gravity $g' \equiv g[1 - (f_0^2 r \cos \theta)/4g]$. For slowly rotating planets² like Neptune, Jupiter, and Earth, the gravity and reduced gravity are the same within 10%.

The textbook TWE can be derived from the equation above by assuming the ideal gas law and replacing $-\frac{g'}{r\rho} \frac{\partial \rho}{\partial \theta} \bigg|_P$ with $\frac{g}{rT} \frac{\partial T}{\partial \theta} \bigg|_P$, and showing that there is a dominant balance between the two terms on the right-hand side of equation A.3.

²Jupiter is generally considered within the planetary community to be a “fast” rotating planet, but in the geophysical community a slow rotator is one in which the gravity is much greater than the centrifugal acceleration so the geopotential surfaces are nearly spherical, or where the reduced gravity g' is approximately equal to the gravity g .

The second-half of the EQTWE derivation makes use of carrying out Taylor series expansions of functions that are symmetric or anti-symmetric about the equator. We assume that T, ρ, v_ϕ , and v_r are symmetric about the equator and that v_θ is anti-symmetric. Such stringent requirements are too unrealistic and not necessary for the proof here, but we present these assumptions here for ease of understanding. For symmetric functions, such as v_ϕ (which in this section is assumed to be mirror-symmetric), we write the series in even powers of θ , with $v_\phi = [v_\phi] + [\partial^2 v_\phi / \partial \theta^2] \theta^2 / 2 + \dots$, where the quantities in the square brackets are evaluated at $\theta = 0$. For an anti-symmetric function such as v_θ , we write the series in odd powers of θ , with $v_\theta = [\partial v_\theta / \partial \theta] \theta + [\partial^3 v_\theta / \partial \theta^3] \theta^3 / 6 + \dots$, where the quantities in the square brackets are evaluated at $\theta = 0$. This means that we Taylor expand $\partial v_\phi / \partial \theta$ at the equator in an odd series as $\partial v_\phi / \partial \theta = [\partial^2 v_\phi / \partial \theta^2] \theta + O(\theta^3)$. Similarly, we expand $\partial v_\theta / \partial \theta$ at the equator in an even series as $\partial v_\theta / \partial \theta = [\partial v_\theta / \partial \theta] + O(\theta^2)$.

The Taylor series expansions in equation A.3 make use of expansions of the vorticity components and the divergence. Expressed as a Taylor series in powers of θ , note that ω_r and ω_ϕ is an odd function of θ , and ω_θ is an even function of θ , with:

$$\omega_r = \frac{1}{r} \left[-\frac{\partial^2 v_\phi}{\partial \theta^2} + v_\phi + \frac{\partial^2 v_\theta}{\partial \phi \partial \theta} \right] \theta + O(\theta^3) \quad (\text{A.4})$$

$$\omega_\theta = -\frac{1}{r} \left[\frac{\partial v_r}{\partial \phi} - v_\phi - r \frac{\partial v_\phi}{\partial r} \right] + O(\theta^2) \quad (\text{A.5})$$

$$\omega_\phi = \frac{1}{r} \left[-r \frac{\partial^2 v_\theta}{\partial r \partial \theta} - \frac{\partial v_\theta}{\partial \theta} + \frac{\partial^2 v_r}{\partial \theta^2} \right] \theta + O(\theta^3) \quad (\text{A.6})$$

The divergence of the velocity is an even power series:

$$\nabla \cdot v = \frac{1}{r} \left[r \frac{\partial v_r}{\partial r} + 2v_r + \frac{\partial v_\theta}{\partial \theta} + \frac{\partial v_\phi}{\partial \phi} \right] + O(\theta^2) \quad (\text{A.7})$$

Below are the Taylor series expansions of each of the terms that appear in eq. A.3, with a label assigned to each term so that we can refer to it when estimating its order of magnitude. The notation that $O(\theta^3)$ means ‘‘terms of order θ^3 and higher’’, and note that all of the quantities and derivatives that have horizontal braces beneath them or in large

square brackets should be evaluated at the equator.

$$f_0 \frac{\cos \theta}{r} \frac{\partial v_\phi}{\partial \theta} = \underbrace{\left[\frac{f_0}{r} \frac{\partial^2 v_\phi}{\partial \theta^2} \right]}_A \theta + O(\theta^3) \quad (\text{A.8})$$

$$(v \cdot \nabla) \omega_\phi = \underbrace{\left\{ v_r \left[-\frac{\partial^3 v_\theta}{\partial r^2 \partial \theta} - \frac{1}{r} \frac{\partial^2 v_\theta}{\partial r \partial \theta} + \frac{1}{r^2} \frac{\partial v_\theta}{\partial \theta} + \frac{1}{r} \frac{\partial^3 v_r}{\partial r \partial \theta^2} - \frac{1}{r^2} \frac{\partial^2 v_r}{\partial \theta^2} \right]}_B \quad (\text{A.9})$$

$$+ \underbrace{\frac{1}{r^2} \frac{\partial v_\theta}{\partial \theta} \left[-r \frac{\partial^2 v_\theta}{\partial r \partial \theta} - \frac{\partial v_\theta}{\partial \theta} + \frac{\partial^2 v_r}{\partial \theta^2} \right]}_C \quad (\text{A.10})$$

$$+ \underbrace{\frac{v_\phi}{r^2} \left[-r \frac{\partial^3 v_\theta}{\partial r \partial \theta \partial \phi} - \frac{\partial^2 v_\theta}{\partial \theta \partial \phi} + \frac{\partial^3 v_r}{\partial \theta^2 \partial \phi} \right]}_D \theta + O(\theta^3) \quad (\text{A.11})$$

$$(v_\phi \omega_r)/r = \underbrace{\frac{v_\phi}{r^2} \left[-\frac{\partial^2 v_\phi}{\partial \theta^2} + v_\phi + \frac{\partial^2 v_\theta}{\partial \phi \partial \theta} \right]}_E \theta + O(\theta^3) \quad (\text{A.12})$$

$$(v_\phi \omega_\theta \tan \theta)/r = \underbrace{-\frac{v_\phi}{r^2} \left[\frac{\partial v_r}{\partial \phi} - v_\phi - r \frac{\partial v_\phi}{\partial r} \right]}_F \theta + O(\theta^3) \quad (\text{A.13})$$

$$\frac{\omega_\phi}{r \cos \theta} \frac{\partial v_\phi}{\partial \phi} = \underbrace{\frac{1}{r^2} \frac{\partial v_\phi}{\partial \phi} \left[-r \frac{\partial^2 v_\theta}{\partial r \partial \theta} - \frac{\partial v_\theta}{\partial \theta} + \frac{\partial^2 v_r}{\partial \theta^2} \right]}_G \theta + O(\theta^3) \quad (\text{A.14})$$

$$(\omega_\phi v_r)/r = \underbrace{\frac{v_r}{r^2} \left[-r \frac{\partial^2 v_\theta}{\partial r \partial \theta} - \frac{\partial v_\theta}{\partial \theta} + \frac{\partial^2 v_r}{\partial \theta^2} \right]}_H \theta + O(\theta^3) \quad (\text{A.15})$$

$$(\omega_\phi v_\theta \tan \theta)/r = \underbrace{0}_I + O(\theta^3) \quad (\text{A.16})$$

Note that the Taylor series for the above expression starts with the θ^3 term.

$$\frac{v_\phi \tan \theta}{r} \frac{\partial v_\phi}{\partial r} = \underbrace{\left[\frac{v_\phi}{r} \frac{\partial v_\phi}{\partial r} \right]}_J \theta + O(\theta^3) \quad (\text{A.17})$$

$$\frac{1}{r \cos \theta} \frac{\partial v_\phi}{\partial r} \frac{\partial v_\theta}{\partial \phi} = \underbrace{\left[\frac{1}{r} \frac{\partial v_\phi}{\partial r} \frac{\partial^2 v_\theta}{\partial \phi \partial \theta} \right]}_K \theta + O(\theta^3) \quad (\text{A.18})$$

$$\frac{1}{r^2} \frac{\partial v_\phi}{\partial \theta} v_\phi = \underbrace{\left[\frac{1}{r^2} \frac{\partial^2 v_\phi}{\partial \theta^2} v_\phi \right]}_L \theta + O(\theta^3) \quad (\text{A.19})$$

$$\frac{1}{r^2} \frac{\partial v_\phi}{\partial \theta} \frac{1}{\cos \theta} \frac{\partial v_r}{\partial \phi} = \underbrace{\left[\frac{1}{r^2} \frac{\partial^2 v_\phi}{\partial \theta^2} \frac{\partial v_r}{\partial \phi} \right]}_M \theta + O(\theta^3) \quad (\text{A.20})$$

$$\omega_\phi (\nabla \cdot v) = \frac{1}{r^2} \underbrace{\left[r \frac{\partial v_r}{\partial r} + 2v_r + \frac{\partial v_\theta}{\partial \theta} + \frac{\partial v_\phi}{\partial \phi} \right] \left[-r \frac{\partial^2 v_\theta}{\partial r \partial \theta} - \frac{\partial v_\theta}{\partial \theta} + \frac{\partial^2 v_r}{\partial \theta^2} \right]}_N \theta + O(\theta^3) \quad (\text{A.21})$$

$$\frac{g'}{rT} \frac{\partial T}{\partial \theta} \Big|_P = \left[\frac{g}{rT} \frac{\partial^2 T}{\partial \theta^2} \Big|_P \right] \theta + O(\theta^3) \quad (\text{A.22})$$

$$f_0 \sin \theta \frac{\partial v_\phi}{\partial r} = \underbrace{\left[f_0 \frac{\partial v_\phi}{\partial r} \right]}_P \theta + O(\theta^3) \quad (\text{A.23})$$

We estimate the magnitude of all of the terms in expressions A.8 - A.23 in terms of the characteristic lengths in the east-west, north-south, and vertical (i.e. radial) directions: L_ϕ , L_θ , and D ; and the characteristic velocities of the east-west and vertical components of the time-averaged velocity at the equator: V_ϕ and V_r . We define V_θ such that the characteristic value of the time-averaged $\partial v_\theta / \partial \theta$ at the equator is $r_0 V_\theta / L_\theta$, where r_0 is the characteristic value of r in the atmosphere where we are carrying out this analysis.

From these definitions, it can be shown that terms A - N are small compared to the P term, and the effect of terms A - N in eq. A.3 can be written as fractional error terms, so that eq. A.3 becomes:

$$\frac{g'}{rT} \frac{\partial^2 T}{\partial \theta^2} \Big|_P = -f_0 \frac{\partial v_\phi}{\partial r} \left\{ 1 + O \left[\overline{Ro} \left(\frac{r_0}{L_\theta} \frac{V_\theta^2}{V_\phi^2}, \frac{r_0}{L_\phi} \frac{V_\theta}{V_\phi}, \frac{r_0}{L_\phi}, \frac{D}{L_\theta} \right), \frac{DV_\phi^2}{gL_\phi^2}, \frac{DV_\theta^2}{gL_\theta^2}, \frac{DV_\phi V_\theta}{gL_\phi L_\theta}, \frac{Dr_0}{L_\theta^2}, \overline{Ro} \right] \right\}. \quad (\text{A.24})$$

If the planet is not rapidly rotating, then g' can be replaced with g .

This derivation required the modest approximations: $D \leq O(r_0)$, $D \leq O(L_\theta)$, $D \leq O(L_\phi)$, and that the flow is sufficiently steady in time that the characteristic value of $\partial \omega_\phi / \partial t$ at the equator is less than or equal to the characteristic value of $v \cdot \nabla \omega_\phi$ at the equator.

To compare our fractional errors of the EQTWE to the reported fractional errors in the textbook TWE, we can take a less cautious approach to estimating error size by assuming (as many other authors have) that the horizontal divergence of the velocity is approximately zero. Then at the equator, we would have $V_\phi/L_\phi \simeq V_\theta/L_\theta$. Using this relationship, the fractional errors in the EQTWE are:

$$O \left[\overline{Ro} \left(\frac{r_0 L_\theta}{L_\phi^2}, \frac{r_0}{L_\phi}, \frac{D}{L_\theta} \right), \frac{DV_\phi^2}{gL_\phi^2}, \frac{Dr_0}{L_\theta^2}, \widetilde{Ro} \right]. \quad (\text{A.25})$$

If we are even less cautious and adopt the traditional assumption that $V_\phi = V_\theta$, then the fractional errors in the EQTWE are:

$$O \left[\overline{Ro} \frac{r_0}{L_\phi}, \frac{DV_\phi^2}{gL_\phi^2}, \frac{Dr_0}{L_\phi^2}, \widetilde{Ro} \right]. \quad (\text{A.26})$$

Thus for a mirror-symmetric flow, the EQTWE is:

$$-\frac{g'}{rT} \frac{\partial^2 T}{\partial \theta^2} \Big|_P = f_0 \frac{\partial v_\phi}{\partial r} \quad (\text{A.27})$$

with fractional errors in eq. A.24, eq. A.25, or eq. A.26.

Bibliography

- Adel, A., Slipher, V. M., 1934a. On the Identification of the Methane Bands in the Solar Spectra of the Major Planets. *Phys. Rev.* 46 (3), 240–241.
- Adel, A., Slipher, V. M., 1934b. The Constitution of the Atmospheres of the Giant Planets. *Phys. Rev.* 46 (10), 902–906.
- Andrews, D. G., Holton, J. R., Leovy, C. B., 1987. *Middle atmosphere dynamics*. Academic press.
- Arregi, J., Rojas, J. F., Sánchez-Lavega, A., Morgado, A., 2006. Phase dispersion relation of the 5-micron hot spot wave from a long-term study of Jupiter in the visible. *Journal of Geophysical Research (Planets)* 111, E09010.
- Asay-Davis, X. S., Marcus, P. S., Wong, M. H., de Pater, I., 2011. Changes in Jupiter’s zonal velocity between 1979 and 2008. *Icarus* 211 (2), 1215–1232.
- Asplund, M., Grevesse, N., Sauval, A. J., Scott, P., 2009. The Chemical Composition of the Sun. *Annual Review of Astron. and Astrophys.* 47, 481–522.
- Atkinson, D. H., Pollack, J. B., Seiff, A., 1998. The Galileo probe doppler wind experiment: Measurement of the deep zonal winds on Jupiter. *Journal of Geophysical Research: Planets* 103 (E10), 22911–22928.
- Baines, K. H., Mickelson, M. E., Larson, L. E., Ferguson, D. W., 1995. The Abundances of Methane and Ortho/Para Hydrogen on Uranus and Neptune: Implications of New Laboratory 4-0 H₂ Quadrupole Line Parameters. *Icarus* 114 (2), 328–340.
- Barrado-Izagirre, N., Pérez-Hoyos, S., García-Melendo, E., Sánchez-Lavega, A., 2009. Evolution of the cloud field and wind structure of Jupiter’s highest speed jet during a huge disturbance. *Astronomy & Astrophysics* 507 (1), 513–522.
- Barrado-Izagirre, N., Rojas, J. F., Hueso, R., Sánchez-Lavega, A., Colas, F., Dauvergne, J. L., Peach, D., Team, IOPW, 2013. Jupiter’s zonal winds and their variability studied with small-size telescopes. *Astronomy & Astrophysics* 554, A74.

- Bjoraker, G. L., Wong, M. H., de Pater, I., Ádámkóvics, M., 2015. Jupiter's Deep Cloud Structure Revealed Using Keck Observations of Spectrally Resolved Line Shapes. *The Astrophysical Journal* 810, 122.
- Bolton, S. J., Adriani, A., Adumitroaie, V., Allison, M., Anderson, J., Atreya, S., Bloxham, J., Brown, S., Connerney, J. E. P., DeJong, E., Folkner, W., Gautier, D., Grassi, D., Gulkis, S., Guillot, T., Hansen, C., Hubbard, W. B., Iess, L., Ingersoll, A., Janssen, M., Jorgensen, J., Kaspi, Y., Levin, S. M., Li, C., Lunine, J., Miguel, Y., Mura, A., Orton, G., Owen, T., Ravine, M., Smith, E., Steffes, P., Stone, E., Stevenson, D., Thorne, R., Waite, J., Durante, D., Ebert, R. W., Greathouse, T. K., Hue, V., Parisi, M., Szalay, J. R., Wilson, R., 2017. Jupiter's interior and deep atmosphere: The initial pole-to-pole passes with the Juno spacecraft. *Science* 356 (6340), 821–825.
- Brogan, C. L., Hunter, T. R., Fomalont, E. B., 2014. Advanced Gain Calibration Techniques in Radio Interferometry, in the Proceedings of the 2014 Synthesis Imaging Workshop held in Socorro, NM on May 13-20, 2014.
- Butler, B. J., Hofstadter, M., Gurwell, M., Orton, G., Norwood, J., 2012. The Deep Atmosphere of Neptune From EVLA Observations. In: AAS/Division for Planetary Sciences Meeting Abstracts. Vol. 44 of AAS/Division for Planetary Sciences Meeting Abstracts. p. 504.06.
- Cheng, A. F., Simon-Miller, A. A., Weaver, H. A., Baines, K. H., Orton, G. S., Yanamandra-Fisher, P. A., Mousis, O., Pantin, E., Vanzi, L., Fletcher, L. N., Spencer, J. R., Stern, S. A., Clarke, J. T., Mutchler, M. J., Noll, K. S., 2008. Changing Characteristics of Jupiter's Little Red Spot. *Astrophysics Journal* 135, 2446–2452.
- Choi, D. S., Showman, A. P., Vasavada, A. R., Simon-Miller, A. A., 2013. Meteorology of Jupiter's equatorial hot spots and plumes from Cassini. *Icarus* 223 (2), 832–843.
- Connerney, J. E. P., Acuna, M. H., Ness, N. F., 1987. The magnetic field of Uranus. *Journal of Geophysical Research* 92, 15329–15336.
- Connerney, J. E. P., Acuna, M. H., Ness, N. F., 1991. The magnetic field of Neptune. *Journal of Geophysical Research* 96, 19.
- Conrath, B., Gierasch, P., Ustinov, E. A., 1998. Thermal Structure and Para Hydrogen Fraction on the Outer Planets from Voyager IRIS Measurements. *Icarus* 135, 501–517.
- Conrath, B. J., Flasar, F. M., Gierasch, P. J., 1991. Thermal structure and dynamics of Neptune's atmosphere from Voyager measurements. *Journal of Geophysical Research: Space Physics* 96 (S01), 18931–18939.
- Cruikshank, D. P., 1985. Variability of Neptune. *Icarus* 64 (1), 107–111.

- de Pater, I., Fletcher, L. N., Luszcz-Cook, S., DeBoer, D., Butler, B., Hammel, H. B., Sitko, M. L., Orton, G., Marcus, P. S., 2014. Neptune's global circulation deduced from multi-wavelength observations. *Icarus* 237, 211–238.
- de Pater, I., Gibbard, S. G., Hammel, H., 2006. Evolution of the dusty rings of Uranus. *Icarus* 180 (1), 186–200.
- de Pater, I., Lissauer, J. J., 2010. *Planetary Sciences: Second Edition*. Cambridge University Press.
- de Pater, I., Massie, S. T., 1985. Models of the millimeter-centimeter spectra of the giant planets. *Icarus* 62 (1), 143–171.
- de Pater, I., Mitchell, D. L., 1993. Radio observations of the planets: The importance of laboratory measurements. *Journal of Geophysical Research: Planets* 98 (E3), 5471–5490.
- de Pater, I., Richmond, M., 1989. Neptune's microwave spectrum from 1 mm to 20 cm. *Icarus* 80 (1), 1–13.
- de Pater, I., Romani, P. N., Atreya, S. K., 1991. Possible microwave absorption by H₂S gas in Uranus' and Neptune's atmospheres. *Icarus* 91 (2), 220 – 233.
- de Pater, I., Sault, R., Wong, M. H., Fletcher, L. N., DeBoer, D., Butler, B., 2019. Jupiter's ammonia distribution derived from VLA maps at 3–37 GHz. *Icarus* 322, 168 – 191.
- de Pater, I., Sault, R. J., Butler, B., DeBoer, D., Wong, M. H., 2016. Peering through Jupiter's clouds with radio spectral imaging. *Science* 352 (6290), 1198–1201.
- Dyudina, U. A., Ingersoll, A. P., Ewald, S. P., Vasavada, A. R., West, R. A., Del Genio, A. D., Barbara, J. M., Porco, C. C., Achterberg, R. K., Flasar, F. M., Simon-Miller, A. A., Fletcher, L. N., 2008. Dynamics of Saturn's South Polar Vortex. *Science* 319 (5871), 1801–1801.
- Elias, J. H., Frogel, J. A., Matthews, K., Neugebauer, G., 1982. Infrared standard stars. *Astronomical Journal* 87, 1029–1034.
- Fegley, Jr., B., Prinn, R. G., 1986. Chemical models of the deep atmosphere of Uranus. *The Astrophysical Journal* 307, 852–865.
- Fincham, A., Delerce, G., 2000. Advanced optimization of correlation imaging velocimetry algorithms. *Experiments in Fluids* 29 (1), S013–S022.
- Fincham, A. M., Spedding, G. R., 1997. Low cost, high resolution DPIV for measurement of turbulent fluid flow. *Experiments in Fluids* 23 (6), 449–462.

- Fitzpatrick, P. J., de Pater, I., Luszcz-Cook, S., Wong, M. H., Hammel, H. B., 2014. Dispersion in Neptune's zonal wind velocities from NIR Keck AO observations in July 2009. *Astrophysics and Space Science* 350 (1), 65–88.
- Flasar, F. M., Kunde, V. G., Achterberg, R. K., Conrath, B. J., Simon-Miller, A. A., Nixon, C. A., Gierasch, P. J., Romani, P. N., Bézard, B., Irwin, P., Bjoraker, G. L., Brasunas, J. C., Jennings, D. E., Pearl, J. C., Smith, M. D., Orton, G. S., Spilker, L. J., Carlson, R., Calcutt, S. B., Read, P. L., Taylor, F. W., Parrish, P., Barucci, A., Courtin, R., Coustenis, A., Gautier, D., Lellouch, E., Marten, A., Prange, R., Biraud, Y., Fouchet, T., Ferrari, C., Owen, T. C., Abbas, M. M., Samuelson, R. E., Raulin, F., Ade, P., Cesarsky, C. J., Grossman, K. U., Coradini, A., 2004. An intense stratospheric jet on Jupiter. *Nature* 427 (6970), 132–135.
- Fletcher, L., Orton, G., Teanby, N., Irwin, P., 2009. Phosphine on jupiter and saturn from cassini/cirs. *Icarus* 202 (2), 543 – 564.
- Fletcher, L. N., Achterberg, R. K., Greathouse, T. K., Orton, G. S., Conrath, B. J., Simon-Miller, A. A., Teanby, N., Guerlet, S., Irwin, P. G., Flasar, F., 2010. Seasonal change on Saturn from Cassini/CIRS observations, 2004-2009. *Icarus* 208 (1), 337–352.
- Fletcher, L. N., Barnes, K., Momary, T. W., Showman, A., Irwin, P., Orton, G. S., Roos-Serote, M., Merlet, C., 2011. Saturn's tropospheric composition and clouds from Cassini/VIMS 4.6?5.1 μm nightside spectroscopy. *Icarus* 214, 510–533.
- Fletcher, L. N., de Pater, I., Orton, G. S., Hammel, H. B., Sitko, M. L., Irwin, P. G., 2014. Neptune at summer solstice: Zonal mean temperatures from ground-based observations, 2003–2007. *Icarus* 231, 146–167.
- Fletcher, L. N., Greathouse, T. K., Orton, G. S., Sinclair, J. A., Giles, R. S., Irwin, P. G. J., Encrenaz, T., 2016. Mid-infrared mapping of Jupiter's temperatures, aerosol opacity and chemical distributions with IRTF/TEXES. *Icarus* 278, 128–161.
- Fletcher, L. N., Irwin, P. G. J., Orton, G. S., Teanby, N. A., Achterberg, R. K., Bjoraker, G. L., Read, P. L., Simon-Miller, A. A., Howett, C., de Kok, R., Bowles, N., Calcutt, S. B., Hesman, B., Flasar, F. M., 2008. Temperature and Composition of Saturn's Polar Hot Spots and Hexagon. *Science* 319 (5859), 79–81.
- Foreman-Mackey, D., Conley, A., Meierjürgen Farr, W., Hogg, D. W., Lang, D., Marshall, P., Price-Whelan, A., Sanders, J., Zuntz, J., 2013. emcee: The MCMC Hammer. *Astrophysics Source Code Library*.
- Fressin, F., Torres, G., Charbonneau, D., Bryson, S. T., Christiansen, J., Dressing, C. D., Jenkins, J. M., Walkowicz, L. M., Batalha, N. M., 2013. The False Positive Rate of Kepler and the Occurrence of Planets. *The Astrophysical Journal* 766, 81.

- Fry, P., Sromovsky, L., 2004. Keck 2 AO Observations of Neptune in 2003 and 2004. *Bull. Am. Astron. Soc.*, 1103.
- Fry, P. M., Sromovsky, L. M., de Pater, I., Hammel, H. B., Rages, K. A., 2012. Detection and tracking of subtle cloud features on Uranus. *The Astronomical Journal* 143 (6), 150–161.
- García-Melendo, E., Pérez-Hoyos, S., Sánchez-Lavega, A., Hueso, R., 2011. Saturn’s zonal wind profile in 2004–2009 from Cassini ISS images and its long-term variability. *Icarus* 215 (1), 62–74.
- García-Melendo, E., Sánchez-Lavega, A., 2001. A Study of the Stability of Jovian Zonal Winds from HST Images: 1995–2000. *Icarus* 152 (2), 316–330.
- García-Melendo, E., Sánchez-Lavega, A., Gómez, J. M., Lecacheux, J., Colas, F., Miyazaki, I., Parker, D., 2000. Long-Lived Vortices and Profile Changes in the 23.7 N High-Speed Jovian Jet. *Icarus* 146, 514–524.
- Gibbard, S. G., de Pater, I., Roe, H. G., Martin, S., Macintosh, B. A., Max, C. E., 2003. The altitude of Neptune cloud features from high-spatial-resolution near-infrared spectra. *Icarus* 166 (2), 359–374.
- Gierasch, P. J., Ingersoll, A. P., Banfield, D., Ewald, S. P., Helfenstein, P., Simon-Miller, A., Vasavada, A., Breneman, H. H., Senske, D. A., Galileo Imaging Team, 2000. Observation of moist convection in Jupiter’s atmosphere. *Nature* 403, 628–630.
- Gierasch, P. J., Magalhaes, J. A., Conrath, B. J., 1986. Zonal mean properties of Jupiter’s upper troposphere from Voyager infrared observations. *Icarus* 67, 456–483.
- Goodman, J., Weare, J., 2010. Ensemble samplers with affine invariance. *Communications in Applied Mathematics and Computational Science*, Vol. 5, No. 1, p. 65–80, 2010 5, 65–80.
- Hammel, H., 1989. Discrete cloud structure on Neptune. *Icarus* 80 (1), 14–22.
- Hammel, H. B., Baines, K. H., Bergstralh, J. T., 1989. Vertical aerosol structure of Neptune: Constraints from center-to-limb profiles. *Icarus* 80 (2), 416–438.
- Hammel, H. B., Lockwood, G. W., 1997. Atmospheric Structure of Neptune in 1994, 1995, and 1996: HST Imaging at Multiple Wavelengths. *Icarus* 129, 466–481.
- Hammel, H. B., Lockwood, G. W., 2007. Suggestive correlations between the brightness of Neptune, solar variability, and Earth’s temperature. *Geophysical Research Letters* 34 (8).
- Hammel, H. B., Sitko, M. L., Lynch, D. K., Orton, G. S., Russell, R. W., Geballe, T. R., de Pater, I., 2007. Distribution of Ethane and Methane Emission on Neptune. *The Astronomical Journal* 134, 637–641.
- Hilbert, B., 2009. WFC3 SMOV Program 11427: UVIS Channel Shutter Shading. Tech. rep.

- Hueso, R., Snchez-Lavega, A., Iurrigarro, P., Rojas, J., Perez-Hoyos, S., Mendikoa, I., Gmez-Forrellad, J., go, C., Peach, D., Colas, F., Vedovato, M., 2017. Jupiter cloud morphology and zonal winds from ground-based observations before and during juno's first perijove: Jupiter cloud morphology before juno. *Geophysical Research Letters* 44.
- Iino, T., Yamada, T., 2018. Spatially Resolved Sub-millimeter Continuum Imaging of Neptune with ALMA. *The Astronomical Journal* 155 (2), 92.
- Ingersoll, A. P., Beebe, R. F., Mitchell, J. L., Garneau, G. W., Yagi, G. M., Mller, J.-P., 1981. Interaction of eddies and mean zonal flow on Jupiter as inferred from Voyager 1 and 2 images. *Journal of Geophysical Research: Space Physics* 86 (A10), 8733–8743.
- Ingersoll, A. P., Dowling, T. E., Gierasch, P. J., Orton, G. S., Read, P. L., Sánchez-Lavega, A., Showman, A. P., Simon-Miller, A. A., Vasavada, A. R., 2004. Dynamics of Jupiter's atmosphere. pp. 105–128.
- Irwin, P., Fletcher, L., Tice, D., Owen, S., Orton, G., Teanby, N., Davis, G., 2016. Time variability of Neptune's horizontal and vertical cloud structure revealed by VLT/SINFONI and Gemini/NIFS from 2009 to 2013. *Icarus* 271, 418–437.
- Irwin, P. G., Toledo, D., Garland, R., Teanby, N. A., Fletcher, L. N., Orton, G. S., Bzard, B., 2019. Probable detection of hydrogen sulphide (H₂S) in Neptunes atmosphere. *Icarus* 321, 550–563.
- Irwin, P. G. J., Teanby, N. A., Davis, G. R., Fletcher, L. N., Orton, G. S., Tice, D., Hurley, J., Calcutt, S. B., 2011. Multispectral imaging observations of Neptune's cloud structure with Gemini-North. *Icarus* 216 (1), 141–158.
- Janssen, M., E. Oswald, J., T. Brown, S., Gulkis, S., M. Levin, S., Bolton, S., D. Allison, M., Sudhir, A., Gautier, D., Ingersoll, A., I. Lunine, J., Orton, G., C. Owen, T., G. Steffes, P., Adumitroaie, V., Bellotti, A., A. Jewell, L., Li, C., Li, L., C. Wang, C., 2017. MWR: Microwave Radiometer for the Juno Mission to Jupiter. *Space Science Reviews* 213, 139–185.
- Johnson, P. E., Morales-Jubereras, R., Simon, A., Gaulme, P., Wong, M. H., Cosentino, R. G., 2018. Longitudinal variability in jupiter's zonal winds derived from multi-wavelength hst observations. *Planetary and Space Science* 155, 2–11.
- Joiner, J., Steffes, P. G., Noll, K. S., 1992. Search for sulfur (H₂S) on Jupiter at millimeter wavelengths. *IEEE Transactions on Microwave Theory Techniques* 40, 1101–1109.
- Karalidi, T., Apai, D., Schneider, G., Hanson, J. R., Pasachoff, J. M., 2015. Aeolus: A Markov Chain Monte Carlo Code for Mapping Ultracool Atmospheres. An Application on Jupiter and Brown Dwarf HST Light Curves. *The Astrophysical Journal* 814, 65.

- Karkoschka, E., Tomasko, M. G., 2011. The haze and methane distributions on Neptune from HST/STIS spectroscopy. *Icarus* 211 (1), 780–797.
- Kellermann, K. I., Pauliny-Toth, I. I. K., 1966. Observations of the Radio Emission of Uranus, Neptune, and Other Planets at 1.9 CM. *The Astrophysical Journal* 145, 954.
- Kozhurina-Platais, V., 2014. Astrometric Correction for WFC3/UVIS Filter-Dependent Component of Distortion. Baltimore: STScI.
- Leovy, C. B., Friedson, A. J., Orton, G. S., 1991. The quasiquadrennial oscillation of Jupiter's equatorial stratosphere. *Nature* 354, 380–382.
- Levin, Z., Borucki, W. J., Toon, O. B., 1983. Lightning generation in planetary atmospheres. *Icarus* 56, 80–115.
- Lewis, J. S., 1969. The clouds of Jupiter and the $\text{NH}_3\text{-H}_2\text{O}$ and $\text{NH}_3\text{-H}_2\text{S}$ systems. *Icarus* 10, 365–378.
- Li, L., Ingersoll, A. P., Vasavada, A. R., Porco, C. C., Del Genio, A. D., Ewald, S. P., 2004. Life cycles of spots on Jupiter from Cassini images. *Icarus* 172, 9–23.
- Li, L., Ingersoll, A. P., Vasavada, A. R., Simon-Miller, A. A., Del Genio, A. D., Ewald, S. P., Porco, C. C., West, R. A., 2006. Vertical wind shear on Jupiter from Cassini images. *Journal of Geophysical Research: Planets* 111 (E4).
- Lii, P. S., Wong, M. H., de Pater, I., 2010. Temporal variation of the tropospheric cloud and haze in the jovian equatorial zone. *Icarus* 209 (2), 591–601.
- Limaye, S. S., 1986. Jupiter - New estimates of the mean zonal flow at the cloud level. *Icarus* 65, 335–352.
- Limaye, S. S., 1989. Jupiter: short-term variations of the mean zonal flow at the cloud level. NASA Special Publication 494, 311–323.
- Limaye, S. S., Revercomb, H. E., Sromovsky, L. A., Krauss, R. J., Santek, D. A., Suomi, V. E., Collins, S. A., Avis, C. C., 1982. Jovian Winds from Voyager 2. Part I: Zonal Mean Circulation. *Journal of the Atmospheric Sciences* 39 (7), 1413–1432.
- Limaye, S. S., Sromovsky, L. A., 1991. Winds of Neptune: Voyager observations of cloud motions. *Journal of Geophysical Research: Space Physics* 96 (S01).
- Lindal, G. F., 1992. The atmosphere of Neptune - an analysis of radio occultation data acquired with Voyager 2. *Astronomical Journal* 103, 967–982.
- Little, B., Anger, C. D., Ingersoll, A. P., Vasavada, A. R., Senske, D. A., Breneman, H. H., Borucki, W. J., The Galileo SSI Team, 1999. Galileo Images of Lightning on Jupiter. *Icarus* 142, 306–323.

- Liu, J., Schneider, T., 2015. Scaling of Off-Equatorial Jets in Giant Planet Atmospheres. *Journal of the Atmospheric Sciences* 72 (1), 389–408.
- Lockwood, G. W., Jerzykiewicz, M., 2006. Photometric variability of Uranus and Neptune, 1950-2004. *Icarus* 180, 442–452.
- Luszcz-Cook, S., 2012. Millimeter and near-infrared observations of Neptune’s atmospheric dynamics. Ph.D. thesis, University of California Berkeley.
- Luszcz-Cook, S., de Kleer, K., de Pater, I., Adamkovics, M., Hammel, H., 2016. Retrieving Neptune’s aerosol properties from Keck OSIRIS observations. I. Dark regions. *Icarus* 276, 52–87.
- Luszcz-Cook, S., de Pater, I., 2013. Constraining the origins of Neptune’s carbon monoxide abundance with CARMA millimeter-wave observations. *Icarus* 222 (1), 379–400.
- Luszcz-Cook, S., de Pater, I., Adamkovics, M., Hammel, H., 2010. Seeing double at Neptune’s south pole. *Icarus* 208 (2), 938–944.
- Luszcz-Cook, S., de Pater, I., Wright, M., 2013. Spatially-resolved millimeter-wavelength maps of Neptune. *Icarus* 226 (1), 437–454.
- Marcus, P. S., Tollefson, J., Wong, M. H., de Pater, I., 2019. An equatorial thermal wind equation: Applications to Jupiter. *Icarus* 324, 198–223.
- Martin, S. C., de Pater, I., Marcus, P., 2012. Neptune’s zonal winds from near-IR Keck adaptive optics imaging in August 2001. *Astrophysics and Space Science* 337 (1), 65–78.
- Massie, S. T., Hunten, D. M., 1982. Conversion of para and ortho hydrogen in the Jovian planets. *Icarus* 49, 213–226.
- Max, C. E., Macintosh, B. A., Gibbard, S. G., Gavel, D. T., Roe, H. G., de Pater, I., Ghez, A. M., Acton, D. S., Lai, O., Stomski, P., Wizinowich, P. L., 2003. Cloud structures on Neptune observed with Keck telescope adaptive optics. *The Astronomical Journal* 125 (1), 364.
- Maxworthy, T., 1984. The dynamics of a high-speed Jovian jet. *Planetary and Space Science* 32 (8), 1053–1058.
- McMaster, Biretta, et al., 2008. WFPC2 Instrument Handbook. Baltimore: STScI.
- Militzer, B., Hubbard, W. B., 2013. Ab initio equation of state for hydrogen-helium mixtures with recalibration of the giant-planet mass-radius relation. *The Astrophysical Journal* 774 (2), 148.

- Molter, E., de Pater, I., Luszcz-Cook, S., Hueso, R., Tollefson, J., Alvarez, C., Sanchez-Lavega, A., Wong, M. H., Hsu, A. I., Sromovsky, L. A., Fry, P. M., Delcroix, M., Campbell, R., de Kleer, K., Gates, E., Lynam, P. D., Ammons, S. M., Coy, B. P., Duchene, G., Gonzales, E. J., Hirsch, L., Magnier, E. A., Ragland, S., Rich, R. M., Wang, F., 2019. Analysis of Neptunes 2017 bright equatorial storm. *Icarus* 321, 324–345.
- Moses, J. I., Fouchet, T., Bezaud, B., Gladstone, G. R., Lellouch, E., Feuchtgruber, H., 2005. Photochemistry and diffusion in Jupiter's stratosphere: Constraints from ISO observations and comparisons with other giant planets. *Journal of Geophysical Research: Planets* 110 (E8), e08001.
- Murphy, R. E., Trafton, L. M., 1974. Evidence for an internal heat source in Neptune. *The Astrophysical Journal* 193, 253–255.
- Ness, N. F., Acuna, M. H., Behannon, K. W., Burlaga, L. F., Connerney, J. E. P., Lepping, R. P., Neubauer, F. M., 1986. Magnetic fields at Uranus. *Science* 233, 85–89.
- Ness, N. F., Acuna, M. H., Burlaga, L. F., Connerney, J. E. P., Lepping, R. P., Neubauer, F. M., 1989. Magnetic fields at Neptune. *Science* 246, 1473–1478.
- Ortiz, J. L., Orton, G. S., Friedson, A. J., Stewart, S. T., Fisher, B. M., Spencer, J. R., 1998. Evolution and persistence of 5-m hot spots at the galileo probe entry latitude. *Journal of Geophysical Research: Planets* 103 (E10), 23051–23069.
- Orton, G. S., Encrenaz, T., Leyrat, C., Puetter, R., Friedson, A. J., 2007. Evidence for methane escape and strong seasonal and dynamical perturbations of Neptune's atmospheric temperatures. *Astronomy & Astrophysics* 473 (1), L5–L8.
- Pasachoff, J. M., Schneider, G., Babcock, B. A., Lu, M., Edelman, E., Reardon, K., Widemann, T., Tanga, P., Dantowitz, R., Silverstone, M. D., Ehrenreich, D., Vidal-Madjar, A., Nicholson, P. D., Willson, R. C., Kopp, G. A., Yurchyshyn, V. B., Sterling, A. C., Scherrer, P. H., Schou, J., Golub, L., McCauley, P., Reeves, K., 2013. Three 2012 Transits of Venus: From Earth, Jupiter, and Saturn. In: *American Astronomical Society Meeting Abstracts #221*. Vol. 221 of *American Astronomical Society Meeting Abstracts*. p. 315.06.
- Pearl, J. C., Conrath, B. J., 1991. The albedo, effective temperature, and energy balance of Neptune, as determined from Voyager data. *Journal of Geophysical Research* 96 (S01), 18921–18930.
- Pedlosky, J., 1987. *Geophysical Fluid Dynamics*. Springer-Verlag New York.
- Pérez-Hoyos, S., Sánchez-Lavega, A., 2006. On the vertical wind shear of Saturn's Equatorial Jet at cloud level. *Icarus* 180, 161–175.

- Porco, C. C., West, R. A., McEwen, A., Del Genio, A. D., Ingersoll, A. P., Thomas, P., Squyres, S., Dones, L., Murray, C. D., Johnson, T. V., Burns, J. A., Brahic, A., Neukum, G., Veverka, J., Barbara, J. M., Denk, T., Evans, M., Ferrier, J. J., Geissler, P., Helfenstein, P., Roatsch, T., Throop, H., Tiscareno, M., Vasavada, A. R., 2003. Cassini Imaging of Jupiter's Atmosphere, Satellites, and Rings. *Science* 299 (5612), 1541–1547.
- Rayner, J. T., Toomey, D. W., Onaka, P. M., Denault, A. J., Stahlberger, W. E., Vacca, W. D., Cushing, M. C., Wang, S., 2003. SpeX: A Medium-Resolution 0.8–5.5 Micron Spectrograph and Imager for the NASA Infrared Telescope Facility. *Publications of the Astronomical Society of the Pacific* 115, 362–382.
- Rogers, J., 2016. Jupiter in 2016/17: Report no.1. First report on the 2016 NTBs outbreak. British Astronomical Association.
- Rogers, J., Adamoli, G., 2012. Jupiter in 2012/13: Interim report no.3 (2012 Sep.20) Progress of Jupiters great northern upheaval. British Astronomical Association.
- Rogers, J., Adamoli, G., Hahn, G., Jacquesson, M., Vedovato, M., Mettig, H. J., 2013. Jupiters South Temperate domain: Behaviour of long-lived features and jets, 2001-2012. British Astronomical Association.
- Sánchez-Lavega, A., García-Melendo, E., Pérez-Hoyos, S., Hueso, R., Wong, M. H., Simon, A., Sanz-Requena, J. F., Antuñano, A., Barrado-Izagirre, N., Garate-Lopez, I., Rojas, J. F., Del Río-Gaztelurrutia, T., Gómez-Forrellad, J. M., de Pater, I., Li, L., Barry, T., 2016. An enduring rapidly moving storm as a guide to Saturn's Equatorial jet's complex structure. *Nature Communications* 7, 13262.
- Sánchez-Lavega, A., Miyazaki, I., Parker, D., Laques, P., Lecacheux, J., 1991. A disturbance in Jupiter's high-speed North temperate jet during 1990. *Icarus* 94 (1), 92–97.
- Sánchez-Lavega, A., Orton, G. S., Hueso, R., Garcia-Melendo, E., Perez-Hoyos, S., Simon-Miller, A., Rojas, J. F., Gomez, J. M., Yanamandra-Fisher, P., Fletcher, L., Joels, J., Kemerer, J., Hora, J., Karkoschka, E., de Pater, I., Wong, M. H., Marcus, P. S., Pinilla-Alonso, N., Carvalho, F., Go, C., Parker, D., Salway, M., Valimberti, M., Wesley, A., Pujic, Z., 2008. Depth of a strong jovian jet from a planetary-scale disturbance driven by storms. *Nature* 451 (7177), 437–440.
- Sánchez-Lavega, A., Rogers, J. H., S., O. G., García-Melendo, E., Legarreta, J., Colas, F., Dauvergne, J. L., Hueso, R., Rojas, J. F., Pérez-Hoyos, S., Mendikoa, I., Iñurrigarro, P., Gómez-Forrellad, J. M., Momary, T., Hansen, C. J., Eichstaedt, G., Miles, P., A., W., 2017. A planetary-scale disturbance in the most intense Jovian atmospheric jet from JunoCam and ground-based observations. *Geophysical Research Letters* In Press.
- Sault, R. J., Teuben, P. J., Wright, M. C. H., 1995. A Retrospective View of MIRIAD. In: Shaw, R. A., Payne, H. E., Hayes, J. J. E. (Eds.), *Astronomical Data Analysis Software and Systems IV*. Vol. 77 of *Astronomical Society of the Pacific Conference Series*. p. 433.

- Seager, S., Kuchner, M., Hier-Majumder, C. A., Militzer, B., 2007. Mass-radius relationships for solid exoplanets. *The Astrophysical Journal* 669 (2), 1279–1297.
- Showman, A., Dowling, T., 2000. Nonlinear Simulations of Jupiter’s 5-Micron Hot Spots. *Science* 289, 1737–1740.
- Simon, A. A., Rowe, J. F., Gaulme, P., Hammel, H. B., Casewell, S. L., Fortney, J. J., Gizis, J. E., Lissauer, J. J., Morales-Juberias, R., Orton, G. S., Wong, M. H., Marley, M. S., 2016. Neptune’s Dynamic Atmosphere from Kepler K2 Observations: Implications for Brown Dwarf Light Curve Analyses. *The Astrophysical Journal* 817 (2), 162–171.
- Simon, A. A., Wong, M. H., Hsu, A. I., 2019. Formation of a new great dark spot on neptune in 2018. *Geophysical Research Letters* 46 (6), 3108–3113.
- Simon, A. A., Wong, M. H., Orton, G. S., 2015. First Results from the Hubble OPAL Program: Jupiter in 2015. *The Astrophysical Journal* 812 (1), 55.
- Simon-Miller, A. A., Conrath, B. J., Gierasch, P. J., Orton, G. S., Achterberg, R. K., Flasar, F. M., Fisher, B. M., 2006. Jupiter’s atmospheric temperatures: From Voyager IRIS to Cassini CIRS. *Icarus* 180 (1), 98–112.
- Simon-Miller, A. A., Gierasch, P. J., 2010. On the long-term variability of Jupiter’s winds and brightness as observed from Hubble. *Icarus* 210, 258–269.
- Simon-Miller, A. A., Poston, B. W., Orton, G. S., Fisher, B., 2007. Wind variations in Jupiter’s equatorial atmosphere: A QJO counterpart? *Icarus* 186, 192–203.
- Simon-Miller, A. A., Rogers, J. H., Gierasch, P. J., Choi, D., Allison, M. D., Adamoli, G., Mettig, H.-J., 2012. Longitudinal variation and waves in Jupiter’s south equatorial wind jet. *Icarus* 218, 817–830.
- Slipher, V. M., 1909. The Spectrum of the Major Planets. *Lowell. Observ. Bull.* (42), 231–238.
- Slipher, V. M., 1933. Spectrographic studies of the planets. *Monthly Notices Roy. Astron. Soc.* 93, 657–668.
- Smith, B. A., Reitsema, H. J., Larson, S. M., 1979. Discrete Cloud Features on Neptune. In: *Bulletin of the American Astronomical Society*. Vol. 11 of . p. 570.
- Smith, B. A., Soderblom, L. A., Banfield, D., Barnet, c., Basilevsky, A. T., Beebe, R. F., Bollinger, K., Boyce, J. M., Brahic, A., Briggs, G. A., Brown, R. H., Chyba, c., Collins, s. A., Colvin, T., Cook, A. F., Crisp, D., Croft, S. K., Cruikshank, D., Cuzzi, J. N., Danielson, G. E., Davies, M. E., De Jong, E., Dones, L., Godfrey, D., Goguen, J., Grenier, I., Haemmerle, V. R., Hammel, H., Hansen, c. J., Helfenstein, c. P., Howell, C., Hunt, G. E., Ingersoll, A. P., Johnson, T. V., Kargel, J., Kirk, R., Kuehn, D. I., Limaye, S.,

- Masursky, H., McEwen, A., Morrison, D., Owen, T., Owen, W., Pollack, J. B., Porco, c. c., Rages, K., Rogers, P., Rudy, D., Sagan, C., Schwartz, J., Shoemaker, E. M., Showalter, M., Sicardy, B., Simonelli, D., Spencer, J., Sromovsky, L. A., Stoker, C., Strom, R. G., Suomi, V. E., Synott, S. P., Terrile, R. J., Thomas, P., Thompson, W. R., Verbiscer, A., Veverka, J., 1989. Voyager 2 at Neptune: Imaging science results. *Science* 246 (4936), 1422–1449.
- Spiegelhalter, D. J., Best, N. G., Carlin, B. P., Van Der Linde, A., 2002. Bayesian measures of model complexity and fit. *Journal of the Royal Statistical Society: Series B (Statistical Methodology)* 64 (4), 583–639.
- Sromovsky, L., Fry, P., Hammel, H., Ahue, W., de Pater, I., Rages, K., Showalter, M., van Dam, M., 2009. Uranus at equinox: Cloud morphology and dynamics. *Icarus* 203 (1), 265–286.
- Sromovsky, L. A., Fry, P. M., 2005. Dynamics of cloud features on Uranus. *Icarus* 179 (2), 459–484.
- Sromovsky, L. A., Fry, P. M., Baines, K. H., Limaye, S. S., Orton, G. S., Dowling, T. E., 2001a. Coordinated 1996 HST and IRTF imaging of Neptune and Triton: I. Observations, navigation, and differential deconvolution. *Icarus* 149 (2), 416–434.
- Sromovsky, L. A., Fry, P. M., Dowling, T. E., Baines, K. H., Limaye, S. S., 2001b. Coordinated 1996 HST and IRTF Imaging of Neptune and Triton: III. Neptune’s Atmospheric Circulation and Cloud Structure. *Icarus* 149 (2), 459–488.
- Sromovsky, L. A., Fry, P. M., Dowling, T. E., Baines, K. H., Limaye, S. S., 2001c. Neptune’s Atmospheric Circulation and Cloud Morphology: Changes Revealed by 1998 HST Imaging. *Icarus* 150, 244–260.
- Sromovsky, L. A., Fry, P. M., Hammel, H. B., de Pater, I., Rages, K. A., 2012. Post-equinox dynamics and polar cloud structure on Uranus. *Icarus* 220 (2), 694–712.
- Sromovsky, L. A., Fry, P. M., Limaye, S. S., Baines, K. H., 2003. The nature of Neptune’s increasing brightness: evidence for a seasonal response. *Icarus* 163 (1), 256–261.
- Sromovsky, L. A., Karkoschka, E., Fry, P. M., Hammel, H. B., de Pater, I., Rages, K., 2014. Methane depletion in both polar regions of Uranus inferred from HST/STIS and Keck/NIRC2 observations. *Icarus* 238, 137 – 155.
- Sromovsky, L. A., Limaye, S. S., Fry, P. M., 1993. Dynamics of Neptune’s major cloud features. *Icarus* 105 (1), 110–141.
- Stanley, S., Bloxham, J., 2004. Convective-region geometry as the cause of Uranus’ and Neptune’s unusual magnetic fields. *Nature* 428, 151–153.

- Stanley, S., Bloxham, J., 2006. Numerical dynamo models of uranus' and neptune's magnetic fields. *Icarus* 184 (2), 556–572.
- Stevenson, D. J., 1982. Interiors of the giant planets. *Annual Review of Earth and Planetary Sciences* 10 (1), 257–295.
- Sun, Z.-P., Stoker, C. R., Schubert, G., 1991. Thermal and humidity winds in outer planet atmospheres. *Icarus* 91 (1), 154–160.
- Tollefson, J., de Pater, I., Luszcz-Cook, S., DeBoer, D., 2019. Neptune's Latitudinal Variations as Viewed with ALMA. *The Astronomical Journal* 157 (6), 251.
- Tollefson, J., Pater, I. d., Marcus, P. S., Luszcz-Cook, S., Sromovsky, L. A., Fry, P. M., Fletcher, L. N., Wong, M. H., 2018. Vertical wind shear in Neptune's upper atmosphere explained with a modified thermal wind equation. *Icarus* 311, 317–339.
- Tollefson, J., Wong, M. H., de Pater, I., Simon, A. A., Orton, G. S., Rogers, J. H., Atreya, S. K., Cosentino, R. G., Januszewski, W., Morales-Juberas, R., Marcus, P. S., 2017. Changes in Jupiters Zonal Wind Profile preceding and during the Juno mission. *Icarus* 296, 163–178.
- Trafton, L. M., 1967. Model atmospheres of the major planets. *The Astrophysical Journal* 147, 765–781.
- Wallace, L., 1980. The structure of the Uranus atmosphere. *Icarus* 43, 231–259.
- Warwick, J. W., Evans, D. R., Peltzer, G. R., Peltzer, R. G., Romig, J. H., Sawyer, C. B., Riddle, A. C., Schweitzer, A. E., Desch, M. D., Kaiser, M. L., Farrell, W. M., Carr, T. D., de Pater, I., Staelin, D. H., Gulkis, S., Poynter, R. L., Boischoy, A., Genova, F., Leblanc, Y., Lecacheux, A., Pedersen, B. M., Zarka, P., 1989. Voyager planetary radio astronomy at Neptune. *Science* 246, 1498–1501.
- Weidenschilling, S., Lewis, J., 1973. Atmospheric and cloud structures of the jovian planets. *Icarus* 20 (4), 465–476.
- Wong, M. H., Atreya, S. K., Kuhn, W. R., Romani, P. N., Mihalka, K. M., 2015a. Fresh clouds: A parameterized updraft method for calculating cloud densities in one-dimensional models. *Icarus* 245, 273–281.
- Wong, M. H., Fry, P. M., Simon, A. A., 2016. Neptune. *IAUC* 4278.
- Wong, M. H., Lunine, J. I., Atreya, S. K., Johnson, T., Mahaffy, P. R., C., O. T., T., E., 2008. Oxygen and Other Volatiles in the Giant Planets and their Satellites. *Reviews in Mineralogy & Geochemistry* 68, 219–246.
- Wong, M. H., Pavlosky, C., Long, K., et al., 2010. *Wide Field Camera 3 Instrument Handbook*. Baltimore: STScI.

- Wong, M. H., Simon, A. A., Orton, G. S., de Pater, I., Sayanagi, K. M., 2015b. Hubble's Long-Term OPAL (Outer Planet Atmospheres Legacy) Program Observes Cloud Activity on Uranus. In: Lunar and Planetary Science Conference. Vol. 46 of Lunar and Planetary Inst. Technical Report. p. 2606.
- Wong, M. H., Tollefson, J., Hsu, A. I., de Pater, I., Simon, A. A., Hueso, R., Sánchez-Lavega, A., Sromovsky, L., Fry, P., Luszcz-Cook, S., Hammel, H., Delcroix, M., de Kleer, K., Orton, G. S., Baranec, C., 2018. A New Dark Vortex on Neptune. *The Astronomical Journal* 155 (3), 117.
- Young, R. E., 2003. The Galileo probe: how it has changed our understanding of Jupiter. *New Astronomy Reviews* 47, 1–51.